Advanced Structured Materials

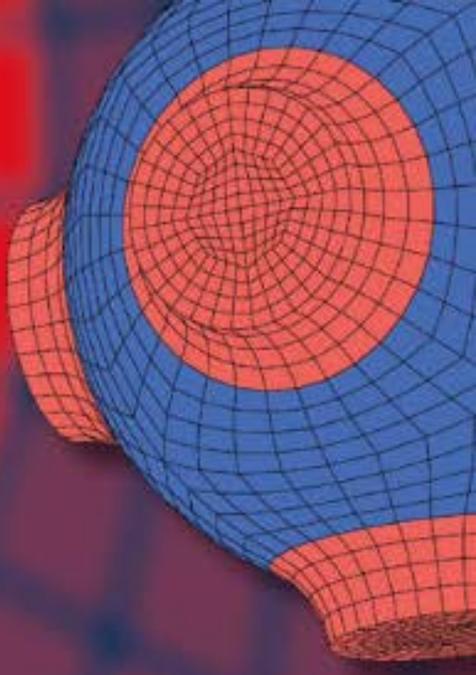

J. M. P. Q. Delgado *Editor*

Heat and Mass Transfer in Porous Media

Springer

Advanced Structured Materials

Volume 13

For further volumes:
http://www.springer.com/series/8611

J. M. P. Q. Delgado
Editor

Heat and Mass Transfer in Porous Media

Springer

J. M. P. Q. Delgado
Laboratorio de Fisica das Construccoes
Faculdade de Engenharia
Universidade do Porto
Rua Dr. Roberto Frias
4200-465 Porto
Portugal
e-mail: jdelgado@fe.up.pt

ISSN 1869-8433
ISBN 978-3-642-21965-8
DOI 10.1007/978-3-642-21966-5
Springer Heidelberg Dordrecht London New York

e-ISSN 1869-8441
e-ISBN 978-3-642-21966-5

Library of Congress Control Number: 2011937769

Cover design: eStudio Calamar, Berlin/Figueres

Printed on acid-free paper

Springer is part of Springer Science+Business Media (www.springer.com)

Contents

Treatment of Rising Damp in Historical Buildings

Ana Sofia Guimarães, Vasco Peixoto de Freitas and João M. P. Q. Delgado

Abstract Humidity is one of the main causes of decay in buildings, particularly rising damp, caused by the migration of moisture from the ground through the materials of the walls and floors via capillary action. This water comes from groundwater and surface water. The height that moisture will reach through capillary action depends upon factors such as the quantity of water in contact with the particular part of the building, surface evaporation conditions, wall thickness, building orientation and the presence of salts.

In historic buildings, rising damp is particularly difficult to treat, due to the thickness and heterogeneity of the walls. Traditional methods of dealing with this problem (chemical or physical barriers, electro-osmosis, etc.) have proved somewhat ineffective. There is therefore a need to study new systems.

In recent years, experimental research into the effectiveness of wall base ventilation systems (natural or hygro-regulated) to reduce the level of rising damp, conducted at the Building Physics Laboratory, Faculty of Engineering, University of Oporto, has yielded interesting results. Numerical simulation studies, using the software WUFI-2D, have given similar findings.

This paper describes a new system for treating rising damp in historic buildings based upon a hygro-regulated wall base ventilation system, and analyses the results obtained following implementation of the system in churches in Portugal.

A. S. Guimarães (✉) · V. P. de Freitas · J. M. P. Q. Delgado
LFC Building Physics Laboratory, Civil Engineering Department, Faculty of Engineering, University of Porto, Porto, Portugal
e-mail: anasofia@fe.up.pt

V. P. de Freitas
e-mail: vpfreita@fe.up.pt

J. M. P. Q. Delgado
e-mail: jdelgado@fe.up.pt

J. M. P. Q. Delgado (ed.), *Heat and Mass Transfer in Porous Media*, Advanced Structured Materials 13, DOI: 10.1007/978-3-642-21966-5_1,

It was defined criterions to avoid condensation problems inside the system and crystallizations/dissolutions problems at the walls.

1 State of the Art: Rising Damp

Humidity is one of the main causes of decay in buildings, particularly rising damp, caused by the migration of moisture from the ground through the materials of the walls and floors via capillary action. This water comes from groundwater and surface water. The height that moisture will reach through capillary action depends upon factors such as the quantity of water in contact with the particular part of the building, surface evaporation conditions, wall thickness, building orientation and the presence of salts.

In historic buildings, rising damp is particularly difficult to treat, due to the thickness and heterogeneity of the walls. Traditional methods of dealing with this problem (chemical or physical barriers, electro-osmosis, etc.) have proved somewhat ineffective. There is therefore a need to study new systems.

In recent years, experimental research into the effectiveness of wall base ventilation systems (natural or hygro-regulated) to reduce the level of rising damp, conducted at the Building Physics Laboratory, Faculty of Engineering, University of Oporto, has yielded interesting results. Numerical simulation studies, using the programme WUFI-2D, have given similar findings.

This paper describes a new system for treating rising damp in historic buildings based upon a hygro-regulated wall base ventilation system, and analyses the results obtained following implementation of the system in churches in Portugal.

It was defined criterions to avoid condensation problems inside the system and crystallizations/dissolutions problems at the walls.

1.1 Mechanisms Underlying Rising Damp

The mechanisms underlying the transportation of moisture through buildings are complex. During the vapour phase, diffusion and convection play a part, while capillary action, gravity and the pressure gradient effect control the transfer of moisture in its liquid phase [1, 2].

In practice, transportation occurs in the liquid and vapour phases simultaneously, and is dependent upon conditions such as temperature, relative humidity, precipitation, solar radiation and atmospheric wind pressure (which define the boundary conditions) and the characteristics of the building materials used.

From the physical point of view, there are three main mechanisms involved in moisture fixation: hygroscopicity, condensation and capillarity. In most cases, these three mechanisms account for variations in moisture content in building

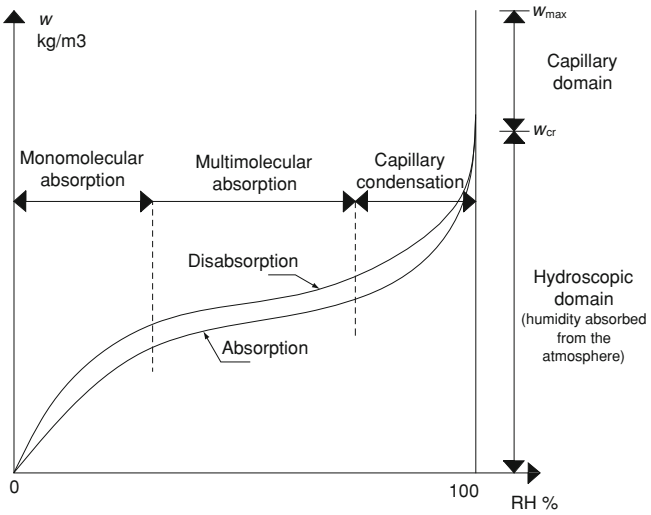

Fig. 1 Hygroscopic behaviour of building materials with relation to relative humidity

materials with a porous structure. Capillarity and hygroscopicity affect rising damp [1].

1.2 Hygroscopicity

The materials currently used in civil engineering are hygroscopic; this means that, when they are placed in an atmosphere where the relative humidity varies, their moisture content will also vary. The phenomenon, represented graphically in (see Fig. 1), is attributed to the action of intermolecular forces that act upon the fluid–solid interface inside the pores. The transfer of moisture between the wall surface and the atmosphere is also conditioned by hygroscopicity. This will be discussed further in Sect. 3.

1.3 Capillarity

Capillarity occurs when a porous material comes into contact with water in its liquid phase. The humidification of the material by capillary action is illustrated in (see Fig. 2).

This phenomenon results from the particular humidification properties of solid matrix, leading to the formation of curved interfaces between the fluid (water) and the air contained inside the pores. At the liquid–gas interface, a pressure gradient is

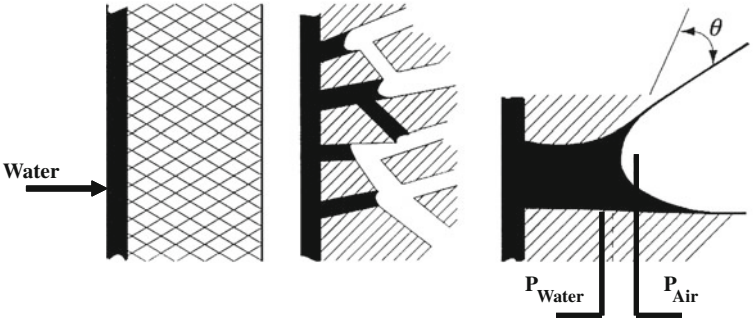

Fig. 2 Capillary action

established designated by capillary pressure, which is a function of interfacial tension s, the radii of the main curvature R and the humidification angle θ_h (1):

$$P_c = P_{air} - P_{water} = \sigma\left(\frac{1}{R_1} + \frac{1}{R_2}\right)\cos\theta_h \quad \left[N/m^2\right] \tag{1}$$

where P_c is the capillary pressure (N/m^2 or Pa), P_{air} is the air pressure (N/m^2 or Pa), P_{water} is the water pressure (N/m^2 or Pa), θ_h is the humidification angle (°), s is the surface tension (N/m) and R_1, R_2 is the Radii of curvature (m).

Capillary pressure is a function of the temperature and moisture content, as s varies with temperature and R with the moisture content. The development of the capillary pressure curve (suction) depends upon the law of distribution, the radius of the pores and their variation. The higher the moisture content, the lower the suction, which is annulled when the moisture rate is equal to the maximum moisture content [2].

1.4 Action of Groundwater on Historic Buildings

Water seeping up from the ground may cause diminished performance in walls and floors. Most traditional building materials have a porous structure that leads to a high level of capillarity. This means water can migrate through capillary action, in the absence of any preventive barrier [3].

This water comes from two basic sources: groundwater and surface water. When it originates in groundwater aquifers, rising damp will manifest itself at a constant level throughout the year, as the source is active all year round. In this situation, damp stains reach a higher level on inside walls than on outside ones due to the fact that the evaporation conditions are less favourable.

When the source is surface water, the level reached by rising damp varies throughout the year. The height of the damp front may also vary from wall to wall, and is usually higher in the outside walls [4].

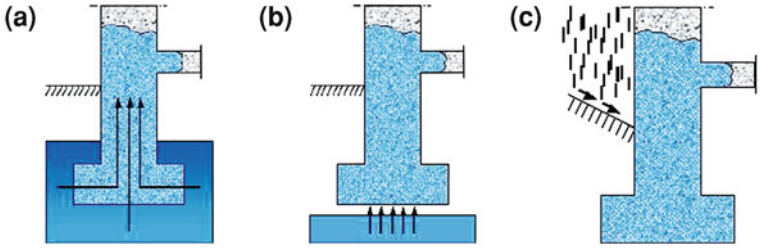

Fig. 3 Humidification of walls by groundwater and surface water. Ground water—wall with foundations **a** beneath the groundwater level, **b** above the groundwater level. **c** Surface water

1.5 Factors Conditioning Rising Damp

The height that moisture will reach through capillary action depends upon factors such as the quantity of water in contact with the particular part of the building, surface evaporation conditions, wall thickness, building orientation and the presence of salts [5, 6]. When atmospheric conditions are constant, the thicker the wall, the greater the height reached by the damp, as a greater quantity of water is absorbed (see Fig. 3).

Another important factor to take into account is the presence of salts, which also increases the height achieved by rising damp. The salts are dissolved when the relative humidity of the air rises and they crystallise again when this humidity declines. This crystallisation/dissolution process causes the materials to decay. There are various water-soluble salts in the walls of buildings, contained in the building materials or emanating from the soil. These dissolved salts are transported to the wall surface where they crystallise in the form of fluorescences or crypto fluorescences, depending upon whether the crystallisation takes place on the surface of the wall or beneath the wall renderings [7].

Rising damp depends upon the following factors [1]:

- Ambient climate (temperature and relative humidity);
- Solar radiation;
- The presence of salts;
- The porosity and porometry of building materials;
- Wall thickness;
- The kind of materials used for wall renderings.

1.5.1 Ambient Climate

The ambient climate affects the drying process and exerts great influence upon the level achieved by rising damp. In places with high relative humidity, evaporation is more difficult and there will consequently be greater progression of the damp front. Conversely, when relative humidity is low, evaporation will be greater and

the damp front will progress more slowly. The drying flow may be defined by the following formula (2):

$$g = \beta.(C'_s - C'_a) \tag{2}$$

where g is the flow density (kg/(m^{2}s), β is the surface moisture transfer coefficient (m/s), C'_s is the water vapour concentration at the surface (kg/m^3) and C'_a is the water vapour concentration in the air (kg/m^3).

Where there is no great temperature difference between the air inside the building and the inner surface of the wall, for high relative humidity, the concentration difference $(C'_s - C'_a)$ tends to zero, as does the drying flow.

1.5.2 Solar Radiation

In a building with identical climate conditions throughout, the progression of the damp front may vary in accordance with the orientation of the building and amount of solar radiation received. Solar radiation and the radiation absorption coefficient alter the surface temperature and temperature distribution, bringing consequences for the drying process.

1.5.3 The Presence of Salts

Salt crystallization is one of the main mechanisms involved in stone degradation. This degradation mechanism is based upon the pressure exerted by salt formation in the porous structures, with an increase in volume. It is dependent upon the types of salts involved, their size and the arrangement of the pores.

Temperature may have some influence in the process, because salt solubility depends upon it.

When the pressure exceeds the material's resistance capacity, and, particularly, when the salt formations result in cycles of crystallisation and dissolution in response to humidity fluctuations, there will typically be material losses.

The most characteristic salts are:

- Chlorides, which absorb large amounts of water;
- Nitrates of organic origin, of which the most common is calcium nitrate, which crystallises at 25°C and 50% relative humidity;
- Sulphates, which are hygroscopic and soluble, and which increase in volume upon crystallization. The most common are sulphates of calcium, sodium and magnesium.

Anomalies caused by the presence of salts may result in a variety of symptoms of degradation in wall renderings. These include: surface alterations (fluorescences or damp patches); cracking; the formation of crusts; the separation of building materials into layers (delamination, exfoliation, the detachment of coatings, etc.); loss of cohesion (e.g. pulverulence of ceramic or stone brick elements, arenization of mortars, etc.), and the formation of voids (such as alveolization).

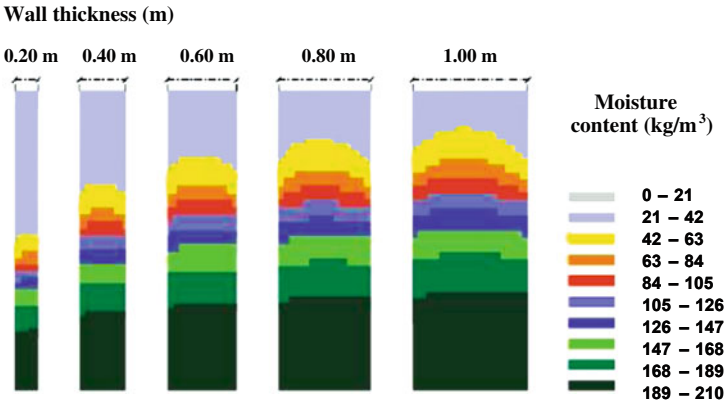

Fig. 4 Variation in moisture content through a cross section

1.5.4 Porosity and Porometry

A material's porosity may be defined as the ratio between the total volume of voids (pores and channels) and its total apparent volume. Practically all building materials are characterised by open porosity, and their moisture imbibitions capacity is directly related to porosity. In the case of closed porosity, when there is no intercommunication between pores, the material is impermeable and water cannot penetrate.

Materials with closed porosity are of interest for the prevention of rising damp, as they may be used to form a water barrier. Materials with open porosity, on the other hand, conduct the moisture by capillary action. Capillarity increases the smaller the diameter of the pores. Thus, porometry studies are useful, as they enable the size of the pores to be assessed.

1.5.5 Wall Thickness

The progression of rising damp stabilises when the flow through the absorbent section is equal to the total wall evaporation; that is to say, the amount of water that enters the wall through absorption is the same as the amount of water that leaves through evaporation.

Wall thickness affects the height reached by rising damp. Simulation studies have shown that the height reached by the damp front is significantly greater when the wall thickness increases from 0.20 to 1.00 m (see Fig. 4).

1.5.6 Kind of Materials Used for Wall Renderings

The damp-proofing of walls generally reduces the evaporation conditions, which increases the level of rising damp, until a new equilibrium is achieved. This is shown in Fig. 5.

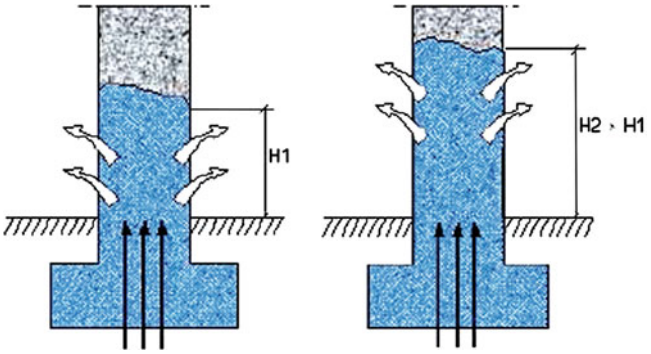

Fig. 5 Influence of impermeable materials placed on the wall surface at the level achieved by rising damp

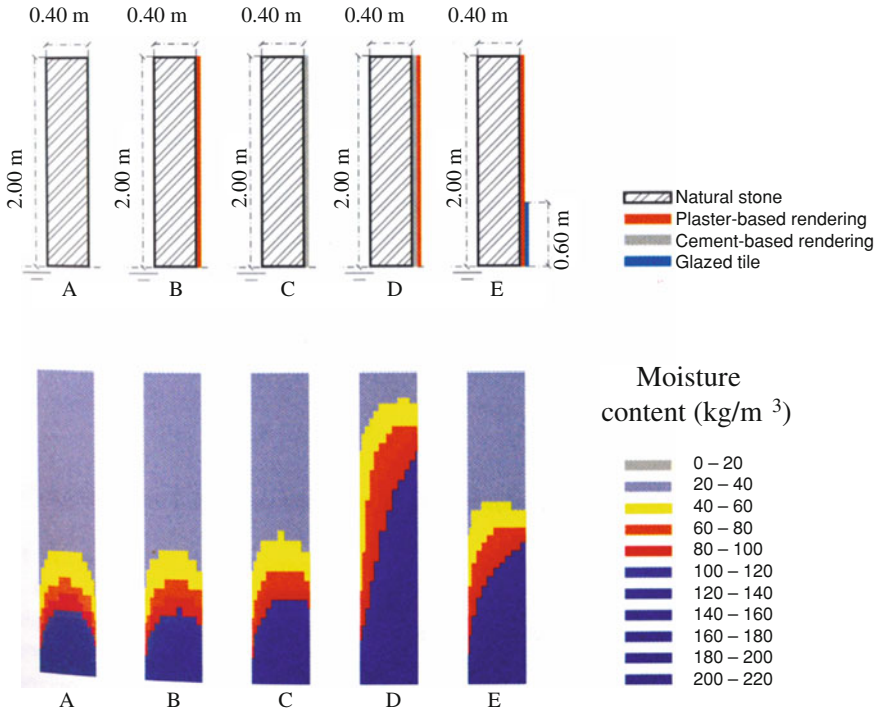

Fig. 6 Influence of the vapour permeability of renders

Figure 6 shows a sensitivity study into the level achieved by the damp front in five different configurations defined in Table 1.

The results clearly show that the lower the vapour permeability of the rendering (as in the case of Configuration D), the higher the level of the damp front.

Table 1 Configurations of walls analysed

Ref.	Configurations
A	Unrendered monolithic stone wall, 0.40 m thick
B	Monolithic stone wall, 0.40 m thick, with plaster-based rendering on one surface
C	Monolithic stone wall, 0.40 m thick, with rendering based on water-activated binders on one surface
D	Monolithic stone wall, 0.40 m thick, with rendering based on water-activated binders on one surface associated to glazed tile
E	Monolithic stone wall, 0.40 m thick, with plaster-based rendering on one surface, associated to 60 cm of glazed tile

1.6 The Problem in Historic Buildings

In Portugal there are several historical buildings damaged by rising damp and by the presence of salts that crystallizes and dissolve. Traditionally used techniques are not effective due to the thickness and heterogeneity of the walls. It was necessary to develop a new technique that solves this problem in these buildings.

In recent years, experimental research into the effectiveness of wall base ventilation systems (natural or hygro-regulated) to reduce the level of rising damp, conducted at the Building Physics Laboratory, Faculty of Engineering, University of Porto, has yielded interesting results. Numerical simulation studies, using the programme WUFI-2D, have given similar findings [1, 5].

2 Experimental Section

2.1 Wall Base Ventilation System

2.1.1 The Idea

The Laboratory of Building Physics (LFC) at the Faculty of Engineering, University of Porto (FEUP), has, for the last ten years, been engaged in experimental research in the area of rising damp, with a view to validating the effectiveness of a new treatment technique applied to the walls of old buildings.

This new technique consists of ventilating the base of walls through the installation of a hygro-regulable mechanical ventilation device. Wall base ventilation increases evaporation, which leads to a reduction in the level achieved by the damp front (see Fig. 7). This is possible only when the groundwater is lower than the base of the wall [1, 5].

It was also possible to develop a new device that controls the ventilator considers some studied parameters. The hygro-regulable engine is now working properly. This device is absolutely new and it was the result of some years of work on this area. This system was validated in laboratory and using a 2D program to

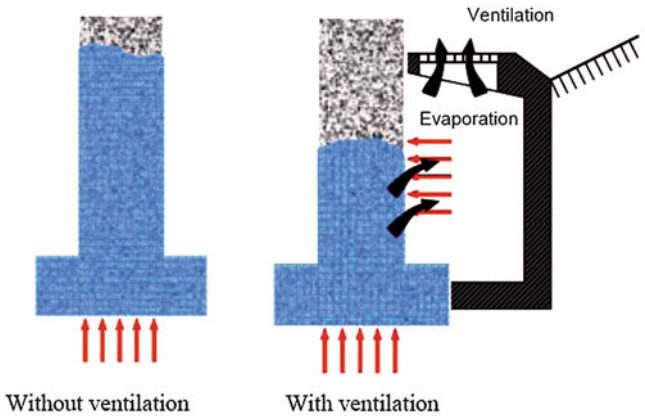

Fig. 7 Functioning principle of the wall base ventilation system

simulate its behaviour [8, 9]. The geometry was characterized experimentally and simultaneously it was monitories a Church in North of Portugal, since 2004. This information was essential to conclude about the best criterions of hygro-regulable mechanical ventilation device.

2.1.2 Validating the Effectiveness of the Ventilation System

Experimental Validation

In the laboratory, the relative humidity profile of 20 cm thick stone (limestone) walls was measured. In Configuration 1, this involved measuring the behaviour of one wall, without a ventilation system, by placing sand on both sides of the wall up to a height of 45 cm. In Configuration 2, in order to assess the effect of the insertion of a wall base ventilation system a ventilation channel was placed on both sides (Fig. 8). In this study it was not evaluated the importance of the velocity of the ventilator so this velocity was not controlled. It was used saturated sand with 45 cm height like the situation performed in the Church studied.

In Configuration 2, a mechanical ventilator was placed at one end of a tube, leaving the other end free. The tube has a diameter of 10 cm. This ventilation system functioned continuously throughout the testing period, so as to ensure that the temperature and relative humidity within the system were similar to the conditions inside the laboratory.

The configurations used are schematically represented in Fig. 9, as are the relative humidity profiles in the section located at Level 9, 61.5 cm above the base of the wall [5, 10]. The probes measure temperature and relative humidity and were placed at different levels, 5 and 10 cm inside the wall, to control the damp front.

Fig. 8 Physical model adopted for the experimental laboratory study

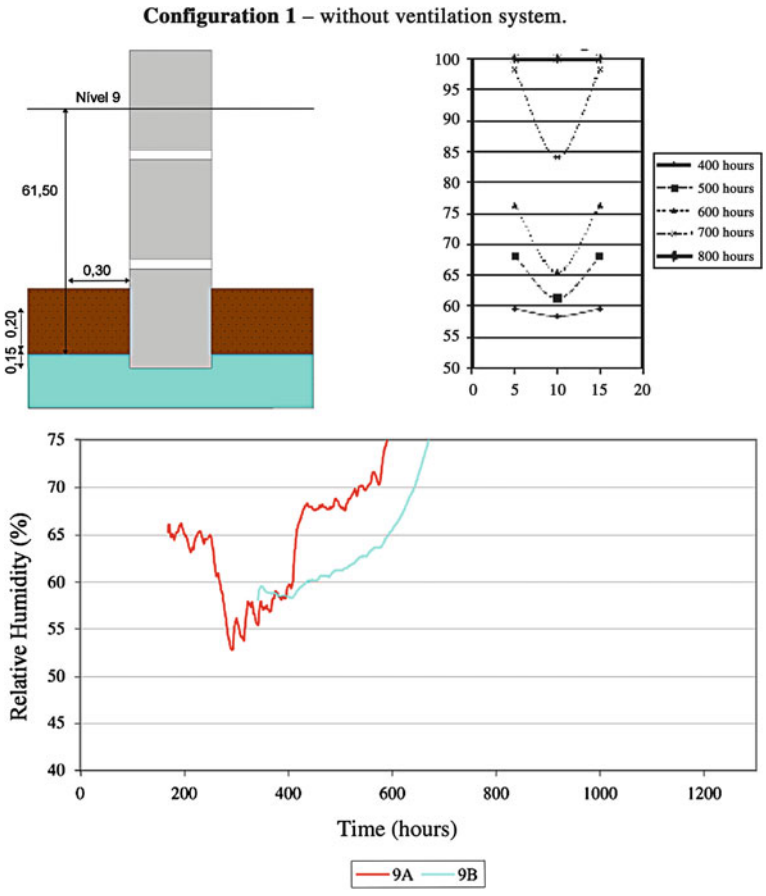

Fig. 9 Relative damp variation at Level 9 in Configurations 1 and 2

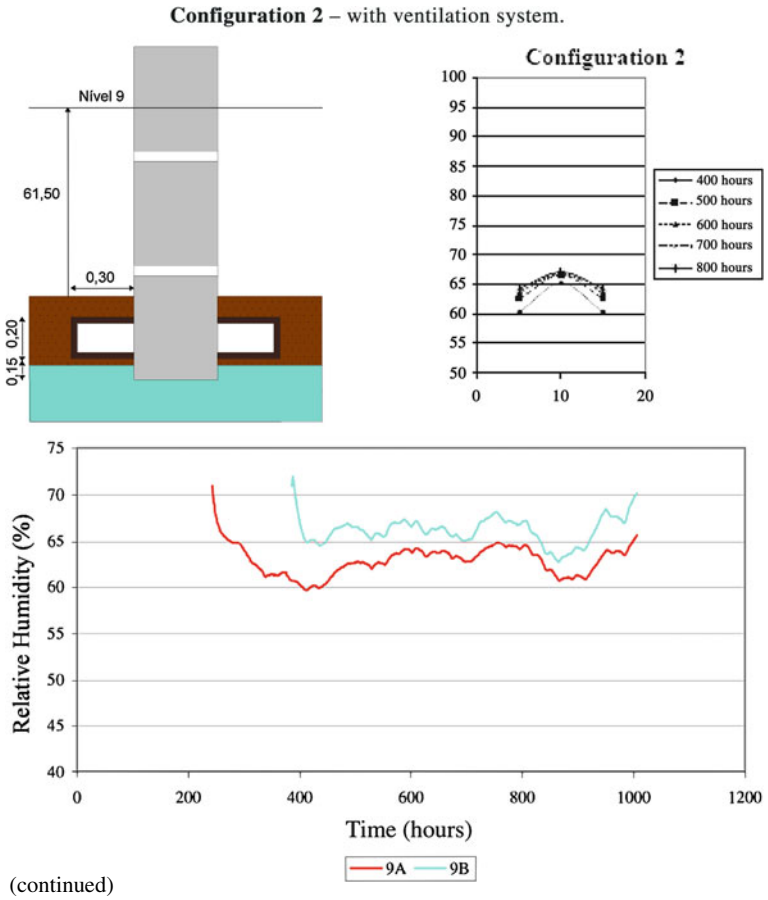

Fig. 9 (continued)

The results of the experiment show that the presence of a wall base ventilation system on both sides prevents the damp front from reaching Level 9 (i.e. a height of 61.5 cm).

Numerical Validation

In order to compare the results of the experiment with numerical results, simulations were performed using the programme "WUFI-2D" designed by the Fraunfofer Institute of Building Physics, which enables a 2D analysis of heat and moisture transfer between building materials [8, 9].

Of all the variables that can be obtained through numerical calculations, we chose those that can be recorded in our experiments: temperature and relative humidity. Since the experiments took place under isothermal conditions, only the change in relative humidity is important.

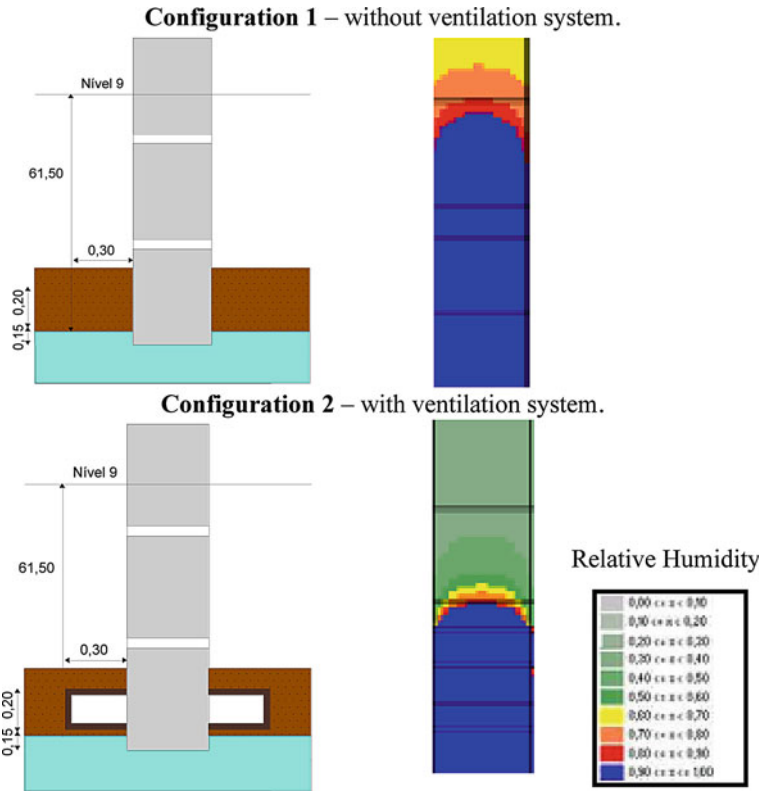

Fig. 10 Result of numerical simulations using the programme WUFI 2D

In the simulations carried out, the properties of the materials were determined experimentally in the Building Physics Laboratory and introduced into the programme, as were the boundary conditions, climatic conditions and the real duration of each simulation. This information was the input of WUFI-2D program.

Fist, it was necessary to design the wall, than it was important to characterize each material: bulk density, heat capacity, porosity, thermal conductivity, vapour diffusion resistance, moisture storage function, capillary transport coefficient, water absorption coefficient and free water saturation, second it was stipulated the climatic conditions (it was consider, by default, that in the base of the wall relative humidity was 100%) and finally it was introduced the real time of the simulation duration [8].

The results of the simulations corresponding to Configurations 1 and 2 are presented in Fig. 10. The damp level was clearly lower in Configuration 2 than in Configuration 1, as expected.

Assessment of the results of both the experiments performed and the numerical simulations allow us to conclude that a ventilation system placed at the base of walls reduces the level reached by the damp front. Wall base ventilation is, therefore, a simple technique that offers great potential [5, 10].

2.2 Experimental Study of the Ventilation System Configuration

2.2.1 Physical Model Adopted and Assessment of Geometry

Two different boundary conditions were used (Configuration A—horizontal waterproofing; Configuration B—system waterproofing). Probes were placed to obtain readings of the temperature and relative humidity at the entrance and exits of the ventilation systems (see Fig. 11) [11, 12].

2.2.2 Results

Figure 12 illustrates the materialization of the system and the means used to calculate the vapour pressure at the entrance and exit through temperature and relative humidity.

Using the temperature and relative humidity values at the entrance and exit of the systems, it was possible to calculate the vapour pressure (3), and then the quantity of water transported (4) and (5).

Figure 13 shows the quantity of accumulated water vapour transported during the testing period for various air circulation speeds. The functioning of the system was much more strongly influenced by the characteristics of the outside air than by the speed of the system. In Configuration A, we can see that, in certain time periods, the quantity of accumulated water vapour transported diminished, which means that condensation had occurred inside the system.

Analysis of vapour pressure variation at the entrance and exit of the system for each of the two configurations studied reveals that vapour pressure at the exit is generally greater than at the entrance. It also reveals the occurrence of periods of flow differences and that these were sometimes negative for Configuration A (see Fig. 14). This means that condensation had occurred inside the system. No condensation was found in Configuration B for the period analysed.

The inversion of pressure gradient occurs only at the exit, which means that the length of the system plays a fundamental role in its functioning.

The experimental characterization of Configurations A and B of the wall base ventilation system, carried out in the Laboratory, enabled the following conclusions to be drawn:

The continuous functioning of the ventilation system may lead to condensation, which can be avoided if a hygro-regulable system is used;

The outside climate is much more important than speed of air circulation for the amount of moisture transported to the exterior;

Configuration A is easier to execute in practice, given the need to waterproof the floor, and its behaviour is interesting, as it controls the risk of condensation.

The following phase in the research consisted of implementing a Type A system in a church in Northern Portugal, so as to acquire in situ validation of its effectiveness and fine-tune the hygro-regulable control system [11].

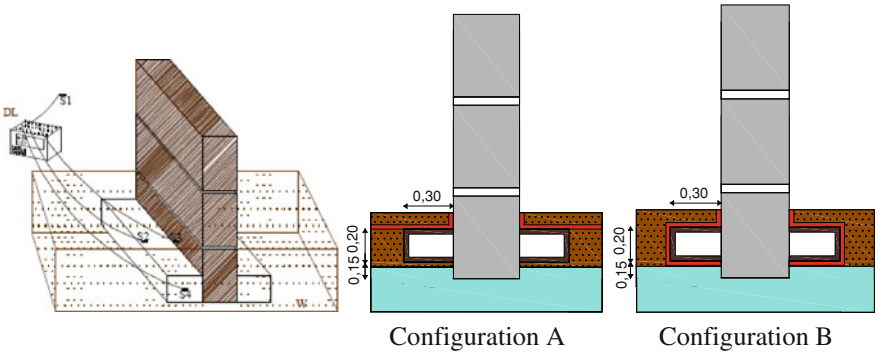

Fig. 11 Physical model—location of probes

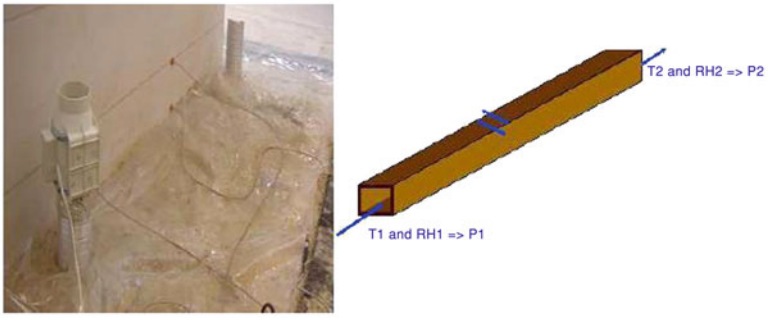

$P = e^{\frac{17.08*\theta}{234.18+\theta}} * HR$ (3)	$w=0.002167*P/\theta$ (4)	$W = (w_{exit}-w_{entrance})*Q*\Delta t$ (5)
P – Vapour pressure (N/m² or Pa); θ – Temperature (°C); RH – Relative Humidity (%)	w – Absolute air humidity (kg/m3); P – Vapour pressure (N/m² or Pa); θ – Air temperature (K).	W – Quantity of water removed (kg); W_{exit} – Absolute air humidity at exit of system (kg/m3); $W_{entrance}$ – Absolute air humidity at entrance of system (kg/m3); Q – Ventilation flow (m³/s); Δt – Time interval (s).
Note: As measurements were taken every 30 minutes, the temperature and relative humidity are considered constant during this time period.		

Fig. 12 Materialization of the system and calculation of vapour pressure

2.3 In Situ Validation and Fine-Tuning of the Hygro-Regulable System

2.3.1 Description

The system in question was installed in a Church in Northern Portugal (see Fig. 15). The exterior ventilation was natural, and therefore beyond the sphere of this paper (see Fig. 16).

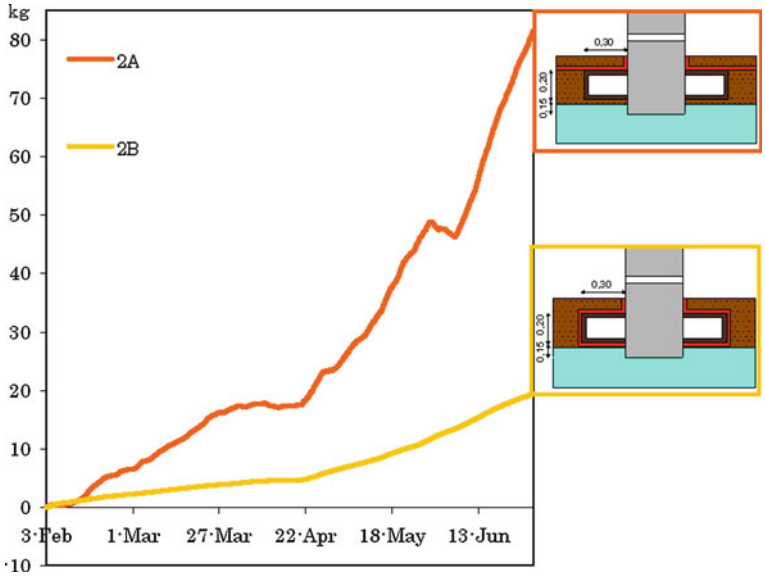

Fig. 13 Quantity of water vapour transported by the ventilation system to the exterior

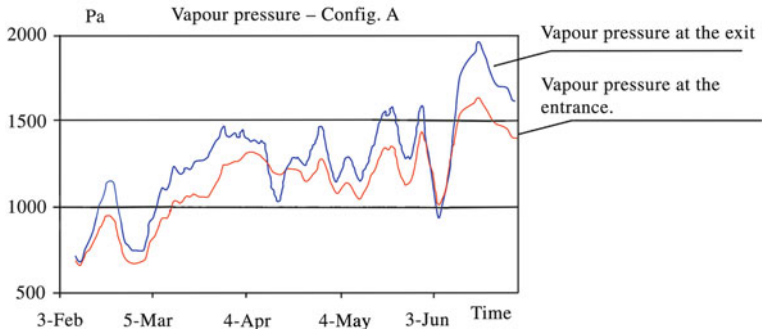

Fig. 14 Variation of vapour pressure at the entrance and exit

Inside the building, two hygro-regulable mechanical ventilation subsystems were installed. In the Southside subsystem, air was admitted through grids located inside the building, and was extracted into the cloister. Extraction was controlled by a hygro-regulable engine of variable speed [12]. In the inner face of the walls was placed a perforated tube with a diameter of 200 mm (concrete), immediately below the granite floor. Only the results of this subsystem are presented here (see Fig. 17).

The system had two probes for measuring relative humidity and temperature, two transmitters, a control module and a data acquisition system for recording results (see Fig. 18).

Fig. 15 Church in Northern Portugal

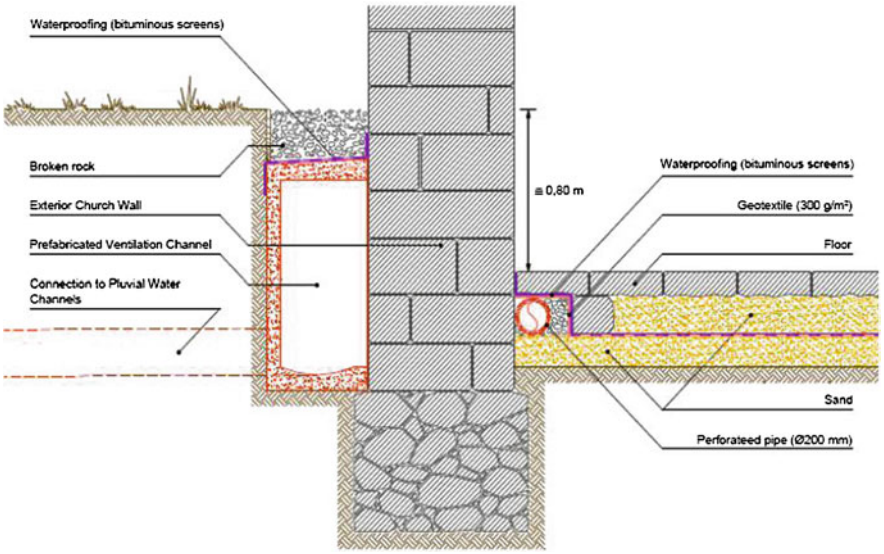

Fig. 16 Wall base ventilation system

The probes were installed, one at the entrance and the other at the exit of the system. Each probe has a transmitter that sends the results (relative humidity and temperature) to a data-logger. The control module gives orders to the ventilator device to turn on or to turn off the system according to the criterion of functioning. This device transforms the system in a hygro-regulable mechanical ventilation.

2.3.2 Results

The system initially began operating whenever the relative humidity at the exit was 5% higher than the relative humidity at the entrance. The idea was to

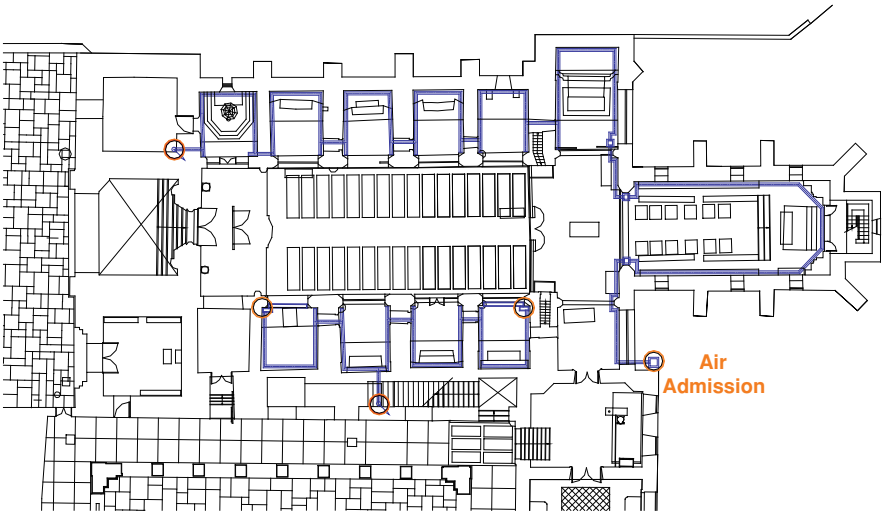

Fig. 17 Hygro-regulable wall base ventilation system with variable speeds

Fig. 18 Data acquisition and recording system

admit dry air comparing to the air inside the system. Figure 19 shows the periods of functioning of the ventilator. This criterion was found to be inadequate, as it meant that the system was operating at periods when condensation occurred inside it. Consequently, a new criterion was proposed with a view to optimizing the system, based upon the difference in vapour pressure (ΔP) at the exit and entrance. The system now began functioning whenever the ΔP was positive.

The entry of air with very low relative humidity could generate the crystallisation of salts existing in the building materials, threatening its durability. For this reason, the relative humidity value at the entrance had to be limited.

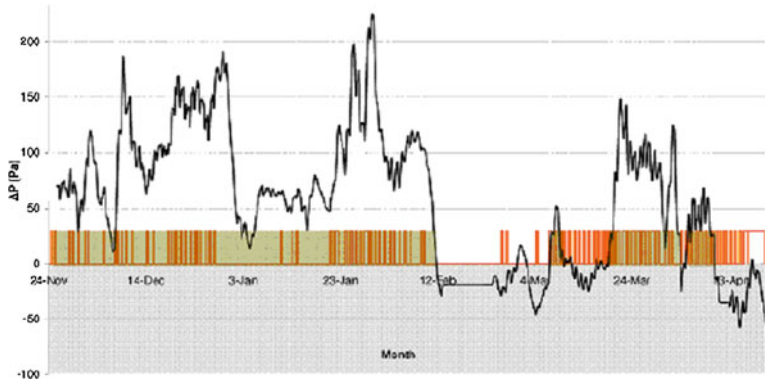

Fig. 19 Pressure differential and functioning of system

The relative humidity scores recorded, which range from 60 to 95%, are not considered to present a risk of salt crystallization/dissolution inside the system, consider the salts detected in those area. However, the problem might arise in another type of external climate or with other salts type [13, 14].

2.3.3 New Device

The work developed could optimise the functioning of the system. The extraction is know controlled by a variable speed motor, hygro-regulated which comes into operation when the water vapour pressure at the entrance is lower than the vapour pressure at the exit, resulted from the combination of the temperature and the relative humidity, and when the relative humidity of the air entry is higher than a certain predefined value to guarantee it will not have problems of salt crystallization/dissolution inside the system (Fig. 20).

The control module receives information from two probes (temperature and relative humidity at the entrance and at the exit), calculates the vapour pressure of water at the entrance and at the exit, evaluates the positive or negative sign of the pressure differential, shutting on or down the fan.

This device is now working with these two new criterions and, as soon as possible, it will be possible to see the results.

This new device called "HUMIVENT" was developed by the Laboratory of Building Physics, Faculty of Engineering, University of Porto, the prototype was developed by ITISE/ROTRONIC and is under Portuguese patent application No. 104,385, from the University of Porto, entitled "Sistema Higro-Regulável de Ventilação da Base das Paredes para Tratamento da Humidade Ascensional" (Hygro-Regulated Wall Base Ventilation System for the Treatment of Rising Damp)–(international extension via PCT/PT2009/000068).

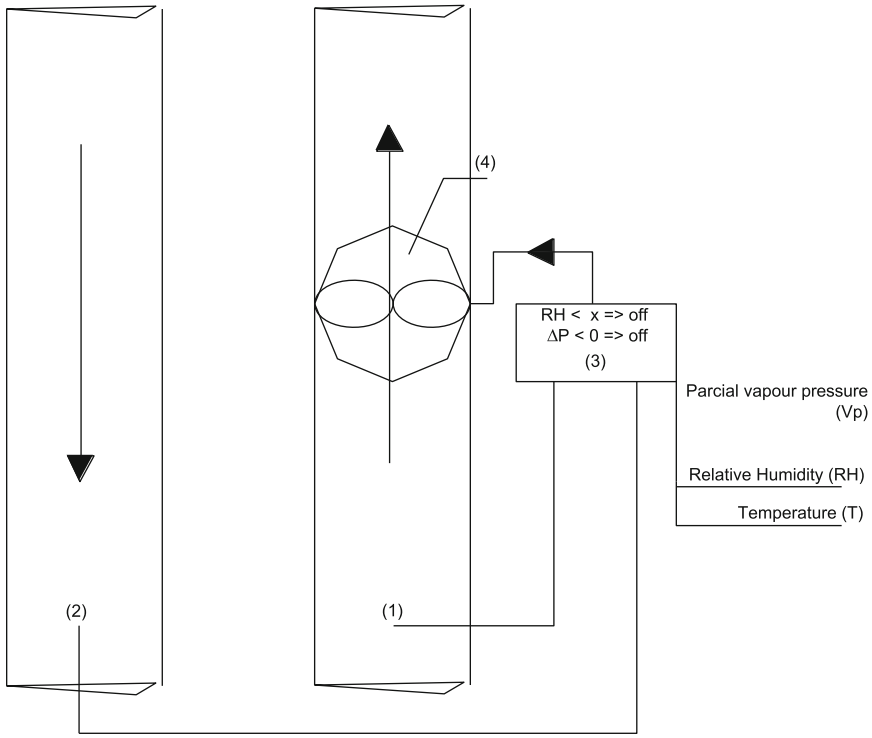

Probe (1) – Entrance (temperature and relative humidity)
Probe (2) – Exit (temperature and relative humidity)
Fan with variable speed (3)
Control module (4):
Probe 1 – θ1 e RH1 => Vapour pressure 1 (Pa)
Probe 2 – θ2 e RH2 => Vapour pressure 2 (Pa)
Calculate ΔP = P2-P1
Instructions of fan operation
On if ΔP ≥0 and RH1 > Predetermined value
Off if ΔP ≤0 or RH1 < Predetermined value

Fig. 20 The Principle of Functioning of a hygro-regulated wall base ventilation system

The prototype produced is composed of a data-logger with programmer, links to two probes of relative humidity (RH) and temperature (T), link up to four fans at the same time, battery, connection to a computer to make the programming of operation of the device, giving instructions to the data-logger logging information temporal RH and T, reading of records and data processing.

All necessary devices, formerly connected as necessary (like in the Church studied), were now compressed into a single optimized device—"HUMIVENT" (Fig. 21).

The operation of the prototype "HUMIVENT" was successfully tested.

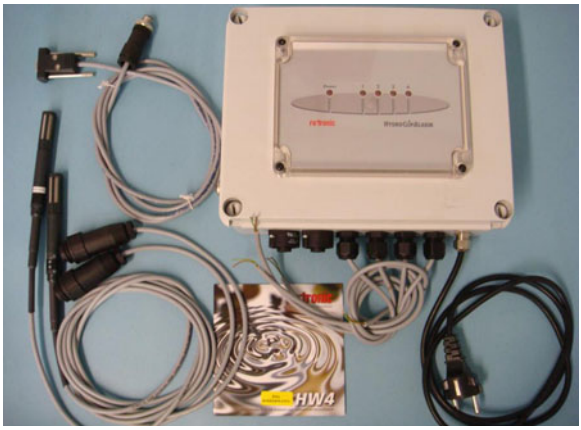

Fig. 21 The Prototype

3 Conclusions

The main conclusions that we can draw are as follows [5, 12]:

- The mechanisms involved in the transfer of moisture are complex, particularly so for rising damp in historic buildings;
- Rising damp is one of the main factors contributing to the degradation of the constructed heritage; it is therefore important to understand the factors causing it;
- The placement of vapour-impermeable layers on the wall surface increases the level reached by rising damp;
- Wall base ventilation is a simple technique that has a great potential in practice;
- The results of experiments performed at LFC-FEUP have shown that the installation of a wall base ventilation system on both side of the wall reduces the level of rising damp;
- Numerical studies presented similar results;
- The continuous functioning of the system may lead to the occurrence of interior condensation;
- A hygro-regulated system is thus essential to control unwanted condensation and crystallisation/dissolution cycles;
- Configuration A of the ventilation system is adequate, the easiest to execute, and may be combined with floor water-proofing.
- The experimental study carried out in situ proves the following [12]:
- The ventilation system implemented on the wall base presents good results in this building with thick and heterogeneous walls;
- It was confirmed that the system allowed, during most of the time, withdraw water walls, increasing evaporation, decreasing the wet front;
- The experimental study carried out in situ shows that the best programming criterion is to turn off the system whenever the vapour pressure at the exit is lower than the vapour pressure at the entrance;

- The mechanical hygro-regulated system, with a new criterion based on the vapour pressure, prevents condensation inside the system;
- The mechanical hygro-regulated system with a new functioning criterion that limits the relative humidity of the entry air prevents the appearance of crystallizations inside the system that be injurious to their own walls also undermines the proper functioning of the system;
- Relative humidity control on the admission can be important in certain climates in the prevention of salts crystallizations/dissolutions occurrence. This salts can already exists on the walls or can be dissolved on the water that flows in the walls interior;
- It was proved that the incoming air conditions are essential in behaviour/efficiency of the system;
- It is a simple and economic system whose maintenance is practically non-existent, so it is an extremely interesting system.

References

1. de Freitas, V.P., Torres, M.I.M., Guimarães, A.S.: Humidade Ascensional. FEUP edições, ISBN: 978-972-752-101-2, 1st edn. Porto (Portuguese) (2008)
2. de Freitas, V.P.: Transferência de humidade em paredes de edifícios. Ph.D. thesis, University of Porto, Portugal (Portuguese) (1992)
3. Centre Scientifique et Tecnhique du Batiment—Les procèdes de traitement des maçonneries contre l'humidité ascensionnelle, Note d'information technique 162, Bruxelles, 32 pgs. Nov–Des (1985)
4. Colombert, R.: L'Humidité des Bâtiments Anciens, Causes et Effets, Diagnostic et Remèdes. Editions du Moniteur, Paris (1975)
5. Torres, M.I.M.: Humidade Ascensional em Paredes de Construções Históricas, Ph.D. thesis, University of Coimbra, Portugal (Portuguese) (2004)
6. Torres, M.I.M., de Freitas, V.P.: Avaliação da eficiência da ventilação da base das paredes em função da sua espessura no tratamento das humidades ascensionais, Proceedings of Patorreb 2006, pp. 369–379. Porto, Portugal (2006)
7. Building Physics—Heat, Air and Moisture—Fundamentals and Engineering Methods with Examples and Exercises Hens. Hugo S, ISBN: 978-3-433-01841-5, 270 pgs. Belgium (2007)
8. Kunzel, H.M.: Simultaneous heat and moisture transport in building components, one and two dimensional calculation using simple parameters. PhD Thesis, University of Stuttgart (1994)
9. Holm, A., Kunzel, H.M.: Two-dimensional transient heat and moisture simulations of rising damp with WUFI-2D. Proceedings of the 2nd International Conference On Building Physics, pp. 363–367. Leuven, Belgium (2003)
10. Torres, M.I.M., de Freitas, V.P.: Rising damp in historical buildings–Research in Building Physics. Proceedings of the 2nd International Conference On Building Physics, pp. 369–375. Leuven, Belgium (2003)
11. de Freitas, V.P., Guimarães, A.S.: Characterization of a hygro-regulated Wall Base Ventilation System for Treatment of Rising Damp in Historical Buildings, Proceedings of the 2nd Nordic Symposium on Building Physics, pp. 911–919. Copenhagen, Denmark (2008)
12. Guimarães, A.S.: Caracterização Experimental do Funcionamento de Sistemas de Ventilação da Base das Paredes para Tratamento da Humidade Ascensional, Master's thesis, University of Porto, Portugal (Portuguese) (2008)

13. Watt, D., Colston, B.: Investigating the effects of humidity and salt crystallization on medieval masonry Building and Environment. The effects of humidity and salt crystallization on medieval masonry. Parish church of Walpole St Andrew, Norfolk (2000)
14. Salt attack and rising damp. A guide to salt damp in historic and older buildings Young, David, Heritage Council of NSW, Heritage Victoria, South Australian Department for Environment and Heritage, Adelaide City Council, ISBN 978-0-9805126-4-9 (print), ISBN 978-0-9805126-5-6 (online) (2008)

The Evaluation of Hygroscopic Inertia and Its Importance to the Hygrothermal Performance of Buildings

Nuno M. M. Ramos and Vasco Peixoto de Freitas

Abstract Heating and ventilating are fundamental actions for the control of humidity in the indoor environment, but the hygroscopic inertia provided by the materials that contact the inside air can be a complement for that control. The hygroscopic behavior of the walls and ceiling finishing materials, as well as furniture and textiles inside the dwellings, defines their hygroscopic inertia. Reducing the persistence of high relative humidity values inside buildings is essential for the control of mould growth on material surfaces, that can otherwise cause degradation and bring about social and economical problems for the users. As the hygroscopic inertia concept can be very difficult to approach for building designers, a definition of daily hygroscopic inertia classes is presented, based on numerical and laboratory work on this subject. An outline of a simple method, using those classes, that allows for the evaluation of the reduction of mould growth potential associated to a configuration of inside finishes is proposed. The extensive experimental campaign aiming the characterization of the moisture buffering capacity of interior finishing system and the assessment of a room's hygroscopic inertia is described. The MBV—Moisture Buffer Value is evaluated for different revetments. The assessment of hygroscopic inertia at room level is implemented using a flux chamber designed specifically for this experiment. A daily hygroscopic inertia index, $I_{h,d}$, is defined using MBV as a basis for the assessment of materials contribution to the buffering capacity of a room. The correlation between that index and peak dampening is proved using the presented experimental results. Systematic simulation of the set of dynamic experiments of transient moisture transfer in

N. M. M. Ramos (✉) · V. P. de Freitas
LFC Building Physics Laboratory, Civil Engineering Department,
Faculty of Engineering, University of Porto, 4200-465 Porto, Portugal
e-mail: nuno.ramos@fe.up.pt

V. P. de Freitas
e-mail: vpfreita@fe.up.pt

J. M. P. Q. Delgado (ed.), *Heat and Mass Transfer in Porous Media*,
Advanced Structured Materials 13, DOI: 10.1007/978-3-642-21966-5_2,

the hygroscopic region is presented; allowing to verifying and correcting the modeling assumptions and the basic data used in simulations, and conclude on the most effective strategies to conduct this type of simulations.

1 Introduction

The variation of inside Relative Humidity (RH) is influenced by the moisture exchange between air and building elements. The relevance of that exchange is linked to the active moisture buffer capacity present in a room, which can be identified with its hygroscopic inertia.

Relative humidity the air inside buildings can have an influence on thermal comfort, on the perception of indoor air quality, users' health, materials durability and energy consumption. This dependency has been established by science but the common user will not always recognize it. Mould growth on building element's surfaces, on the other hand, is easily associated with the persistence of high RH levels even by users and can be tied not only to durability but also to PAQ and health.

The work of several researchers has already demonstrated the benefits from inside relative humidity variation control provided by hygroscopic materials [7, 11], and the International Energy Agency (IEA) research project, IEA-Annex 41 contributed to a deeper understanding of that process.

Laboratory experiments are a way of demonstrating and quantifying that capacity and can be implemented in three different levels.

At material level, international standards already support the determination of the basic properties that condition moisture storage performance, such as sorption isotherms (ISO 12571 [3]) and vapour permeability (ISO 12572 [4]). A property defined as MBV, Moisture Buffer Value, was proposed by [9], allowing for a direct experimental measure of the moisture accumulation capacity of a material under transient conditions.

At element level, where several materials can be combined by their application in different thicknesses, MBV can also be applied as an experimental measure of each specific element configuration moisture accumulation capacity.

At room level, the authors believe that a laboratory measurement of the active moisture buffer capacity should be directly linked to the RH peak dampening promoted by the room's interior configuration, compared to the peaks in the same room without any active hygroscopic surfaces.

The relation between the three levels of experimental measurements is explored using numerical simulation of element and room behaviour using the material properties measured in the first level.

This text also defines daily hygroscopic inertia classes and proposes their implementation as an easy way of including the building materials moisture

storage capacity influence on RH variation and mould growth risk analysis. A proper selection of interior finishes can obviously benefit from that inclusion.

2 Material Properties

2.1 Materials

In these experiments, an option was made in using specimens of common commercial materials used finishing systems for walls and ceilings. The experiments were therefore performed in specimens of, gypsum plaster ($\rho = 1200$ kg/m^3) as base material, either naked or combined with a coating.

This type of gypsum is blended in factory and, after addition of water, can immediately be applied. The coating is also commercially available and, therefore, formulation is unknown. It was known, however, that it was composed of 25 μm acrylic primer and 50 μm vinyl finishing layer.

The procedure for the preparation of the gypsum plaster specimens tried to replicate the conditions that are used in practice. The dry plaster powder (2 kg) was mechanically mixed with water (1 dm^3), during 5 min, to produce a homogeneous mass. After casting in wood frames for 24 h, the specimens were dried in the air.

2.2 Sorption Isotherm

Most building materials are hygroscopic, which means that they adsorb vapour from the environment until equilibrium conditions are achieved. This behaviour can be described by sorption curves over a humidity range of 0–95% RH. The sorption isotherms represent the equilibrium moisture contents of a porous material as a function of relative humidity at a specific temperature.

The experiments were performed in accordance with ISO 12571 standard. At a temperature of 23 ± 2°C, four of five available relative humidity ambiences were used in the characterization of each of the three base materials. Each ambience was obtained in desiccators using a specific saturated salt solution (NH4Cl-77%, NH4Cl-84% and KNO3-91%) or in a climatic chamber (33 and 50%).

The gypsum plaster specimens had dimensions of 60 × 60 × 6 mm^3. The specimens were initially dried at ambient temperature, during 30 days, in desiccators containing $CaCl_2$, guaranteeing a relative humidity below 0.5%.

For sorption measurements, the test specimen is placed consecutively in a series of test environments, with relative humidity increasing in stages, until equilibrium is reached in each environment. Equilibrium between moisture content and relative humidity has been reached when successive weightings,

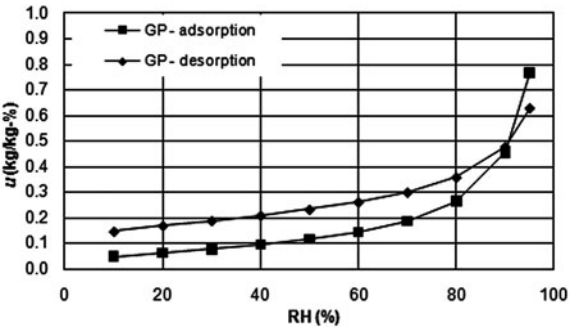

Fig. 1 Sorption isotherms obtained for gypsum plaster

at time intervals of at least one week, show a difference in mass lesser than 0.1%. The starting point for the desorption measurements was above 91% RH. While maintaining a constant temperature, the specimen is placed consecutively in a series of test environments, with relative humidity decreasing in stages, until equilibrium is reached in each environment. With the objective to gain time, different specimens were used for the different ambiences in the sorption phase. Finally, the specimens were dried at the appropriate temperature to constant mass. From the measured mass changes, the equilibrium moisture content (u), at each test condition, could be calculated and the sorption/desorption isotherm drawn (see Fig. 1).

2.3 Vapour Permeability

Vapour permeability was determined for samples of the base material, both naked and combined with the coating. The tests were conducted according to ISO 12572 standard. For each combination of base material and coating, three permeability values were defined, corresponding to three different ranges of RH differences across the sample.

Prior to testing, all the specimens are preconditioned in a climatic chamber at 23 ± 2°C and 50% RH, for a period long enough to obtain three successive daily determinations of their weight lesser than 0.5%.

After stabilisation, the specimens are placed in cups with a saturated salt solution below the bottom surface of the specimen. The sides of the specimens were covered with vapour impermeable tape. Due to the dimensions of the cups, the dimensions of the samples corresponded to 210 × 210 × 11 mm.

The change of weight of the cup was measured periodically, with a precision of 0.1 mg, on an electronic balance until the steady state was obtained.

The sketch presented in Fig. 2 shows the relative humidity profiles admitted for the painted samples during the permeability experiments, in accordance with the theory presented below.

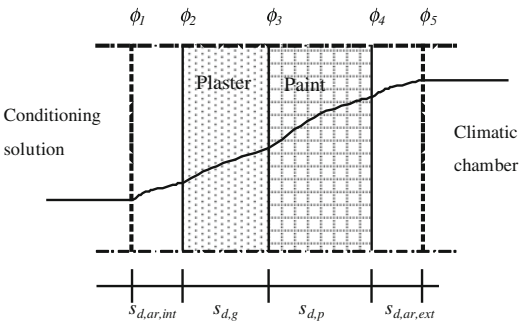

Fig. 2 Relative humidity profiles during the vapour permeability experiments

The vapour permeability, δ_P, is a material property defined as the transport coefficient for vapour diffusion in a porous material subjected to a vapour pressure gradient. The permeability can be calculated using,

$$\delta_P = g\frac{d}{\Delta P} \tag{1}$$

where g is the mass flux density and d is the sample thickness exposed to a vapour pressure gradient ΔP.

Other properties derived from vapour permeability can be used, as the transport coefficient under a vapour concentration gradient: vapour resistance factor, $\mu = \delta_a/\delta_p$ or vapour diffusion thickness, $s_d = \mu \cdot d$.

Although a constant value is derived for δ_P after each permeability test, it's well established that this property is RH dependant, $\delta_p(\phi)$. To determine these functions for the tested materials, the permeability type Eq. 2, and its adapted form for $s_d(\phi)$ value (3), proposed by Galbraith et al. [2], was used and the regressions were carried out using the Levenberg–Marquardt method and SPSS 14.0 program.

$$\delta_p(\phi) = A_1 + A_2 \cdot \phi^{A_3} \tag{2}$$

$$s_d(\phi) = \frac{\delta_a \cdot d}{A_1 + A_2 \cdot \phi^{A_3}} \tag{3}$$

The empirical constants of Eq. 3 were derived by the regression method described above for naked specimens as $A_1 = 1.83 \times 10^{-11}$, $A_2 = 2.91 \times 10^{-11}$ and $A_3 = 3.21$.

For the coated samples, however, a more complex methodology was applied in the results analysis. With the knowledge of the base materials $\delta_p(\phi)$ function, assuming fixed values for $s_{d,air,int}$ and $s_{d,air,ext}$, and accepting that for each test $s_{d,g+p} = s_{d,g} + s_{d,p}$, as represented in Fig. 2, it was possible to obtain the A_1, A_2, A_3 coefficients for the $s_d(\phi)$ function of the coating applied on the gypsum base material. The results were $A1 = 2.51 \times 10^{-14}$, $A2 = 8.44 \times 10^{-13}$ and $A3 = 6.031$.

Figure 3 shows the results obtained for the measurement results for the vapour permeability of the unpainted specimens and sd value of the applied paint.

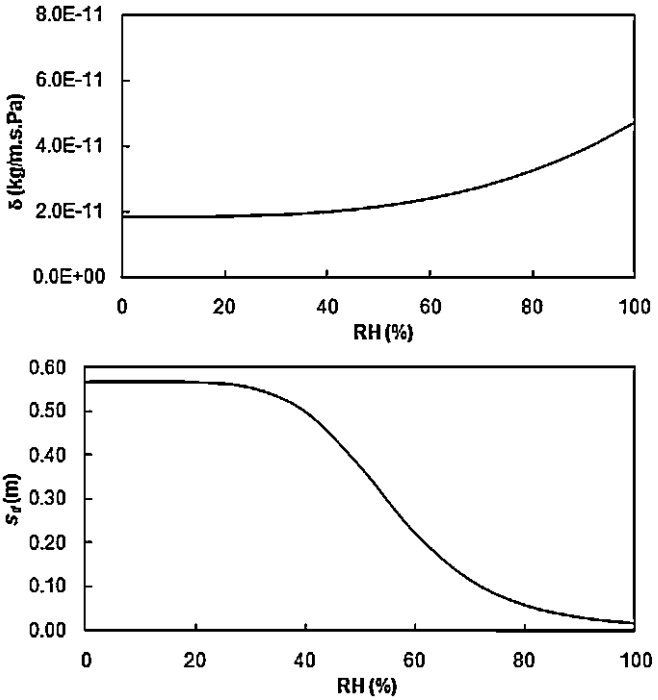

Fig. 3 Vapour permeability of gypsum plaster and sd value of applied paint

3 Moisture Buffer Value

The MBV experiments, as described in [9], propose a cyclic climatic exposure which consists of 8 h of high relative humidity, followed by 16 h of low relative humidity. This test tries to replicate the cycle seen in bedrooms. For the specific tests described in this article, low value was fixed at 33% RH and the high value at 75% RH, for a constant temperature of 23°C, which is the basic test configuration proposed in the protocol. The cycles were repeated until the specimen weight over the cycle varied less than 5% from day to day.

The tests were conducted in a climate chamber ensuring a good control level of the test conditions. All the samples tested were put into the chamber at the same time. Three similar samples were tested for each configuration. Each sample was put on a balance when it was likely to have reached a stable mass variation over the cycle. With this procedure it was possible to test a large number of samples. The balance was connected to a computer allowing for a continuous record of the sample mass variation.

The samples were placed horizontally on the balance. The back of the samples was previously treated with epoxy paint and the four edges were covered with aluminium tape, allowing vapour transfer only in the main face.

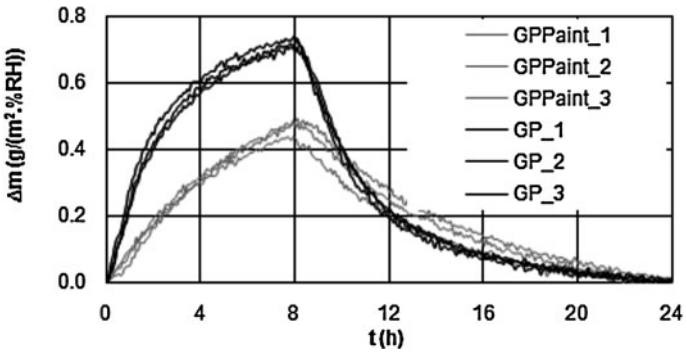

Fig. 4 Mass variation stable cycle in MBV experiments with gypsum plaster based materials

The stable cycle for each configuration is presented in Fig. 4. This type of experiment is interesting in the way it provides an easy assessment of the transient behaviour of a building element. Just by watching the curves, the effect of painting is easily highlighted.

4 Flux Chamber Tests

4.1 Test Facility

The test facility is a small compartment where finishing materials contribution to hygroscopic inertia can be evaluated. To do so, a flux chamber where RH can float freely as a function of boundary conditions and amount of moisture buffering was developed. A strict control of the heat, air and moisture balances of that chamber was therefore crucial. According to this idea, several guidelines were defined: the base element should be a small size chamber with control of moisture and air fluxes; the whole set should have temperature control and; temperature and RH should be continuously monitored. Figure 5 displays a scheme of the test facility, following these guidelines.

The flux chamber was built inside an existing climatic chamber (Fig. 6). This chamber has a capacity for controlling temperature in the range 15–35°C and RH in the range 30–90%. That control can be done using fixed values or using programmable cycles including variation of one or both parameters. A continuous log of the actual values is registered in a computer.

The size of the flux chamber (Fig. 7), to be stored inside, corresponds to a box with a volume of (1500 × 524 × 584) mm^3. Thinking of a regular bedroom with (3 × 4 × 2.7) m^3, the volume scale factor is around 1/70.

By placing all the elements inside a climatic chamber, a strict temperature control was secured. The ventilation system uses a pump (Fig. 8) controlled by flow meters (Fig. 9) that extracts air in two points inside the box and an inlet on

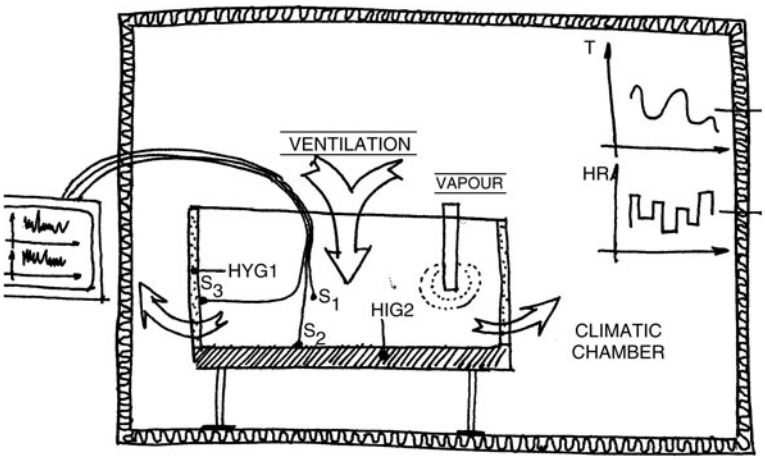

Fig. 5 Flux chamber scheme

Fig. 6 Climatica chamber

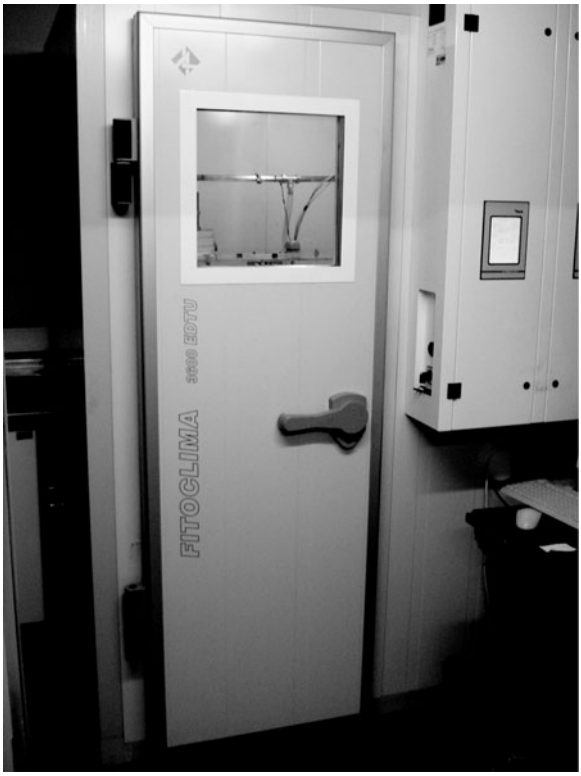

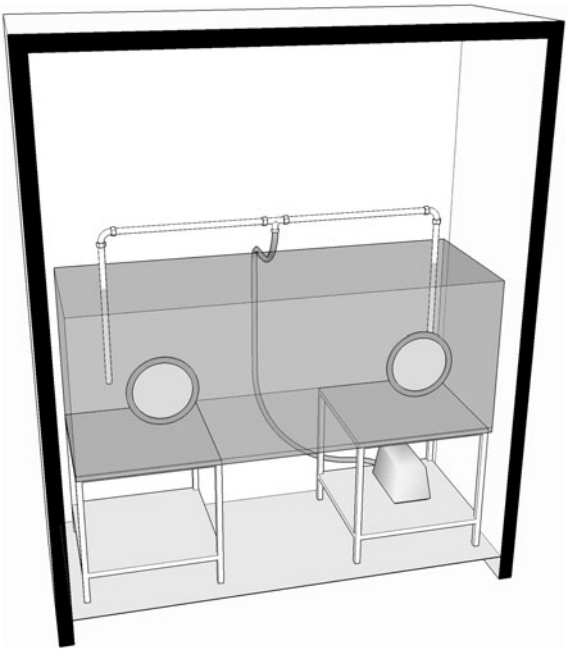

Fig. 7 Flux chamber

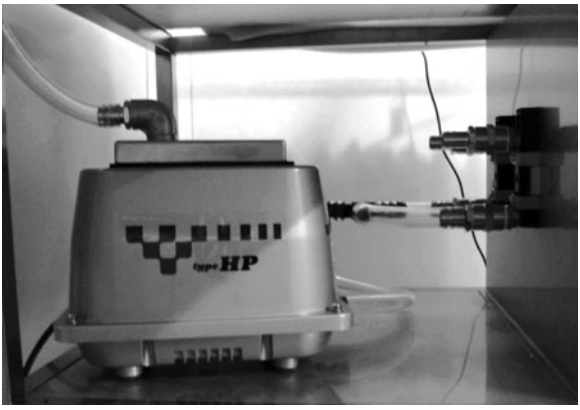

Fig. 8 Air pump

top allows for the air to get in and, at the same time, prevents pressure differences. The air that enters the box comes directly from the climatic chamber, and therefore its characteristics are known. The air flux value corresponds to a range of the air exchange rate (ach) of 0.26 –17 h^{-1}.

The temperature and humidity of the air being sucked inside are known, since the whole set is inside the climatic chamber. Also for that reason, infiltration through the openings doesn't affect the overall balances of heat, air and moisture.

The monitoring system (Figs. 10, 11, 12) is composed of a set of temperature and Relative Humidity sensors connected to a data logger. The data logger is

Fig. 9 Flow meters

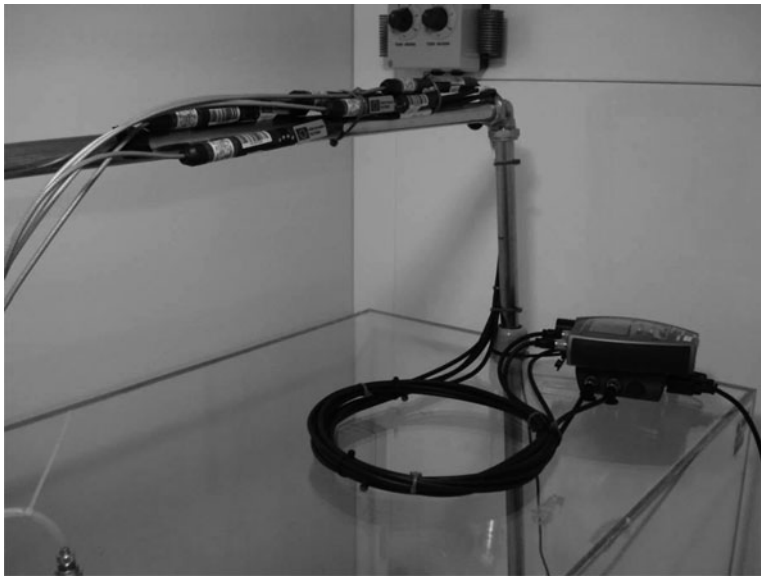

Fig. 10 Monitoring system

Fig. 11 Data logger

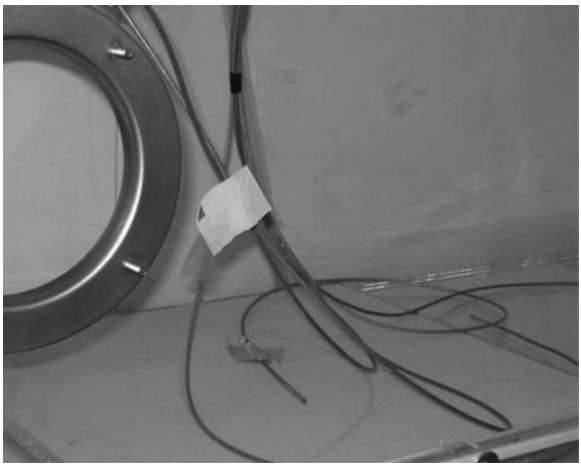

Fig. 12 Temperature and relative humidity sensors

Table 1 Flux chamber tests configuration

Test	Period (h)	Climatic chamber		Flux chamber	
		T (°C)	RH (%)	Rph (h^{-1})	Samples
HI1	0–8	23	80	0.5	–
	8–24	23	40		
HI2	0–8	23	80	0.5	0.75 m^2 GP
	8–24	23	40		
HI3	0–8	23	80	0.5	0.75 m^2 GPPaint
	8–24	23	40		

Table 2 Flux chamber tests results

Ensaio	RH_m (%)	RH_{90} (%)	RH_{90}–RH_m (%)
HI1	54.6	73.2	18.6
HI2	54.3	63.9	9.6
HI3	54.7	66.8	12.1

connected to a computer allowing to keep track of results and store them in a hard-drive.

4.2 Test Results

The tests performed in the flux chamber reported in this text, consisted of the definition of the stable daily RH cycle for a hygrothermal scenario. The selected scenario was defined assuming the number of air changes per hour, Rph, of 0.5 h^{-1} and a vapour production of 2 g/h, during 8 h in the daily cycle. As the temperature of the system was fixed at 23°C, the vapour production was obtained with the RH variation of the climatic chamber between 40 and 80% RH. Using those scenarios, different combinations of samples were placed inside the flux chamber, resulting in different RH cycles. For each configuration, the daily hygrothermal cycle is repeated until the flux chamber RH falls in a stable cycle. The different test conditions used are specified in Table 1.

The results of the tests are presented in Table 2 and Fig. 13 displays the RH variation inside the flux chamber for the tested combinations. For quantification of the test results, the difference between the average RH and the RH 90th percentile, RH_{90}–RH_m, is used. The average RH value obtained for each stable cycle showed a small variation, demonstrating the high control level of the experiments.

These results clearly illustrate the application of the flux chamber in measuring the actual RH dampening caused by the presence of different levels of moisture buffering in contact with inside air.

The observed variations highlight the contribution of different elements to hygroscopic inertia and its effect on RH peak dampening. Test HI1 resulted in a

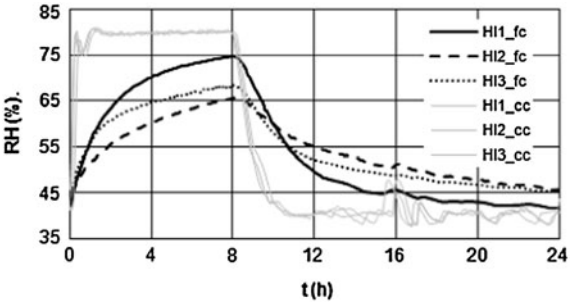

Fig. 13 RH variation inside the flux chamber (fc) and the climatic chamber (cc)

difference between peak and average of 18.6% RH. The introduction in the flux chamber of a porous material, naked gypsum plaster, in HI2 test resulted in a difference between peak and average of 9.6%, a clear effect of hygroscopic inertia. The same type of material, but with a coating applied, corresponding to test HI3, resulted in less peak dampening, a difference between peak and average of 12.1% RH. This result clearly demonstrates how a coating influences materials contribution to hygroscopic inertia.

5 Hygroscopic Inertia Classes

A method of bringing the hygroscopic inertia concept closer to practitioners has been developed and experimentally evaluated by [8]. The basic idea, illustrated in Fig. 14, is to have a prediction tool that can establish a relation between the dampening of the RH variation in a room and its hygroscopicity level, which is mainly dependant on the surface finishing materials and furnishing.

According to the principle, a hygroscopic inertia index was defined as a single number, representing the hygroscopic inertia of a room and that can correlate to the expected reduction of the RH fluctuation. It was decided that this index should concentrate only on daily cycles and it should be derived from room configuration and known material properties.

The MBV—Moisture Buffer Value was the selected material/element property thus acting as a base for that index definition. The proposed daily hygroscopic inertia index, $I_{h,d}$, is defined by [8] as a function of MBV, according to expression (1), where MBV_i = Moisture buffer value of element i (g/(m^2.%RH)); S_i = surface of element i; MBV_{obj} = Moisture buffer value of complex element j (g/%RH); C_r = Imperfect mixing reduction coefficient (−); N = air exchange rate (h^{-1}); V = room volume (m^3); TG = Vapour production period (h). The $I_{h,d}$ can be understood as the room MBV, homogenized to air renovation conditions and vapour production period variations.

$$I_{h,d} = \frac{\sum_i^n C_{r,i} \cdot MBV_i \cdot S_i + \sum_j^m C_{r,j} \cdot MBV_{obj,j}}{N \cdot V \cdot TG} \rightarrow \left[\frac{g}{m^3 \cdot \%HR}\right] \quad (4)$$

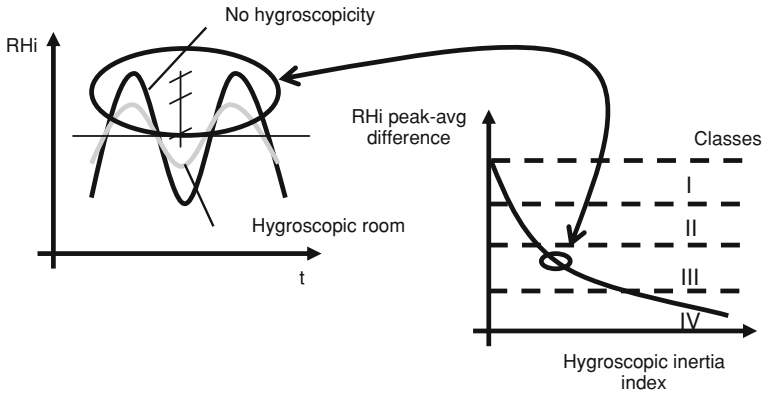

Fig. 14 Hygroscopic inertia classes definition principle

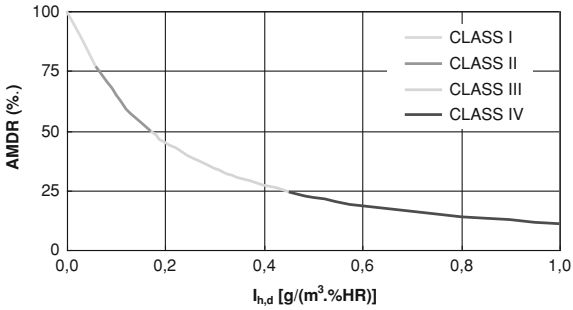

Fig. 15 Graphic relation between AMDR and $I_{h,d}$

The evaluation of a RH variation curve in time should be based on a single number, keeping in mind the principle described.

The AMDR parameter was defined according to Eq. 5, where HR_m is the average relative humidity variation and $\overline{HR_{90}}$ stands for the daily average of the 90th percentile of the relative humidity variation. The index *ref* refers to the base scenario of a room without hygroscopicity and *sim* identifies a scenario under study for that same room. The AMDR parameter can therefore be interpreted as relative daily average amplitude of a RH variation of a room hygroscopic configuration. This parameter is interesting since the average RH variation in long-term analysis will not be affected by daily hygroscopic inertia.

$$AMDR = \frac{\left(\overline{HR_{90}} - HR_m\right)_{sim}}{\left(\overline{HR_{90}} - HR_m\right)_{ref}} \tag{5}$$

The selected parameters were proven by [8] to be connected by Eq. 6. The resulting curve supports the definition of daily hygroscopic inertia classes, according to Fig. 15.

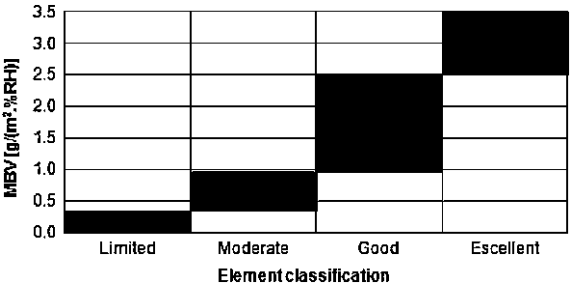

Fig. 16 Building element classification as a function of their contribution to a room's hygroscopic inertia

$$AMDR = \frac{1}{0.00998 + 0.0793 \cdot I_{h,d}^{1.16}} \% \tag{6}$$

The adopted classes support a new classification of building elements contribution to the hygroscopic inertia of a room, based on their MBV and on a ratio between room volume and area of application of 0.7 (Fig. 16).

6 Numerical Simulation

6.1 Numerical Model

A decision was made to numerically simulate the behaviour of a room and the moisture buffer capacity of the materials used in the room simulation. This provided data that can illustrate the desired relation between hygroscopic inertia and room configuration.

The authors chose to use for these simulations the software program HAM-Tools [5]. The International Building Physics Toolbox, is a software library specially constructed for HAM system analysis in building physics.

As part of IBPT, HAM-Tools is open source and publicly available on the Internet. The library contains blocks for 1D calculation of Heat, Air and Moisture transfer through building materials. The toolbox is constructed as a modular structure of the standard building elements using the graphical programming language Simulink. All models are made as block diagrams and are easily assembled in a complex system through the well-defined communication signals and ports.

6.2 MBV Simulations

An assembly of HAM-Tools modules was used for simulating the MBV experiment. The simulations were performed using the virtual specimens listed in Table 3. The data for the chosen materials used in the simulations was retrieved from [6]. The different β (convective water vapour transfer coefficient) values used

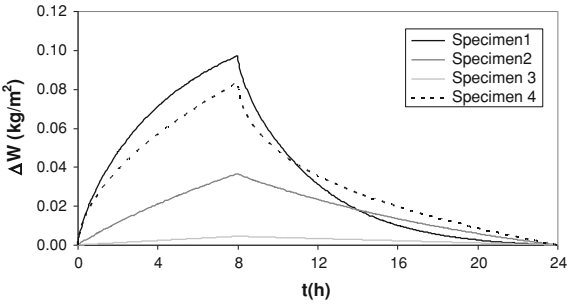

Fig. 17 Moisture content variation of all the specimens in a stable cycle

Table 3 Virtual specimen's characteristics

Specimen	Material	β (s/m)	Thickness (m)
1	Gypsum board	2e-8	0.01
2	Gypsum board	2e-9	0.01
3	Gypsum board	2e-10	0.01
4	Spruce	2e-8	0.01

represent the possibility of coatings with different additional vapour resistances applied in the gypsum board specimens.

In Fig. 17, the mass variation of all the specimens in the steady cycle is presented. The MBV for each specimen is presented in Table 4. As we can see, this number, when associated to the tested elements, provides the means to compare them. But as it was said before, this number is used ahead for hygroscopic inertia analysis.

6.3 Room Simulations

A different HAM-Tools modules association allowed for the simulation of a room's hygrothermal behaviour in yearly cycles. The virtual room is $3.5 \times 3.5 \times 2.5$ m^3, with one exterior wall, containing a 1 m^2 window, facing south. The surrounding rooms are assumed to have similar conditions of temperature and relative humidity as the simulated room. The climate conditions were defined for Lisbon, using Meteonorm software. The inside temperature was allowed to float between Tmin and 28°C, and RH was allowed to float below 90%. The ventilation rate is constant and the vapour production takes place between 0 and 8 h, with a constant value. On walls and ceiling the admitted material was gypsum board and on the floor spruce. Tables 5 and 6 describe the conditions that were changed for each simulation. It can be easily inferred that the room configuration in the first line of Table 6 stands for the room with no hygroscopic inertia, the reference room.

Partial results from simulations SG1 and SG2 are presented in Figs. 18, 19, 20 and 21 illustrating the tested scenarios.

Table 4 MBV for the four specimens tested

Specimen	1	2	3	4
MBV(kg/m^2)	0.0971	0.0366	0.0045	0.0832

Table 5 Hygrothermal parameters adopted in simulations

Simulations	Tmin (°C)	G (g/h)	N (h^{-1})
SG1–SG2	18	100	1.0
SG11–SG12	18	150	1.0
SG15–SG16	15	100	1.0
SG19–SG20	21	100	1.0
SG23–SG24	18	100	0.67
SG27–SG28	18	100	0.33

Table 6 Room configurations

Simulations	Walls		Ceiling		Floor	
	Area (m^2)	β (s/m)	Area (m^2)	β (s/m)	Area (m^2)	β (s/m)
SG: 1-11-15-19-23-27	34	2e-12	12.25	2e-12	12.25	2e-12
SG: 2-12-16-20-24-28	34	2e-8	12.25	2e-8	12.25	2e-12

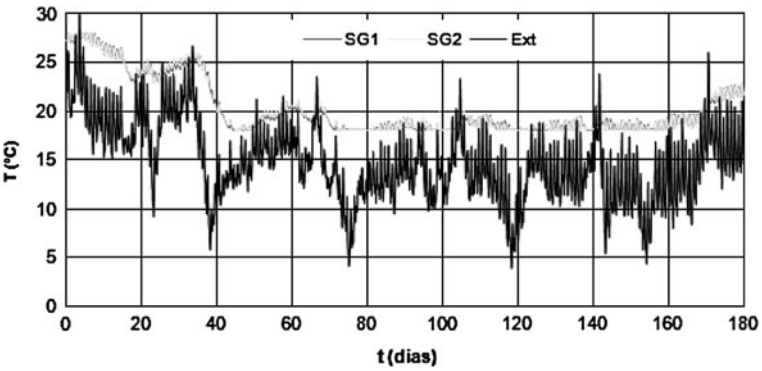

Fig. 18 Results from simulations SG1 and SG2—temperature values from October to March

The temperature variations, presented in Fig. 18 showed almost no influence of hygroscopic inertia.

The relative humidity variation, on the other hand, is highly influenced by hygroscopic inertia, as it can be seen in Fig. 19. That result is also visible in vapour pressure variation, presented in Fig. 20. That influence however, is only important on peak level. The average values will tend to be the same, with or without hygroscopic inertia. That is quite clear on Fig. 21 where monthly values are close and as periods are more extended, that difference tends to be even smaller.

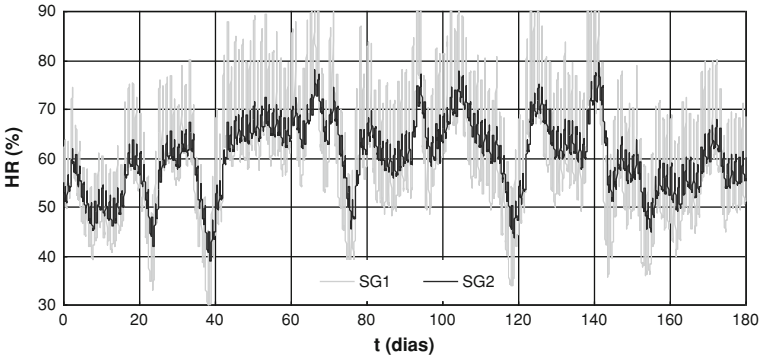

Fig. 19 Results from simulations SG1 and SG2—relative humidity values from October to March

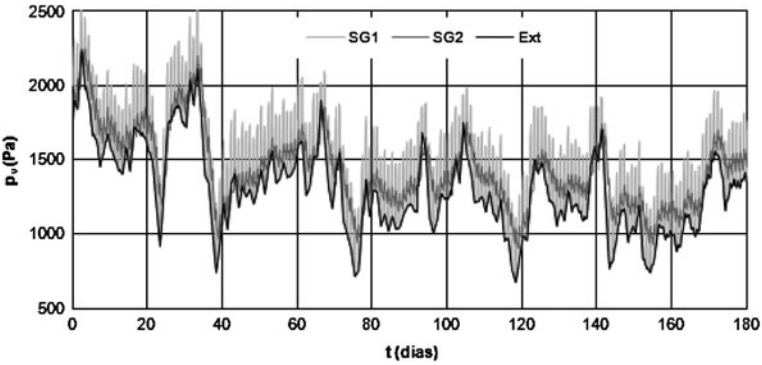

Fig. 20 Results from simulations SG1 and SG2—vapour pressure values from October to March

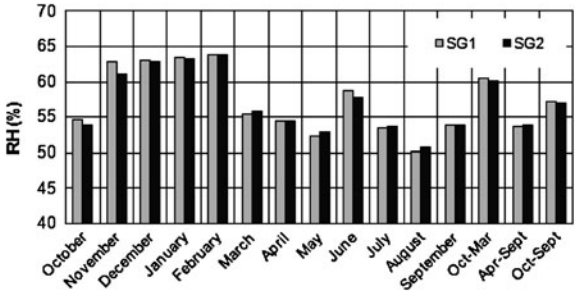

Fig. 21 Results from simulations SG1 and SG2—relative humidity average values

Table 7 Parameters for hygroscopic inertia analysis

Simulations	$I_{h,d}$ (g/(m^3.%RH))	AMDR (%)
SG: 1-11-15-19-23-27	0	1.0
SG2	0.438	0.23
SG12	0.438	0.24
SG16	0.438	0.24
SG20	0.438	0.23
SG24	0.653	0.18
SG28	1.326	0.12

6.4 Hygroscopic Inertia Analysis

The application of the hygroscopic inertia classes method allows for the definition of parameters AMDR and $I_{h,d}$ corresponding to the simulation scenarios. The values obtained are presented in Table 7, and reveal that the scenarios hygroscopicaly active would be placed in class III-IV.

6.5 Mould Growth Risk Assessment

Several authors have studied the relationship between water activity in a substrate and the development of mould on its surface (e.g. [1, 10]). The mould development under transient conditions of temperature and humidity is highly complex. Reference [1] proposed a model based on the TOW (time of wetness) concept to solve this problem. TOW is the quotient between the time period where the surface RH is above 80% and the total duration of the period under analysis. Using that model in several laboratory tests, there was evidence that for TOW < 0.5 the risk for mould growth is very low. Using the TOW concept when simulating a room's hygrothermal behaviour it is possible to define the number of days with TOW > 0.5, $nd_{tow\ >\ 0.5}$, as a simplistic indicator of the mould growth risk. This approach loses accuracy if the simulations indicate actual surface condensation and the analysis tool is unable to treat that process with high precision.

Additionally, the authors use another parameter, nd_{cond}, representing the number of days when surface condensation was detected. The objective of these indicators is not to accurately estimate mould growth risk, but rather to compare hygrothermal scenarios. Using these parameters in the above simulated scenarios and imposing an additional condition of the existence of a rather extreme thermal bridge, defined by $f_{Rsi} = \frac{T_{surf,i} - T_e}{T_i - Te} = 0.5$, the results for each scenario are as presented in Fig. 22.

This result shows the importance of hygroscopic inertia and the benefits that can derive from a sss RH variation with important peak reduction. A design method for the prevention of mould growth can be derived from this analysis. The method itself can have different levels of complexity. The basic idea is:

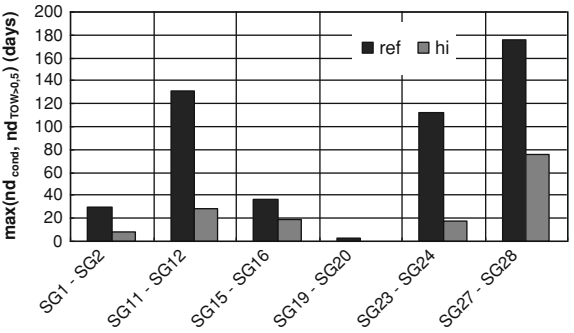

Fig. 22 Mould growth risk analysis

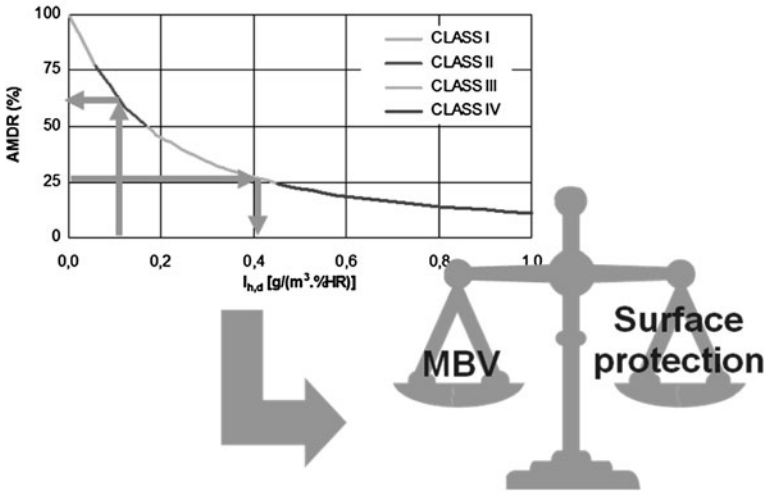

Fig. 23 The relevance of balance between hygroscopic inertia and surface protection

- define the risk associated with the room's RH variation for the four classes of hygroscopic inertia;
- select the adequate $I_{h,d}$ value and define the room's renderings to provide that value.

7 Conclusions

This text presents research that allows for the following conclusions:

- Moisture buffering tests were conducted at element level. Renderings finished with different coatings were tested for MBV determination, allowing for buffer effect comparison. The finishing coating has a relevant influence on that effect.

- Hygroscopic inertia tests were conducted in a flux chamber that represents a small scale room. The influence of different elements on RH variation was obtained. The experimental evidence of daily hygroscopic inertia was demonstrated.
- The definition of daily hygroscopic inertia classes based on a room's index allows for the prediction of the RH variation amplitude;
- The MBV property can be used as an indicator of an element's contribution to the room's hygroscopic inertia;
- Mould growth risk is lower for higher values of hygroscopic inertia, admitting the same composition of the surface's final rendering;
- The design and selection of interior finishes in practice can benefit from the proposed approach to the hygroscopic inertia concept. But the balance between the MBV supplied by a surface and its protection against biological defacement (Fig. 23) must be achieved.

References

1. Adan, O.: On the fungal defacement of interior finishes. Ph.D. thesis, Eindhoven University of Technology (1994)
2. Galbraith, G., MClean, R., Guo, J.: Moisture permeability data presented as a mathematical relationship. Build. Res. Inf. **26**(3), 157–168 (1998)
3. ISO 12571:2000: Hygrothermal performance of building materials and products—Determination of hygroscopic sorption properties (2000)
4. ISO 12572:2001: Hygrothermal performance of building materials and products—Determination of water vapour transmission properties (2001)
5. Kalagasidis, A.: HAM-Tools: an integrated simulation tool for heat, air and moisture transfer analyses in building physics, Department of Building Technology, Building Physics Division, Chalmers University of Technology, Gothemburg, Sweden (2004)
6. Kumaran, M.: Heat, air and moisture transfer through new and retrofitted insulated envelope parts (Hamtie), IEA ANNEX 24 (1996)
7. Padfield, T.: The role of absorbent building materials in moderating changes of relative humidity. Ph.D. thesis. Department of Structural Engineering and Materials, Lyngby, Technical University of Denmark 150 (1998)
8. Ramos, N.: The importance of hygroscopic inertia in the hygrothermal behaviour of buildings (in Portuguese). Ph.D. thesis, Department of Civil Engineering, FEUP, Porto, Portugal (2007)
9. Rode, C., Peuhkuri, R., Mortensen, L., Hansen, K., Time, B., Gus-Tavsen, A., Svennberg, K., Arfvidsson, J., Harderup, L., Ojanen, T., Ahonnen, J.: Moisture buffering of building materials, Report BYG-DTU R-126, Department of Civil Engineering, DTU, Lyngby, Denmark (2005)
10. Sedlbauer, K.: Prediction of mould fungus formation on the surface of and inside building components. Ph.D. thesis—report, Fraunhofer Institute for Building Physics, Germany (2001)
11. Simonson, C., Salonvaara, M., Ojanen, T.: The effect of structures on indoor humidity-possibility to improve comfort and perceived air quality. Indoor Air **12**, 243–251 (2002)

Two-Phase Flow and Heat Transfer in Micro-Channels and Their Applications in Micro-System Cooling

Yuan Wang, Khellil Sefiane, Souad Harmand and Rachid Bennacer

Abstract Heat management in high thermal-density systems is confronting rising challenges due to the extremely high heat dissipation capacity requirement in ever more miniaturized and intensified processes. Efforts have been made for heat transfer enhancement. A number of heat transfer technologies including natural convention and radiation, forced convection, pool boiling, micro-channel flow boiling, heat pipes and capillary pumps were introduced. However, the drastically increasing heat transfer requirements are still calling for extensive experimental investigations, especially on the phase change processes in micro-scale. A review of the experimental studies on two-phase flow boiling and heat transfer in small flow passages was presented. Some experimental results published in the year 1993–2010 were overviewed, revealing some controversial conclusions on micro-scale flow boiling heat transfer mechanisms. Besides, several existing heat transfer correlations were assessed. It should be admitted that the existing database is still limited, especially for flow boiling in passages with unique geometries such as high-aspect-ratio cross section. Extensive explorations on two-phase flow boiling

Y. Wang (✉) · K. Sefiane
School of Engineering, University of Edinburgh, Kings Buildings,
Edinburgh, EH9 3JL, UK
e-mail: yuan.wang@ed.ac.uk

K. Sefiane
e-mail: K.Sefiane@ed.ac.uk

S. Harmand
Laboratoire de Mécanique et Energétique, Université de Valenciennes et du
Hainaut-Cambrésis, Le Mont Houy, 59313 Valenciennes Cedex 9, France
e-mail: Souud.harmand@univ-valenciennes.fr

R. Bennacer
ENS-Cachan Dpt GC/LMT, 61, Av du Président
Wilson, 94235 Cachan Cedex, France
e-mail: rachid.bennacer@ens-cachan.fr

J. M. P. Q. Delgado (ed.), *Heat and Mass Transfer in Porous Media*,
Advanced Structured Materials 13, DOI: 10.1007/978-3-642-21966-5_3,

and heat transfer in micro-channels are essential for heat transfer predictions and applications in micro-systems.

Nomenclature

Bo	Boiling number $Bo = \frac{q}{h_{\mathrm{lv}} G}$
Co	Convection number: Kandlikar [1] confinement number: Bertsch et al. [2] $Co = \left(\frac{\sigma}{g(\rho_{\mathrm{L}} - \rho_{\mathrm{v}}) d_{\mathrm{h}}^2}\right)^{1/2}$
C_p	specific heat capacity [$\mathrm{J{\cdot}kg^{-1}{\cdot}K^{-1}}$]
d	diameter [m]
d_{h}	hydraulic diameter [m]
F	Reynolds number factor, $F = f(X_{\mathrm{tt}})$
F_{fL}	fluid-dependent parameter
Fr	Froude number $Fr = \frac{G^2}{\rho_{\mathrm{L}}^2 \cdot g \cdot d}$
G	mass flux [$\mathrm{kg{\cdot}m^{-2}{\cdot}s^{-1}}$]
g_c	gravitational constant
h	heat transfer coefficient [$\mathrm{W{\cdot}m^{-2}{\cdot}K^{-1}}$]
h_{lv}	latent heat of vaporization [$\mathrm{J{\cdot}g^{-1}}$]
i_e	exit liquid enthalpy
i_f	saturated liquid enthalpy
k	thermal conductivity [$\mathrm{W{\cdot}m^{-1}{\cdot}K^{-1}}$]
M	molecular mass of the fluid [$\mathrm{kg{\cdot}kmol^{-1}}$]
N	number of data
P	pressure [Pa]
P_r	reduced pressure
P_{sat}	saturation pressure [Pa]
Pr	Prandtl number $\mathrm{Pr} = \frac{C_p \mu}{k}$
Q	heat [J]
q	heat flux [$\mathrm{kW{\cdot}m^{-2}}$]
Re	Reynolds number $\mathrm{Re} = \frac{\rho \cdot u_{\mathrm{L}} \cdot d}{\mu_{\mathrm{L}}}$
R_{P}	surface roughness parameter [μm]
S	suppression factor, $S = f(\mathrm{Re_{tp}})$
T	temperature [°C]
T_{sat}	liquid saturation temperature [K]
T_{sub}	liquid subcooling [K]
u	velocity [$\mathrm{m{\cdot}s^{-1}}$]
x	vapour quality
We	Weber number $We = \frac{G^2 d}{\rho \sigma}$
ONB	onset of nucleate boiling
MAE	Mean absolute error
CVQ	Critical vapour quality
CNT	Carbon nano tube
HP	Heat pipe

MHP	Micro heat pipe
VCHP	Variable conductance heat pipe
NCG	Non-condensable gas
PHP or OHP	Pulsating or oscillating heat pipe
LHP	Loop heat pipes

Subscript

avg	averaged
channel	parameters within the channel
conv	convective
cor.	correlation predicted
exp.	experimental
L	Liquid
in	inlet, inner
local	local
nb	nucleate boiling
out	outlet, outer
sp	single phase
tp	two-phase
v	vapour

Greek Symbol

ε emissivity of micro-channel deposit
μ dynamic viscosity [$kg \cdot m^{-1} \cdot s^{-1}$]
ϕ heat transfer efficiency
ρ density [$kg \cdot m^{-3}$]
σ channel aspect ratio (W_{in}/d_{in}) or surface tension [$N \cdot m^{-1}$]
ω Stefan-Boltzmann constant

1 Introduction

Energy conversion and transportation is one of the foundations of modern society. Energy is becoming the single most important issue facing humanity in the next fifty years following the diminishing availability of fossil fuels and increasing concerns on global warming. Among all the forms of energy used today, over 70% are produced in or through the form of heat. In the principle of thermodynamic cycle or in many industrial systems, heat must be transferred either to add energy to the system or to remove energy produced by the system. Considering the rapid increase in energy demand worldwide, the heat transfer processes enhancement and the irreversibility reduction due to the friction and heat losses, have become an

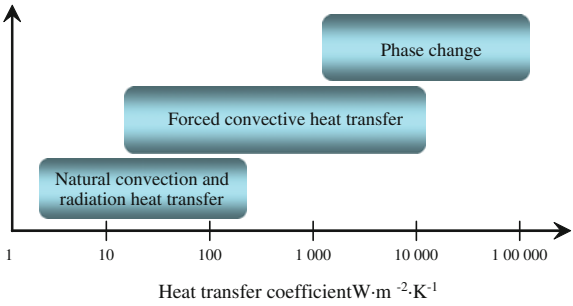

Fig. 1 Heat transfer coefficients for thermal management (moderate temperature)

increasingly important task. Heat removal and control in high heat flux systems such as nuclear fusion, fuel cells, micro/nano electro-mechanical systems (MEMS/NEMS), and micro chemical reactions present challenges on both size and time scale.

The increasing heat flux generated by the industrial systems can cause thermal problems as overheating, which can reduce the performance levels as well as the lifespan and reliability of these devices. For this reason, managing the thermal dissipation, while maintaining the devices temperatures within the specified temperature range, has become a crucial factor for safety and reliability in numerous engineering domains. For example, thermal management within the overall design of electric and electronic products is increasingly important since each new generation devices squeezes more power and performance into ever-smaller packages.

Many technologies are under development to transport heat within the equipments to allow it to be dissipated into the surroundings via conduction, natural convection, radiation, two-phase change, etc. In recent years, many innovations of modern materials and technologies have increased the thermal conductivity by for example, including diamond in the basic materials because of its attractive thermal properties. The thermal conductivity of diamond is the highest among all the materials found in nature. It is reported that high-quality single crystals of diamond have a thermal conductivity of 1,800 $W \cdot m^{-1} \cdot K^{-1}$ at room temperature and the thermal conductivity for a variety of diamond films on a silicon substrate ranges from 600 to 1,200 $W \cdot m^{-1} \cdot K^{-1}$.

Carbon nanotubes (CNTs) have also been extensively studied due to their outstanding physical properties such as high Young's modulus, electrical and thermal conductivities ranging from 600 to 3,000 $W \cdot m^{-1} \cdot K^{-1}$. The CNT is of keen interest to scientists and engineers as it has many potential applications including nanoprobes.

The technology and methodology to use for the thermal management of industrial systems is strongly linked to the range of heat transfer coefficient needed to guarantee the efficiency and reliability (life time and degradation) of the devices as shown in Fig. 1.

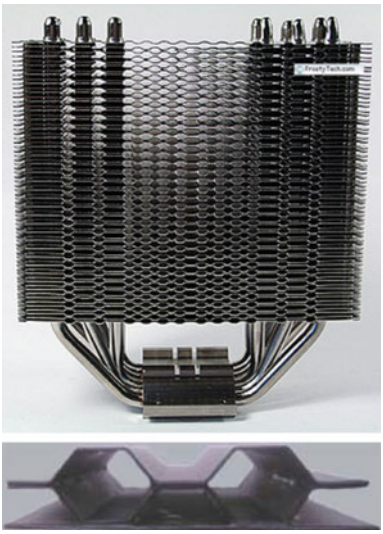

Fig. 2 Honeycomb heat sink for natural convection heat transfer [3]

1.1 Natural Convection and Radiation Heat Transfer

The natural convection and radiation are well adapted to the thermal management of low heat power devices (as in Fig. 1). To improve the efficiency of this kind of equipments, it is possible to use fins shaped cellular metals or honeycomb heat sinks which are low density materials that combine certain stiffness, strength, crushing energy absorption and thermal characteristics, such as high surface to volume ratios and high conductivity, in a way that makes them attractive for use in heat sinks.

Honeycomb heat sinks are heat sinks with honeycomb-shaped fins (Fig. 2). These heat sinks are generally made of copper or aluminium depending on the requested characteristics. Special coating could be used to resist to the corrosion and to increase the radiative properties of the heat sinks. The thermal performances of this type of heat sinks are revealed in natural convection since they allow creating chimney effect which guides the cooling air on critical components. Regarding to a standard solution, honeycomb heat sinks allow a volume reduction from 30 to 50%. For example, the cell sizes could be about 5 mm to 12 m and the cells thickness from 50 μm to 2 mm. The common heat sink dimensions vary from 10 to 100 mm and the dissipated power varies from a few Watts to tens of Watts.

1.2 Forced Convection

Forced convection air-cooling relies on a fan instead of density differences to set up the fluid motion. This results in higher fluid velocities and higher heat fluxes and consequently a heat transfer coefficient in the order of 100 $W \cdot m^{-2} \cdot K^{-1}$. Placing barriers or turbulators in the flow can increase the maximum heat transfer coefficient

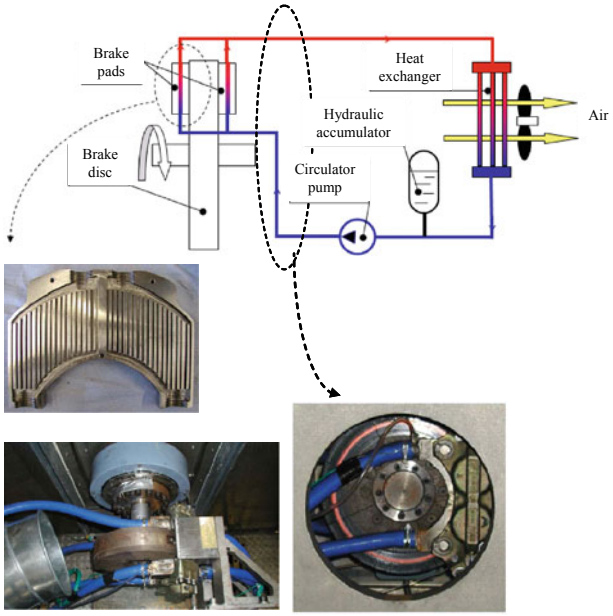

Fig. 3 Liquid-Cooled railway disk brake [4]

by 30–50%. This is because of the increased turbulence in the flow breaking down the boundary layer hence reducing the thermal resistance. Currently, forced convention air-cooling is the standard technique used for cooling personal computers (PCs). Unfortunately, the cooling capabilities of forced convection air-cooling, although better than natural convection, are still limited. The use of a fan to provide the fluid motion can also cause difficulties due to mechanical failure. Hence, maintenance could increase the overall cost of the system.

Liquid forced convection cooling involves a mechanically induced liquid flow (e.g. with the aid of a pump) over the device to produce the desired cooling effect. The maximum heat transfer coefficient for a fluorochemical liquid under forced convection is approximately 2,000 $W \cdot m^{-2} \cdot K^{-1}$. The extra equipment required for liquid forced convection cooling inevitably results in an increased overall equipment volume. It is therefore not suitable for cooling where space is at a premium. Figure 3 gives an example of brake disk liquid cooling.

This equipment is developed to enhance the railway brake disk intended for an urban exploitation. Because of the increase in the rates of trains and subways as well as the number of passengers, brake disks have increasingly become a major safety component. In urban exploitation, these systems are subjected to multiple braking actions with operational limits. The concept of liquid-cooled railway disk brake is based on a liquid-cooled system to decrease the energy storage in the disk. The temperature reached on a single stop with the liquid-cooled concept is higher than those of a classical brake. However, a significant temperature decrease is

Fig. 4 Pool boiling [5]

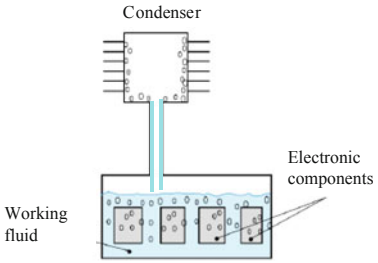

observed at the end of braking so that, for successive braking, the liquid-cooling principle causes an overall decrease in temperature. Moreover, the use of material with high thermal effusivity increases the part of the flow generated at the interface transmitted to the pad and consequently reduces the surface temperature.

1.3 Pool Boiling

Due to the limitation of the conventional forced convective fan or pump cooling methods and increasing heat generation, the widely used fan cooling method using forced convection by air as the working fluid, however, is not suitable for high heat fluxes higher than 10^5 W·m^{-2}. Besides, there are problems such as noise, electrical failure, and high power consumption. Therefore, a direct immersion cooling has been recommended as an alternative to the forced convective air cooling methods for the electronics devices for instance. Liquids have the advantages of higher thermal conductivity, density, and specific heat over air, ensuring higher dissipated heat flux. In applications where it is desirable to maintain a boiling surface at low temperature, reducing the saturation pressure may be a useful solution. A reduction in the saturation pressure causes a corresponding decrease in the saturation temperature, allowing a given superheat level to be achieved with a lower surface temperature. This approach is particularly useful when water is used as the boiling liquid. Water is a desirable liquid since it has such a high heat of vaporization, high thermal conductivity, and is non-toxic and non-flammable.

Figure 4 gives an example of a pool boiling for electronic components. Pool boiling involves heat transfer from the electronic component to a stagnant pool of liquid through an intermediate material. As there is an intermediate material, it is possible to use water as the working fluid. The liquid will vaporise, allowing high heat transfer rates to be obtained. The vapour will then come into contact with a further heat sink, give up its heat of vaporisation, and the liquid formed will return to the pool by gravity. The maximum heat transfer coefficient for boiling water is 4×10^4 W·m^{-2}·K^{-1}. The corresponding maximum heat fluxes are shown along with the liquid forced convection heat fluxes in Fig. 5.

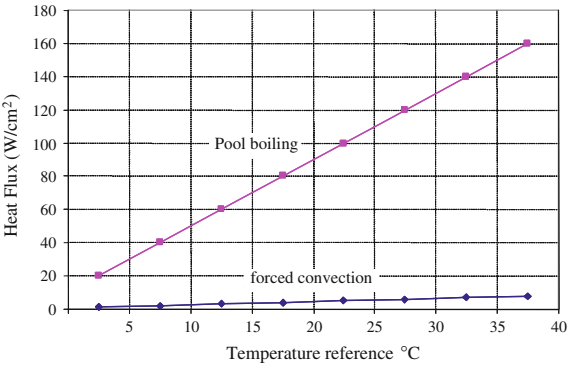

Fig. 5 Boiling heat fluxes [5]

1.4 Micro-Channel Flow Boiling

Micro-channel heat sinks undergoing two-phase heat transport can provide very high heat transfer rates while maintaining the wall temperature relatively uniform, and have therefore been investigated as an attractive solution for the cooling of high-power electronics. Since the working fluid in the micro-channels may be in direct contact with the electronics, the use of dielectric liquids has drawn recent attention for these applications.

Micro-channel flow boiling involves a liquid coolant being forced through micro-channels underneath an electronic chip or circuit board. Boiling of the fluid maximizes the heat fluxes that can be obtained. Ideally a closed loop system containing a pump and a condenser would be utilised (Fig. 6). Micro-channels normally have inner diameters in the range 1–1,000 μm. Heat fluxes of 3×10^6 $W{\cdot}m^{-2}$ are obtained using micro-channels, compared to 2×10^6 $W{\cdot}m^{-2}$ with mini-channels. An inclusive survey on micro-channel flow boiling investigations is presented in the second part of this chapter to exhibit the heat transfer enhancement in micro-channels flow boiling and the corresponding micro-scale heat transfer mechanisms both qualitatively and quantitatively.

1.5 Conventional Heat Pipes

Heat transport through phase change is the most efficient way of transferring heat thanks to the high latent heat of the working fluids. The heat pipe (HP) is a comparatively recent addition to the family of systems that employ evaporation–condensation to transfer heat from a high-flux heat source to a (usually) lower-flux heat sink. It is a passive device with fluid motion between the heat source and sink driven by pressure pulsations due to the internal heat transfer processes of bubble growth and collapse in addition to natural/Marongoni convection, so it can operate in adverse or zero gravity. Because of this advantage, the pumping effect of an

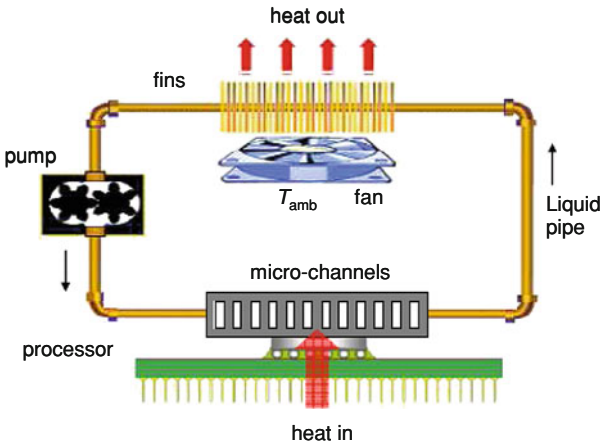

Fig. 6 Schematic of micro-channel flow boiling equipment [6]

Fig. 7 Heat pipe

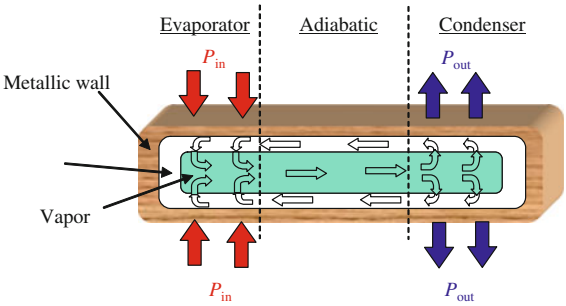

expanding/contracting vapour bubble confined in a tube is employed in bubble jet printers and MEMS actuators.

Heat pipes constitute highly reliable, effective energy transport systems. They can be an effective means of homogenizing the temperature from various heat sources (e.g. a spreader), or of transferring heat from heat sources to heat sinks. Heat pipes have been known since the 19th century but were not really used until the 1960s. Their numerous advantages have stimulated the development of many models over the last few years.

Heat pipe (HP) cooling technology is spreading out for many applications (microelectronics, moulds, medical equipments, etc.). Heat pipe consists of a closed tube with an inner porous layer (the wick) as depicted in Fig. 7.

By means of evaporation and condensation of a working fluid inside the tube, the heat is transported from the evaporator zone, which is in contact with the hot source, to the condenser zone, in contact with a cold sink. A sintered wick HP is usually made of metal, the diameter is usually less than 10 mm and its length is between 100 and 500 mm; furthermore, it provides high heat transfer rates with small temperature gradients.

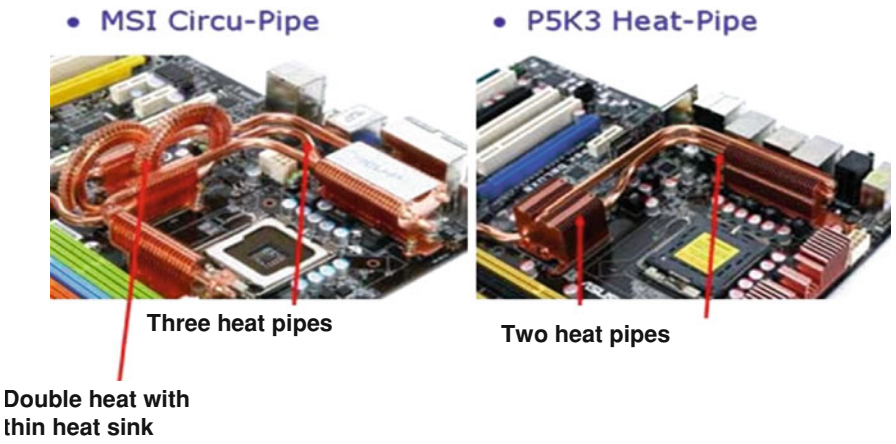

Fig. 8 Heat pipe for electronic components cooling [53]

Heat pipes (HP) are widely used in thermal management of many high temperature devices. Appeared almost three decades ago for space applications, heat pipes are now extensively and successfully applied to electronics and microelectronics cooling (Fig. 8), bio-medical products and many others devices [3–6]. Lack of moving components and simple operation makes HP a very attractive, reliable and cost effective technology. HP are capable of transferring large heat fluxes (up to 200 $MW \cdot m^{-2}$) over a distance of the order of meters driven by small temperature drops (i.e. few tenths degree), thus drastically reducing thermal stresses in the materials using a small quantity of working fluid.

The equivalent thermal conductivity of HP is $\sim 10^4$ times that of copper and silver. The HP solution is very suitable for space requirements because of their reliability and low weight, thus with positive impact on mission costs. In space applications, HP have been extensively used for satellite thermal control and have been proposed to cool wing leading edges in future hypersonic vehicles.

1.6 Micro Heat Pipes (MHPs)

Micro heat pipes have emerged as a reliable approach for cooling high-heat-flux devices such as computer chips and thyristors. The International Technology Roadmap for Semiconductors 2005 predicted that the allowable maximum power for high performance devices would exceed 300 $W \cdot m^{-2}$. Heat fluxes generated by metal-oxide semiconductor-controlled thyristors are already in the range of 100–300 $W \cdot cm^{-2}$. As the power density of critical electronic components increases, heat pipes with improved thermal performance are required. In order to enhance the thermal performance of the micro heat pipe, it is necessary to identify

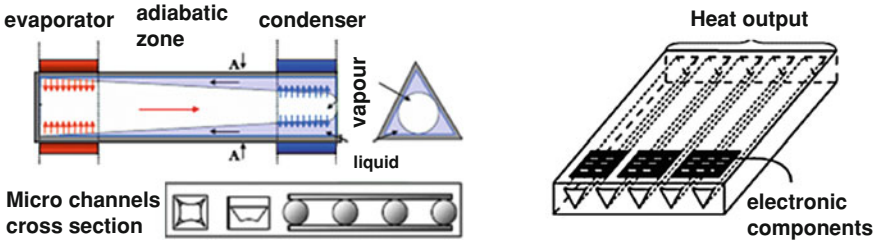

Fig. 9 Micro heat pipe [54]

and better understand the phenomena that govern its performance, and to optimize the wick structure of a micro heat pipe (Fig. 9).

One way to obtain such or higher thermal conductivities at a lower cost is to use micromachined two-phase micro heat pipes (MHPs) in a cheaper substrate of high conductivity material like copper, aluminum or silicon. A MHP is a cavity of small thickness, less than 1 mm, which is filled with a two-phase working fluid. Heat sources and heat sinks are located anywhere on the cavity with the other parts being thermally insulated. The heat sources can be electronic components or any system dissipating high heat fluxes and having to be maintained at a low or a constant temperature. The heat sinks can be any classical cooling devices. Vapour is generated at the heat source level and is condensated at the heat sink level. The liquid returns from the condenser to the evaporator through a capillary structure. For the cooling of electronic components, the more common working fluids are water, acetone, ethanol or methanol.

For both metallic and silicon MHPs, three types of capillary structure can be found in literature. The simplest MHPs have a single non-circular channel for both the liquid and the vapour phases. For these MHPs, the liquid returns from the condenser to the evaporator by capillary flow in the sharp corners of the pipe. These types of MHP are generally placed in an array of parallel MHPs in order to increase the heat exchange area. The second configuration deals with MHPs having a single vapour core and a one dimensional capillary structure such as parallel grooves. There is also another configuration deals with MHPs having a single vapour core and a 2D capillary structure, such as metallic meshes or crossed grooves.

1.7 Variable Conductance Heat Pipe

A variable conductance heat pipe (VCHP) is an active thermal control device used in applications where there is a demand to reduce (controlled conductance) or to block (OFF mode) the thermal conductance during some operational modes of the spacecraft. The heat pipe conductance in a VCHP is reduced or blocked by the

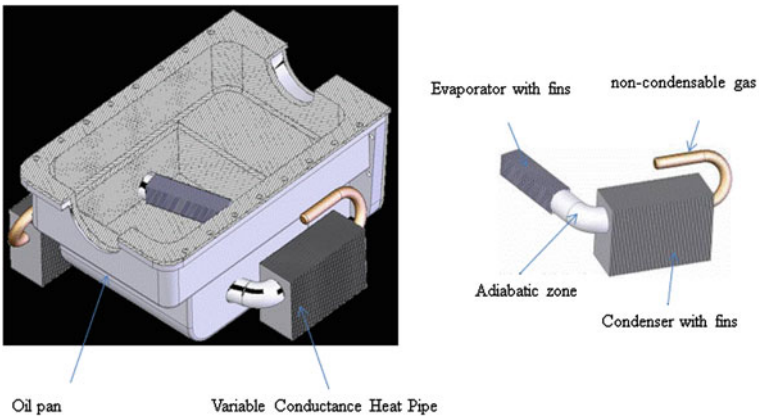

Fig. 10 Variable conductance heat pipe [55]

introduction of a certain amount of non-condensable gas (NCG) in the condensing section of the heat pipe.

VCHP controls the evaporator temperature change by altering the amount of available condenser area. Decreasing ambient temperatures decreases the vapour pressure of the working fluid and increases the volume of NCG, lowering the condenser area. Because NCG is swept to the end of the condenser by the condensing working fluid vapour, it blocks a portion of the condenser, effectively reducing its conductance. If the ambient temperature increases, decreasing the available temperature difference between the condenser and the ambient operating temperature of the heat pipe will increase. This increases the operating pressure (i.e. saturation pressure of the working fluid at the heat pipe operating temperature), compressing the NCG into a smaller volume. Thus more of the condenser area is available for condensing working fluid.

The degree of control depends on the working fluid saturation curve, the desired operating temperature set point, the ranges of ambient temperature and heat load and the volume of gas relative to the volume of the vapour space in the condenser.

Figure 10 is an example of a thermal solution to reduce the overconsumption of a car engine after a cold start: oil pan with internal insulation and equipped with variable conductance heat pipes. An engine consumes substantially more cold than hot, because of the internal friction increased in the high viscosity of cold oil, and bad bumming. Compliance with anti-pollution standards requires even more to limit the overcomsumption cold. The equipment presented in Fig. 10 is an oil sump isolated and equipped with a variable conductance heat pipes. The internal insulation of the engine's oil pan accelerates the oil temperature rise in reducing heat loss. However, oil should not be overheated when the engine runs hot at high load. That is why variable conductance heat pipes are used to cool oil from a certain temperature level in the area of the oil pan, in order to replace the cooling by the walls which becomes inefficient due to insulation. The low thermal inertia of the heat pipes will not annihilate the effect of the oil pan internal insulation.

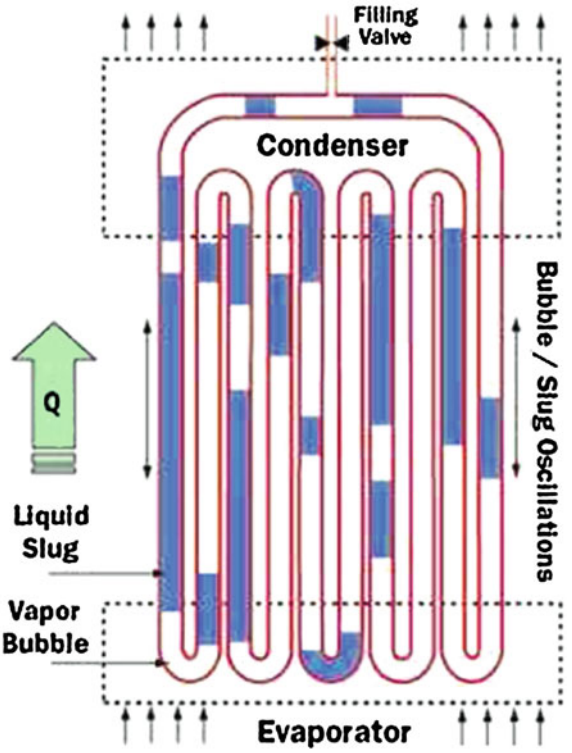

Fig. 11 Pulsating heat pipe [56]

1.8 Pulsating Heat Pipe

The pulsating or oscillating heat pipe (PHP or OHP) is a passive heat transfer device with a potential application in high-heat-fluxes systems. PHPs differ from the conventional heat pipes in several major ways. A PHP is a snake-shaped capillary tube which is partially filled with liquid (Fig. 11). The tube is bent back and forth parallel to itself, and the ends of the tube may be connected to one another in a closed loop, or pinched off and welded shut in an open loop.

Partially filled liquid in capillaries involves segmented liquid slugs and vapour plugs. When heating is applied on the evaporation section, pressures in parallel capillary channels may be different due to the non-uniform lengths of vapour plugs and liquid slugs, causing fluid movement in capillaries. The fluid movement changes the initial distribution of vapour and liquid phases, causing the change of pressure distribution in parallel channels and leading to fluid transport in the direction that is inversed to the initial fluid movement. Continuous heating sustains the oscillation flow. When the fluid is transported from the evaporation section to the condensation section, heat is transferred from the higher temperature zone to the lower temperature zone.

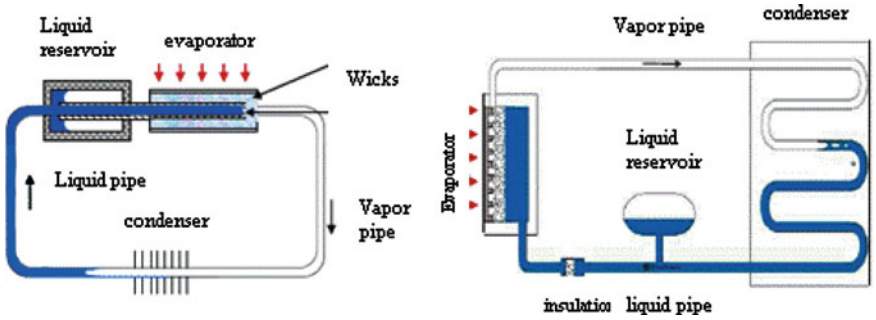

Fig. 12 **a** Loop heat pipe [57]; **b** Capillary heat pipe [58]

1.9 Loop Heat Pipes and Capillary Pumped Loops

Loop heat pipes (LHP) are highly promising two-phase heat transfer devices. Compared to similar two-phase devices such as heat pipes and capillary pumped loops (CPL), LHPs have superior heat transfer capacity, reliable operation in a gravitational field and structural simplicity (Fig. 12a, b). This is because of the structural differences such as the wick being located only in the evaporator and the incorporation of a compensation chamber into the evaporator. With these advantages, the LHPs have mostly been used in challenging fields such as space technologies as almost the only measure for the thermal control of heat generating devices of some critical missions.

Nowadays, the use of LHP and CPL has been extended in many devices related to land based (terrestrial) applications, such as electronic equipment cooling and heat recovery devices, which require high heat transfer efficiency. The effect of gravity, more specifically of elevations and tilts, is considered to be one of the most important factors influencing LHP performance. It is generally known that at an adverse elevation, with the condenser located below the compensation chamber, the operating temperature of the LHP is increased. This is due to the increased hydrostatic head which increases saturation pressure and temperature differences across the wick.

2 Two-Phase Flow Boiling and Heat Transfer in Micro-Channels

As mentioned above, phase change plays a crucial role in heat transfer enhancement in industrial applications. Fundamental investigations have been conducted by various researchers. For instance, liquid–vapour interfacial behaviours in capillary tubes; boiling crisis, recoiling instability and contact angle in pool boiling; boiling behaviours such as bubble nucleation and departure have been

examined by Buffone et al. [7], Sefiane et al. [8] and Hutter et al. [9], respectively. Accordingly, certain simulation methods have been experimentally verified for pool nucleate boiling [10]. On the other hand, in the high-power electronic devices, flow boiling in micro-passages is considered as an effective cooling method. Micro-channels become attractive because of numerous advantages such as high heat dissipation capacity, high surface-to-volume ratio, small size and the flexibility of designing. Lin et al. [11] made a comprehensive review on the prospects of confined flow boiling in future thermal management of micro-systems, which highlighted that confined flow boiling will be an attractive option for micro-system cooling but challenge issues are still waiting to be solved before this technique could be widely used in practice. So far, flow boiling and heat transfer in micro-channels have been widely studied. Remarkable outcomes from the studies on micro-channel flow boiling and heat transfer are summarized as follows.

2.1 Two-Phase Flow Patterns

Flow boiling heat transfer and two-phase pressure drop are closely related with the liquid and vapour phase distribution within the micro-channels. With the aid of high speed photography techniques, it is feasible to visualise the flow patterns during two-phase boiling. Various types of patterns have been identified by different researchers, but the most widely described were bubbly flow, slug flow, churn flow, annular flow and drop flow in vertical tubes and bubbly flow, plug flow, slug flow, wavy and annular flow in horizontal tubes (Fig. 13a, b). Due to varying experimental conditions, especially the geometries of the flow passages, several distinctive flow patterns have been mentioned. In horizontal channels, for example, stratifies flow appears when gravity is non-negligible compared with surface tension, shear and inertia forces within the flow. Flow patterns are also classified into sub-categories according to detailed observations. In Fig. 14a, transition flow occurs when bubble coalescence happens and vapour slugs exist among bubbles, transferring from bubbly flow to slug flow; coalescence of slugs is noted as liquid ring flow (or throat-annular flow in Saisorn et al. [12]) and frothy annular flow with bubbles underneath the large vapour core of annular flow. Besides, Wedging flow [13] consists of slug-droplets and annular-droplets, which is different from the widely reported Taylor bubble flow [14]. Xu et al. [14] compared the flow patterns in different sized rectangular channels and found that in larger channels with a gap of 1.0 and 0.6 mm, bubbly flow, slug flow, churn-turbulent flow and annular flows were observed. However, when channel gap is 0.3 mm, flow patterns can be identified as cap-bubbly flow, slug-droplet flow, churn flow and annular-droplet flow. The decrease of channel gap significantly changed the liquid vapour distribution. Moreover, wispy flow is captured at relatively high mass flow rate, during which entrained droplets attach on the channel wall and form wisps in the centre of the vapour core [15]. In some other

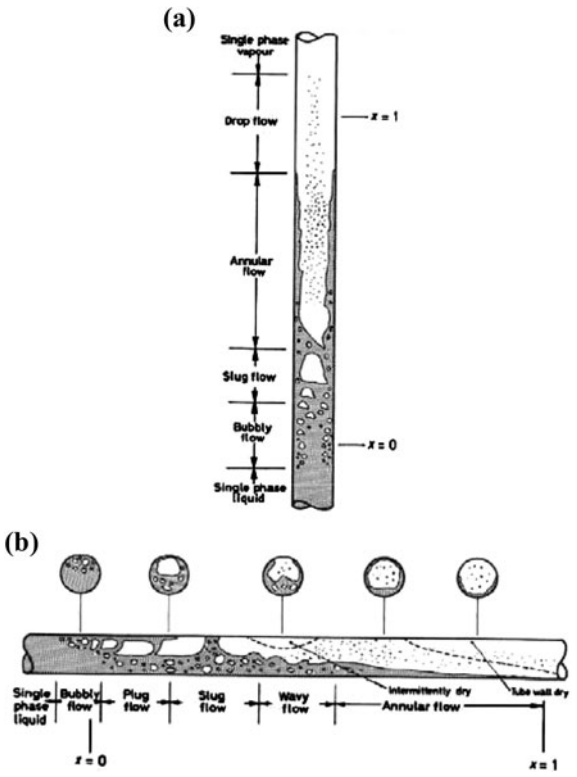

Fig. 13 Flow patterns in a **a** Vertical and, **b** Horizontal evaporator tube [59]

studies, bubbly flow is also named as dispersed flow [16]. Slug flow, elongated bubble flow and churn flow are all classified into intermittent flow.

However, these results are mostly obtained in circular tubes [12, 16–19], square [13] or low aspect ratio rectangular channels [15, 20, 21] and trapezoidal channels [22, 23]. Only very limited studies utilised channels with high aspect ratio [24], $\sigma = 9.668$; and [14], $\sigma = 40$, 20 and 12. Figure 14b exhibits several typical flow regimes encountered in flow boiling within high-aspect-ratio rectangular micro-channels. Tests with similar channel geometry were also conducted by Barber et al. [25]. Flow turns into annular flow shortly after the onset of nucleate boiling due to the confinement of the narrow channel gap. Therefore, the corresponding hydraulic and thermal performances are expected to be distinctive.

2.2 Two-Phase Flow Instabilities

The flow instability is defined as an unstable flow condition induced by the dynamic interaction between the internal and external systems and has various

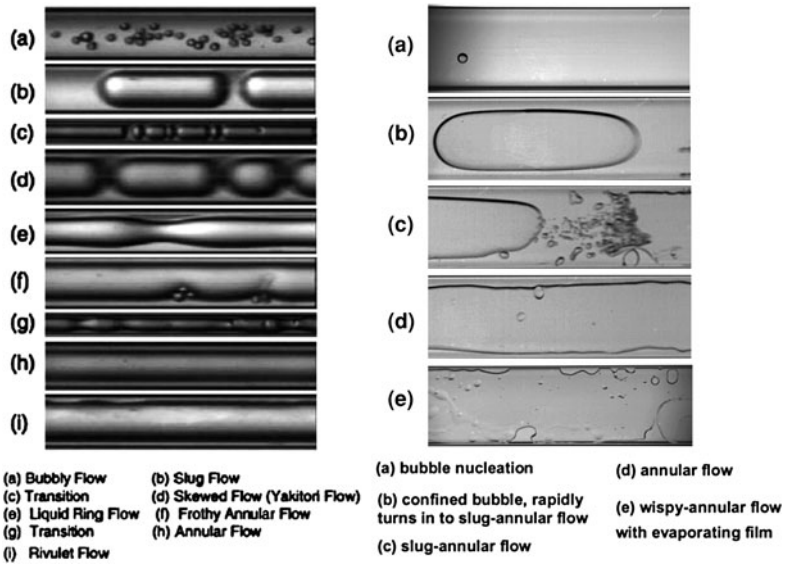

Fig. 14 Flow patterns observed in horizontal. **a** Tube, (air/water, $d = 100$ μm by Serizawa et al. [60]) **b** High-aspect-ratio rectangular channel: ($d_h = 1{,}454$ μm, $\sigma = 10$, FC-72)

types or modes with different mechanisms [26]. Flow instabilities are classified into three main categories (Table 1):

It is essential to identify flow instability prior to further investigations. Kew and Cornwell [27] suggested the threshold of instability to be when the initial bubble diameter approached the channel hydraulic diameter. Kennedy et al. [28] defined the onset of instability according to the pressure drop versus mass flux trend, i.e. the demand curve. The relative minimum point of the demand curve was considered as the onset of flow instability. Further criterion was proposed by Celata et al. [19] who described the flow as unstable when not only the back and forth movement of bubbles but also reverse flow were observed.

Various types of instabilities and corresponding unstable flow behaviors in micro-scale flows have been published in literature. The tendency that instabilities are more severe in micro-channels than macro-channels could be expected, as individual bubbles are more influential on local pressure in smaller internal volume [29]. Flow instabilities were proved to cause pressure drop fluctuations and to deteriorate the heat transfer during flow boiling in uniformly heated micro-channels [30]. The pressure fluctuation consequently resulted in fluctuating channel wall temperatures.

So far, there is no theoretical criterion to identify stable and unstable boiling. Several stability criteria were proposed in the previous studies based on

Table 1 Classification of flow instabilities in boiling channel system [26]

Category	Pattern	Mechanism	Feature
Negative resistance instability	Flow excursion or ledinegg instability	Negative damping in 1st-order system	Transitional, significant flow maldistribution appears in parallel-channel system
	Pressure drop oscillation	Dynamic interaction between flow excursion and accumulation mechanism of mass and momentum	Relaxation oscillation with large amplitude and long period
Time-delayed feedback instability	Density wave oscillation	Propagation delay of void wave (kinematic wave) and feedback effect provide negative damping	Oscillation, period comparable with residence time, appears in positive resistance region of pressure drop versus flow rate
Thermal non-equilibrium instability	Geysering chugging	Insufficient nucleation sites bring about large superheat followed by violent boiling or condensation	Relaxation oscillation if liquid refilling mechanism exists

experimental data with the aid of visualization as well as synchronous pressure and temperature measurements.

Brutin et al. [31] suggested a stability diagram in term of heat flux versus mass flow rate (Fig. 15) based on limited sets of experimental results. The steady state referred to a low fluctuation amplitude (<1 kPa) and no characteristic oscillation frequency while unsteady state was defined by high fluctuation amplitude and a characteristic frequency of a ratio higher than 20.

Chang and Pan [32] studied the two-phase flow instability for boiling in a micro-channel heat sink with 15 parallel rectangular channels ($d_h = 86.3$ μm), the width and depth of which were 99.4 and 76.3 μm respectively. They suggested that the amplitude of pressure drop oscillation might be used as an index for the occurrence of reverse flow. They pointed out that reverse flow to inlet chamber would occur when the deviation between the maximum and the minimum pressure drops became larger than 6 kPa. Additionally, the stability map in term of inlet subcooling number versus phase change number showed conspicuous difference from that for an ordinarily sized channel. Only a very narrow region of stable two-phase flow or mild two-phase flow oscillations was near the zero vapour quality line. In an ordinarily sized channel, on the other hand, unstable region occupied the upper right part of the map.

Unstable flow boiling was also classified into two sub-types according to the oscillation period length ([33], Fig. 16). Based on the visualization results, it was found that the unstable flow boiling with long-period oscillation was induced by the transition from annular to mist flow. On the other hand, the unstable flow boiling with short-period oscillation was a result of vapour expansion.

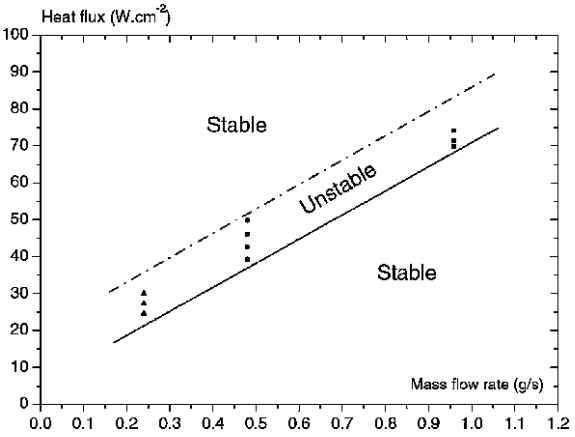

Fig. 15 Stability diagram of heat flux supplied as a function of the mass flow rate in a $0.5 \times 4 \times 50$ mm^{3}mini-channel [31]

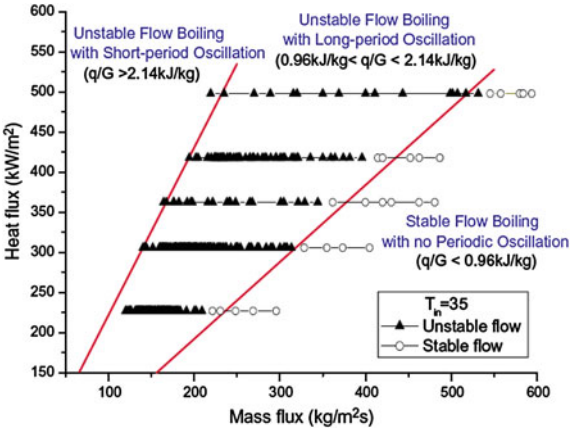

Fig. 16 Stable and unstable flow boiling regimes in parallel micro-channels [33]

Wang and Cheng [34] suggested a criterion to determine stable and unstable flow regime using the thermodynamic exit vapour quality, which was defined as $(i_e - i_f)/h_{lv}$, where i_e and i_f are the exit liquid enthalpy and saturated liquid enthalpy. A critical vapour quality of 0.013 was proposed, beyond which the flow would turn into unstable. This critical exit vapour quality, however, was independent of inlet fluid temperature, heat flux, mass flux, working fluid and the test section geometry.

Even for unstable flows, the instability behaviours vary from time to time. Balasubramanian and Kandlikar [35] found that the magnitude of pressure drop and the dominant frequency increase with increasing wall temperature, i.e. a higher heat flux. However, opposite trend of fluctuation frequency was reported by Muwanga et al. [36] where decreasing frequency and higher amplitude of liquid temperatures as well as pressures were obtained at higher heat flux.

There are also some other parameters which were found influential to the two-phase flow stability. Effects of inlet conditions on two-phase flow pressure fluctuation amplitude and frequency were discussed by Brutin and Tadrist [37]. Two types of inlet conditions were fabricated. The first corresponded to the constant liquid velocity at the mini-channel entrance which was called the confinement case; the second was to provide a constant velocity at the syringe outlet by connecting a buffer tank between the syringe and mini-channel. The second inlet condition corresponded to the compliant case. For all the inlet Reynolds numbers ($0 < \mathrm{Re} < 10{,}000$) and heat fluxes ($15.7 \sim 125.6\ \mathrm{kW \cdot m^{-2}}$), the fluctuation amplitude was much smaller in the confinement case, but the oscillation frequencies were higher in the compliant case.

In addition, differences between single channel and parallel channels were evidenced by some researchers.

Ding et al. [38] believed that less upstream compressible volume was required in single channel to initiate pressure-drop instability than in parallel channels. Therefore it was easier to detect the flow instability in single micro-channel.

Wang et al. [33] conducted the separate flow boiling experiments in eight parallel micro-channels and in a single micro-channel with water. All the channels had the identical trapezoidal cross-section and a hydraulic diameter of 186 μm. They emphasized the much longer temperature fluctuation in single channel than in parallel channels which they believed was a result of the significant flow interaction from neighboring parallel channels.

Singh et al. [39] experimentally studied the pressure drop characteristics in parallel trapezoidal micro-channels with a hydraulic diameter of 109 μm over a wide range of heat flux and mass flux. For both single channel and multi-channel conditions, averaged pressure drop increased with increasing heat flux for a constant mass flux. However, the fluctuations in parallel channels were not as periodic as in single channel. Nevertheless, higher pressure drop was found in parallel channels, reinforcing the explanation that fluctuation was caused by periodic bubble formation and departure.

Moreover, flow instability was evidenced to be affected by other experimental parameters such as surface roughness. Bhide et al. [40] compared the two-phase pressure drop and stability in smooth micro-channels with hydraulic diameters of 45 and 65 μm and a rough micro-channel with a hydraulic diameter of 70 μm. They concluded that for rougher surface conditions, more nucleation sites induced larger amount of bubbles in two-phase flow. Therefore the transition from nucleate boiling bubbly flow to annular flow would be completed in a shorter period. Compared with bubbly flow, annular flow was much steadier. Thus the oscillation was largely suppressed.

Recently published investigations revealed some new flow instability characteristics. A fluctuation minimum with increasing heat flux was firstly reported by Singh et al. [39]. The pressure fluctuation showed peculiar trends which firstly increased, then dropped a minimum and kept on increasing as heat flux increased. This was different from previous studies that mostly showed monotonic increase in pressure fluctuation with increasing vapour quality [36] and [41]. Additionally, the

transitions between flow patterns showed different stabilities depending on the heat flux and mass flux [19]. Stable alternation was observed at high or very high heat flux and mass flux conditions while oscillating flow with instabilities were captured at low heat flux and mass flux. Besides, system instability owing to the usage of constant flow pump, a buffer tank, and a constant heating pre-heater should also be considered in micro-channel systems [42].

In addition, the improvement of experimental setups plays an important role in further exploring the flow instabilities. Barber et al. [43] managed to obtain simultaneous measurements of channel wall temperature in conjunction with local flow visualization and pressure drop measurements across a high aspect ratio micro-channel with the aid of infrared camera and transparent heating technique. Data acquisition synchronization and noble transparent heating technique are helpful in disclosing the complex internal flow boiling in micro-channels.

2.3 Boiling Heat Transfer

2.3.1 Overview of Experimental Results of Flow Boiling Heat Transfer

Because of the appreciable potential applications of two-phase flow in high-thermal density devices, flow boiling heat transfer characteristics have been studied widely. Great efforts have been made to reveal the heat transfer mechanisms in small scale flow passages. However, different heat transfer characteristics were reported due to various experimental conditions such as channel geometry, working liquid, saturation pressure as well as the applied heat flux and mass flux, etc.

Table 2 summaries a number of experimental studies on flow boiling heat transfer in mini- and micro-channels with circular, rectangular, square and trapezoidal cross-section geometries since 1990s. Various ranges of vapour quality are achieved, the corresponding dependency of heat transfer on flow and thermal conditions are described differently. More importantly, the dominant heat transfer mechanisms more or less vary in different studies, indicating the necessity of further experimental investigations.

Apparently, limited attention has been paid in the past 20 years on the flow boiling in high aspect ratio micro-channel. More concentration is required because high aspect ratio channels can be potentially used in various industry applications thanks to its unique advantages: first, high aspect ratio channels have a large surface-to cross-sectional area ratio. Second, channels with high aspect ratio can reduce vapour side pressure drop and increase vapour side heat transfer [44].

In recent experimental studies, flow boiling in high aspect ratio micro-channels show distinctive heat transfer characteristics. As shown in Fig. 17, the local heat transfer coefficient h_{local} along the channel stream-wise direction is a strong decreasing function of vapour quality. Also, h_{local} increases with increasing q. Moreover, the effect of heat flux is larger in high vapour quality region as the

Table 2 Review of experimental investigations on boiling heat transfer in small flow passages

Author(s) (References)	Channel dimension; hydraulic diameter d_h(mm)	Working liquid; mass flux G [kg·m^{-2}·s^{-1}]; heat flux q [kW·m^{-2}]	Vapour quality x	Pressure [bar]; temperature [°C] and others	Heat transfer mechanism	Remarks of heat transfer characteristics
Peng and Wang [64]	3 parallel, rectangular; (0.6 × 0.7 mm^2); d_h = 0.646	Deionized water; liquid velocity: 1.5–4.0 m/s		P = 1 atm; T_{sub} = 40–70°C	Nucleate boiling	Temperature overshoot was observed by increasing heat flux; distinct effects of u_L and T_{sub} were found in single phase region but not in the nucleate boiling region.
Tran et al. [62]	Single, circularand rectangular; d_h = 2.46 and 2.4	R12; G: 44–832; q: 3.6–129	0–0.94	P_{sat} = 8.25; Boiling number: 0.0002–0.0016	Nucleate boiling	Heat transfer coefficient h increased with q but was independent of G or x; No significant influence of d_h was found.
Bao et al. [65]	Single, circular; d_h = 1.95	R11, R123; G: 50–1,500; q: 5–200	0–0.9	P_{sat} = 2.94–5.09	Nucleate boiling	Heat transfer coefficients were independent of G and x, but were strong functions of the q and P_{sat}.
Lin et al. [66]	Single, circular; d_h = 1.1, 1.8 and 2.8, rectangular (square); d_h = 2	R141b; G:15–3,500; q: 1–300	0–1.0	P_{in} = 1.0–3.0; Boiling number: 0.00022–0.00078	Transfer from nucleate boiling to convective boiling	Average h was largely affected by q and x, but slightly increased with G in the convective region; h reached a peak at x = 0.05–0.1, then decreased with increasing x; channel diameter and geometry affected heat transfer after dry-out occurrence; Dryout prone to occur under increased confinement; transform from nucleate boiling to convective boiling happened at higher quality in smaller tubes.
Warrier et al. [63]	5 parallel, rectangular; d_h = 0.75	FC-84; G: 557–1,600; q: 0–59.9	0–0.55	T_{in} = 26, 40 and 60°C; Boiling number: 0.00043–0.00089		For a given heat flux, h decreased with x in low x range, but independent of x in high quality range.
Yu et al. [67]	Single, circular; d_{in} = 2.98	Water; G: 50–200	0–1.0	P = 2 bar; T_{in}: up to 80°C	Nucleate boiling was dominant till vapour quality reached 0.5.	Heat transfer was heat–flux-dependent but essentially mass-flux-independent, which was significantly different from the large-sized channels; CHF decreased with decreased mass flux.

(continued)

Table 2 (continued)

Author(s) (References)	Channel dimension; hydraulic diameter d_h(mm)	Working liquid; mass flux G [kg·m^{-2}·s^{-1}]; heat flux q [kW·m^{-2}]	Vapour quality x	Pressure [bar]; temperature[°C] and others	Heat transfer mechanism	Remarks of heat transfer characteristics
Qu and Mudawar [68]	21 parallel, rectangular, (0.231 × 0.713 mm^2); d_h = 0.349	Water; G: 135–402	0–0.2		Convective boiling	h decreased with x in all the vapour quality range. Besides, h strongly depended on G, but only weakly relied on q; Note: similar trend was reported by Bhide et al. [40], but Bhide et al. did not consider forced convection heat transfer to be dominant because of the decreasing trend of h on x. Instead, they emphasised the effects of thermal instabilities.
Yen et al. [69] (2003)	Single, circular; d_{in} = 0.19, 0.30 and 0.51	HCFC123,FC72; G: 50–300; q: 1–13	0–1.0	P_{system} = 1.10–1.25 for 0.51 mm ID and 1.35–1.45 for 0.19 mm ID; Boiling number: ~ 0.0006	Nucleate boiling with minor convective boiling contribution	Superheat occurred at low boiling number, indicating a heat flux threshold for nucleation cavity activation. In saturated boiling, h monotonically decreased with increasing x, but was independent of G. Annular flow prevailed in micro-tubes.
Huo et al. [70]	Single, circular; d_h = 4.26 and 2.01	R134a; G:100–500; q: 13–150	0–0.9	P_{in} = 8–12	Transfer from nucleate boiling to convective boiling	h versus x trends varied with channel sizes. Smaller channel lowered the vapour quality corresponding to the peak h; For larger channel: x = 0.45–0.5, but for the smaller channel: x = 0.2–0.3; dependence of h on x increased with increasing q. Succeedingly, the effect of q diminished, transferring to the convective boiling domination.
Steinke and Kandlikar [71]	6 parallel, trapezoidal, average dimention: (0.214 × 0.2 mm^2); d_h = 0.204	Water; G: 157–1,782; q: 5–930	0–1.0	T_{in} = 22°C	Nucleate boiling	A heat flux of 930 kW/m^2 was achieved with a high heat transfer coefficient of 192 kW/m^{2}K; two-phase heat transfer coefficient decreased with increasing vapour quality.

(continued)

Table 2 (continued)

Author(s) (References)	Channel dimension; hydraulic diameter d_h(mm)	Working liquid; mass flux G [kg·m^{-2}·s^{-1}]; heat flux q [kW·m^{-2}]	Vapour quality x	Pressure [bar]; temperature[°C] and others	Heat transfer mechanism	Remarks of heat transfer characteristics
Greco and Vanoli [72]	Single, circular; $d_{in} = 6$	R410A, R404A; G: 290–1,100; q: 11–39	0–1.0	$P_{sat} = 3$–12	Nucleate boiling	Nucleate boiling and liquid convection dominance varied with vapour quality and the flow conditions: for high q and high P_{sat}: nucleate boiling was dominant; For low q and low P_{sat}: convective boiling was dominant. Effect of working liquid changed with P_{sat}: at low P_{sat}, h of R410 was larger than h of R404A, but the difference decreased as P_{sat} was higher.
Lee and Mudawar [46]	53 micro-slots; (0.231 × 0.713 mm^2)	R134a; G: 127–654; q: 159–938	0.26– 0.87	$P_{in} = 1.44$–6.60	Annular film evaporation in medium to high quality	Bubbly flow and nucleate boiling occurred only at $x_e < 0.05$ and at very low q. For $0.05 < x_e < 0.55$ or $0.55 < x_e < 1.0$, annular film evaporation dominated; as x_e increased, slope of h versus x_e reduced from steep to almost zero.
Saitoh et al. [73]	Single, circular; $d_h = 0.51$, 1.12 and 3.1	R134a; G: 150–450; q: 5–39	0–1.0 inlet $x = 0$–0.2	$T_{sat} = 5$, 10 and 15°C	Nucleate boiling was dominant in low quality region and forced convective evaporation was dominant in high quality region.	Critical vapour quality (CVQ) was decreased by decreasing channel diameter; In smaller channel, flow approached homogeneous flow and the effect of G decreased, but the effect of T_{sat} became more considerable.
Yun et al. [74]	Single, circular; $d_h = 0.98$ and 2.0	CO_2; G: 500–3,570; q: 7–48	0–1.0	$T_{sat} = 0$, 5 and 10°C		Heat transfer coefficient before the CVQ was a strong function of q at all G, but G had an impact restrained by Weber number value. CVQ decreased with increasing q, then kept constant for higher q; post-CVQ region showed negligible effect of q and no significant effect of channel diameter on heat transfer. The heat transfer after CVQ was explained by the partially dried liquid film and rate of liquid droplets in the vapour core.

(continued)

Table 2 (continued)

Author(s) (References)	Channel dimension; hydraulic diameter d_h(mm)	Working liquid; mass flux G [kg·m^{-2}·s^{-1}]; heat flux q [kW·m^{-2}]	Vapour quality x	Pressure [bar]; temperature[°C] and others	Heat transfer mechanism	Remarks of heat transfer characteristics
Chen and Garimella [75]	10 parallel, rectangular, (0.504 × 2.5 mm^2); d_h = 0.839	FC–77; G: 30–50 ml/min; q: 0–240		$P_{channel}$ = 1 atm		Different flow rates resulted in different wall temperatures. For low wall temperature, higher h was achieved at lower flow rate. In fully developed boiling region, T_w weakly depended on q, i.e. very small increase of T_w caused rapid increase of q, indicating an appreciable heat dissipating capacity.
Choi et al. [76]	Single, circular; d_h = 1.5 and 3.0	CO_2; G: 200–600; q: 20–40	0–1.0	T_{sat} = 10°C	Nucleate boiling in low x region	Insignificant effects of G and x were found in low vapour quality region; geometric effects must be considered because laminar flow appeared during flow boiling in small tubes.
Díaz and Schmidt [77]	Single, rectangular, (0.3 × 12.7 mm^2); d_h = 0.586	Water and ethanol; G: 50–500; q: up to 400	−0.1–0.7	P_{in} = 1.13–2.60	Water: nucleate boiling; ethanol: both nucleate and convective boiling	Different heat transfer characteristics in water and ethanol were found: for water: h decreased with x from x = 0; For ethanol: h increased with x in high quality region and low heat flux, h decreased at high heat fluxes.
Huh and Kim [21]	Single, rectangular; d_h = 0.10	Water; G: 90, 169, 267; q: 200–500	0–0.4		Nucleate boiling	Although nucleate boiling was dominant, the observed flow pattern was similar to the conventional annular flow.
Liu and Garimella [47]	Single, rectangular; channel I: (275 × 636 μm^2); channel II: (406 × 1,063 μm^2)	Water; G: 221–1,283; q: 0–1,290	0–0.2	T_{in} = 67–95°C	Nucleate boiling	Inlet liquid temperature T_{in} and flow velocity affected ONB, but became less influential afterward; Contribution of convective component was suppressed by boiling heat transfer from fully developed boiling region. Wall temperature T_w near channel exit dropped lower than those at upstream locations due to reduced T_{sat} after saturated boiling.

(continued)

Table 2 (continued)

Author(s) (References)	Channel dimension; hydraulic diameter d_h(mm)	Working liquid; mass flux G [kg·m^{-2}·s^{-1}]; heat flux q [kW·m^{-2}]	Vapour quality x	Pressure [bar]; temperature[°C] and others	Heat transfer mechanism	Remarks of heat transfer characteristics
Agostini et al. [45] (a)	67 parallel, rectangular, (0.223 × 0.68 mm^2); d_h = 0.336	(a) R236fa; G:281–1,501; q: 36–2,210	(a) 0.02– 0.75	(a) P_{sat} = 2.73	(a) Nucleate boiling	(a) At low q, low x and low G, h increased with x but independent of q or G; At medium q, h was independent of x and increased with q but weakly changed with G; At very high q: h weakly increased with G but decreased with further increase of q; convective boiling did not exist.
Agostini et al. [78] (b)		(b) R245fa; G: 281–1,501; q: 36–2,900	(b) 0–0.78	(b) P_{sat} = 1.41–2.73	(b) Nucleate boiling and convective boiling	(b) Heat transfer coefficient h increased with P_{sat} but was independent of T_{sub}; For low q: h increased with x but was independent of q or G; for medium q: h increased with q and slightly increased with G, but was independent of x; while for high q: h decreased with q and x but increased with G.
Bertsch et al. [79]	17 parallel, rectangular; d_h = 1.09	HFC-134a; G: 20.3–81; q: 0–200	0–1.0	P_{sat} = 4.7, 5.5 and 7.5	Nucleate boiling	No obvious temperature overshoot was observed in the boiling curves; h increased with q and G, and strongly depended on x. CVQ was around 0.2; The decrease of d_h lowered the CVQ; The effect of P_{sat} was negligible.
Lee and Garimella [80]	Parallel micro-channel array, rectangular; (102 ~997 × 400 μm^2)	Water; G: 46–126 ml/min; q: 10–340	−0.02–0.20	T_{in} = 90.6–95.1°C	Transfer from nucleate boiling to convective boiling	No temperature overshoot was observed in the boiling curves measured at five stream-wise locations at a given G and q. Local h increased linearly with q for low to medium q, but for higher q, h became insensitive to q, indicating a transition from nucleate boiling dominance to convective boiling dominance.

(continued)

Table 2 (continued)

Author(s) (References)	Channel dimension; hydraulic diameter d_h(mm)	Working liquid; mass flux G [kg·m^{-2}·s^{-1}]; heat flux q [kW·m^{-2}]	Vapour quality x	Pressure [bar]; temperature[°C] and others	Heat transfer mechanism	Remarks of heat transfer characteristics
Bertsch et al. [81]	17 parallel, rectangular; $d_h = 1.09$; 33 parallel, rectangular; $d_h = 0.54$	R134a and R245fa; *G*: 20–350; *q:* 0–220	−0.2–0.9	$T_{sat} = 8$–30°C; $P_{sat} = 1.25$–7.5	Nucleate boiling	Heat transfer coefficient h was a strong function of q and x but only slightly changed with G and P_{sat}; smaller channel slightly enahnced heat transfer; Compare with previous study Bertsch et al. [79] where CVQ was 0.2, CVQ = 0.5 in the present study, showing that CVQ was higher at higher G.
da Silva Lima et al. [82]	Single, circular, copper; $d_{in} = 13.84$	R134a; *G*: 300–500; *q*: 7.5–17.5	0.01–0.99	$T_{sat} = 5$, 15 and 20°C	Nucleate boiling and convective boiling	Newly found that for slug flow, heat transfer was not a simple juxtaposition of nucleate and convective boiling contributions, but that the integration of these two heat transfer mechanisms was also a function of flow parameters such as mass flux and geometrical modifications the flow was suffering. h increased with T_{sat} at low x region.
In and Jeong [17]	Single, circular; $d_h = 0.19$	R123 and R134a; *G*: 314,392, 470; *q*: 10,15,20	0.2–0.85	$P_{sat} = 1.58$, 2.08 for R123 and 9, 11 for R134a	Transfer from nucleate boiling to convective boiling	Strong effect of G was shown on h versus x trends at low P_{sat}, but increase of G resulted in deterioration of h at high quality region; effect of q was different for the two liquids: for R123: h increased with q, effect of q was more profound for higher x; while for R134a, effect of q was reduced as x increased. The decline of the effect of heat flux was more evident as G was higher.
Kuznetsov and Shamirzaev [83]	10 parallel, rectangular, (0.64 × 2.05 mm^2); $d_h = 0.975$	water; *G*: 17, 51; *q*: 30–150	0–0.8	$P_{channel} = 1$ atm	Nucleate boiling and liquid film evaporation	Negligible effect of G was found. When G was low, liquid film evaporation became dominant. Effect of q decreased as G decreased.

(continued)

Table 2 (continued)

Author(s) (References)	Channel dimension; hydraulic diameter d_h(mm)	Working liquid; mass flux G [kg·m^{-2}·s^{-1}]; heat flux q [kW·m^{-2}]	Vapour quality x	Pressure [bar]; temperature[°C] and others	Heat transfer mechanism	Remarks of heat transfer characteristics
Ong and Thome [84]	Single, circular; $d_h = 1.03$	R134a, R236fa and R245fa; G: 200–1,600; q: 2.3–250	0–1.0	$T_{sat} = 31$°C	Nucleate boiling and convective boiling	Heat transfer coefficient h depended on q, G and x but not on T_{sub}; h increased with x even in annular flow region; significant differences were found in the three liquids due to different surface tensions.
Saisorn et al. [12]	Single, circular; $d_h = 1.75$	R134a; G: 200–1,000; q: 1–83	0–1.0	$P_{sat} = 8$–13		Channel average h_{avg} increased with q till a peak then h_{avg} decreased after partial dry-out occurred; h decreased as P_{sat} was higher but was independent of G and x; Five flow regimes were observed.
Hamdar et al. [85]	Single, square; $d_h = 1.0$	HFC-152a; G: 200–600; q: 10–60	0–1.0	$P_{sat} = 6$	Nucleate boiling	Heat transfer coefficient h was a strong function of q but was independent of x and strictly independent of G; Boiling curves were also independent of G.

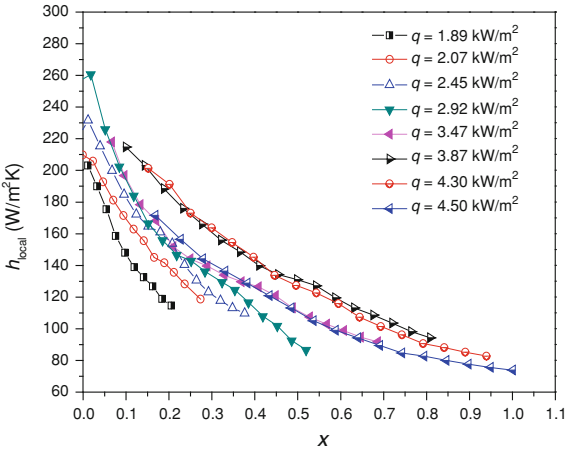

Fig. 17 Local heat transfer coefficient versus vapour quality in a rectangular micro-channel with a hydraulic diameter $d_h = 762$ μm and an aspect ratio 20, $G = 11.2$ kg·m^{-2}·s^{-1}, $T_{in} = 25$°C, FC-72

curves become more divergent as x increases. It is interesting to find that h_{local} starts to decrease with further increase of q in high heat flux region. Similar trend of h decreases with further increase of q was also reported by Agostini et al. [45]. Intermittent dry-out prior to CHF probably has caused the deterioration of heat transfer.

The unique geometry of high aspect ratio channel results in an annular flow regime and the dominance of convective boiling, the corresponding heat transfer coefficient of which is largely affected by heat flux and mass flux. Comprehensive experimental investigations on flow boiling in high aspect ratio channel are needed to better understand the heat transfer mechanisms and to seek for more applicable flow pattern transition criteria.

2.3.2 Overview of Flow Boiling Heat Transfer Correlations

A large number of two-phase heat transfer correlations have been developed from existing experimental data. Table 3 includes several basic flow boiling heat transfer correlations. Many other correlations were modified and developed on the foundation of these basic correlations using different databases (e.g. [46–52]).

Specifically, some newly obtained heat transfer results (426 data points) in high aspect ratio micro-channels were compared with the correlations specified for rectangular mini- and micro-channels in Table 3. Experimental data show significant disagreements with the prediction, less than 15% data fall into the ±30% prediction range. The discrepancies indicate that, apart from circular or low aspect ratio rectangular channels, heat transfer correlations for high aspect ratio channel geometries need to be further explored (Fig. 18).

Table 3 Summary of fundamental correlations for saturated flow boiling heat transfer in macro-, mini- and micro-channels

References	Experimental parameters	Correlation for h	MAE[1](%)
Chen [86]	Water and organic fluids; vertical tubes; $u_L = 0.061 \sim 4.481$ m·s^{-1}; $x = 0.01 \sim 0.71$; $P = 0.56 \sim 35.28$ bar; macro-tube and annulus	$h_{tp} = Fh_{sp} + Sh_{nb}$ $h_{sp} = 0.023(\mathrm{Re_L})^{0.8}(\mathrm{Pr_L})^{0.4}(k_L/D)$ $h_{nb} = 0.00122\left(\frac{k_L^{0.79}C_{p,L}^{0.45}\rho_L^{0.49}g_c^{0.25}}{\sigma^{0.5}\mu_L^{0.29}h_{lv}^{0.24}\rho_v^{0.24}}\right)(\Delta T)^{0.24}(\Delta P)^{0.75}$ $F = (1 + 1/X^{0.5})^{1.78}$, $S = 0.9622 - 0.5822\left[\tan^{-1}\left(\frac{\mathrm{Re_L F}^{1.25}}{6.18 \times 10^4}\right)\right]$ X: Martinelli parameter, $X = \left(\frac{1-x}{x}\right)^{0.9}\left(\frac{\rho_v}{\rho_L}\right)^{0.5}\left(\frac{\mu_L}{\mu_v}\right)^{0.5}$ $\mathrm{Re_L} = \frac{G(1-x)d_h}{\mu_L}$, $\mathrm{Pr_L} = \frac{c_{p,L}\cdot\mu_L}{k_L}$	12
Lazarek and Black [61]	$G = 125$–750 kg·m^{-2}·s^{-1}; $q = 14$–380 kW·m^{-2}; static pressure: 1.3–4.1 bar; Re: 860–5,500 Bo: 2.3×10^4–76×10^4; mini- and micro-channels	$h_{tp} = 30\mathrm{Re}^{0.857}\,\mathrm{Bo}^{0.714}k_L/d_h$ $\mathrm{Re} = Gd/\mu_L$ $\mathrm{Bo} = q/(Gh_{lv})$	
Kandlikar [1] and Kandlikar and Balasubramanian [51]	Water, refrigerants, neon and nitrogen; vertical and horizontal; $d_h = 4.6 \sim 32$ mm; $G = 13 \sim 8{,}179$ kg·m^{-2}s^{-1}; $q = 0.3 \sim 2{,}280$ kW·m^{-2}; $x = 0.001 \sim 0.987$; $P = 0.6 \sim 64.2$ bar; macro-channels	$h_{tp} = \left(C_1 Co^{C_2}(25Fr_L)^{C_5} + C_3 Bo^{C_4}F_{fL}\right)\cdot h_{sp}$ $h_{sp} = 0.023\mathrm{Re_L^{0.8}}\,\mathrm{Pr_L^{0.4}}(k_L/d)$ $\mathrm{Co} = \left(\frac{1-x}{x}\right)^{0.8}\left(\frac{\rho_v}{\rho_L}\right)^{0.5}$ values of C_1–C_5 were given for convective and nucleate boiling regions respectively; F_{fL}: fluid-dependent parameter; Co: convection number Extension of the correlation neglects channel orientation in mini-channels, thus Froude number effect is deleted.	13.0–23.2

(continued)

Table 3 (continued)

References	Experimental parameters	Correlation for h	MAE[1](%)
Tran et al. [62]	R12; single, circular and rectangular; $d_h = 2.4 \sim 2.92$ mm; $G = 44 \sim 832$ kg·m^{-2}·s^{-1}; $q = 3.6 \sim 129$ kW·m^{-2}; $x = 0 \sim 0.94$; reduced pressure: 0.045 $\sim$ 0.20 bar; mini-channels	$h = (8.4 \times 10^5)(\mathrm{Bo}^2\mathrm{We_L})^{0.3}\left(\frac{\rho_L}{\rho_v}\right)^{-0.4}$	15
Warrier et al. [63]	FC-84; 5 parallel, rectangular, $d_h = 0.75$ mm; $G = 557 \sim 1{,}600$ kg·m^{-2}·s^{-1}; $q = 0 \sim 59.9$ kW·m^{-2}; $x = 0 \sim 0.55$; $T_{in} = 26$, 40 and 60°C; mini- and micro-channels	$h_{tp}/h_{sp\_FD} = 1 + 6.0\ \mathrm{Bo}^{1/16} - 5.3(1 - 855\ \mathrm{Bo})x^{0.65}$	Maximum difference: ± 28
Yu et al. [67]	Water; single, circular, $d_{in} = 2.98$ mm $G = 50 \sim 200$ kg·m^{-2}·s^{-1}; T_{in} = up to 80°C; $P = 2$ bar; mini- and micro-channels	$h_{tp} = 6400000(\mathrm{B_o^2We_L})^{0.27}(\rho_v/\rho_L)^{-0.2}$	Mostly fell in ± 30
Bertsch et al. [2]	Water, refrigerants, FC-77 and nitrogen; circular and rectangular, $d_h = 0.16 \sim 2.92$ mm; $G = 20 \sim 3{,}000$ kg·m^{-2}·s^{-1}; $q = 0.4 \sim 115$ kW·m^{-2}; $x = 0 \sim 1.0$, $T_{sat} = -194 \sim 97$°C; Confinement number: 0.3 $\sim$ 4.0; mini- and micro-channels	$h_{tp} = h_{nb} \cdot (1 - x) + h_{conv,tp} \cdot \left[1 + 80(x^2 - x^6) \cdot e^{-0.6Co}\right]$ $h_{nb} = 55P_r^{0.12-0.2\log_{10}R_p} \cdot (-\log_{10} P_r)^{-0.55} M^{-0.5} q^{0.67}$, R_P : surface roughness parameter (μm); P_r : reduced pressure $h_{conv,tp} = h_{conv,L} \cdot (1 - x) + h_{conv,v} \cdot x$ $h_{conv,L} = \left(3.66 + \frac{0.0668 \cdot \mathrm{Re} \cdot \mathrm{Pr} \cdot d_h/L}{1 + 0.04 \cdot [\mathrm{Re} \cdot \mathrm{Pr}\ d_h/L]^{2/3}}\right) \cdot \frac{k_L}{d_h}$ $h_{conv,v}$is calculated using the properties of saturated vapour instead	30

[1] MAE: mean absolute error, defined as $(1/N)\sum(|h_{exp.} - h_{cor.}|/h_{exp.})$

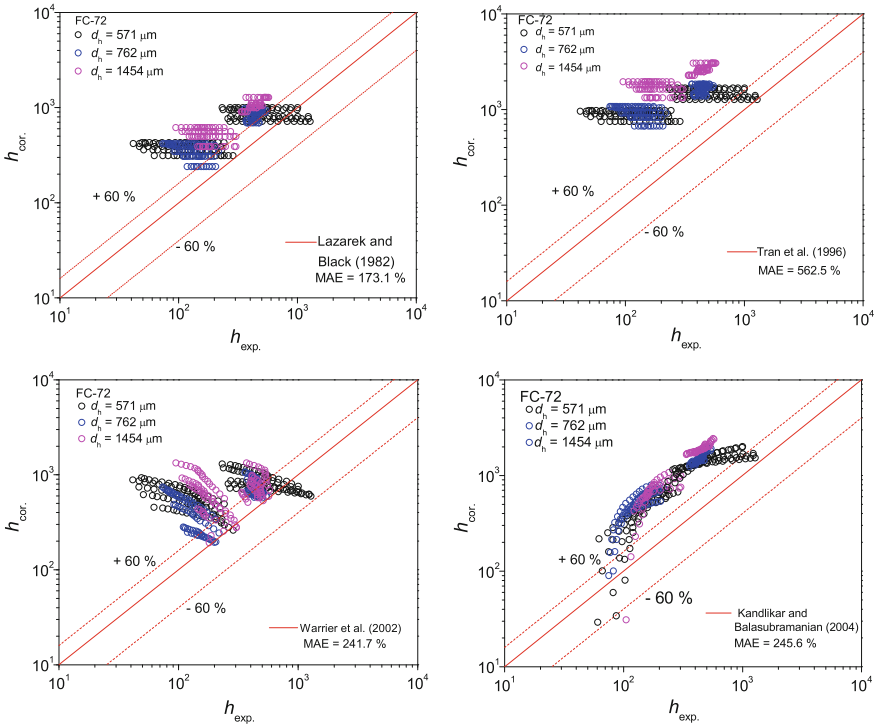

Fig. 18 Heat transfer experimental results of FC-72 flow boiling in three high aspect ratio rectangular micro-channels and the comparisons with four selected correlations. **a** Lazarek and Black [61], **b** Tran et al. [62], **c** Warrier et al. [63], **d** Kandlikar and Balasubramanian [51]

3 Conclusions

Two-phase flow and heat transfer in micro-channels and their applications in micro-system cooling are becoming increasingly important due to the extremely high requirement of heat dissipation capacity in ever more miniaturized and intensified processes. Though phase change and heat transfer have already been utilized in systems such as nuclear reactor cooling systems, heat exchangers, power stations and micro/nano electronics mechanical systems (MEMS/NEMS), heat management is still confronting demanding challenges in high thermal density devices owing to insufficient knowledge of heat transfer mechanisms at different conditions. Investigations on flow boiling heat transfer in literature have revealed numbers of criteria of system classification, flow instabilities and varying trends of heat transfer characteristics and provided correlations with respect to diverse conditions. However, the existing database is still limited especially for flow boiling in passages with unique geometries such as high-aspect-ratio cross section. Extensive explorations on two-phase flow boiling and heat transfer in micro-

channels are essential for heat transfer prediction, cooling system design, and ultimately, further applications in micro-systems.

Acknowledgments The experimental research in Edinburgh was supported by the UK Engineering and Physical Sciences Research Council (EPSRC). The authors would also like to acknowledge the support from the China Scholarship Council (CSC) and National University of Defense Technology in China.

References

1. Kandlikar, S.G.: A general correlation for saturated two-phase flow boiling heat transfer inside horizontal and vertical tubes. J. Heat Transf. **112**(1), 219–228 (1990)
2. Bertsch, S.S., Groll, E.A., Garimella, S.V.: A composite heat transfer correlation for saturated flow boiling in small channels. Int. J. Heat Mass Transf. **52**(7–8), 2110–2118 (2009)
3. http://www.cecla-ahtt.fr/nida.html
4. Cartigny, F., Desmet, B., Dufrenoy, P.: Numerical and experimental study of a liquid-cooled railway disk brake phototype. Progress in Computational Heat and Mass Transfer, Editeur R. Bennacer, Edition Lavoisier (2005)
5. Petit, J.P.: Dissipation thermique dans les systèmes électroniques, Techniques de l'ingénieur, Ref E3952
6. Gillot, C.: Etude et réalisation d'une fonction interrupteur en technologie hybride à haute intégration. Thèse de doctorat de l'INP Grenoble, (2000)
7. Buffone, C., Sefiane K., Christy, J.R.E.: Experimental investigation of self-induced thermocapillary convection for an evaporating meniscus in capillary tubes using micro-particle image velocimetry. Phys. Fluids **17**, 052104 (2005); doi:10.1063/1.1901688
8. Sefiane, K., Benielli, D., Steinchen, A.: A new mechanism for pool boiling crisis, recoil instability and contact angle influence. Colloids Surf. Physicochem. Eng. A. **142**(2–3), 361–373 (1998)
9. Hutter, C., Kenning, D.B.R., Sefiane, K., Karayiannis, T.G., Lin, H., Cummins, G., Walton, A.J.: Experimental pool boiling investigations of FC-72 on silicon with artificial cavities and integrated temperature microsensors. Exp. Therm. Fluid Sci. **34**(4), 422–433 (2010)
10. Sanna, A., Karayiannis, T.G., Kenning, D.B.R., Hutter, C., Sefiane, K., Walton, A.J., Golobic, I., Pavlovic, E., Nelson, R.A.: Steps towards the development of an experimentally verified simulation of pool nucleate boiling on a silicon wafer with artificial sites. Appl. Therm. Eng. **29**(7), 1327–1337 (2009)
11. Lin, S., Sefiane, K., Christy, J.R.E.: Prospects of confined flow boiling in thermal management of microsystems. Appl. Therm. Eng. **22**(7), 825–837 (2002)
12. Saisorn, S., Kaew-On, J., Wongwises, S.: Flow pattern and heat transfer characteristics of R-134a refrigerant during flow boiling in a horizontal circular mini-channel. Int. J. Heat Mass Transf. **53**(19–20), 4023–4038 (2010)
13. Cubaud, T., Ho, C.-M.: Transport of bubbles in square microchannels. Phys. Fluids **16**(12), 4575–4585 (2004)
14. Xu, J.L., Cheng, P., Zhao, T.S.: Gas-liquid two-phase flow regimes in rectangular channels with mini/micro gaps. Int. J. Multiphase Flow **25**(3), 411–432 (1999)
15. Harirchian T., Garimella, S.V.: An investigation of flow boiling regimes in microchannels of different sizes by means of high-speed visualization. Thermal and thermomechanical phenomena in electronic systems. ITHERM 2008. 11th Intersociety Conference on. 197–206 (2008)
16. Arcanjo, A.A., Tibiriçá, C.B., Ribatski, G.: Evaluation of flow patterns and elongated bubble characteristics during the flow boiling of halocarbon refrigerants in a micro-scale channel. Exp. Therm. Fluid Sci. **34**(6), 766–775 (2010)

17. In, S., Jeong, S.: Flow boiling heat transfer characteristics of R123 and R134a in a microchannel. Int. J. Multiphase Flow **35**(11), 987–1000 (2009)
18. Kawahara, A., Sadatomi, M., Nei, K., Matsuo, H.: Experimental study on bubble velocity, void fraction and pressure drop for gas-liquid two-phase flow in a circular microchannel. Int. J. Heat Fluid Flow **30**(5), 831–841 (2009)
19. Celata, G.P., Saha, S.K., Zummo, G., Dossevi, D.: Heat transfer characteristics of flow boiling in a single horizontal microchannel. Int. J. Therm. Sci. **49**(7), 1086–1094 (2010)
20. Megahed, A., Hassan, I.: Two-phase pressure drop and flow visualization of FC-72 in a silicon microchannel heat sink. Int. J. Heat Fluid Flow **30**(6), 1171–1182 (2009)
21. Huh, C., Kim, M.H.: Pressure drop, boiling heat transfer and flow patterns during flow boiling in a single microchannel. Heat Transf. Eng. **28**(8), 730–737 (2007)
22. Lee, P.C., Tseng, F.G., Pan, C.: Bubble dynamics in microchannels part I: single microchannel. Int. J. Heat Mass Trans. **47**(25), 5575–5589 (2004)
23. Chen, G., Cheng, P.: Nucleate and film boiling on a microheater under pulse heating in a microchannel. Int. Commun. Heat Mass Transf. **36**(5), 391–396 (2009)
24. Wu, J., Shi, M., Chen, Y., Li, X.: Visualization study of steam condensation in wide rectangular silicon microchannels. Int. J. Therm. Sci. **49**(6), 922–930 (2010)
25. Barber, J., Brutin, D., Sefiane, K., Tadrist, L.: Bubble confinement in flow boiling of FC-72 in a "rectangular" microchannel of high aspect ratio. Exp. Therm. Fluid Sci. **34**(8), 1375–1388 (2010)
26. Kandlikar, S.G., Shoji, M., Dhir, V.K.: Two-Phase Flow Instabilities. Handbook of Phase Changes: Boiling and Condenation, p. 263. Taylor and Francis, London (1999)
27. Kew, P.A., Cornwell, K.: Confined bubble flow and boiling in narrow spaces. IHTC 10, Brighton, England 473–478 (1994)
28. Kennedy, J.E., Roach, J.G.M., Dowling, M.F., Abdel-Khalik, S.I., Ghiaasiaan, S.M., Jeter, S.M., Quershi, Z.H.: The onset of flow instability in uniformly heated horizontal microchannels. J. Heat Transf. **122**(1), 118–125 (2000)
29. Zhang, L., Wang, E.N., Goodson, K.E., Kenny, T.W.: Phase change phenomena in silicon microchannels. Int. J. Heat Mass Transf. **48**(8), 1572–1582 (2005)
30. Hetsroni, G., Mosyak, A., Segal, Z., Ziskind, G.: A uniform temperature heat sink for cooling of electronic devices. Int. J. Heat Mass Transf. **45**(16), 3275–3286 (2002)
31. Brutin, D., Topin, F., Tadrist, L.: Experimental study of unsteady convective boiling in heated minichannels. Int. J. Heat Mass Transf. **46**(16), 2957–2965 (2003)
32. Chang, K.H., Pan, C.: Two-phase flow instability for boiling in a microchannel heat sink. Int. J. Heat Mass Transf. **50**(11–12), 2078–2088 (2007)
33. Wang, G., Cheng, P., Wu, H.: Unstable and stable flow boiling in parallel microchannels and in a single microchannel. Int. J. Heat Mass Transf. **50**(21–22), 4297–4310 (2007)
34. Wang, G., Cheng, P.: An experimental study of flow boiling instability in a single microchannel. Int. Commun. Heat Mass Transf. **35**(10), 1229–1234 (2008)
35. Balasubramanian, P., Kandlikar, S.G.: Experimental study of flow patterns, pressure drop, and flow instabilities in parallel rectangular minichannels. Heat Transf. Eng. **26**(3), 20–27 (2005)
36. Muwanga, R., Hassan, I., MacDonald, R.: Characteristics of Flow Boiling Oscillations in Silicon Microchannel Heat Sinks. J. Heat Transf. **129**(10), 1341–1351 (2007)
37. Brutin, D., Tadrist, L.: Pressure drop and heat transfer analysis of flow boiling in a minichannel: influence of the inlet condition on two-phase flow stability. Int. J. Heat Mass Transf. **47**(10–11), 2365–2377 (2004)
38. Ding, Y., Kakaç, S., Chen, X.J.: Dynamic instabilities of boiling two-phase flow in a single horizontal channel. Exp. Therm. Fluid Sci. **11**(4), 327–342 (1995)
39. Singh, S.G., Bhide, R.R., Duttagupta, S.P., Puranik, B.P., Agrawal, A.: Two-phase flow pressure drop characteristics in trapezoidal silicon microchannelstechnologies. IEEE Trans. Compon. Packag. **32**(4), 887–900 (2009)

40. Bhide, R.R., Singh, S.G., Sridharan, A., Duttagupta, S.P., Agrawal, A.: Pressure drop and heat transfer characteristics of boiling water in sub-hundred micron channel. Exp. Therm. Fluid Sci. **33**(6), 963–975 (2009)
41. Hetsroni, G., Mosyak, A., Pogrebnyak, E., Segal, Z.: Explosive boiling of water in parallel micro-channels. Int. J. Multiph. Flow **1**(4), 371–392 (2005)
42. Lee, H.J., Yao, S.-c.: System instability of evaporative micro-channels. Int. J. Heat Mass Transf. **53**(9–10), 1731–1739 (2010)
43. Barber, J., Sefiane, K., Brutin, D., Tadrist, L.: Hydrodynamics and heat transfer during flow boiling instabilities in a single microchannel. Appl. Therm. Eng. **29**(7), 1299–1308 (2009)
44. Mokrani, O., Bourouga, B., Castelain, C., Peerhossaini, H.: Fluid flow and convective heat transfer in flat microchannels. Int. J. Heat Mass Transf. **52**(5–6), 1337–1352 (2009)
45. Agostini, B., Thome, J.R., Fabbri, M., Michel, B., Calmi, D., Kloter, U.: High heat flux flow boiling in silicon multi-microchannels-part I: Heat transfer characteristics of refrigerant R236fa. Int. J. Heat Mass Transf. **51**(21–22), 5400–5414 (2008a)
46. Lee, J., Mudawar, I.: Two-phase flow in high-heat-flux micro-channel heat sink for refrigeration cooling applications: Part II–heat transfer characteristics. Int. J. Heat Mass Transf. **48**(5), 941–955 (2005)
47. Liu, D., Garimella, S.V.: Flow boiling heat transfer in microchannels. J. Heat Transf. **129**, 1321–1332 (2007)
48. Gungor, K.E., Winterton, R.H.S.: A general correlation for flow boiling in tubes and annuli. Int. J. Heat Mass Transf. **29**(3), 351–358 (1986)
49. Liu, Z., Winterton, R.H.S.: A general correlation for saturated and subcooled flow boiling in tubes and annuli, based on a nucleate pool boiling equation. Int. J. Heat Mass Transf. **34**(11), 2759–2766 (1991)
50. Lee, H.J., Lee, S.Y.: Heat transfer correlation for boiling flows in small rectangular horizontal channels with low aspect ratios. Int. J. Multiphase Flow **27**(12), 2043–2062 (2001)
51. Kandlikar, S.G., Balasubramanian, P.: An extension of the flow boiling correlation to transition, laminar, and deep laminar flows in minichannels and microchannels. Heat Transf. Eng. **25**(3), 86–93 (2004)
52. Zhang, W., Hibiki, T., Mishima, K.: Correlation for flow boiling heat transfer in mini-channels. Int. J. Heat Mass Transf. **47**(26), 5749–5763 (2004)
53. http://www.pcinpact.com/affichage/36835-MSI-Circupipe-Asus/42258.htm
54. Lallemand, M.: Les microcaloducs. Les diffuseurs thermiques diphasiques. Congrès français de thermique, SFT (2003)
55. Roudnitzki, S.: Etude et validation d'une solution thermique pour réduire la surconsommation à froid d'un moteur thermique automobile : Carter avec isolation interne équipé de caloducs à conductance variable. Thesis of Doctor of Philosophy, University of Valenciennes (2009)
56. Khandekar, S.: Thermo-hydrodynamics of closed loop pulsating heat pipes. Thesis of Doctor of Philosophy, University of Stuttgart (2004)
57. Coquard, T.: Transferts couplés de masse et de chaleur dans un élément d'évaporateur capillaire. Thèse de doctorat de l'INP de Toulouse (2006)
58. Serin, V.: Etude expérimentale et modélisation d'une micro-boucle diphasique à pompage capillaire. Rapport DEA, Laboratoire d'Energétique, Toulouse
59. Collier, J.G.: Convective Boiling and Condensation. McGRAW-HILL, Oxford, UK (1972)
60. Serizawa, A., Feng, Z., Kawara, Z.: Two-phase flow in microchannels. Exp. Therm. Fluid Sci. **26**, 703–714 (2002)
61. Lazarek, G.M., Black, S.H.: Evaporative heat transfer, pressure drop and critical heat flux in a small vertical tube with R-113. Int. J. Heat Mass Transf. **25**(7), 945–960 (1982)
62. Tran, T.N., Wambsganss, M.W., France, D.M.: Small circular- and rectangular-channel boiling with two refrigerants. Int. J. Multiphase Flow **22**(3), 485–498 (1996)
63. Warrier, G.R., Dhir, V.K., Momoda, L.A.: Heat transfer and pressure drop in narrow rectangular channels. Exp. Therm. Fluid Sci. **26**(1), 53–64 (2002)

64. Peng, X.F., Wang, B.X.: Forced convection and flow boiling heat transfer for liquid flowing through microchannels. Int. J. Heat Mass Transf. **36**(14), 3421–3427 (1993)
65. Bao, Z.Y., Fletcher, D.F., Haynes, B.S.: Flow boiling heat transfer of Freon R11 and HCFC123 in narrow passages. Int. J. Heat Mass Transf. **43**(18), 3347–3358 (2000)
66. Lin, S., Kew, P.A., Cornwell, K.: Flow boiling of refrigerant R141B in small tubes. Chem. Eng. Res. Des. **79**(4), 417–424 (2001)
67. Yu, W., France, D.M., Wambsganss, M.W., Hull, J.R.: Two-phase pressure drop, boiling heat transfer, and critical heat flux to water in a small-diameter horizontal tube. Int. J. Multiphase Flow **28**(6), 927–941 (2002)
68. Qu, W., Mudawar, I.: Flow boiling heat transfer in two-phase micro-channel heat sinks–I. Experimental investigation and assessment of correlation methods. Int. J. Heat Mass Transf. **46**(15), 2755–2771 (2003)
69. Yen, T.-H., Kasagi, N., Suzuki, Y.: Forced convective boiling heat transfer in microtubes at low mass and heat fluxes. Int. J. Multiphase Flow **29**(12), 1771–1792 (2003)
70. Huo, X., Chen, L., Tian, Y.S., Karayiannis, T.G.: Flow boiling and flow regimes in small diameter tubes. Appl. Therm. Eng. **24**(8–9), 1225–1239 (2004)
71. Steinke, M.E., Kandlikar, S.G.: An experimental investigation of flow boiling characteristics of water in parallel microchannels. J. Heat Transf. **126**(4), 518–526 (2004)
72. Greco, A., Vanoli, G.P.: Flow boiling heat transfer with HFC mixtures in a smooth horizontal tube. Part I: Experimental investigations. Exp. Therm. Fluid Sci. **29**(2), 189–198 (2005)
73. Saitoh, S., Daiguji, H., Hihara, E.: Effect of tube diameter on boiling heat transfer of R-134a in horizontal small-diameter tubes. Int. J. Heat Mass Transf. **48**(23–24), 4973–4984 (2005)
74. Yun, R., Kim, Y., Soo Kim, M.: Flow boiling heat transfer of carbon dioxide in horizontal mini tubes. Int. J. Heat Fluid Flow **26**(5), 801–809 (2005)
75. Chen, T., Garimella, S.V.: Flow boiling heat transfer to a dielectric coolant in a microchannel heat sink. IEEE Trans. Compon. Packag. Technol. **30**(1), 24–31 (2007)
76. Choi, K.-I., Pamitran, A.S., Oh, J.-T.: Two-phase flow heat transfer of CO2 vaporization in smooth horizontal minichannels. Int. J. Refrig. **30**(5), 767–777 (2007)
77. Díaz, M.C., Schmidt, J.: Experimental investigation of transient boiling heat transfer in microchannels. Int. J. Heat Fluid Flow **28**(1), 95–102 (2007)
78. Agostini, B., Thome, J.R., Fabbri, M., Michel, B., Calmi, D., Kloter, U.: High heat flux flow boiling in silicon multi-microchannels-part II: Heat transfer characteristics of refrigerant R245fa. Int. J. Heat Mass Transf. **51**(21–22), 5415–5425 (2008)
79. Bertsch, S.S., Groll, E.A., Garimella, S.V.: Refrigerant flow boiling heat transfer in parallel microchannels as a function of local vapor quality. Int. J. Heat Mass Transf. **51**(19–20), 4775–4787 (2008)
80. Lee, P.-S., Garimella, S.V.: Saturated flow boiling heat transfer and pressure drop in silicon microchannel arrays. Int. J. Heat Mass Transf. **51**(3–4), 789–806 (2008)
81. Bertsch, S.S., Groll, E.A., Garimella, S.V.: Effects of heat flux, mass flux, vapor quality, and saturation temperature on flow boiling heat transfer in microchannels. Int. J. Multiphase Flow **35**(2), 142–154 (2009)
82. da Silva Lima, R.J., Quibén, J.M., Thome, J.R.: Flow boiling in horizontal smooth tubes: New heat transfer results for R-134a at three saturation temperatures. Appl. Therm. Eng. **29**(7), 1289–1298 (2009)
83. Kuznetsov, V., Shamirzaev, A.: Flow boiling heat transfer in two-phase micro channel heat sink at low water mass flux. Microgravity Sci. Technol. **21**, 305–311 (2009)
84. Ong, C.L., Thome, J.R.: Flow boiling heat transfer of R134a, R236fa and R245fa in a horizontal 1.030 mm circular channel. Exp. Therm. Fluid Sci. **33**(4), 651–663 (2009)
85. Hamdar, M., Zoughaib, A., Clodic, D.: Flow boiling heat transfer and pressure drop of pure HFC-152a in a horizontal mini-channel. Int. J. Refrig. **33**(3), 566–577 (2010)
86. Chen, J.C.: Correlation for boiling heat transfer to saturated fluids in convective flow. Ind. Eng. Chem Process Des. Dev. **5**(3), 322–329 (1966)

Numerical Methods for Flow in Fractured Porous Media

Sabine Stichel, Dmitriy Logashenko, Alfio Grillo, Sebastian Reiter, Michael Lampe and Gabriel Wittum

Abstract We present a numerical technique for the simulation of salinity- as well as thermohaline-driven flows in fractured porous media. In this technique, the fractures are represented by low-dimensional manifolds, on which a low-dimensional variant of the PDEs of variable-density flow is formulated. The latter is obtained from the full-dimensional model by the average-along-the-vertical. The discretization of the resulting coupled system of the full- and low-dimensional PDEs is based on a finite-volume method. This requires a special construction of the discretization grid which can be obtained by the algorithm presented in this work. This technique allows to reconstruct in particular the jumps of the solution at the fracture. Its precision is demonstrated in the numerical comparisons with the results obtained in the simulations where the fractures are represented by the full-dimensional subdomains.

S. Stichel · D. Logashenko · A. Grillo (✉) · S. Reiter · M. Lampe · G. Wittum
G-CSC University of Frankfurt, Kettenhofweg 139, 60325, Frankfurt am Main, Germany
e-mail: alfio.grillo@gcsc.uni-frankfurt.de

S. Stichel
e-mail: stichel@gcsc.uni-frankfurt.de

D. Logashenko
e-mail: dimitriy.logashenko@gcsc.uni-frankfurt.de

S. Reiter
e-mail: sreiter@gcsc.uni-frankfurt.de

M. Lampe
e-mail: lampe@gcsc.uni-frankfurt.de

G. Wittum
e-mail: wittum@gcsc.uni-frankfurt.de

J. M. P. Q. Delgado (ed.), *Heat and Mass Transfer in Porous Media*,
Advanced Structured Materials 13, DOI: 10.1007/978-3-642-21966-5_4,

1 Introduction

Variable-density groundwater flow in highly heterogeneous porous media is subject of many hydrogeological studies because of its repercussions on environmental and industrial problems. Fractures constitute one of the origins of heterogeneity. They are thin subregions of a hydrogeological domain characterized by flow properties that are usually very different from those of the medium in which they are enclosed. The fractures studied in our contribution are fissures filled with a porous medium (e.g. sand, clay, or silt) much more permeable than the enclosing porous medium. The heterogeneity is thus given by the strong permeability contrast between the porous media inside and outside the fracture.

The formation of fracture networks in a hydrogeological domain is responsible for increasing the capability of the domain of conveying fluid. For this reason, the study of flow in fractured porous media is often part of forecasting problems. This is the case, for example, of flow in fractured domains situated in the neighbourhood of repositories of radioactive waste, or flow in fractured aquifers [5].

In many hydrogeological situations, flow is induced, or altered, by the variation of the groundwater mass density in response to salinity or thermal gradients. When the forces acting on the fluid do not equilibrate, a flow is originated which is said to be salinity- or thermohaline-driven flow, depending on whether the variation of the fluid density is due to solely salinity gradients or to the combined effect of salinity and thermal gradients. The presence of fractures renders these studies even more challenging because heterogeneity demands more sophisticated theoretical models and numerical methods. An incomplete list of authors who studied flow in fractured media is [18, 19, 23, 24, 33, 35, 37, 39, 42].

Numerical simulations of flows in fractured porous media follow two main approaches. In the first one, the same numerical methods are used for the enclosing medium and the fractures, i.e. the fractures are considered as full-dimensional subdomains. This approach guarantees a good resolution of all physical phenomena taking place in the fractures but encounters essential problems in the numerical solvers due to the thickness of the subdomains representing the fractures. In particular, for media with a large number of intersecting fractures, the generation of a proper computational grid becomes a complicated task. Furthermore, the convergence of linear solvers deteriorates due to the jumping coefficients of the problem and the anisotropy of the grid. All this makes the first approach numerically very expensive and restricts its applicability to the case of a small number of thick fractures.

In the second approach, the full-dimensional fractures are represented by low-dimensional manifolds. The full-dimensional model for the flow and the transport in the fractures is transformed into a system of low-dimensional PDEs by *average-along-the-vertical* (cf. [4, 6–8]). Then the new model consisting of the system of the full-dimensional PDEs for the enclosing medium and the low-dimensional PDEs for the fractures is solved numerically. Such techniques have been proposed by many authors for various problems (cf. [1, 3, 22, 34, 41]). In this contribution,

we consider an approach of this type in detail. Numerically it is much cheaper than the first one but provides a good precision for not only the values of the unknown functions but also for the jumps of the unknown function at the fractures.

After recalling in Sects. 2 and 3 the mathematical model and the averaging technique elaborated in [22], we present the discretization scheme in Sect. 4. Then, in Sect. 5, we perform numerical simulations for modified versions of the Henry and Elder problems [12, 25], where the domain features a fracture. In order to validate the model, we compare these results with results obtained by the simulations with the d-dimensional fracture representation.

2 Variable-Density Flow in Fractured Porous Media

In our formulation the entire porous medium domain is denoted by $\Omega \subset \mathbb{R}^d$ (with $d = 2$ or $d = 3$), a fracture or a fracture network in Ω is indicated by $\mathfrak{F}$, and the region enclosing $\mathfrak{F}$ is referred to as $\mathfrak{M}$(so that $\Omega = \mathfrak{F} \cup \mathfrak{M} \cup \partial\mathfrak{F}$). It is postulated that the thickness of $\mathfrak{F}$ be much smaller than the smallest macroscopic length-scale associated with $\mathfrak{M}$.

The porous media in $\mathfrak{F}$ and $\mathfrak{M}$ are denoted by $\mathcal{P}_f$ and $\mathcal{P}_m$, respectively. It is assumed that $\mathcal{P}_f$ is much more permeable than $\mathcal{P}_m$. The fluid-phase consists of water and brine, and is prescribed to experience single-phase flow throughout Ω. The saturation condition holds.

The starting hypothesis of our approach is that both $\mathfrak{F}$ and $\mathfrak{M}$ can be modeled at the same scale of observation. This means that the fractures, although being very thin, are considered as a d-dimensional subdomain of Ω. The equations describing thermohaline-driven flow are thus taken in the same form both in $\mathfrak{F}$ and in $\mathfrak{M}$. Furthermore, it is assumed that the flow in the fractures obeys Darcy's law, and that brine and heat transport follow Fick's and Fourier's law, respectively.

Under the hypotheses usually adopted in groundwater problems, the equations of thermohaline-driven flow are the laws of mass balance of brine and the fluid-phase as a whole. In the absence of mass sources, these equations read (cf. for example [11, 20, 21, 26, 36]),

$$\partial_t(\phi_\alpha \rho_\alpha) + \nabla \cdot (\rho_\alpha \mathbf{q}_\alpha) = 0, \tag{1}$$

$$\partial_t(\phi_\alpha \rho_\alpha \omega_\alpha) + \nabla \cdot (\rho_\alpha \omega_\alpha \mathbf{q}_\alpha + \mathbf{J}_\alpha) = 0, \tag{2}$$

$$\partial_t(\phi_\alpha \rho_\alpha C_{\alpha\ell} + (1 - \phi_\alpha)\rho_{\alpha s} C_{\alpha s})\Theta_\alpha + \nabla \cdot (\rho_\alpha C_{\alpha\ell} \Theta_\alpha \mathbf{q}_\alpha + \boldsymbol{\psi}_\alpha) = 0, \tag{3}$$

where ϕ_α is porosity, ρ_α is the fluid-phase mass density, ω_α is the mass fraction of brine, $\mathbf{q}_\alpha$ is the specific discharge ($\mathbf{q}_\alpha := \phi_\alpha \mathbf{v}_\alpha$, with $\mathbf{v}_\alpha$ being the velocity of the fluid-phase), Θ_α is temperature, $\mathbf{J}_\alpha$ is the diffusive mass flux of the brine, $C_{\alpha\ell}$ and $C_{\alpha s}$ are the heat capacities per unit mass of the fluid- and the solid-phase, and $\boldsymbol{\psi}_\alpha$ is the conductive heat flux vector. The index $\alpha \in \{f, m\}$ specifies whether a physical quantity is defined in $\mathfrak{F}$ or in $\mathfrak{M}$.

The use of Darcy's, Fick's, and Fourier's law leads to the following expressions of $\mathbf{q}_\alpha$, $\mathbf{J}_\alpha$ and $\boldsymbol{\psi}_\alpha$:

$$\mathbf{q}_\alpha = -\frac{1}{\mu_\alpha}\mathbf{K}_\alpha(\nabla p_\alpha - \rho_\alpha \mathbf{g}), \tag{4}$$

$$\mathbf{J}_\alpha = -\rho_\alpha \mathbf{D}_\alpha \nabla \omega_\alpha, \tag{5}$$

$$\boldsymbol{\psi}_\alpha = -\boldsymbol{\Lambda}_\alpha \nabla \Theta_\alpha, \tag{6}$$

where p_α is pressure, $\mathbf{g}$ is the gravity acceleration vector, μ_α is viscosity, $\mathbf{K}_\alpha$ and $\mathbf{D}_\alpha$ denote permeability and diffusion–dispersion tensor, respectively, and $\boldsymbol{\Lambda}_\alpha$ is thermal conductivity.

In this contribution, we take the same value of viscosity everywhere in Ω, neglect dispersion, and consider only the case in which the porous media $\mathcal{P}_f$ and $\mathcal{P}_m$ are isotropic. According to the latter assumption $\mathbf{K}_\alpha$, $\mathbf{D}_\alpha$, and $\boldsymbol{\Lambda}_\alpha$ become [7]

$$\mathbf{K}_\alpha = K_\alpha \mathbf{I}, \quad \mathbf{D}_\alpha = D_\alpha \mathbf{I} = DT_\alpha \mathbf{I}, \quad \Lambda_\alpha = \phi_\alpha \Lambda_{\alpha\ell} + (1-\phi_\alpha)\Lambda_{\alpha s} \tag{7}$$

where $\mathbf{I}$ is the identity tensor, D is the diffusivity coefficient of the brine, T_α is the scalar tortuosity, and $\Lambda_{\alpha\ell}$ and $\Lambda_{\alpha s}$ are the thermal conductivities of the fluid- and solid-phase in the αth subregion.

To simplify the notation, we consider only the case of one planar fracture. Nevertheless, the theory presented below can be generalized for an arbitrary network of intersecting piecewise planar fractures. Furthermore, we accept the hypothesis that $\mathbf{K}_\alpha$, $\mathbf{D}_\alpha$, and $\boldsymbol{\Lambda}_\alpha$ are piecewise continuous functions, the discontinuity being situated at the interface between the fracture and the enclosing medium.

In the field Eqs. (1)–(3), the fluid-phase mass density is prescribed to be a constitutive function of brine mass fraction and temperature. Following [36], we write

$$\rho_\alpha = \rho(\omega_\alpha, \Theta_\alpha) := \frac{\rho^{pW}(\Theta_\alpha)\rho^{pB}(\Theta_\alpha)}{\rho^{pB}(\Theta_\alpha) - [\rho^{pB}(\Theta_\alpha) - \rho^{pW}(\Theta_\alpha)]\omega_\alpha}, \tag{8}$$

where $\rho^{pB}(\Theta_\alpha) = \rho_r^{pB} e^{-\beta^B(\Theta_\alpha - \Theta_r)}$ and $\rho^{pW}(\Theta_\alpha) = \rho_r^{pW} e^{-\beta^W(\Theta_\alpha - \Theta_r)}$, β^B and β^W are the (constant) coefficients of thermal expansion of brine and water, and ρ_r^{pB} and ρ_r^{pW} are the constant densities computed at the reference temperature Θ_r.

The field Eqs. (1)–(3) have to be supplied with conditions at the fracture–medium interface, $\partial\mathfrak{F}$. The fracture is a very thin d-dimensional domain of shell-type geometry delimited by two parallel surfaces $\mathscr{S}^{(1)}$ and $\mathscr{S}^{(2)}$ and a band-shaped lateral boundary $\mathscr{B}$, as shown in Fig. 1. By letting $\mathbf{n}^{(1)}$, $\mathbf{n}^{(2)}$ and $\boldsymbol{\tau}$ denote the unit vectors normal to $\mathscr{S}^{(1)}$, $\mathscr{S}^{(2)}$ and $\mathscr{B}$, the conditions at the fracture–medium interface read

$$\text{on } \mathscr{S}^{(k)}, \mathbf{q}_f^{(k)} \cdot \mathbf{n}^{(k)} = \mathbf{q}_m^{(k)} \cdot \mathbf{n}^{(k)}, \quad \mathbf{J}_f^{(k)} \cdot \mathbf{n}^{(k)} = \mathbf{J}_m^{(k)} \cdot \mathbf{n}^{(k)}, \quad k = 1, 2, \tag{9}$$

$$\text{on } \mathscr{B}, \quad \mathbf{q}_f \cdot \boldsymbol{\tau} = \mathbf{q}_m \cdot \boldsymbol{\tau}, \quad \mathbf{J}_f \cdot \boldsymbol{\tau} = \mathbf{J}_m \cdot \boldsymbol{\tau}, \tag{10}$$

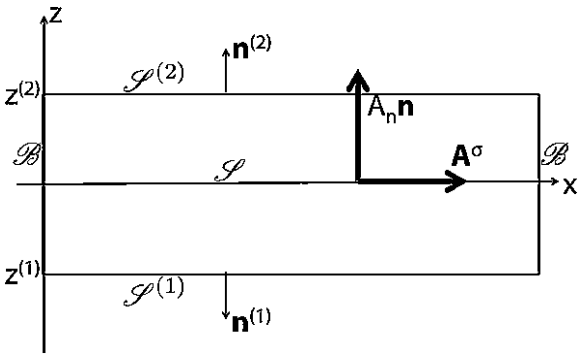

Fig. 1 Scheme of a planar d-dimensional fracture in the averaging process

$$on\ \partial\mathfrak{F},\quad \omega_f = \omega_m,\quad p_f = p_m. \tag{11}$$

Analogously, temperature and thermal flux have to satisfy the continuity conditions

$$on\ \mathscr{S}^{(k)}, \boldsymbol{\psi}_f^{(k)} \cdot \mathbf{n}^{(k)} = \boldsymbol{\psi}_m^{(k)} \cdot \mathbf{n}^{(k)},\quad k = 1, 2, \tag{12}$$

$$on\ \mathscr{B},\quad \boldsymbol{\psi}_f \cdot \boldsymbol{\tau} = \boldsymbol{\psi}_m \cdot \boldsymbol{\tau}, \tag{13}$$

$$on\ \partial\mathfrak{F},\quad \Theta_f = \Theta_m. \tag{14}$$

Explicitly, conditions (9) have the following form

$$-\frac{K_f}{\mu}\left[\partial_{n^{(k)}} p_f|_{\mathscr{S}^{(k)}} - \rho\left(\omega_f^{(k)}\right)\mathbf{g}\cdot\mathbf{n}^{(k)}\right] = -\frac{K_m}{\mu}\left[\partial_{n^{(k)}} p_m|_{\mathscr{S}^{(k)}} - \rho\left(\omega_m^{(k)}\right)\mathbf{g}\cdot\mathbf{n}^{(k)}\right], \tag{15}$$

$$-\rho(\omega_f, \Theta_f) D_f \partial_{n^{(k)}} \omega_f|_{\mathscr{S}^{(k)}} = -\rho(\omega_m, \Theta_m) D_m \partial_{n^{(k)}} \omega_m|_{\mathscr{S}^{(k)}}. \tag{16}$$

The conditions to impose on the outer boundary of Ω characterize the problem to solve, and are thus specified in Sect. 5, where Henry and Elder problems are presented.

A comparison between (2) and (3) shows that the transport of brine and heat occur at different velocities. Indeed, whereas brine is transported at the pore velocity $|\mathbf{v}_\alpha| = |\mathbf{q}_\alpha|/\phi_\alpha$, heat is transported at the lower velocity $|\mathbf{q}_\alpha|/R_\alpha$, where $R_\alpha > 1$, the retardation factor [36], is estimated through the formula

$$R_\alpha = \frac{\phi_\alpha \rho_\alpha C_{\alpha\ell} + (1-\phi_\alpha)\rho_{\alpha s} C_{\alpha s}}{\phi_\alpha \rho_\alpha C_{\alpha\ell}}. \tag{17}$$

In the presence of fractures, two retardation factors have to be introduced, i.e. R_f and R_m, since the properties of the porous media $\mathscr{P}_f$ and $\mathscr{P}_m$ differ from each other.

In order to show the influence of the fractures on flow and transport, we consider a modified version of the Elder problem [12, 13] where the domain, a rectangle

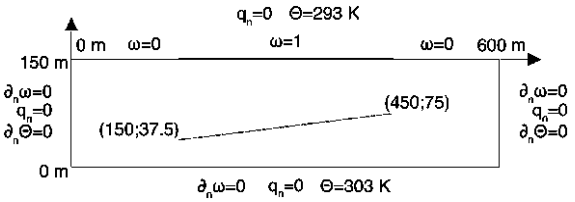

Fig. 2 Geometry and boundary conditions for the modified Elder problem featuring a fracture

Table 1 Simulation parameters for the modified Henry and Elder problems for salinity-driven flow

Symbol	Quantity	Value for Henry	Value for Elder	Unit
D_m	Diffusion coefficient in the medium	6.6×10^{-6}	3.565×10^{-6}	$m^2\ s^{-1}$
D_f	Diffusion coefficient in the fracture	13.2×10^{-6}	10.695×10^{-6}	$m^2\ s^{-1}$
g	Gravity	9.81	9.81	$m\ s^{-2}$
K_m	Permeability of the medium	1.019368×10^{-9}	4.845×10^{-13}	m^2
K_f	Permeability of the fracture	1.019368×10^{-6}	4.845×10^{-10}	m^2
ϕ_m	Porosity of the medium	0.35	0.1	–
ϕ_f	Porosity of the fracture	0.7	0.3	–
μ	Viscosity	10^{-3}	10^{-3}	$kg\ m^{-1}\ s^{-1}$
ρ^{pW}	Density of water	1×10^3	1×10^3	$kg\ m^{-3}$
ρ^{pB}	Density of brine	1.025×10^{-3}	1.2×10^3	$kg\ m^{-3}$
a_α^t, a_α^ℓ	Dispersivity lengths	0	0	m

$600 \times 150\ m^2$, features a fracture (cf. Fig. 2). Boundary conditions can be found in Fig. 2 and the parameters used for computations are listed in Tables 1 and 2.

The main results of Elder's problem in the absence of fractures were summarized, for example, in [11]. The presence of the fracture manifests itself by affecting the velocity distribution in the entire domain. This occurs because the fracture, being characterized by a very big permeability, constitutes the preferential flow region of the considered domain.

The velocity distribution corresponding to the chosen fracture orientation leads to deflections of the concentration isolines of brine mass fraction (Fig. 3a) and temperature (Fig. 3b). Since the evolution of brine is mainly driven by convection, the distribution of brine in the domain follows the velocity pattern. This behavior can be appreciated by looking at the brine fingers shown in Fig. 3c. As soon as a finger approaches the fracture, the brine tends either to spread along the fracture or to flow across it. Figure 3a and c refer to the case in which the brine flows downward along the fracture. It is also possible, however, that the brine flows upward along the fracture. This happens, for example, when a finger approaches the left end of the fracture, and the up-swelling fluid motion tends to move the brine upward. In this circumstance, the brine flows into the fracture because this is the region of higher permeability. The combination of motions along the fracture

Table 2 Parameters for the modified Elder problem for thermohaline flow (additional to Table 1)

Symbol	Quantity	Value	Unit
Λ_m	Thermal conductivity in the medium	1.8	W m^{-1} K^{-1}
Λ_f	Thermal conductivity in the fracture	1.6	W m^{-1} K^{-1}
C_ℓ	Heat capacity of the fluid	4186	J kg^{-1} K^{-1}
C_{ms}	Heat capacity of the solid (medium)	900	J kg^{-1} K^{-1}
C_{fs}	Heat capacity of the solid (fracture)	840	J kg^{-1} K^{-1}
ρ_{ms}	Mass density of the solid (medium)	2280	kg m^{-3}
ρ_{fs}	Mass density of the solid (fracture)	2350	kg m^{-3}

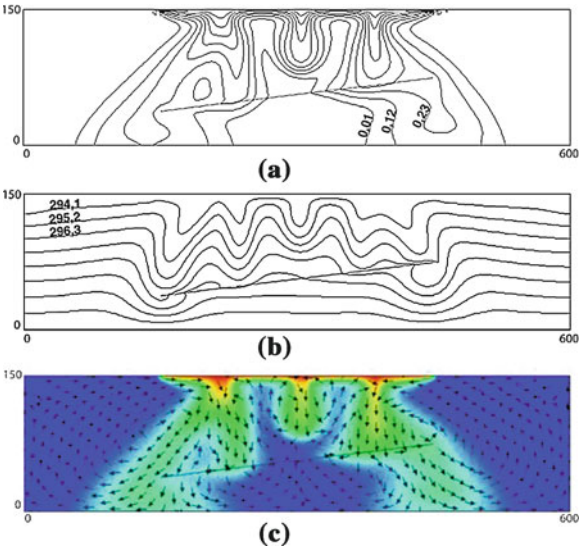

Fig. 3 Isolines of **a** the mass fraction (corresponding to $\omega_0 = 0.01$ and $\omega_i = \omega_0 + i \cdot 0.11$, $i = 1, \ldots, 9$) and **b** the temperature (corresponding to $\Theta_0 = 294.1$ and $\Theta_i = \Theta_0 + i \cdot 1.1$, $i = 1, \ldots, 9$) for Elder's problem with a fracture of width $\varepsilon = 1$ m at time $t = 4.9$ a. **c** Corresponding velocity field. The colours represent the distribution of the concentration

directed both downward and upward results in "oscillations" of the brine and leads to flipping the deflections of the mass fraction isolines.

With reference to heat transport, we mention the following observations. Since the temperature of the brine reservoir is smaller than the temperature of the domain, the intruding brine tends to cool down the domain. This situation is described by Fig. 3b. Heat transport is also characterized by two retardation factors (cf. [17]), which account for the fact that heat is conducted slower than brine. For the choice of parameters in Tables 1 and 2, the retardation factors R_f and R_m are such that $R_f < R_m$, which means that heat in the fracture is convected at $1/R_f$th of the convective velocity. This effect has to be considered together with the velocity distribution, according to which the velocity is higher in the fracture (Fig. 3).

3 Transition to the $(d-1)$-Dimensional Model for Salinity-Driven Flow

When the mathematical model presented in Sect. 2 is restricted to the case of constant temperature, we speak of salinity-driven flow. For this type of flow, the field equations are (1) and (2), the mass densities ρ^{pW} and ρ^{pB} in (8) are constant, and the conditions (12)–(14) are automatically satisfied.

We present two methods for the study of salinity-driven flow in fractured porous media. In the first one, referred to as *d-dimensional model*, the fracture $\mathfrak{F}$ has the same geometric dimension as the enclosing medium $\mathfrak{M}$, and the field equations are solved in the same form both in $\mathfrak{F}$ and in $\mathfrak{M}$. This method, which is well-known, requires neither approximation of the fracture geometry nor further reduction of the field equations. It is general but computationally expensive. In the second method, named $(d-1)$-*dimensional model*, the fracture $\mathfrak{F}$ is ideally replaced by a $(d-1)$-dimensional manifold, $\hat{\mathscr{S}}$, and the field equations defined in $\mathfrak{F}$ are averaged over the fracture width. The $(d-1)$-dimensional representation of flow and transport in the fracture is obtained by defining the averaged equations on $\hat{\mathscr{S}}$, and coupling them with the equations defined in the enclosing medium. The $(d-1)$-dimensional model demands some approximations of the averaged equations as well as the formulation of dedicated numerical schemes. It is thus less general but computationally cheaper. In our contribution, we compare the $(d-1)$- and d-dimensional models for some benchmark problems in order to evaluate the reliability of the former model.

3.1 Change of Variables

Equations 1 and 2 can be reformulated in such a way that the brine concentration c_α (whose units are $\frac{mass\ of\ brine}{volume\ of\ fluid-phase}$), rather than the mass fraction, ω_α, features in the field equations [22]. In terms of c_α, the constitutive law (8) admits the equivalent form

$$\rho(c_\alpha) = \rho^{pW} + \rho' c_\alpha, \tag{18}$$

with $\rho\prime := \frac{\rho^{pB}-\rho^{pW}}{\rho^{pB}}$. By using (18), the field equations become

$$\nabla \cdot (\rho^{pW}\mathbf{q}_\alpha - \rho'\mathbf{J}_\alpha) = 0, \tag{19}$$

$$\phi_\alpha \partial_t c_\alpha + \nabla \cdot (c_\alpha \mathbf{q}_\alpha + \mathbf{J}_\alpha) = 0, \tag{20}$$

where

$$\mathbf{q}_\alpha = -\frac{1}{\mu_\alpha} K_\alpha (\nabla p_\alpha - \rho(c_\alpha)\mathbf{g}), \tag{21}$$

$$\mathbf{J}_\alpha = -\left(\frac{\rho^{pW}}{\rho^{pW} + \rho' c_\alpha} D_\alpha\right) \nabla c_\alpha. \tag{22}$$

In the d-dimensional model, we solve (1) and (2) in the same form for both the fracture and the enclosing medium. In the $(d-1)$-dimensional model, we use (19)–(20) for the medium, and an averaged form of them for the fracture. The conditions at the fracture–medium interface have to be reformulated accordingly.

3.2 Averaging Along the Fracture Width

In this section, we briefly recall the fundamental relations needed to perform Bear's method [6] of averaging the field equations along the fracture width [22]. With respect to the reference frame sketched in Fig. 1, the equations defining the surfaces $\mathscr{S}^{(1)}$ and $\mathscr{S}^{(2)}$ are given by

$$\mathscr{S}^{(1)} : \; z - z^{(1)} = 0, \quad \mathscr{S}^{(2)} : \; z - z^{(2)} = 0. \tag{23}$$

The fracture mean plane, denoted by $\mathscr{S}$, is individuated by $z = 0$. The width of the fracture, given by $\varepsilon = z^{(2)} - z^{(1)}$, satisfies the relations $\ell \ll \varepsilon \ll \mathrm{L}$, with ℓ and L being the pore- and macro-scale characteristic lengths in Ω, respectively.

Because of the geometric features of the considered fracture, the average of a given field Φ over the fracture width takes on the form

$$\langle \Phi \rangle (t, x, y) := \frac{1}{\varepsilon} \int_{-\varepsilon/2}^{+\varepsilon/2} \Phi(t, x, y, z) dz. \tag{24}$$

Given a scalar and a vector field, denoted by Φ and $\mathbf{A}$, respectively, the average of $\Phi\mathbf{A}$ is given by

$$\langle \Phi \mathbf{A} \rangle = \langle \Phi \rangle \langle \mathbf{A} \rangle + \langle \tilde{\Phi} \tilde{\mathbf{A}} \rangle, \tag{25}$$

where $\tilde{\Phi} := \Phi - \langle \Phi \rangle$ and $\tilde{\mathbf{A}} := \mathbf{A} - \langle \mathbf{A} \rangle$ are said to be fluctuations.

Under the hypothesis that the fracture width is constant in time and space, the following relations hold

$$\langle \partial_t \Phi \rangle = \partial_t \langle \Phi \rangle, \tag{26}$$

$$\langle \nabla \cdot \mathbf{A} \rangle = \nabla^\sigma \cdot \langle \mathbf{A}^\sigma \rangle + \frac{A_n^{(2)} + A_n^{(1)}}{\varepsilon}, \tag{27}$$

where $\mathbf{A}^\sigma$ is the projection of $\mathbf{A}$ onto the fracture mean plane $\mathscr{S}$, ∇^σ is the tangential part of the ∇-operator, and the notation $A_n^{(k)}$ (with $k = 1, 2$) means $A_n^{(k)} = \mathbf{A}^{(k)} \cdot \mathbf{n}^{(k)}$, with $\mathbf{A}^{(k)}$ being the restriction of $\mathbf{A}$ onto $\mathscr{S}^{(k)}$, and $\mathbf{n}^{(k)}$ the unit

vector normal to $\mathscr{S}^{(k)}$. In the rest of this contribution, the averages of concentration and pressure will be denoted by $\bar{c}_f = \langle c_f \rangle$ and $\bar{p}_f = \langle p_f \rangle$.

The constitutive prescription (18) expresses the fluid-phase mass density as an affine function of the brine concentration. Therefore, the function $\rho_f = \rho_f(c_f)$ has the following property

$$\langle \rho(c_f) \rangle = \rho(\langle c_f \rangle) = \rho^{pW} + \rho' \langle c_f \rangle = \rho^{pW} + \rho' \bar{c}_f \tag{28}$$

By using of formulae (24)–(28), and introducing the notation

$$\mathbf{Q}_\alpha := \rho^{pW} \mathbf{q}_\alpha - \rho' \mathbf{J}_\alpha, \quad \mathbf{P}_\alpha := c_\alpha \mathbf{q}_\alpha + \mathbf{J}_\alpha, \quad \text{with} \quad \alpha \in \{f, m\}. \tag{29}$$

the field equations can be written in the following averaged form

$$\nabla^\sigma \cdot \left(\rho^{pW} \langle \mathbf{q}_f^\sigma \rangle - \rho' \langle \mathbf{J}_f^\sigma \rangle \right) + \frac{Q_{fn}^{(2)} + Q_{fn}^{(1)}}{\varepsilon} = 0, \tag{30}$$

$$\phi_f \partial_t \bar{c}_f + \nabla^\sigma \cdot (\bar{c}_f \langle \mathbf{q}_f^\sigma \rangle + \langle \tilde{c}_f \tilde{\mathbf{q}}_f^\sigma \rangle + \langle \mathbf{J}_f^\sigma \rangle) + \frac{P_{fn}^{(2)} + P_{fn}^{(1)}}{\varepsilon} = 0, \tag{31}$$

where $Q_{fn}^{(k)} = \mathbf{Q}_f^{(k)} \cdot \mathbf{n}^{(k)}$, $P_{fn}^{(k)} = \mathbf{P}_f^{(k)} \cdot \mathbf{n}^{(k)}$ (with k = 1, 2), and

$$\langle \mathbf{q}_f^\sigma \rangle = -\frac{K_f}{\mu} \left[\nabla^\sigma \bar{p}_f - \left(\rho^{pW} + \rho' \bar{c}_f \right) \mathbf{g}^\sigma \right], \tag{32}$$

$$\langle \tilde{c}_f \tilde{\mathbf{q}}_f^\sigma \rangle = -\left\langle \tilde{c}_f \frac{K_f}{\mu} [\nabla^\sigma \tilde{p}_f - \rho' \tilde{c}_f \mathbf{g}^\sigma] \right\rangle, \tag{33}$$

$$\langle \mathbf{J}_f^\sigma \rangle = -\left\langle \left(\frac{\rho^{pW}}{\rho^{pW} + \rho' c_f} D_f \right) \nabla^\sigma c_f \right\rangle. \tag{34}$$

The conditions at the fracture–medium interface (9)–(11) become

$$\text{on } \mathscr{S}^{(k)}, Q_{fn}^{(k)} = Q_{mn}^{(k)}, \quad P_{fn}^{(k)} = P_{mn}^{(k)}, \quad k = 1, 2, \tag{35}$$

$$\text{on } \mathscr{B}, \quad \mathbf{q}_f^\sigma \cdot \boldsymbol{\tau} = \mathbf{q}_m^\sigma \cdot \boldsymbol{\tau}, \quad \mathbf{J}_f^\sigma \cdot \boldsymbol{\tau} = \mathbf{J}_m^\sigma \cdot \boldsymbol{\tau}, \tag{36}$$

$$\text{on } \partial\tilde{\mathfrak{F}}, \quad c_f = c_m, \quad p_f = p_m. \tag{37}$$

Following [22], we simplify (31) by requiring $\langle \tilde{c}_f \tilde{\mathbf{q}}_f^\sigma \rangle$ to be negligible (i.e. which amounts to disregard mechanical macrodispersion [5, 7]), and approximating $\langle \mathbf{J}_f^\sigma \rangle$ as

$$\langle \mathbf{J}_f^\sigma \rangle \approx -D_f \left(1 - \frac{\rho'}{\rho^{pW}} \bar{c}_f \right) \nabla^\sigma \bar{c}_f. \tag{38}$$

3.3 The $(d-1)$-Dimensional Model

The $(d-1)$-dimensional model is formulated by letting the surfaces $\mathscr{S}^{(1)}$ and $\mathscr{S}^{(2)}$ ideally lie one above the other and coincide with the fracture mean plane $\mathscr{S}$. The band-shaped boundary $\mathscr{B}$ shrinks to a closed line, i.e. the contour of $\mathscr{S}$, which is denoted by $\hat{\mathscr{B}} = \mathscr{B} \cap \mathscr{S}$. The surface $\mathscr{S}$ is the $(d-1)$-dimensional representation of the fracture. The two sides of $\mathscr{S}$ are denoted by $\hat{\mathscr{S}}^{(1)}$ and $\hat{\mathscr{S}}^{(2)}$. These correspond to $\mathscr{S}^{(1)}$ and $\mathscr{S}^{(2)}$, respectively, and, although geometrically indistinguishable from $\mathscr{S}$, are introduced in order to describe the physical processes that in the d-dimensional model take place on $\mathscr{S}^{(1)}$ and $\mathscr{S}^{(2)}$.

Viewing the fracture as a $(d-1)$-dimensional domain implies that the volume originally occupied by $\mathfrak{F}$ is "given" to the enclosing medium, which thus extends over the wider region $\hat{\mathfrak{M}} = \Omega / \mathscr{S}$, rather than $\mathfrak{M} = \Omega / \mathfrak{F}$. Consequently, the fields c_m and p_m, which denote concentration and pressure in $\mathfrak{M}$, have to be replaced by their prolongations onto $\hat{\mathfrak{M}}$, i.e. $\hat{c}_m : \hat{\mathfrak{M}} \to \mathbb{R}_0^+$, and $\hat{p}_m : \hat{\mathfrak{M}} \to \mathbb{R}$.

The quantities $Q_{fn}^{(k)}$ and $P_{fn}^{(k)}$, computed on $\mathscr{S}^{(k)}$ in the d-dimensional model, have to be computed on $\hat{\mathscr{S}}^{(k)}$ in the $(d-1)$-dimensional model. Therefore, the sums $\left(Q_{fn}^{(1)} + Q_{fn}^{(2)}\right)$ and $\left(P_{fn}^{(1)} + P_{fn}^{(2)}\right)$, which express the net rate at which mass leaves or enters the fracture at $\mathscr{S}^{(1)}$ and $\mathscr{S}^{(2)}$, acquire now the meaning of "jumps" of fluxes of the physical quantities that are processed in the fracture and exchanged with the enclosing medium at $\hat{\mathscr{S}}^{(1)}$ and $\hat{\mathscr{S}}^{(2)}$. Consequently, $\mathscr{S}$ is treated as a surface of discontinuity in the $(d-1)$-dimensional model. Furthermore, since the values of concentration and pressure on $\mathscr{S}^{(1)}$, $\mathscr{S}^{(2)}$, and in $\mathfrak{F}$ are generally different from one another, we require that at each point of $\hat{\mathscr{S}}$ there exist three values of concentration and three values of pressure. In order to express this condition, we denote by $\hat{c}_m^{(k)}$ and $\hat{p}_m^{(k)}$ the values taken by concentration and pressure at $\hat{\mathscr{S}}^{(k)}$ $(k = 1, 2)$ as computed within the $(d-1)$-dimensional model, and we allow for the following conditions

$$\hat{c}_m^{(1)} \neq \bar{c}_f \neq \hat{c}_m^{(2)}, \quad \hat{p}_m^{(1)} \neq \bar{p}_f \neq \hat{p}_m^{(2)}. \tag{39}$$

In accordance with condition (11) (or (37)), which states that mass and pressure are continuous on the boundary of the fracture, we interpret $\hat{c}_m^{(k)}$ and $\hat{p}_m^{(k)}$ $(k = 1, 2)$ as the values of concentration and pressure that fracture and medium have in common on $\hat{\mathscr{S}}^{(1)}$ and $\hat{\mathscr{S}}^{(2)}$, i.e. the $(d-1)$-dimensional representation of interfaces $\mathscr{S}^{(1)}$ and $\mathscr{S}^{(2)}$ shared by the fracture and the enclosing medium.

In order to account for the normal gradients of concentration and pressure across the fracture, it is also necessary to reformulate the terms $Q_{fn}^{(k)}$ and $P_{fn}^{(k)}$ $(k = 1, 2)$. The $(d-1)$-dimensional representation of these terms reads [22]

$$\hat{Q}_{fn}^{(k)} := \rho^{pW} \hat{q}_{fn}^{(k)} - \rho' \hat{J}_{fn}^{(k)}, \quad k = 1, 2 \tag{40}$$

$$\hat{P}_{fn}^{(k)} = c_{\text{upwind}}^{(k)} \hat{q}_{fn}^{(k)} + \hat{J}_{fn}^{(k)}, \quad k = 1, 2, \tag{41}$$

where $\hat{q}_{fn}^{(k)}$ and $\hat{J}_{fn}^{(k)}$ approximate $q_{fn}^{(k)}$ and $J_{fn}^{(k)}$, respectively, and are computed on $\hat{\mathscr{S}}^{(k)}$. The concentration $c_{\text{upwind}}^{(k)}$ is used for a consistent description of convection, and is taken to be either $c_{\text{upwind}}^{(k)} = \hat{c}_m^{(k)}$, if $\hat{q}_{fn}^{(k)} < 0$, or $c_{\text{upwind}}^{(k)} = \bar{c}_f$, if $\hat{q}_{fn}^{(k)} \geq 0$. The quantities $\hat{q}_{fn}^{(k)}$ and $\hat{J}_{fn}^{(k)}$ are computed as follows

$$\hat{q}_{fn}^{(k)} := -\frac{K_f}{\mu} \left[\frac{\hat{p}_m^{(k)} - \bar{p}_f}{\varepsilon/2} - \left(\rho\left(\hat{c}_m^{(k)}\right) - \rho\left(\bar{c}_f\right) \right) \mathbf{g} \cdot \mathbf{n}^{(k)} \right], \tag{42}$$

$$\hat{J}_{fn}^{(k)} := -D_f \left(1 - \frac{\rho'}{\rho^{pW}} \hat{c}_m^{(k)} \right) \frac{\hat{c}_m^{(k)} - \bar{c}_f}{\varepsilon/2}, \tag{43}$$

where

$$\partial_{n^{(k)}} p|_{\mathscr{S}^{(k)}} \approx \frac{\hat{p}_m^{(k)} - \bar{p}_f}{\varepsilon/2}, \quad \textit{and} \quad \partial_{n^{(k)}} c|_{\mathscr{S}^{(k)}} \approx \frac{\hat{c}_m^{(k)} - \bar{c}_f}{\varepsilon/2}, \quad k = 1, 2. \tag{44}$$

The approximations (44) account for the continuity of concentration and pressure on the two sides of $\mathscr{S}$, as required by the interface condition (37).

Comparing the definition of $\hat{q}_{fn}^{(k)}$ in (42) with the expression of $q_{fn}^{(k)} = \mathbf{q}_f^{(k)} \cdot \mathbf{n}^{(k)}$ in (21) shows that $\hat{q}_{fn}^{(k)}$ is obtained from $q_{fn}^{(k)}$ by approximating the normal derivative of pressure as shown in (44), and replacing the gravitational term $-\rho\left(c_f^{(k)}\right)\mathbf{g} \cdot \mathbf{n}^{(k)}$ by $-\left(\rho\left(\hat{c}_m^{(k)}\right) - \rho\left(\bar{c}_f\right)\right)\mathbf{g} \cdot \mathbf{n}^{(k)}$, where $c_f^{(k)}$ is the restriction of c_f on $\mathscr{S}^{(k)}$. The use of $\rho\left(\hat{c}_m^{(k)}\right)$ instead of $\rho\left(c_f^{(k)}\right)$ descends for the continuity of concentration at the fracture–medium interface, while the term $-\rho(\bar{c}_f)\mathbf{g} \cdot \mathbf{n}^{(k)}$ is introduced in order to eliminate artificial (or "parasite") flows, which would otherwise arise when the fracture is modeled as a $(d-1)$-dimensional domain.

The approximations (39)–(44) allow for replacing the sum $\left(Q_{fn}^{(1)} + Q_{fn}^{(2)}\right)$ in (30) and $\left(P_{fn}^{(1)} + P_{fn}^{(2)}\right)$ in (31) as follows

$$\left(Q_{fn}^{(1)} + Q_{fn}^{(2)}\right) \to \left(\hat{Q}_{fn}^{(1)} + \hat{Q}_{fn}^{(2)}\right), \quad \left(P_{fn}^{(1)} + P_{fn}^{(2)}\right) \to \left(\hat{P}_{fn}^{(1)} + \hat{P}_{fn}^{(2)}\right). \tag{45}$$

In the absence of the correction $-\rho(\bar{c}_f)\mathbf{g} \cdot \mathbf{n}^{(k)}$ in the definition $\hat{q}_{fn}^{(k)}$, the emergence of parasite flows is due to the fact that the jumps described by $\left(\hat{Q}_{fn}^{(1)} + \hat{Q}_{fn}^{(2)}\right)$ and $\left(\hat{P}_{fn}^{(1)} + \hat{P}_{fn}^{(2)}\right)$, which are physically meaningful at the inner

points of $\mathscr{S}$, may lead to unphysical pressure jumps at $\hat{\mathscr{B}} = \mathscr{B} \cap \mathscr{S}$ and, consequently, to artificial velocities [22]. For example, in the d-dimensional representation of a horizontal fracture, the pressure drop across the fracture width is given by $\delta p = g \int_{-\varepsilon/2}^{+\varepsilon/2} \rho(c_f) \mathrm{d}z = \varepsilon \rho(\bar{c}_f) g$. In the $(d-1)$-dimensional model, δp is no longer distributed along the fracture width. Rather, it becomes a discontinuity jump across the surface $\mathscr{S}$. However, this contradicts the pressure distribution in the medium, which has no discontinuity at a point at same height as $\mathscr{S}$ situated in $\Omega \backslash \mathscr{S}$. This inconsistency results in parasite flows, whose velocities are proportional to ε. These parasite flows are reduced by using

$$p_m|_{\mathscr{S}^{(k)}} \approx \hat{p}_m^{(k)} + \frac{\varepsilon}{2} \rho(\bar{c}_f) \mathbf{g} \cdot \mathbf{n}^{(k)}. \tag{46}$$

The approximations discussed so far allow for formulating the field equations of the $(d-1)$-dimensional model in the following way. The equations describing fluid flow and brine transport in the $(d-1)$-dimensional representation of fracture, i.e. the surface $\mathscr{S}$, read

$$\nabla^\sigma \cdot \left(\varepsilon \rho^{pW} \langle \mathbf{q}_f^\sigma \rangle - \rho' \varepsilon \langle \mathbf{J}_f^\sigma \rangle \right) + \left(\hat{Q}_{fn}^{(2)} + \hat{Q}_{fn}^{(1)} \right) = 0, \tag{47}$$

$$\phi_f \partial_t (\varepsilon \bar{c}_f) + \nabla^\sigma \cdot \left(\varepsilon \bar{c}_f \langle \mathbf{q}_f^\sigma \rangle + \varepsilon \langle \mathbf{J}_f^\sigma \rangle \right) + \left(\hat{P}_{fn}^{(2)} + \hat{P}_{fn}^{(1)} \right) = 0, \tag{48}$$

with

$$\langle \mathbf{q}_f^\sigma \rangle = -\frac{K_f}{\mu} \left[\nabla^\sigma \bar{p}_f - \left(\rho^{pW} + \rho' \bar{c}_f \right) \mathbf{g}^\sigma \right], \tag{49}$$

$$\langle \mathbf{J}_f^\sigma \rangle = -D_f \left(1 - \frac{\rho'}{\rho^{pW}} \bar{c}_f \right) \nabla^\sigma \bar{c}_f. \tag{50}$$

The quantities $\varepsilon \rho^{pW}$ and $\varepsilon \bar{c}_f$ represent, respectively, the densities per unit surface of pure water and brine that are transported by the averaged tangential velocity field $\langle \mathbf{q}_f^\sigma \rangle$. Diffusion of brine along $\mathscr{S}$ occurs by means of the tangential mass flux per unit length $\varepsilon \langle \mathbf{J}_f^\sigma \rangle$.

In the medium $\hat{\mathfrak{M}} = \Omega \backslash \mathscr{S}$, the field equations are given by

$$\nabla \cdot \left(\rho^{pW} \hat{\mathbf{q}}_m - \rho' \hat{\mathbf{J}}_m \right) = 0, \tag{51}$$

$$\phi_m \partial_t \hat{c}_m + \nabla \cdot \left(c_m \hat{\mathbf{q}}_m + \hat{\mathbf{J}}_m \right) = 0, \tag{52}$$

where $\hat{\mathbf{q}}_m$ and $\hat{\mathbf{J}}_m$ represent the specific discharge and Fick's mass flux associated with the concentration $\hat{c}_m$ and pressure $\hat{p}_m$ defined in $\hat{\mathfrak{M}}$, i.e.

$$\hat{\mathbf{q}}_m = -\frac{K_m}{\mu} (\nabla \hat{p}_m - \rho(\hat{c}_m) \mathbf{g}), \tag{53}$$

$$\hat{\mathbf{J}}_m = -D_m\left(1 - \frac{\rho'}{\rho^{pW}}\hat{c}_m\right)\nabla\hat{c}_m. \tag{54}$$

The interface conditions at the sides $\hat{\mathscr{S}}^{(1)}$ and $\hat{\mathscr{S}}^{(2)}$ are

$$\hat{Q}_{fn}^{(k)} = \hat{Q}_{mn}^{(k)}, \quad \text{and} \quad \hat{P}_{fn}^{(k)} = \hat{P}_{mn}^{(k)}, \quad k = 1, 2, \tag{55}$$

where $\hat{\mathbf{Q}}_m := \rho^{pW}\hat{\mathbf{q}}_m - \rho'\hat{\mathbf{J}}_m$, and $\hat{\mathbf{P}}_m := \hat{c}_m\hat{\mathbf{q}}_m + \hat{\mathbf{J}}_m$. Finally, we require the fracture boundary $\hat{\mathrm{B}}$ to be impervious (cf. [1]), that the mass fluxes $\rho(\bar{c}_f)\langle\mathbf{q}_f^{\sigma}\rangle \cdot \boldsymbol{\tau}$ and $\langle\mathbf{J}_f^{\sigma}\rangle \cdot \boldsymbol{\tau}$ vanish on $\hat{\mathscr{B}}$, i.e.

$$-\rho(\bar{c}_f)\frac{K_f}{\mu}(\partial_\tau\bar{p}_f - \rho(\bar{c}_f)g_\tau) = 0, \quad \text{and} \quad -D_f\left(1 - \frac{\rho'}{\rho^{pW}}\bar{c}_f\right)\partial_\tau\bar{c}_f = 0, \tag{56}$$

where $\boldsymbol{\tau}$ is the unit vector normal to $\hat{\mathscr{B}}$ and tangential to $\mathscr{S}$. Analogous conditions hold on $\hat{\mathscr{B}}$ for the averaged fluxes defined in $\hat{\mathfrak{M}}$.

3.4 Vorticity

Salinity- and thermohaline-driven flow are, in general, non-potential flows [4], i.e. the curl of velocity $\mathbf{v}_\alpha = \mathbf{q}_\alpha/\phi_\alpha$ does not vanish everywhere in Ω. In the case of uniform porosity, the rotation of velocity can be characterized entirely in terms of $\mathbf{q}_\alpha$ by introducing the quantity $\boldsymbol{\omega}_\alpha = \nabla \times \mathbf{q}_\alpha$, with $\alpha \in \{f, m\}$. Under the hypotheses of uniform viscosity, isotropic and piecewise constant permeability, and validity of Darcy's law (4), the vorticity $\boldsymbol{\omega}_\alpha$ can be expressed by the formula

$$\boldsymbol{\omega}_\alpha = \nabla \times \mathbf{q}_\alpha = \frac{K_\alpha}{\mu}\nabla\rho_\alpha \times \mathbf{g} \tag{57}$$

(this formula follows from $\nabla \times \nabla p = \mathbf{0}$, which is valid where pressure obeys Schwarz's conditions). For salinity-driven flow, substitution of (18) into (57) yields

$$\boldsymbol{\omega}_\alpha = \frac{K_\alpha}{\mu}\rho'(\nabla c_\alpha \times \mathbf{g}), \tag{58}$$

which means that the absolute value of vorticity is maximal when the gradient of the brine concentration is orthogonal to the gravity acceleration vector.

The presence of vorticity is connected with the recirculating motions by which brine is convected. These motions are typical in several benchmark problems of groundwater flow. In fractured porous media, the distribution of vorticity depends both on the position and on the thickness of the fracture. In particular, if a fracture is thick enough, then, for a given cross section of the fracture, the profile of brine concentration tends to deviate from its mean value, and vorticity varies along the fracture width.

The d-dimensional model computes the vorticity along the fracture width with the same accuracy for both thick and thin fractures. The $(d-1)$-dimensional model, instead, is only able to provide an average value of vorticity in the fracture. This approximation is acceptable only if the fracture is thin, but fails to give good results for sufficiently thick fractures.

4 Finite-Volume Discretization and Numerical Solution

The coupled systems (47)–(48) and (51)–(52) have different dimensionalities and separate unknown functions defined in the same domain. This feature is important for the discretization. In this section, we present a vertex-centered finite volume discretization of (47)–(48) and (51)–(52).

The finite-volume method also known as the control volume [31] or finite volume element methods [9] is very popular in the numerical solution of PDEs. Application of this method to (1)–(2) in domains with no fractures was presented in [16]. We use a similar method for both (47)–(48) and (51)–(52). The essential difference of the presented method from the one described in [16] is that the $(d-1)$-dimensional fractures embedded in the d-dimensional domain have their own degrees of freedom. Furthermore, the proposed method allows to resolve the jumps of the d-dimensional part of the solution at the fractures.

4.1 Discretization Grids and Degrees of Freedom

We use the following notation. The time interval is covered by a grid $\{t^n : n \geq 0\}$ with $0 = t^0 < \ldots < t^n < \ldots$; $\tau^n := t^n - t^{n-1}$. We assume that Ω is polygonal, and the $(d-1)$-dimensional network of fractures $\mathscr{S} \subset \Omega$ is piecewise planar. The domain Ω is covered by a conformal triangulation $\mathbf{T}_\Omega$ that consists of triangles and quadrilaterals if $d = 2$ and tetrahedra, prisms and hexahedra if $d = 3$. It is supposed that for every element $e \in \mathbf{T}_\Omega$, $e \cap \mathscr{S}$ is either empty or consists only of corners, *whole* sides and *whole* edges of e. Thus, $\mathscr{S}$ is covered by the $(d-1)$-dimensional triangulation $T_\mathscr{S} := \{e \cap \mathscr{S} : e \in \mathbf{T}_\Omega,\ e \cap \mathscr{S} \text{ is a side of } e\}$. To simplify the notation, we assume that every $e \in \mathbf{T}_\Omega$ has at most one side on $\mathscr{S}$ and at most one on $\partial\Omega$. Similarly, $e \in \mathbf{T}_\mathscr{S}$ may not have more than one side on $\hat{\mathscr{B}}$. The generalization is straightforward.

Denote by Ω_h the set of all grid points, i.e. corners of the elements of $\mathbf{T}_\Omega$. Let $\mathscr{S}_h := \Omega_h \cap \mathscr{S}$. For the approximation of the discontinuities on $\mathscr{S}$, we consider grid functions that may have several values at every $x \in \mathscr{S}_h$. To define them properly, we introduce a special enumeration of the grid points so that several indices correspond to the same x. Degrees of freedom are uniquely assigned to these indices and not directly to geometric positions.

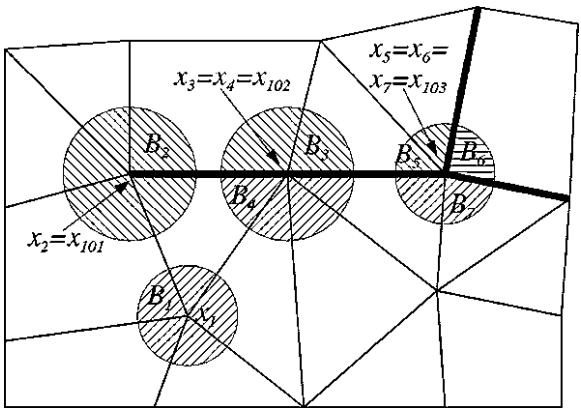

Fig. 4 Enumeration of the grid nodes in a piece of a grid with $N = 100$. The thick lines denote the fractures

To this end, for every $x \in \Omega_h$, consider a ball

$$B(x) = \left\{ y : \|y - x\|_2 < \frac{1}{2}\mathrm{dist}(x, \mathbf{T}_\Omega) \right\},$$

where $\mathrm{dist}(x, \mathbf{T}_\Omega)$ is the minimum distance between x and those sides and edges of elements $e \in \mathbf{T}_\Omega$ which do not contain x. Fractures $\mathscr{S}$ cut these balls into disjoint open subsets (cf. Fig. 4). Denote these subsets of $B(x)$ for all $x \in \Omega_h$ by B_1, B_N, where $N \geq |\Omega_h|$ is the total number of them. Every $\overline{B_i}$ contains only one $x \in \Omega_h$, and we denote this point by x_i. Under this enumeration, there may be $x_i = x_j \in \mathscr{S}_h$ for $i \neq j$. For simple straight fractures, points $x \in \mathscr{S}_h \backslash \hat{\mathscr{B}}$ have two different indices, and the intersection points of the fractures have even more ones. For $x \in \Omega_h \backslash \mathscr{S}_h$ or $x \in \mathscr{S}_h \cap \hat{\mathscr{B}}$, $\mathscr{S}$ does not split $B(x)$ and we say that $\mathscr{S}$ cuts $B(x)$ into one part. For $e \in \mathbf{T}_\Omega$, denote $\Lambda^e := \{i : 1 \leq i \leq N,\ x_i \in e,\ B_i \cap e \neq \varnothing\}$. These are indices of corners of e regarding the orientation of e w.r.t. the fractures.

To represent the numerical solution of (51)–(52), we introduce for time t^n and index $1 \leq i \leq N$ the degrees of freedom $\hat{c}^n_{mi}$ and $\hat{p}^n_{mi}$. For each i, $\hat{c}_m(t, x)$ and $\hat{p}_m(t, x)$ in the solution of (51)–(52) are continuous in B_i. In the numerical solution, $\hat{c}^n_{mi}$ and $\hat{p}^n_{mi}$ approximate the limits

$$\hat{c}^n_{mi} \approx \lim_{x \to x_i,\, x \in B_i} \hat{c}_m(t_n, x), \quad \hat{p}^n_{mi} \approx \lim_{x \to x_i,\, x \in B_i} \hat{p}_m(t_n, x). \tag{59}$$

We define piecewise linear functions $\hat{c}^n_{mh}, \hat{p}^n_{mh} : \Omega \to \mathbb{R}$ by the linear interpolation of the values $\hat{c}^n_{mi}$ and $\hat{p}^n_{mi}$ for $i \in \Lambda^e$ in every $e \in \mathbf{T}_\Omega$. These functions may be discontinuous only at $\mathscr{S}$.

In the fractures, we introduce grid functions $\bar{c}^n_{fh}$ and $\bar{p}^n_{fh}$ approximating $\bar{c}_f$ and $\bar{p}_f$ at time t^n independently on $\hat{c}^n_{mh}$ and $\hat{p}^n_{mh}$. Let $N_f := |\mathscr{S}_h|$. Additionally to the enumeration above, we assign indices $N + 1, \ldots, N + N_f$ to all the points from $\mathscr{S}_h$, so that $\mathscr{S}_h = \{x_{N+1}, \ldots, x_{N+N_f}\}$. Then $\bar{c}^n_{fh}$ and $\bar{p}^n_{fh} : \mathscr{S} \to \mathbb{R}$ are continuous piecewise linear functions with nodal values $\bar{c}^n_{f,i}$ and $\bar{p}^n_{f,i}$ at $x_i \in \mathscr{S}_h$. For $e \in \mathbf{T}_\mathscr{S}$, let $\Lambda^e := \{i : N < i \leq N + N_f, x_i \in e\}$.

Furthermore, let $\Lambda_i^e := \Lambda^e \backslash \{i\}$, if $i \in \Lambda^e$, and $\Lambda_i^e := \varnothing$ otherwise. Then $\Lambda_i := \bigcup_{e \in \mathbf{T}_\Omega} \Lambda_i^e$ is the set of all the indices of neighbour grid points of x_i. For $1 \le i \le N$, $\Lambda_i \subset \{1, \ldots, N\}$, whereas for $i > N$, $\Lambda_i \subset \{N+1, \ldots, N+N_f\}$. Besides this, for $i \le N$, let $\hat{\Lambda}_i := \{j : N < j \le N + N_f, x_i = x_j\}$ and, for $i > N$, let $\hat{\Lambda}_i := \{j : 1 \le j \le N, x_i = x_j\}$. Sets $\hat{\Lambda}_i$ represent the relations between the "fracture DOF indices" and the "bulk medium DOF indices" of points $x_i \in \mathscr{S}_h$. Note that for $i \le N$, $|\hat{\Lambda}_i| \le 1$.

4.2 The Finite-Volume Scheme

With each i, $1 \le i \le N$, we associate a computation cell ("control volume") by constructing a conformal dual mesh of finite volumes $V_i \subset \mathbb{R}^d$. Our choice are the so-called barycenter based control volumes. We define V_i as a union of V_i^e for all $e \in \mathbf{T}_\Omega$ such that $i \in \Lambda^e$. To get V_i^e, we cut the element e by the segments of the straight lines connecting the barycenter of this element with the centers of its sides (for $d = 2$), or by the segments of the plains spanning the barycenter of the element, the centers of the edges and the barycenters of the sides (for $d = 3$). Then V_i^e is the part of e containing x_i. The segments are denoted by γ_{ij}^e, i.e. $\gamma_{ij}^e := e \cap \partial V_i \cap \partial V_j$ for $j \le N$. Besides, we define $\gamma_{ij}^e := e \cap \partial V_i \cap \mathscr{S}$ with $j \in \hat{\Lambda}_i$ and $\gamma_{i0}^e := e \cap \partial V_i \cap \partial\Omega$. Then

$$\partial V_i = \bigcup_{e : i \in \Lambda^e} \bigcup_{j \in \Lambda_i^e \cup \hat{\Lambda}_i \cup \{0\}} \gamma_{ij}^e. \tag{60}$$

By $\mathbf{n}_{ij}^e$ we denote the unit normal vector to γ_{ij}^e pointing out of V_i, i.e. $\mathbf{n}_{ji}^e = -\mathbf{n}_{ij}^e$. Normals $\mathbf{n}^{(1)}$ and $\mathbf{n}^{(2)}$ are constant on γ_{ij}^e. One of them is $\mathbf{n}_{ij}^e$, the other one $-\mathbf{n}_{ij}^e$.

Control volumes V_i are used in the discretization of (51)–(52). For every i, $1 \le i \le N$, if x_i does not lie on the Dirichlet boundary, (51)–(52) are integrated over V_i. After the application of the divergence theorem, we get:

$$\sum_{e,j} \int_{\gamma_{ij}^e} \left(\rho^{pW} \hat{\mathbf{q}}_m - \rho \prime \hat{\mathbf{J}}_m \right) \cdot \mathbf{n}_{ij}^e \, \mathrm{d}s = 0, \tag{61}$$

$$\phi_m \int_{V_i} \partial_t \hat{c}_{mh} \, dx + \sum_{e,j} \int_{\gamma_{ij}^e} \left(\hat{c}_{mh}^n \hat{\mathbf{q}}_m + \hat{\mathbf{J}}_m \right) \cdot \mathbf{n}_{ij}^e \, \mathrm{d}s = 0, \tag{62}$$

where the summation runs over all $e \in \mathbf{T}_\Omega$, such that $i \in \Lambda^e$, and $j \in \Lambda_i^e \cup \hat{\Lambda}_i \cup \{0\}$. In this work, for the approximation of the time derivative we use the backward Euler scheme:

$$\int_{V_i} \partial_t \hat{c}_{mh} \, \mathrm{d}x = |V_i| \left(\hat{c}_{mi}^n - \hat{c}_{mi}^{n-1} \right) / \tau^n. \tag{63}$$

The summands in (61)–(62) corresponding to the indices $j \in \Lambda_i^e \cup \{0\}$ depend only on $\hat{c}_{mh}^n$ and $\hat{p}_{mh}^n$. For them, we use the approximation from [16]. In particular, the so-called consistent velocity is used for $\hat{\mathbf{q}}_m\big(\hat{c}_{mh}^n, \hat{p}_{mh}^n\big)$, cf. [15, 17], and an upwind method is applied for the discretization of the convection term $\hat{c}_{mh}^n \hat{\mathbf{q}}_m$. Consider the summand with $j \in \hat{\Lambda}_i$. It requires a special treatment. Let e be such an element that $i \in \Lambda^e$ and $\gamma_{ij}^e \neq \emptyset$. Let $k \in \{1, 2\}$ be such that $\mathbf{n}_{ij}^e = -\mathbf{n}^{(k)}$. We use (55) and the following approximations:

$$\int_{\gamma_{ij}^e} \left(\rho^{pW} \hat{\mathbf{q}}_m - \rho' \hat{\mathbf{J}}_m\right) \cdot \mathbf{n}_{ij}^e \, ds = \int_{\gamma_{ij}^e} \hat{Q}_{fn}^{(k)} ds \approx |\gamma_{ij}^e| \hat{Q}_{fn}^{(k)} \left(\hat{p}_{mi}^n, \bar{p}_{fj}^n; \hat{c}_{mi}^n, \bar{c}_{fj}^n\right), \tag{64}$$

$$\int_{\gamma_{ij}^e} \left(\hat{c}_{mh}^n \hat{\mathbf{q}}_m + \hat{\mathbf{J}}_m\right) \cdot \mathbf{n}_{ij}^e \, ds = \int_{\gamma_{ij}^e} \hat{P}_{fn}^{(k)} ds \approx |\gamma_{ij}^e| \hat{P}_{fn}^{(k)} \left(\hat{p}_{mi}^n, \bar{p}_{fj}^n; \hat{c}_{mi}^n, \bar{c}_{fj}^n\right). \tag{65}$$

These approximations are algebraic functions of $\hat{c}_{mh}^n$, $\hat{p}_{mh}^n$, $\bar{c}_{fh}^n$ and $\bar{p}_{fh}^n$.

For the discretization of (47)–(48), we construct $(d-1)$-dimensional computation cells in $\mathscr{S}$: With every $i > N$, we associate the $(d-1)$-dimensional control volume $S_i := \bigcup_{j \in \hat{\Lambda}_i} \bigcup_{e \in \mathbf{T}_\Omega : j \in \Lambda^e} \gamma_{ji}^e$. At the intersections of the fractures, S_i may lie in several intersecting planes. For $e \in \mathbf{T}_\mathscr{S}$, we introduce boundary segments σ_{ij}^e of S_i analogously to γ_{ij}^e: For $i, j > N$, $\sigma_{ij}^e := e \cap \partial S_i \cap \partial S_j$. Besides this, σ_{i0}^e is the intersection of $e \cap \partial S_i$ with the edge of the fracture. For every σ_{ij}^e, $\mathbf{n}_{ij}^e$ is the unit normal vector that lies in the plane of e and points out of S_i. Note that S_i are barycenter based control volumes, too. Integration of (47)–(48) over S_i yields:

$$\sum_{e,j} \int_{\sigma_{ij}^e} \varepsilon \left(\rho^{pW} \langle \mathbf{q}_f^\sigma \rangle - \rho' \langle \mathbf{J}_f^\sigma \rangle\right) \cdot \mathbf{n}_{ij}^e \, dl + \int_{S_i} \left(\hat{Q}_{fn}^{(2)} + \hat{Q}_{fn}^{(1)}\right) ds = 0, \tag{66}$$

$$\phi_f \int_{S_i} \varepsilon \partial_t \bar{c}_{fh} \, dx + \sum_{e,j} \int_{\sigma_{ij}^e} \varepsilon \left(\bar{c}_{fh}^n \langle \mathbf{q}_f^\sigma \rangle + \langle \mathbf{J}_f^\sigma \rangle\right) \cdot \mathbf{n}_{ij}^e \, ds + \int_{S_i} \left(\hat{P}_{fn}^{(2)} + \hat{P}_{fn}^{(1)}\right) ds = 0, \tag{67}$$

where the summation runs over all $e \in \mathbf{T}_\mathscr{S}$, such that $i \in \Lambda^e$, and $j \in \Lambda_i^e \cup \hat{\Lambda}_i \cup \{0\}$. For the approximation of the time derivative in (67), we use the backward Euler scheme, too:

$$\int_{S_i} \varepsilon \partial_t \bar{c}_{f,h} \, dx = \varepsilon |S_i| \left(\bar{c}_{f,i}^n - \bar{c}_{f,i}^{n-1}\right) / \tau^n. \tag{68}$$

As σ_{ij}^e are segments of straight lines (for $d = 3$) or points (for $d = 2$), we discretize the integrals over them in (66)–(67) using the method from [16]

formulated in $d-1$ dimensions for $\bar{c}_{fh}$ and $\bar{p}_{fh}$. For $\langle \mathbf{q}_f^\sigma \rangle$, the consistent velocity from [17] is used. For the convection term in (67), a $(d-1)$-dimensional version of the upwind method for the discretization of (62) is applied.

To approximate the integrals of $\hat{Q}_{fn}^{(k)}$ and $\hat{P}_{fn}^{(k)}$ [cf. (40)–(41)] in (66)–(67), we use the fact that $S_i = \bigcup_{j\in\hat{\Lambda}_i} \bigcup_{e:j\in\Lambda^e,\mathbf{n}_{ji}^e=-\mathbf{n}^{(k)}} \gamma_{ij}^e$ where γ_{ji}^e are disjoint planar sets:

$$\int_{S_i} \hat{Q}_{fn}^{(k)}\, ds \approx \sum_{j\in\hat{\Lambda}_i} \sum_{e:j\in\Lambda^e,\mathbf{n}_{ji}^e=-\mathbf{n}^{(k)}} |\gamma_{ji}^e| \hat{Q}_{fn}^{(k)}\left(\hat{p}_{mj}^n, \bar{p}_{fi}^n; \hat{c}_{mj}^n, \bar{c}_{fi}^n\right), \tag{69}$$

$$\int_{S_i} \hat{P}_{fn}^{(k)}\, ds \approx \sum_{j\in\hat{\Lambda}_i} \sum_{e:j\in\Lambda^e,\mathbf{n}_{ji}^e=-\mathbf{n}^{(k)}} |\gamma_{ji}^e| \hat{P}_{fn}^{(k)}\left(\hat{p}_{mj}^n, \bar{p}_{fi}^n; \hat{c}_{mj}^n, \bar{c}_{fi}^n\right). \tag{70}$$

The contribution of (69)–(70) to (66)–(67) is exactly the same as the contribution of the terms (64)–(65) to (61)–(62) so that the entire discretization is conservative w.r.t. the mass of the total fluid phase and mass of the brain.

Conditions (56) at $\hat{\mathscr{B}}$ are natural boundary conditions for the finite-volume discretization. They introduce no additional terms in (61)–(62) and (66)–(67). Further boundary conditions should be used for $\bar{c}_f$ and $\bar{p}_f$ at $\mathscr{S} \cap \partial\Omega$.

Using the introduced approximations of the integrals in (61)–(62) for all V_i and in (66)–(67) for all S_i, we obtain a sparse system of $N + N_f$ nonlinear algebraic equations. In our simulations, this system is solved by the Newton method. To make use of the sparsity of the linear systems in the iterations of the nonlinear solver, we solve them by the BiCGStab method with the multigrid preconditioning (cf. [2]) which proved to be very efficient in this case. In the multigrid cycle, we use the ILU_β-smoothers. The matrices in the grid hierarchy are not computed by the Galerkin formula but assembled as the Jacobians of the discretized nonlinear systems for each grid.

In Sect. 5, we compare results from the simulations with the proposed model with results from the simulations with (1)–(2) and the fractures considered as d-dimensional subdomains. For the latter model, the finite-volume discretization from [16] is used and the discretized system is solved by the same methods as above. However, due to the geometric anisotropy and the jumps of the coefficients introduced by the thin subdomains, the convergence rate of the multigrid solver deteriorates. To overcome this problem, we compute the matrices on the several coarse levels in the grid hierarchy not for (1)–(2) but for a model obtained from (1) to (2) by averaging the equations in the fracture as in the model presented above (but under much stronger assumptions). By a special choice of the restriction and the prolongation, we introduce a dimension-transfer. The fractures are resolved as d-dimensional objects on finest grid levels, but on coarse grids they may be treated as $(d-1)$-dimensional objects. This improves the convergence of the multigrid solver essentially.

4.3 Grid Preparation and Assembling of the Discretized System

To construct a grid having the properties specified at the beginning of Sect. 4.1, first a d-dimensional triangulation of the domain bounded by $\partial\Omega$ is generated. This can be done by using, e.g. constrained Delaunay triangulation [10, 38]. This class of algorithms generates grids not only fulfilling the properties stated above but also featuring elements of overall "good quality", meaning that the minimal interior angle is maximized. The triangulation produces triangles for ($d = 2$) and tetrahedrons (for $d = 3$).

We denote the resulting grid by $\mathscr{G} := \{\mathscr{V}, \mathscr{E}\}$ where $\mathscr{V} := \{v_1, \ldots, v_{N_v}\}$ denotes the set of vertices and $\mathscr{E} := \{\mathfrak{e}_1, \ldots, \mathfrak{e}_{N_e}\}$ the set of d-dimensional elements in $\mathscr{G}$, N_v and N_e being the number of vertices and elements of $\mathscr{G}$. In this context an element $\mathfrak{e} \in \mathscr{E}$ is identified with a tuple of vertices, which describe the corners of $\mathfrak{e}$. We use the following notation: $\mathfrak{e} \in \mathscr{E} \Rightarrow \exists v_{i_1}, \ldots, v_{i_{d+1}} \in \mathscr{V} : \mathfrak{e} = \left[v_{i_1}, \ldots, v_{i_{d+1}}\right]$. By $p : \mathscr{V} \to \Omega \subset \mathbb{R}^d$ we denote the mapping that associates a vertex with its position in $\mathbb{R}^d$ and by $conv : \mathscr{E} \to \mathbf{T}_\Omega \subset \mathbb{R}^d$, the mapping that associates an element $\mathfrak{e} \in \mathscr{E}$ with its convex hull. We use analogous notation for the $(d-1)$-dimensional elements in the fracture.

Let $\mathscr{G}_\mathscr{S} := \{\mathscr{V}_\mathscr{S}, \mathscr{E}_\mathscr{S}\}$ with $\mathscr{V}_\mathscr{S} := \{v \in \mathscr{V} | p(v) \in \mathscr{S}\}$ and $\mathscr{E}_\mathscr{S} := \{[v_{i_1}, \ldots, v_{i_d}] | v_{i_j} \in \mathscr{V}, \exists \mathfrak{e} \in \mathscr{E} : p(v_{i_j}) \in conv(\mathfrak{e}) \cap \mathscr{S}, j = 1, \ldots, d\}$ be the grid subset representing the fractures.

Our discretization requires additional degrees of freedom at the fracture vertices. We create an additional vertex for each additional DoF required. In order to associate them with the surrounding grid, we introduce degenerated elements–elements with vertices having pairwise the same position so that the elements have zero width. In two dimensions, these are e.g. quadrilaterals resembling an edge and in three dimensions we use prisms and pyramids that degenerate to a triangle. Note that, since we need additional DoFs on both sides of the fracture, the fracture has to be expanded into two layers of degenerated elements (cf. Fig. 5 for the case of Fig. 4).

One could think of constructing the degenerated elements by iterating over all fracture elements $\mathfrak{s} \in \mathscr{E}_\mathfrak{s}$, creating degenerated elements on both sides of each $\mathfrak{s}$. However, this approach leads to complications at fracture junctions, where special cases have to be implemented depending on the number of intersecting fractures. This becomes even more evident in three dimensions, where a multitude of special cases would be required to handle the different intersection constellations. Rather we operate on the elements adjacent to the fracture. To this end, we introduce new vertices v_{i,i_j} for each $v_i \in \mathscr{V}_\mathscr{S}$ and for associated subsets $B_{i_1}, \ldots, B_{i_k}$, $p(v_i) \in \overline{B_{i_j}}$, $0 < i_j \leq N$, $j = 1, \ldots, k$, $i_1 < \ldots < i_k$ with $p(v_{i,i_j}) = p(v_i)$. Let then $\mathscr{V}^*$ be the set that contains those new vertices.

For each element $\mathfrak{e} \in \mathscr{E}_\mathscr{S}$ that shares a side with a fracture, consider each side $\mathfrak{s} \in \mathscr{E}_\mathscr{S}$ of $\mathfrak{e}$, so that $conv(\mathfrak{s}) \subset conv(\mathfrak{e})$. Let $v_{i_1}, \ldots, v_{i_d} \in \mathscr{V}_\mathscr{S}$, $v_{i_1}, \ldots, v_{i_d} \in \mathfrak{s}$ be

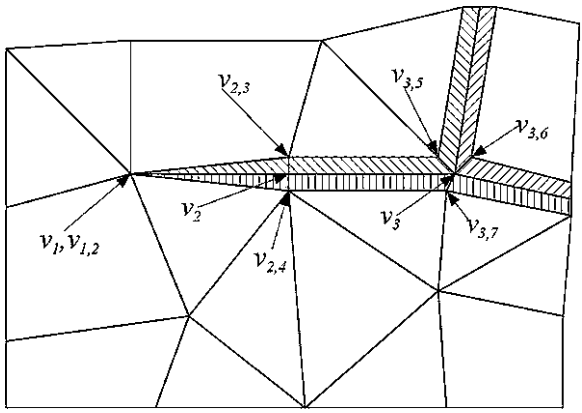

Fig. 5 Topological scheme of the degenerated elements and additional vertices in the fracture

the corners of side $\mathfrak{s}$. Let $B_{j_1}, \ldots, B_{j_d}$ be the subsets for which $B_{j_l} \cap conv[\mathfrak{e}] \neq \emptyset$, $p(v_{i_l}) \subset \overline{B_{j_l}}$, $l = 1, \ldots, d$ hold. Then, we construct a degenerated element from the vertices v_{i_l} and the newly inserted vertices $v_{i_l j_l}$, $l = 1, \ldots, d$. Let $\mathscr{E}^*$ be the set that contains all those new degenerated elements.

Finally we have to reconnect the fracture neighboring elements so that they use the new vertices. Let $\mathscr{E}^{\mathscr{N}} := \{\mathfrak{e} \in \mathscr{E} | \exists v \in \mathscr{V}_{\mathscr{S}}, v \in \mathfrak{e}\}$ be the set of all elements that share a vertex with the fracture. We create new elements $\mathfrak{e}'$ by replacing each vertex $v_i \in \mathscr{V}, v_i \in \mathfrak{e}, v_i \in \mathscr{V}_{\mathscr{S}}$ with the associated vertex $v_{i,j} \in \mathscr{V}^*$, where $p(v_i) \in \overline{B_j}$ and $conv(\mathfrak{e}) \cap B_j \neq \emptyset$. Let $\mathscr{E}'$ be the set that contains those new elements $\mathfrak{e}'$.

By merging and reordering the vertices in $\mathscr{V}$ and $\mathscr{V}^*$ and by using the elements from $\mathscr{E}$ and $\mathscr{E}'$, we obtain the sets $\Omega_h := \{p(v) \in \Omega | v \in \mathscr{V} \cup \mathscr{V}^*\}$ and $\mathrm{T}_\Omega := \{conv(\mathfrak{e}) \subset \Omega | \mathfrak{e} \in \mathscr{E} \cup \mathscr{E}' \backslash \mathscr{E}^{\mathscr{N}}\}$ as introduced in Sect. 4.

To keep the special structure of the grid in the fracture during the creation of the grid hierarchy, anisotropic refinement rules must be used for the degenerated elements. Furthermore, the degenerated elements adjacent over their non-degenerated sides should be refined simultaneously. This maintains the two-layer topology of the grid in the fracture.

The created degenerated elements not only allow us to use multiple degrees of freedom at one position, they also help in associating the different sides of the fracture with the adjacent media. Technically, assembling the defect and the stiffness matrix of the discretization can be implemented as a cycle over all the elements including the degenerated ones. When assembling the contribution of e.g. quadrilateral $[v_3, v_2, v_{2,4}, v_{3,7}]$ in Fig. 5, we compute a part of the local matrix for (66)–(67) for the segment $[x_{102}, x_{103}]$ (cf. Fig. 4). This part consists of (a) the integrals of $\hat{Q}_{fn}^{(k)}$ and $\hat{P}_{fn}^{(k)}$ for only one k such that $\mathbf{n}^{(k)}$ is the inner normal for the adjacent triangle and (b) the terms with the time derivative and the integrals over σ_{ij}^e multiplied by $\frac{1}{2}$. As soon as the contribution of the degenerated element on the opposite side of the fracture is assembled, the terms (a) with the second k as well as the same value of terms (b) are added to the local matrix of $[x_{102}, x_{103}]$ (so that

the factors $\frac{1}{2}$ sum up to unity). Thus we avoid distinguishing between the sides of the fractures.

5 Verification by Numerical Experiments

In this section we present numerical results for both the d- and the $(d-1)$-dimensional model for salinity-driven flow. In the $(d-1)$-dimensional model, the "real" fracture (i.e. a d-dimensional subdomain) is replaced by a $(d-1)$-dimensional geometric object. The problem of salinity-driven flow in the whole region of observation is formulated by using (47) and (48) with (49), (50) in the fracture, and (51)–(54) in the embedding medium. The interface conditions are expressed by (55)–(56).

In order to validate these results, we also perform simulations with the d-dimensional fracture (cf. [29, 30]). In this case, we solve (1) and (2) with (4) and (5), with the appropriate coefficients, both in the fracture and in the embedding medium, and we use the interface conditions (9)–(11).

The results of these two approaches are compared and agree until the fracture width exceeds a certain value. When the fracture width is bigger than this value, the fracture becomes too thick for the averaging procedure to give reliable results. However, below this value, the results obtained by the two approaches seem to be in satisfactory agreement.

Simulations were performed using the software tool d^3f [14], which is based on the simulation software package *UG* [3, 32] and provides the discretization for density-driven flow for the d- and the $(d-1)$-dimensional model [22].

5.1 Henry's Problem with Fractures

We consider a modified version of the classic seawater intrusion problem by Henry [25] where the domain, a rectangle $2 \times 1\ \mathrm{m}^2$, features a fracture. Boundary conditions can be found in Fig. 6, where the constant flux at the inland side is $q = -3.3 \times 10^{-5}\ \mathrm{ms}^{-1}$ according to [40]. The parameters used for computations are listed in Table 1.

The main results of Henry's problem in the absence of fractures were summarized, for example, in [11]. In the presence of fractures, vortices are also generated by the discontinuity of the permeability field in the domain. Both the flow and the profile of the mass fraction are strongly affected, for fixed values of physical parameters, by the geometrical properties and the location of the fractures. For the fracture we try two different positions:

1. *Fracture* ($\varepsilon = 3 \times 10^{-3}\ m$) *with endpoints at* $(x, z) = (1\ m, -0.875\ m)$ and $(2\ m, -0.875\ m)$ (cf. Fig. 7): The fundamental result is that the velocity in the fracture produces a deflection of the isolines of the mass fraction, which is

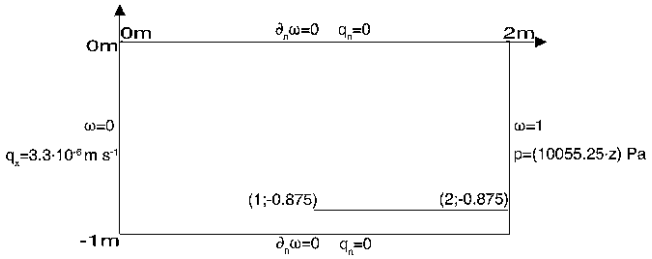

Fig. 6 Geometry and boundary conditions for the modified Henry problem featuring a fracture

maximal at the right end of the fracture (sea side). The magnitude and the direction of the velocity in the fracture (from left to right) hinders the spreading of the brine in the fracture. This happens because of the strong permeability contrast between the fracture and the medium. In [22] was observed that variations of the slope of the fracture do not change the essence of the described phenomenology.

2. *Fracture* ($\varepsilon = 3 \times 10^{-3}$ *m*) *with endpoints at* (x, z) = (1 *m*,−0.125 *m*) and (2 *m*,−0.125 *m*) (cf. Fig. 8): The velocity in the fracture points from right to left. This is a consequence of density-driven flow and is independent on the presence of the fracture. However, the higher permeability of the fracture enhances the magnitude of convection. This results into a marked spreading of the brine. A comparison with Fig. 7 shows that this result strongly depends on the location of the fracture and the higher brine concentration in the lower part of the domain. In this experiment we also observed an inversion of the direction of velocity near the left end of the fracture. At this point fresh water meets brine and a "vortex" is generated.

From the d-dimensional simulation, we further learn that for increasing fracture width there are also phenomena taking place inside the fractures. For a fracture of width $\varepsilon = 24 \times 10^{-3}$ m laying at $z = -0.875$ m (cf. Fig. 9a) the major effect is given by the production of vortices in the fracture. Indeed, it can be observed that velocity is directed from right to left in the lower part of the fracture and from left to right in the upper part. We believe that this result follows from the fact that the fracture is thick enough to develop the density contrast necessary for the rotation of velocity. To punctuate this observation, we also show the vorticity (cf. Fig. 9b), in two dimensions given by $\nabla \times \mathbf{q} = \left(\frac{\partial q_x}{\partial z} - \frac{\partial q_z}{\partial x}\right)\mathbf{e}_y$. These effects are not reproduced by the $(d-1)$-dimensional simulation.

For the validation of the proposed model we compare simulation results of the $(d-1)$-dimensional formulation with those derived by the d-dimensional simulation. In the d-dimensional simulation we consider Eqs. (1) and (2) which provide resulting values for mass fraction ω, whereas in the $(d-1)$-dimensional

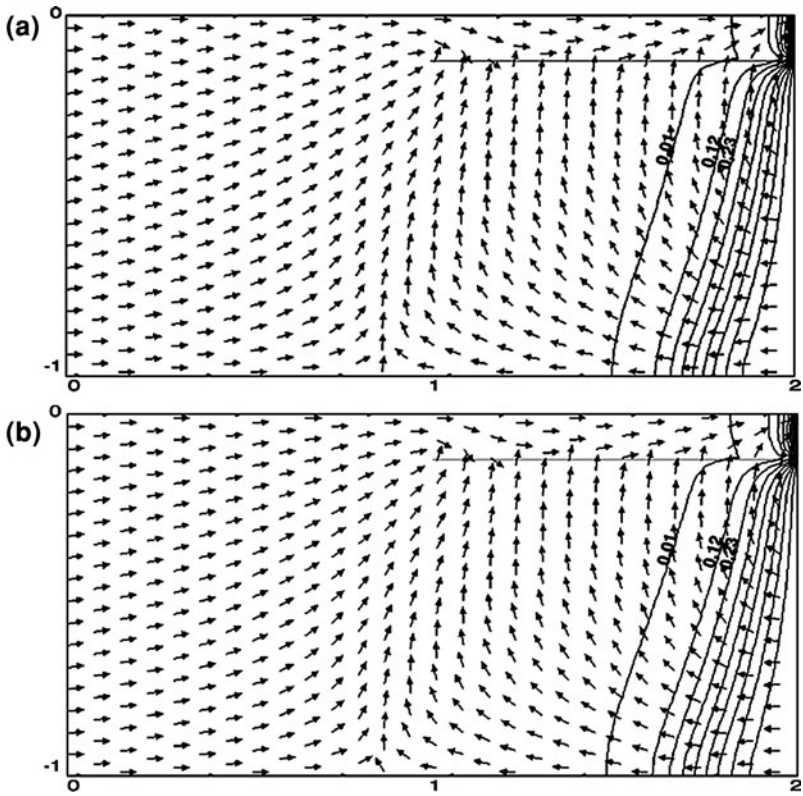

Fig. 7 Isolines of the mass fraction (corresponding to $\omega_0 = 0.01$ and $\omega_i = \omega_0 + i \cdot 0.11$, $i = 1$, …, 9) and velocity directions of the **a** d- and **b** $(d-1)$-dimensional simulation of Henry's problem with a fracture of width $\varepsilon = 3 \times 10^{-3}$ m at position $z = -0.125$ m at time $t = 5$ min

formulation, (47) and (48), the concentration c is provided. Therefore, we convert the result by using the inverse formula

$$c(\omega) = \frac{\rho^{pW}\rho^{pB}\omega}{\rho^{pB} + (\rho^{pW} - \rho^{pB})\omega} \tag{71}$$

and we average along the fracture width to obtain a value comparable to the one gained by the $(d-1)$-dimensional formulation.

Simulations were performed with about 6×10^4 degrees of freedom and the timestep was chosen $\tau^n = 15$ s. In the d-dimensional simulation fracture width was resolved by 8 layers of elements inside the fracture.

We first compare the solutions of the two simulations at the same time by providing plots of them (Figs. 7 and 8). By comparing the plots of the $(d-1)$- with the d-dimensional results, we observe that in both cases the concentration isolines and the velocity directions are of good resemblance.

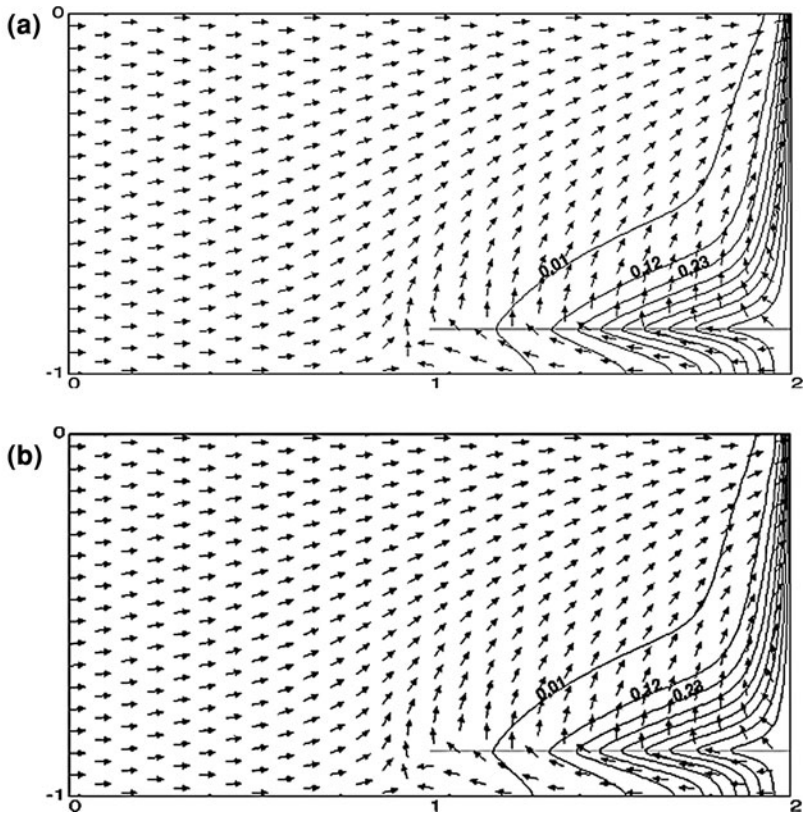

Fig. 8 Isolines of the mass fraction (corresponding to $\omega_0 = 0.01$ and $\omega_i = \omega_0 + i \cdot 0.11$, $i = 1$, …, 9) and velocity directions of the **a** d- and **b** $(d-1)$-dimensional simulation of Henry's problem with a fracture of width $\varepsilon = 3 \times 10^{-3}$ m at position $z = -0.875$ m at time $t = 5$ min

For a more quantitative comparison, we fix points in the fracture and compare the values for concentration and pressure at these points for varying time. By defining the volume fraction $\varphi_f := c_f/\rho^{pB}$, we get a value that describes a non-dimensional concentration. We compare the values for φ_f (and p) and watch the absolute error between resulting non-dimensional concentrations $E(c_f/\rho^{pB}) = E(\varphi_f) = |\langle \varphi_f^{full} \rangle - \overline{\varphi}_f|$ (and resulting pressures $E(p) = |\langle p_f^{full} \rangle - \overline{p}_f|$) of the two simulations.

We observe a very good consistency between the d- and the $(d-1)$-dimensional simulations. For the non-dimensional concentration the absolute error is found to be $E(c_f/\rho^{pB}) < 3.8 \times 10^{-3}$ (cf. Fig. 10a) and for the averaged pressure (Fig. 11a) the absolute error is $E(p) < 2.9 \times 10^{-2}$. This good consistency is also the case for other points in the fracture, e.g. at $x = 1.75$ m it is $E(c_f/\rho^{pB}) < 6.7 \times 10^{-3}$.

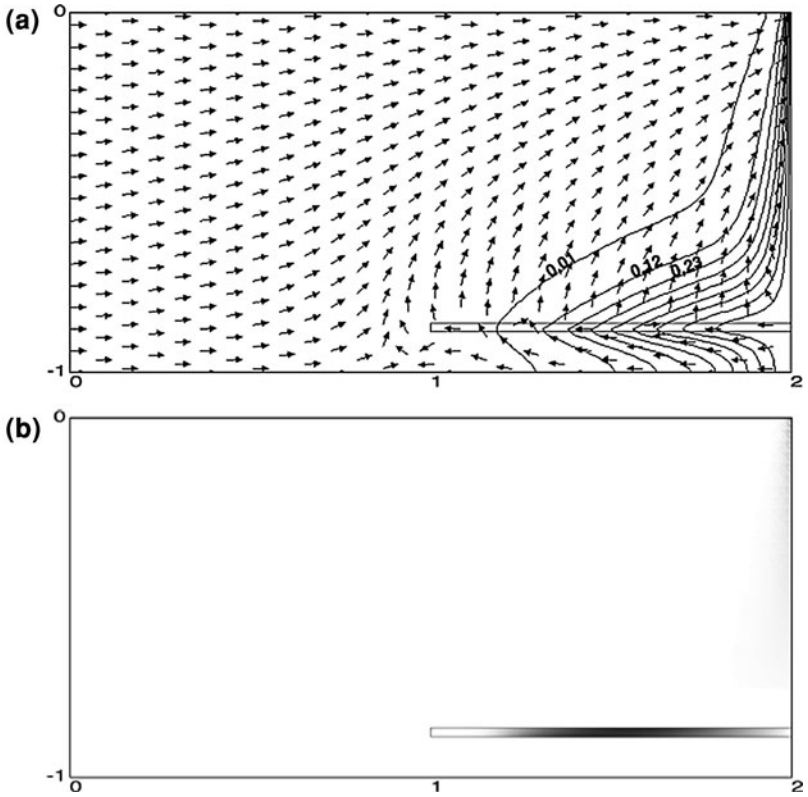

Fig. 9 Henry's problem with a fracture of width $\varepsilon = 24 \times 10^{-3}$ m at positions $z = -0.875$ m at time $t = 5$ min: **a** Isolines of the mass fraction (corresponding to $\omega_0 = 0.01$ and $\omega_i = \omega_0 + i \,.\, 0.11$, $i = 1, \ldots, 9$) and velocity directions. **b** Vorticity $\nabla \times \mathbf{q}$

Though, in [22] it was observed that for fractures with increasing width the $(d - 1)$-dimensional simulation ceases to give reliable results.

As our model yields not only averaged values inside the fracture, but also values at the interfaces between fracture and medium, it is worthwile to compare these values as well. Therefore, we compare the jumps $\left(\varphi_f^{(2)} - \varphi_f^{(1)}\right)$ (and $\left(p_f^{(2)} - p_f^{(1)}\right)$) between non-dimensional concentrations (and pressures) at upper and lower interfaces of fracture and medium and watch the absolute error of the jumps given by the two simulations $E\left(\varphi_f^{(2)} - \varphi_f^{(1)}\right) = \left|\left(\varphi_f^{(2)} - \varphi_f^{(1)}\right)^{full} - \left(\varphi_f^{(2)} - \varphi_f^{(1)}\right)^{low}\right|$ (and $E\left(p_f^{(2)} - p_f^{(1)}\right) = \left|\left(p_f^{(2)} - p_f^{(1)}\right)^{full} - \left(p_f^{(2)} - p_f^{(1)}\right)^{low}\right|$).

For the jumps of the pressure (Fig. 11b) the two simulations are in good consistency. The jumps of the non-dimensional concentration are in satisfactory agreement, but do not yield results as good as the others (Fig. 10b). Even though,

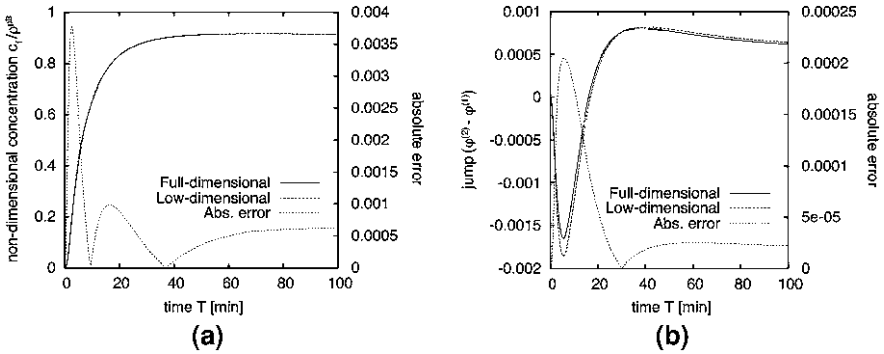

Fig. 10 Comparison between d- and $(d-1)$-dimensional simulations at $x = 1.5$ m for a fracture of width $\varepsilon = 3 \times 10^{-3}$ m at position $z = -0.875$ m (cf. Fig. 8): **a** non-dimensional concentrations c_f/ρ^{pB} in the fracture and absolute error $E(c_f/\rho^{pB})$. **b** Jumps of the nondimensional concentration $\left(\varphi_f^{(2)} - \varphi_f^{(1)}\right)$ at the fracture interfaces and absolute error $E\left(\varphi_f^{(2)} - \varphi_f^{(1)}\right)$

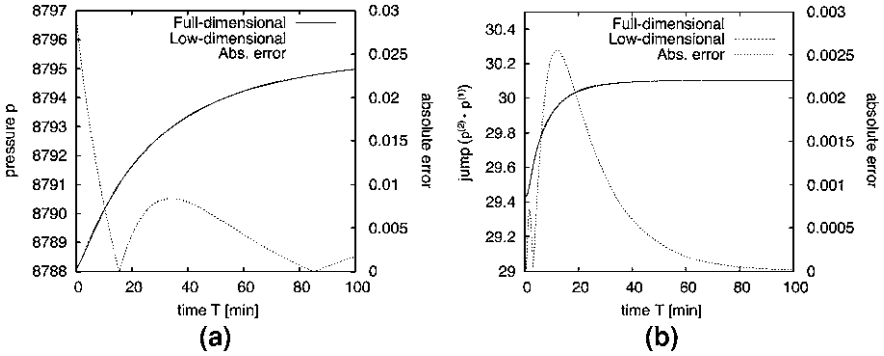

Fig. 11 Comparison between d- and $(d-1)$-dimensional simulations at $x = 1.5$ m for a fracture of width $\varepsilon = 3 \times 10^{-3}$ m at position $z = -0.875$ m (cf. Fig. 8): **a** pressure p_f in the fracture and absolute error $E(p_f)$. **b** Jumps of the pressure $\left(p_f^{(2)} - p_f^{(1)}\right)$ at the fracture interfaces and absolute error $E\left(p_f^{(2)} - p_f^{(1)}\right)$

the averaged concentration has only a very small error, the absolute error of the jumps is only $E(\varphi_f^{(2)} - \varphi_f^{(1)}) < 2.1 \times 10^{-4}$. We observed that this is getting a lot worse when increasing the fracture width, e.g. for a fracture of width $\varepsilon = 24 \times 10^{-3}$ m (cf. Fig. 9a) we get a relative error of nearly 100%. Moreover, in this case not only the error is really big, but we observed that the behaviour at the beginning is different. Whereas in the d-dimensional case the jump $\left(\varphi_f^{(2)} - \varphi_f^{(1)}\right) > 0$, it is $\left(\varphi_f^{(2)} - \varphi_f^{(1)}\right) < 0$ in the $(d-1)$-dimensional case. Therefore, for fractures of this width and at this geometric position, we already

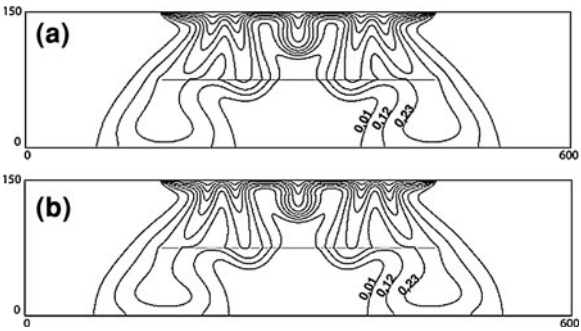

Fig. 12 Isolines of the mass fraction (corresponding to $\omega_0 = 0.01$ and $\omega_i = \omega_0 + i \cdot 0.11$, $i = 1, \ldots, 9$) of the **a** d- and **b** $(d-1)$-dimensional simulation of Elder's problem with a fracture of width $\varepsilon = 1 \times 10^{-1}$ m at position $z = 75$ m at time $t = 5$ a

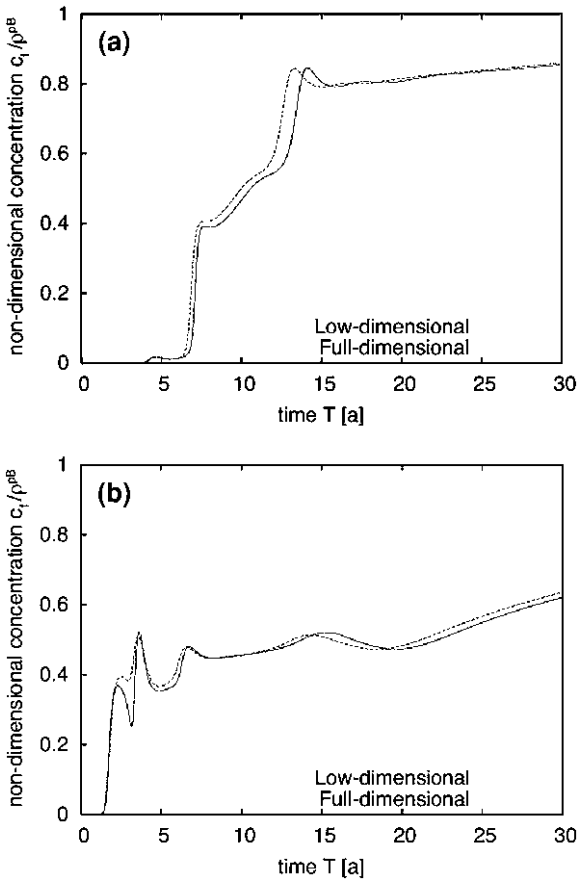

Fig. 13 Comparison of non-dimensional concentrations c_f/ρ^{pB} in the fracture between d- and $(d-1)$-dimensional simulations at **a** $x = 300$ m and **b** $x = 440$ for a fracture of width $\varepsilon = 1 \times 10^{-1}$ m at position $z = 75$ m (cf. Fig. 12)

have a problem in our model while calculating $q_{fn}^{(2)} + q_{fn}^{(1)}$. Though, for smaller fracture widths the jumps of the d- and the $(d-1)$-dimensional simulations are in good consistency.

5.2 Elder's Problem with Fractures

We consider a modified version of the Elder problem [12, 13] where the domain, a rectangle 600×150 m^2, features a fracture (cf. Fig. 2). The original thermally driven flow problem set up by Elder has been reformulated for salinity-driven flow by [43], among others. Here the density differences are due to heavy brine. Boundary conditions can be found in Fig. 2, with the only exception that temperature Θ is constant for this reformulated problem. The parameters used for computations are listed in Table 1.

By comparing the plots of the $(d-1)$- with the d-dimensional results (cf. Fig. 12), we observe that in both cases the concentration isolines and the velocity directions in the porous medium enclosing the fractures are not completely superposable, but of acceptable resemblance. It is well known that the Elder problem has a history for its multiple solutions which are associated, e.g. with the number of fingers at its stationary solution (cf. e.g. [27, 28]). Therefore, by keeping in mind that the computational grids for the $(d-1)$- and the d-dimensional simulations are not the same, this result is satisfactory. By comparing the non-dimensional concentrations c_f/ρ^{pB} at different points in the fracture (cf. Fig. 13), we observe that the main behaviour, including all peaks, is resembled by the $(d-1)$-dimensional simulation. Though, a little shift between the two results can be observed. We find this very interesting and are going to investigate further, whether this comes from the instability of the Elder problem or maybe from our model.

Acknowledgements This work was supported by the Goethe-Universität Frankfurt am Main, Germany, the German Ministry for Economy and Technology (Bundesministerium für, Wirtschaft und Technologie), contract 02E10326, and a fellowship from HIC4FAIR in the LOEWE program of the state Hessen.

References

1. Angot, P., Boyer, F., Hubert, F.: Asymptotic and numerical modelling of flow in fractured porous media. ESAIM: M2AN. Math. Model. Numer. Anal. **43**, 239–275 (2009)
2. Barrett, R., Berry, M., Chan, T.F., Demmel, J., Donato, J., Dongarra, J., Eijkhout, V., Pozo, R., Romine, C., van der Vorst, H.: Templates for the Solution of Linear Systems: Building Blocks for Iterative Methods. SIAM, Philadelphia (1993)
3. Bastian, P., Birken, K., Johannsen, K., Lang, S., Reichenberger, V., Wieners, C., Wittum, G., Wrobel, C.: Parallel solution of partial differential equations with adaptive multigrid methods

on unstructured grids. In: Jäger, W., Krause, E. (eds.) High Performance Computing in Science, Engineering, pp. 506–519. Springer, Berlin (2000)
4. Bear, J.: Dynamics of Fluid in Porous Media. Dover Publications, Inc, New York (1972)
5. Bear, J.: Hydraulics of Groundwater. Dover Publications, Inc., Mineola (1979)
6. Bear, J.: On the aquifer's integrated balance equations. Adv. Water Resour. **1**(1), 15–23 (1977)
7. Bear, J., Bachmat, Y.: Introduction to Modeling of Transport Phenomena in Porous Media. Kluwer Academic Publishers, Dordrecht (1990)
8. Bear, J., Tsang, C.-F., deMarsily, G.: Flow and Contaminant Transport in Fractured Rocks. Academic, New York (1993)
9. Cai, Z.: On the finite volume element method. Numer. Math. **58**(1), 713–735 (1990)
10. Chew, L.P.: Constrained delaunay triangulation. Algorithmica **4**(1), 97–108 (1989)
11. Diersch, H.-J.-G., Kolditz, O.: Variable-density flow and transport in porous media: approaches and challenges. Wasy Software FEFLOW Finite Element Subsurface flow and Transport Simulation System. Wasy GmbH (2005)
12. Elder, J.W.: Steady free convection in a porous medium heated from below. J. Fluid Mech. **27**, 29–48 (1967)
13. Elder, J.W.: Transient convection in a porous medium. J. Fluid Mech. **27**, 609–623 (1967)
14. Fein, E.: Ein Programmpaket zur Modellierung von Dichteströmungen, p. 139. GRS, Braunschweig (1999)
15. Frolkovič, P.: Consistent velocity approximation for density driven flow and transport. In: Van Keer, R., et al. (eds.) Advanced Computational Methods in Engineering, Part 2: Contributed papers, pp. 603–611. Shaker Publishing, Maastricht (1998)
16. Frolkovič, P.: Maximum principle and local mass balance for numerical solutions of transport equation coupled with variable density flow. Acta Mathematica Universitatis Comenianae **1**(68), 137–157 (1998)
17. Frolkovič, P., Knabner, P.: Consistent velocity approximations in finite element or volume discretizations of density driven flow. In: Aldama, A.A., et al. (eds.) Computational Methods in Water Resources XI, pp. 93–100. Computational Mechanics Publication, Southhampten (1996)
18. Graf, T., Therrier, R.: Stable-unstable flow of geothermal fluids in fractured rock. Geofluids **9**, 138–152 (2009)
19. Graf, T., Therrier, R.: Variable-density groundwater flow and solute transport in porous media containing nonuniform discrete fractures. Adv. Water Resour. **28**, 1351–1367 (2005)
20. Grillo, A., Lampe, M., Wittum, G.: Modelling and simulation of temperature-density-driven flow and thermodiffusion in porous media. J. Porous Media **14**(8), 671–690 (2011)
21. Grillo, A., Lampe, M., Wittum, G.: Three-dimensional simulation of the thermohaline-driven buoyancy of a brine parcel. Comput. Visual. Sci. **13**(6), 287–297 (2010)
22. Grillo, A., Logashenko, D., Stichel, S., Wittum, G.: Simulation of density-driven flow in fractured porous media. Adv. Water Resour. **33**(12), 1494–1507 (2010)
23. Grisak, G.E., Pickens, J.F.: An analytic solution for solute transport through fractured media with matrix diffusion. J. Hydrol. **52**, 47–57 (1981)
24. Grisak, G.E., Pickens, J.F.: Solute transport through fractured media. Water Resour. Res. **16**(4), 719–730 (1980)
25. Henry, H.R.: Effects of dispersion on salt encroachment in coastal aquifers. Sea water in coastal aquifers, pp. 70–84. USGS Water Supply Paper 1613-c
26. Holstad, A.: Temperature-driven flow in porous media using a Mixed Finite Element Method and Finite Volume Method. Adv. Water Resour. **24**(8), 843–862 (2001)
27. Johannsen, K.: On the validity of the Boussinesq approximation for the Elder problem. Comput. Geosci. **7**(3), 169–182 (2003)
28. Johannsen, K.: The Elder problem—bifurcations and steady state solutions. In: Hassanizadeh, S.M., et al. (eds.), Computational Methods in Water Resources, pp. 485–492 (2002)

29. Johannsen, K., Kinzelbach, W., Oswald, S., Wittum, G.: The saltpool benchmark problem—numerical simulation of saltwater upconing in a porous medium. Adv. Water Resour. **25**(3), 335–348 (2002)
30. Johannsen, K., Oswald, S., Held, R., Kinzelbach, W.: Numerical simulation of three-dimensional saltwater-freshwater fingering instabilities observed in a porous medium. Adv. Water Resour. **29**(11), 1690–1704 (2006)
31. Karimian, S.M., Schneider, G.E.: Pressure-based control-volume finite element method for flow at all speeds. AIAA J. **33**(9), 1611–1618 (1995)
32. Lang, S., Wittum, G.: Large-scale density-driven flow simulations using parallel unstructured Grid adaptation and local multigrid methods. Concurrency Computat.: Pract. Exper. **17**, 1415–1440 (2005)
33. Malkovsky, V.I., Pek, A.A.: Conditions for the onset of thermal convection of a homogeneous fluid in a vertical fault. Petrology **5**, 381–387 (1997)
34. Martinez-Landa, L., Carrera, J.: A methodology to interpret cross-hole tests in a granite block. J. Hydrol. **325**(1–4), 222–240 (2006)
35. Murphy, H.D.: Convective instabilities in vertical fractures and faults. J. Geophys. Res. **84**, 6121–6130 (1979)
36. Oldenburg, C.M., Pruess, K.: Layered thermohaline convection in hypersaline geothermal systems. Transp. Porous Med. **33**, 29–63 (1998)
37. Sharp Jr., J.M., Shi, M.: Heterogeneity effects on possible salinity-driven free convection in low-permeability strata. Geofluids **34**, 263–274 (2009)
38. Shewchuk, J.R.: Constrained Delaunay Tetrahedralizations and Provably Good Boundary Recovery. Eleventh International Meshing Roundtable, pp. 193–204. Sandia National Laboratories, Ithaca (2002)
39. Shikaze, S.G., Sudicky, E.A., Schwartz, F.W.: Density-dependent solute transport in discretely-fractured geologic media: is prediction possible? J. Contam. Hydrol. **34**, 273–291 (1998)
40. Simpson, M.J., Clement, T.P.: Improving the worthiness of the Henry problem as a benchmark for density-dependent groundwater flow models. Water. Resour. Res. **40** (2004)
41. Sorek, S., Borisov, V., Yakirevich, A.: A two-dimensional areal model for density dependent flow regime. Trans. Porous Med. **43**, 87–105 (2001)
42. Tang, D.H., Frind, E.O., Sudicky, E.A.: Contaminant transport in fractured porous media: analytical solution for a single fracture. Water Resour. Res. **17**(3), 555–564 (1981)
43. Voss, C.I., Souza, W.R.: Variable density flow and solute transport simulation of regional aquifers containing a narrow freshwater-saltwater transition zone. Water Resour. Res. **26**, 2097–2106 (1987)

Lungs as a Natural Porous Media: Architecture, Airflow Characteristics and Transport of Suspended Particles

António F. Miguel

Abstract Lungs are natural porous structures that are unique, challenging, and high-value media to study. There are multiple drivers to obtain an improved understanding of their architecture and function: to increase high-value information and insights that can be applied in healthcare, to devise control strategies that will limit some hazards effects, and to expand boundaries of what is known that can be applied to produce new (improved) materials. This chapter covers three major topics: shape and structure of lungs, airflow characteristics and the interaction of suspension of particles with the respiratory tract. It is focused on the biological and physical mechanisms involved, in the hope that this will allow an overview of the science related to the respiratory tract.

1 Natural Porous Media

Porous media are ubiquitous in nature, either in inanimate and animate flow systems. Sand, sandstone, limestone, rye bread, wood but also the human lung, kidneys, liver and bone are examples of porous media. All these systems are made of a solid matrix with its void filled with fluid. A review of porous materials is given in [1, 2] and the physical properties of porous media are reviewed by [2, 3].

In contrast to compact materials, porous media have a very large surface area. In truth, they are composed almost entirely of "surface". This observation explains why porous media are ubiquitous in animate systems, where surface phenomena are of crucial importance. In fact, flows in porous materials have important

A. F. Miguel (✉)
Department of Physics and CGE, University of Évora,
Rua Romão Ramalho 59, 7000-671 Évora, Portugal
e-mail: afm@uevora.pt

J. M. P. Q. Delgado (ed.), *Heat and Mass Transfer in Porous Media*,
Advanced Structured Materials 13, DOI: 10.1007/978-3-642-21966-5_5,

biological and therapeutic issues, because life is flow. New aspects in therapy, diagnostic, analysis and treatment must involve an exact knowledge of these media. Human lungs fully exemplify these features.

The proper functioning of respiratory tract is crucial to survival. Lung morphology is determined by tree major constraints [3]: limited volume allocated to the structure, a need to protect the delicate gas exchange airways, and the large surface that is needed for air-blood oxygen and carbon dioxide exchange. Lungs, enclosed in a cage bounded by the diaphragm and the chest wall, have a surface area larger than the size of a tennis court [4, 5]. The evolutionary solution to these constraints seems to be a branching network of cartilage and smooth muscle-lined tubes that constitutes the flow distribution systems, which allows at each breath oxygen and carbon dioxide to be exchanged at the lung surface [2].

The entire lung pathway can be described from the trachea to alveoli—through each successive dichotomous branching pattern, the airways become smaller, but because of growth in the number of airways, the total cross-section and surface increase rapidly—but also in the reverse direction, from small to large (i.e., alveoli to trachea), from the tips of the smallest tree branches to the trunk [2]. In this direction, the branches coalesce and instead of bifurcations, we speak of pairings.

The lung can be divided into conducting airways and respiratory zone depending upon the presence of gas exchange [2, 4, 5]. The conducting airways (also referred to as the tracheobronchial tree) consist of a set of ducts that delivers gases to and collects them from the respiratory zone. The walls of conducting airways are lined by ciliated cells, with an overlying layer of mucous. The cilia help to impel this mucous blanket from the lower respiratory tract to the throat (oropharynx) and serve an important role in removal of particulate matter. Therefore, this region performs functions of humidification and temperature regulation (conditioning the air), but also particles and macrophages removal and, antibacterial and immunological defense. The daily clearance is about 100 ml [5]. At respiratory zone the gas exchange takes place and, unlike the conduction airways, this volume is not covered by a protective mucus layer. This region contains membranous outpouchings called alveoli that are responsible for gas exchange. The fine structure of the alveolar wall (less than 1 μm thick) and the large specific surface area (greater than 200 cm^2/cm^3 airspace volume) are well suited to gas exchange (O_2 and CO_2) but also to the absorption of air pollutants. It is estimated that an adult has approximately 300 million alveoli with a surface area for gas exchange of about 75 m^2, which are perfused by more than 2,000 km of capillaries [2].

2 Human Lung Structure and Function

Our ability to breathe and trade oxygen for carbon dioxide is one of the roots that support life. Lungs are sophisticated systems for channeling air into the blood vessels but also for filtering out particles (such as dust, soot, mold, fungi, bacteria and viruses) that can be deposited in the our airways.

2.1 Lung Anatomy

Lungs are tree-shaped structures that end with clusters of air sacs called alveoli. Each air sac is surrounded by a dense network of tiny capillaries that allows the blood to pick up oxygen and release carbon dioxide into the alveoli.

The tracheobronchial tree (or conducting airways) has what is known as a dichotomous branching pattern (i.e., each segment (parent) gives rise to two daughter branches). This pattern seems to be asymmetric [6] being one of the daughter branches (the major daughter) less than 30% larger than the minor daughter. Branching transport networks in biology are constructed of vessels via a bifurcating structure, where the parent and daughter vessels, of diameters D_0, D_1, and D_2, respectively, satisfy a bifurcation design relationship $D_0^a = D_1^a + D_2^a$. If a symmetrical dichotomous system is considered, the geometric ration between the diameters of daughter and parent vessels is 1.26 ($\sim 2^{1/3}$). This relationship is usually termed as Murray or Hess–Murray law [7, 8]. In the literature, this model has been justified based on minimum principles: power [9, 10], resistance [11], volume [12], drag [13], etc.

Structural models of the branching vessel systems of lung are useful for studying the correlation between structure and function. In the 1960s, Weibel [4] proposed structural airway models that include airway dimensions and connectivity. These morphometric models are based on sets of data obtained primarily from measurements of airways dimensions by using corrosion cast techniques. Weibel used a plastic airways cast and measured the lengths, diameters, and branching angles. These measurements were used to build two morphometric models of the human lung: Weibel lung model A, which emphasized the regular features of airways and their patterns, and Weibel lung model B, which attempted to take into account irregularities encountered in the measurements. Later, Horsfield et al. [14] described a morphometric model based on data obtained from measurements of a resin cast of a normal human bronchial tree. Their model includes an asymmetric branching. Koblinger and Hofmann [15] also developed a morphometric model based on statistical relations between geometrical parameters of a given parent airways and those of the two branching daughter airways. The model presents a significant variability of airways lengths, diameters and numbers of airways generations along different pathways. The lung airways and other branching transport networks are fractal-like structures. Based on this, Mandelbrot [16] suggested that the structure of tree is the outcome of a self-similar, recursive growth development from bud to tree.

Although important, these studies did not explain, for example, why the lung is a tree-shaped network or the respiratory tree is composed by 23 levels of bifurcation. According to the second law of thermodynamics, flows through resistances

cause destruction of the useful portion of energy (exergy[1]) and irreversibility. In this sense, perfection means flows that travel without resistances. Therefore, the perfect lung geometry would be very large and without a network of small vessels that destroys exergy by fluid friction. Are lungs imperfect for their function?

2.2 Constructal View of Flow Architecture of Lung

During the last decade there is a renewed interest in the explanation of design of biological systems [7, 8, 18, 19]. Adrian Bejan is at the origin of the constructal paradigm, which had its start in 1996 [20]. Before, no straightforward connection had been envisaged in order to bring together configuration and dynamics, in describing the evolution of the systems in space and in time. "Flow" represents the movement of one entity relative to another (the background). To describe a flow, we need to speak of what the flow carries (fluid, heat, mass), how much it carries (mass flow rate, heat current, species flow rate), and "where" the stream is located in the available space. The "where" is the configuration—the design [7, 18]. Therefore, the occurrence of configuration in nature is a physics phenomenon, and the constructal theory is about the physics principle from which configuration can be deduced.

The constructal theory begins the conceptual design (configuration) with a clean sheet, and the "designer" is invited to recognize and consider all the possible and competing configurations. It is supported on the following law—the constructal law: "For a finite-size system to persist in time (to live), it must evolve in such a way that it provides easier access to the imposed (global) currents that flow through it" [7]. This law states that there is a time arrow "associated with the sequence of flow configurations that constitutes the existence of the system" [18, 21, 22]. Besides, the system shape and structure do not develop by chance but result from the permanent struggle for better performance. Better performance means minimization and balance of the resistances (i.e., imperfection) faced by the various internal and external streams under the existing constraints. The morphim structure is the result of optimal distribution of imperfection.

[1] The idea of available energy dates back to Sadi Carnot (1796–1832) for the specialized case of heat engines. The concept, further developed theoretically by scientists like H. Helmholtz and J. W. Gibbs, has been applied to many kinds of processes, under several different names (available work, information, etc.). Only in second half of last century, a standard definition was formulated and the designation exergy adopted. Exergy is an extensive non-conservative quantity which synthesizes both first and second law of thermodynamics. Exergy is a measure of the ability to do work of a great variety of streams (mass, fluid, heat) that flow through a system [17]. The exergy concept makes possible to compare on a common basis inputs or outputs that are different from the physical point of view, and by accounting for all the exergy streams it makes possible to determine the extent to which the system destroy exergy.

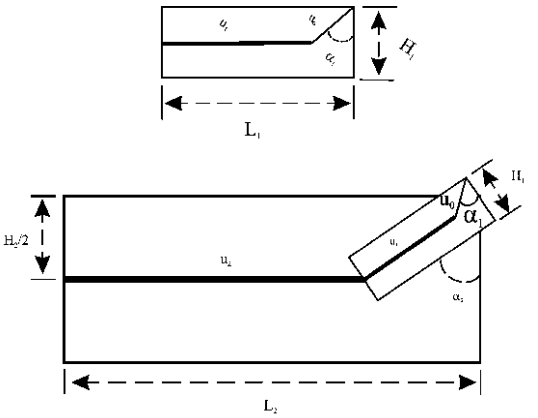

Fig. 1 Rectangular domains with fixed areas A_1 ($=L_1H_1$) and A_2 ($=L_2H_2$) (adapted from [24, 25])

2.2.1 Tree Flow Networks to Connect One Point with Infinity of Points or Vice Versa

Why lungs are shaped the way they are? There are two flow mechanisms to accomplish the purpose of oxygenation and drainage of carbon dioxide: streams (low-resistivity flow) and diffusion (high-resistivity flow). In the limit, lungs could be duct systems or simple single sacs (volume) open to the external air from which the oxygen diffuses to the blood (and carbon dioxide diffuses after being released from the blood). This second possibility is clearly noncompetitive as compared to a duct system: the former has a small access time for duct (stream) flow of order 1 s (characteristics length $\sim$0.5 m and air speed $\sim$0.5 m/s) whereas the latter has an access time for a diffusive process of order 10^4 s (diffusion coefficient $\sim 2 \times 10^{-5}$ m^2/s). According to classical thermodynamics, "bigger is better" because a large element destroys less exergy [23]. A vessel with larger cross-section destroys less exergy by fluid friction and requires less pumping power. But lungs are compact and formed by a network of small (imperfect) ducts which destroys exergy by fluid friction. Why is the lung a network of ducts that ends with alveolar sacs?

The lungs are situated in the thoracic cavity which constitutes a volume constraint, and connects one point (mouth/nose) to infinity of points (alveoli) and vice versa. Consider the case of a flow between one point (source or sink) and an infinity of points (volume, area, line). According to the constructal method, the flow path is constructed as a sequence of steps starting with the smallest building block, the size of which is fixed, and continued in time with larger building blocks (constructs). A simple illustration is the minimization of travel time between a finite size territory (area) and one point or vice versa (Fig. 1).

Elements (fluid elements, travelers, etc.) have access to different fluid flow regimes or locomotion modes, starting at the slowest speed u_0 and proceeding towards ever faster modes ($u_0 < u_1 < u_2 \ldots$). Constructal theory begins with the objective and constraints. The constraint is the size of territory. The purpose is to

obtain a space-filling configuration that minimizes the travel time of the elements. The acquisition of the flow architecture is from small to large. Therefore, the task is to cover this fixed area with a sequence of optimized area elements of increasing sizes. The finite territory is covered in steps of corresponding increasingly larger constructs ($A_1 < A_2 < A_3 \ldots$). Both the shape and the angle between each path are optimized at each stage. This problem was solved by Bejan and Ledezma [24] as following: starting from an elemental rectangular domain with fixed area H_1L_1, one seeks to minimize the travel time from anywhere within that dominium to the exit point at its periphery. There is a slower travel regime at speed u_0 everywhere (this corresponds, for example, to a diffusive flow) and a faster regime at speed u_1 along a centered longitudinal path (i.e., channeled or convective flow). The aspect ratio H_1/L_1 (i.e., the ratio between the width and the length) is optimized to the stated purpose, yielding an optimal configuration ratio and a characteristic travel time t_1 (from the farthest away point in the dominium till its exit point). Therefore,

$$\left(\frac{H_1}{L_1}\right)_{opt} = \frac{2}{f_1}\frac{u_0}{u_1} \qquad \alpha_{1,opt} = \sin^{-1}\left(\frac{u_0}{u_1}\right) \tag{1}$$

with $f_1 = (\cos \alpha_1)^{-1} - (u_0/u_1)\,\mathrm{tg}\,\alpha_1$. Here α_1 is the deviation from the normal for the angle between the slower and the faster paths, and the subscript opt means optimal. Consider next a larger fixed area A_2 and a faster regime at speed u_2 along a centered longitudinal path and, once again, seek to optimize the access from an arbitrary point of A_2 to a common exit point on its periphery. This problem can be addressed by filling or tiling A_2 with optimized A_1 areas, in a manner similar to the foregoing reasoning, the results being very similar apart constant numerical factors of order 1. The number of elements A_1 required to fill A_2 is $A_2/A_1 = 2f_1f_2(u_2/u_0)(1 - u_1^2/(4u_2^2))$, and the optimized configuration for a fixed area A_i ($i \geq 2$) is

$$\left(\frac{H_i}{L_i}\right)_{opt} = \frac{1}{f_i}\frac{u_{i-1}}{u_i} \qquad \alpha_{i,opt} = \sin^{-1}\left(\frac{u_{i-1}}{u_i}\right) \tag{2}$$

with $f_i = (\cos \alpha_i)^{-1} - (u_{i-1}/u_i)\,\mathrm{tg}\,\alpha_i$.

According to Eqs. 1 and 2 the architecture that emerges is a tree (Fig. 2) in which every geometric detail is a result. Is it this configuration a singular result? If the fluid exhibits at least two regimes (for example, diffusion and convection) and the purpose is to connect a finite size territory (volume, area) and one port (or vice versa), the architecture that emerges is still a tree network (details can be obtained in [7, 18]).

In conclusion, if the purposes is to connect the mouth/nose to alveoli and vice versa, and diffusion and convection are available, the best organ is not the one recommended by the thermodynamics—infinitely large [23]. A tree-shaped flow network (huge number of air passages) that ends with alveolar sacs makes the respiratory tract the least imperfect that it can be (i.e., it represents the optimal distribution of resistances). Therefore, lungs exist not because of compactness or complexity but because of maximization of the flow access.

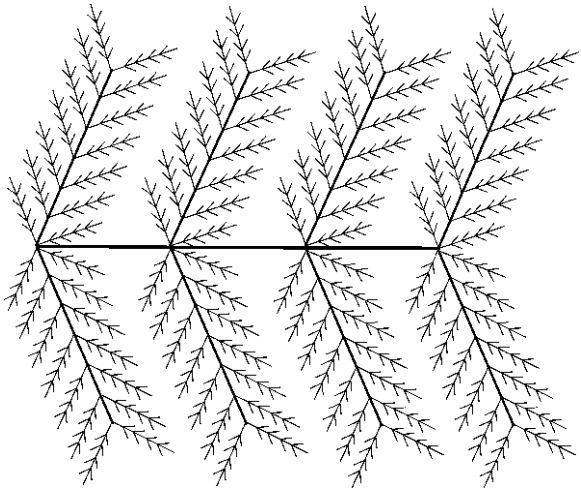

Fig. 2 The constructal law generates every geometric feature of the path (u_0, u_1, …, u_n) that connects one to an infinity of points (and vice versa), and the resulting configuration is a tree-shaped network (adapted from [24])

2.2.2 The Configuration of Dichotomous Branching Ducts

The respiratory tract is a dichotomous branching tree. A large part of the branching vasculature of the mammalian circulatory and respiratory systems obeys Hess–Murray's law, which states that the cube of the radius of a parent vessel equals the sum of the cubes of the radii of the daughters. Bejan et al. [26] also focused on a stream (parent) that branch into tributaries streams in a constrained space. Consider a steady incompressible flow through a y-shaped assembly of ducts depicted in Fig. 3. For simplicity, a one-dimensional fully developed flow is assumed, and pressure losses at each node of bifurcation are neglected.[2] The fluid flow rate, Q, through each vessel can be related to the pressure difference, Δp, as

$$\nu\left(\frac{\lambda Re}{2}\right)\left(\frac{L}{D^2A}\right)Q = \frac{1}{\rho}\Delta p \tag{3}$$

Here ρ is the fluid density, ν is the kinematic fluid viscosity, Re is the Reynolds number (=$QD/\rho\nu A$), and λ is the friction factor. In the laminar region (Hagen–Poiseuille flow)

[2] Wechsatol et al. [27] studied the effect of junction losses on the optimal geometry of bifurcation. They concluded that in case of laminar flow, the junction losses have sizable effects on the optimal diameter ratio at each node of bifurcation only when the dimensionless parameter called svelteness, defined by the ratio between the external and internal length scales, is lower than the square root of 10.

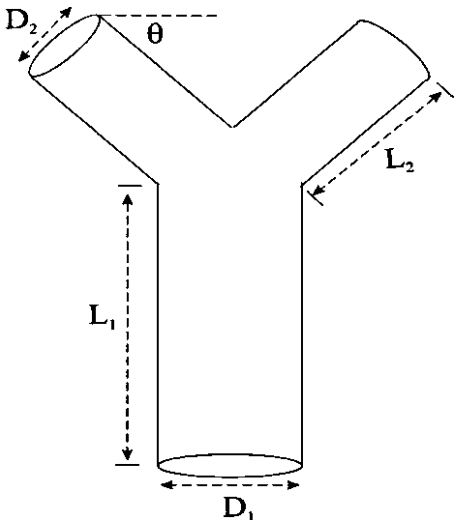

Fig. 3 Dichotomous branching assembly of ducts (adapted from [26])

$$\lambda = \frac{64}{Re} \tag{4}$$

How do we identify the geometry of the system that brings architecture to the highest level of performance? Constructal theory begins with the objective and constraints. In living systems the space occupied by ducts is at a premium. Accordingly is appropriate to consider that the constraints are total volume occupied by the ducts, V, and total space occupied by the planar structure, A [26]

$$V = \frac{\pi}{4}(D_1^2 L_1 + 2D_2^2 L_2) = \text{const.} \tag{5}$$

$$A = 2L_2 \cos\theta (L_1 + L_2 \sin\theta) = \text{const.} \tag{6}$$

where θ is a variable angle (see Fig. 3). The aim is the maximization of the system performance by minimizing the global flow resistance (imperfection) of the fluid stream. Consider that the two tributary ducts are similar. According to Eqs. 3 and 4 the flow resistance is $\Delta p/Q$, and the total resistance of the flow configuration is

$$R = R_1 + \frac{R_2}{2} \tag{7}$$

Here R_1 and R_2 are flow resistance of parent and tributary vessels, respectively. The goal is to minimize the total flow resistance (Eq. 7) subject to constraints (Eqs. 5 and 6). First, D_1/D_2 is optimized and the following expression is obtained [7]

$$\frac{D_1}{D_2} = 2^{1/3} \tag{8}$$

Equation 8 is nothing more than the Hess–Murray law [7, 8]. Minimizing resistance at constant volume subject to the area constraint allocated (Eq. 6), the ratio between parent and tributary duct lengths is

$$\frac{L_1}{L_2} = 2^{1/3} - 2\sin\theta \quad 0 \le \theta \le 39^\circ \tag{9}$$

In the same study, Bejan et al. [28] also obtained the aspect ratios D_1/D_2 and L_1/L_2 for turbulent flow regime.

2.2.3 Branching Levels of the Respiratory Tree

In the previous sections, we saw that ducts connected like the branches of a tree are the best flow access architectures, if the purpose is to connect one point (source or sink) with an infinity of points (volume, area, and line), and the fluid exhibit at least two flow mechanisms to accomplish the purpose. The question is now focused on the branching levels. Direct observations show that the respiratory tree is composed by 23 levels of bifurcation [4, 6]. Why?

The respiratory tract was also accessed via the constructal principle by Reis et al. [28], with its characteristics being the result of this appraisal. Consider that the flow within the tracheobronchial tree is laminar, incompressible and isothermal. As this flow is also adiabatic (i.e., the entropy variation is zero), the generalized Gibbs–Duhem equation yields

$$\Delta\mu = \frac{\Delta p}{\rho} + \Delta\varepsilon \tag{10}$$

where p is the pressure, ε is the kinetic energy per unit mass along the bronchial tree, μ is the chemical potential and ρ is the fluid density. If the gases within the bronchial tree (i.e., oxygen and carbon dioxide) are in equilibrium with the flowing air, then all gases have the same chemical potential and the Hagen–Poiseuille flow, Q, can be expressed as

$$Q = \frac{\pi D^4}{128 \nu L}\Delta\mu \tag{11}$$

where ν is the dynamic viscosity, and D and L are given by Eqs. 8 and 9. The resistance ($\Delta\mu$/Q) of the nth bronchial ducts is

$$r_d = 2^n \frac{128 \nu L_1}{\pi \rho D_1^4} \tag{12}$$

and the resistance in the bifurcation is

$$r_b = 2^{n/3} \frac{Q}{8\pi\rho^2 D_1^4} \tag{13}$$

where L_1 and D_1 are the geometric characteristics of first duct (trachea).

Consider that the variation of chemical potential in the network of ducts is the summation of the chemical potential variation along the duct and in the bifurcation. Taking into account that in nth bronchial bifurcation there are 2^n ducts, the tracheobronchial resistance reads

$$r_{db,n} = \frac{128L_1}{\pi\rho D_1^4}\left[\nu + \frac{2^{-2n/3}Q}{1,024\pi\rho L_1}\right] \tag{14}$$

and, the resistance from trachea ($n = 0$) to $N - 1$ bifurcation levels is

$$r_{db} = \frac{128L_1}{\pi\rho D_1^4}\left[N\nu + \frac{\left(1 - 2^{-2N/3}\right)Q}{\pi\rho L_1}\right] \tag{15}$$

Notice that the second term between brackets, for a normal breathing frequency, is much less than one and can be neglected. The average oxygen flow within the tracheobronchial tree is

$$Q_{ox} = 0.5(\phi_{ox,0} - \phi_{ox})Q = \frac{\Delta\mu}{r_{ox}} \tag{16}$$

where ϕ_{ox} and $\phi_{ox,0}$ are the relative concentration of oxygen in the alveoli and in the outside air.

At the alveolar sacs, there is no equilibrium between the components of air. The chemical potential of carbon dioxide in the tissues is higher than that in the alveolar sacs. On the other hand, the chemical potential of oxygen in the alveolar tissues is lower than in the alveolar air. Therefore, carbon dioxide diffuses from the tissues to alveolar air, while oxygen diffuses in the opposite direction. Assuming Fickian diffusion, the alveolar diffusive resistance reads

$$r_{dif} = 2^{-2N/3}\frac{0.13R_{g,ox}T}{\pi\phi_{ox}\rho L_1 D_{ox}} \tag{17}$$

Here D_{ox} is the diffusivity of oxygen in the air, ϕ_{ox} is the concentration of oxygen in the alveolar air, T is the air temperature and $R_{g,ox}$ is the gas constant for oxygen. After some mathematical manipulation, the total oxygen flow resistance from the external air to alveolar surface (Eqs. 15 and 17) is

$$r_{total} = \frac{256\nu L_1}{\pi\rho D_1^4\left(\phi_{ox,0} - \phi_{ox}\right)}(N + 1) + 2^{-2N/3}\frac{0.13R_{g,ox}T}{\pi\phi_{ox}\rho L_1 D_{0x}} \tag{18}$$

The parameter N represents the number of bifurcations of the tree and is a free parameter that can be optimized. According to the Constructal law, the tracheobronchial tree that persists in time is the one that maximizes the flow access. In other words, the optimal number of bifurcations, N_{opt}, corresponds to the minimum total resistance to oxygen access

$$N_{opt} = 2.164 \ln\left[\frac{0.000235 D_1^4 R_{g,ox} T}{\nu D_{ox} L_1^2}\left(\frac{\phi_{ox,0}}{\phi_{ox}} - 1\right)\right] \tag{19}$$

Data available in the literature indicates that L_1 and D_1 are $\sim$15 and $\sim$1.5 cm, respectively, the oxygen relative concentration at the entrance of trachea, $\phi_{ox,0}$, is $\sim$0.5 when ϕ_{ox} is $\sim$0.1095 [28]. The optimal number of bifurcations can be obtained by assuming a body temperature of 36°C and taking all pertinent values at this temperature. Using these values in Eq. 19 the optimal number of bifurcations of tracheobronchial tree (an integer number) is 23. The calculation made for carbon dioxide transport (the respiratory tree perform oxygenation of the blood but also removal of carbon dioxide), a N_{opt} of 23 is also obtained. These results agree with the observations of Weibel [4] and Horsfield [6]. Therefore, the reason for 23 levels of bifurcation lies in the fact that corresponds to the minimum total resistance to oxygen/carbon dioxide access.

Equation 19 also shows that the optimal number of bifurcations of tracheobronchial tree depends on environmental parameters ($T, \phi_{ox}, \nu, D_{ox}, R_g$) but also on the morphological length D_1^4/L_1^2 (i.e., the ratio of the fourth power of trachea diameter to its square length). For the case of same average environmental parameters, another important conclusion is

$$\frac{L_1^2}{D_1^4} e^{0.4621 N_{opt}} = \frac{0.000235 R_{g,ox} T}{\nu D_{ox}}\left(\frac{\phi_{ox,0}}{\phi_{ox}} - 1\right) = \text{constant} \tag{20}$$

As the living beings are subjected to the same average environmental parameters, and N_{opt} is a constant, thus the morphological length D_1^2/L_1 is a constant for humans.

3 Airflow in Respiratory Tree: Porosity, Permeability, and Transient Effects

This section is devoted to the analysis of airflow characteristics and transient effects of flow in the tracheobronchial tree, based on the studies presented by Miguel [29, 30].

3.1 Porosity and Permeability

In the previous sections, we show that the tracheobronchial tree has 23 branches of ducts and each duct branches into 2 daughter branches at the next level (Fig. 4). The diameter and length of these ducts are sized relative to one another, in accordance with Eqs. 8 and 9. The relationship between the size of the first duct (level 1) and the size of the ducts at level i, is given by

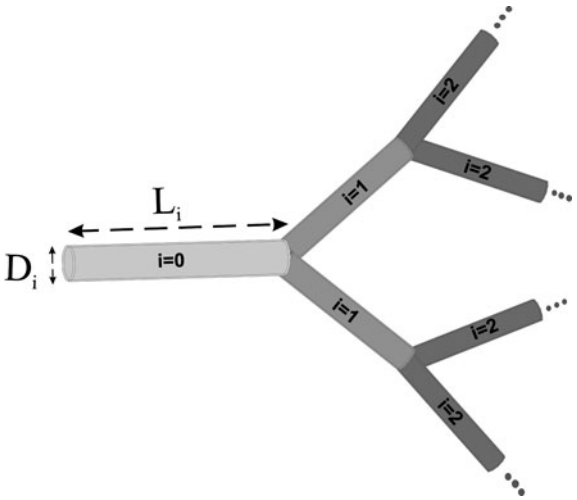

Fig. 4 Tracheobronchial tree (detail of the first three branches of ducts)

$$\frac{D_i}{D_0} = a_D^i \frac{L_i}{L_0} = a_L^i \tag{21}$$

with $a_D = a_L = 2^{-1/3}$.

The effective length of the network, L, the cross-sectional area, A, and the volume of the network, V, are

$$L = \sum_{i=0}^{n} L_i \quad A = \sum_{i=0}^{n} 2^i \alpha_{sf} D_i^2 \quad V = \sum_{i=0}^{n} 2^i \alpha_{sf} D_i^2 L_i \tag{22}$$

where α_{sf} is a shape factor (i.e., $\pi/4$ for round ducts). By substituting Eq. 21 into 22 one obtains

$$L = L_0 \frac{1 - a_L^{n+1}}{1 - a_L} \quad A = \alpha_{sf} D_0^2 \frac{1 - (2a_D^2)^{n+1}}{1 - 2a_D^2} \quad V = \alpha_{sf} D_0^2 L_0 \frac{1 - (2a_D^2 a_L)^{n+1}}{1 - 2a_D^2 a_L} \tag{23}$$

where D_0 and L_0 are the trachea diameter and length, respectively. This means that the effective length, cross-sectional area and volume of the tracheobronchial tree can be expressed in terms of the geometric characteristics of the trachea, branching level and scale factors.

An important structural parameter of the tree pattern of ducts in the chest cavity is the porosity. The porosity or void fraction, ε, is defined as the ratio between the tree network volume and the chest cavity volume

$$\varepsilon = \frac{\alpha_{sf} D_0^2 L_0}{V_{chest}} \frac{1 - (2a_D^2 a_L)^{n+1}}{1 - 2a_D^2 a_L} \tag{24}$$

Equation 24 shows the porosity of the tracheobronchial tree in terms of the size of the first tube, number of branches, branching level and volume of the chest cavity, V_{chest}.

We now turn our attention to the airflow characteristics of the tree-shaped network. In accordance with the Hagen–Poiseuille equation (Eq. 3)

$$32\nu\left(\frac{L}{D^2A}\right)Q = \frac{1}{\rho}\Delta p \tag{25}$$

According to the mass conservation, the fluid flow is a constant in every level of the tree network. Therefore,

$$\Delta p = \sum_{i=0}^{n} \Delta p_i \tag{26}$$

Substituting Eqs. 23 and 25 into Eq. 26, we obtain

$$\Delta p = 32\rho\nu Q \sum_{i=0}^{n} \left(\frac{L}{D^2A}\right)_i = 32\frac{\rho\nu L_0}{\alpha_{sf} D_0^4} \frac{1 - 2a_D^4/a_L}{1 - \left(2a_D^4/a_L\right)^{n+1}} Q \tag{27}$$

A standard approach in the investigation of fluid flow through porous materials is to characterize the system in terms of Darcy's law. Darcy's law, just as the Hagen–Poiseuille equation, is valid at small values of the Reynolds number and establishes a linear relation between the pressure difference and the fluid flow with the proportional coefficient depending on the intrinsic permeability (transport property for flow) and fluid viscosity. Combining Darcy Equation with Eq. 27 yields

$$K = \frac{1}{32} \frac{1 - \left(2a_D^4/a_L\right)^{n+1}}{1 - 2a_D^4/a_L} \frac{L_{chest}}{L_0} D_0^2 \tag{28}$$

Equation 28 shows that the intrinsic permeability, K, of the tracheobronchial tree is only a function of the geometry and size of both the tree patterns of tubes and the length of the chest cavity, L_{chest}.

3.2 Transient Pressure Effects

According to the transient form of Darcy law, the airflow through the tracheobronchial tree is

$$\frac{4L_{chest}}{\pi D_0^2}\frac{dQ}{dt} + \frac{4L_{chest}}{\pi D_0^2}\frac{\nu}{K}Q = \frac{1}{\rho}\Delta p \tag{29}$$

and the equation of mass conservation is

$$\frac{d(V\rho)}{dt} = \rho Q \tag{30}$$

where K is the intrinsic permeability given by Eq. 28. An extra equation is required for closure (i.e., an equation of state). For a polytropic expansion or a compression of ideal gas with constant heat capacity, the state equation can be written as $\rho = \rho_0(p/p_0)^{\delta}$, where δ is the polytropic index ranging from 1 (isothermal) to 1.4 (isentropic gas expansion/compression). Substituting the state equation and Eq. 30 into Eq. 29 yields

$$c_{p1}\frac{d^2p}{dt^2} + c_{p2}\frac{dp}{dt}\frac{dp}{dt} + c_{p3}\frac{dp}{dt} + p = p_0 \tag{31}$$

with

$$c_{p1} = \frac{4\alpha_{sf}L_0L_{chest}}{\pi}\frac{1-(2a_D^2a_L)^{n+1}}{1-2a_D^2a_L}\delta(\delta-1)\left(\frac{p}{p_0}\right)^{\delta-2} \tag{32.1}$$

$$c_{p2} = \frac{4\alpha_{sf}L_0L_{chest}}{\pi}\frac{1-(2a_D^2a_L)^{n+1}}{1-2a_D^2a_L}\delta^2\left(\frac{p}{p_0}\right)^{\delta-2} \tag{32.2}$$

$$c_{p3} = \frac{4\alpha_{sf}L_0L_{chest}}{\pi}\frac{1-(2a_D^2a_L)^{n+1}}{1-2a_D^2a_L}\delta\left(\frac{p}{p_0}\right)^{\delta-1}\frac{\nu}{K} \tag{32.3}$$

Equation 31 describes the transient response of the pressure variation within a tree-shaped flow structure. Notice that this equation is similar to the one governing the damped harmonic oscillator.

4 On the Fate of Inhaled Particles

The air we breathe is a mixture of gases but also small particles (i.e., small droplets or solids, inorganic or organic) [31]. Every day billions of particles are inhaled with the ambient air. Thus, the respiratory tree serves as a door of entry for inhaled particles into the human body. The importance of understanding particle-lung interaction encompasses the following:

1. Assessing the health hazards of particles [2, 32, 33]: atmospheric particles may be detrimental to human health. Micrometer particles (>1 μm) may be captured in the tracheobronchial tree, and subsequently cleared by the action of the mucus layer but submicrometric particles may reach the gas exchange surface of the alveolar region. A number of occupational diseases are directly linked to deposition and retention of inhaled particles such as coal, silica, and asbestos. Deposition of inhaled allergens may also cause acute bronchoconstriction for bronchitis and asthma sufferers, as well as tissue injuries and lung diseases. Asbestos, lead, mold, soot particles, for example, are very harmful to human health [5]. Epidemiological studies have also shown a consistent, increased risk for heart and stroke events in relation to exposure to particulate matter [34].

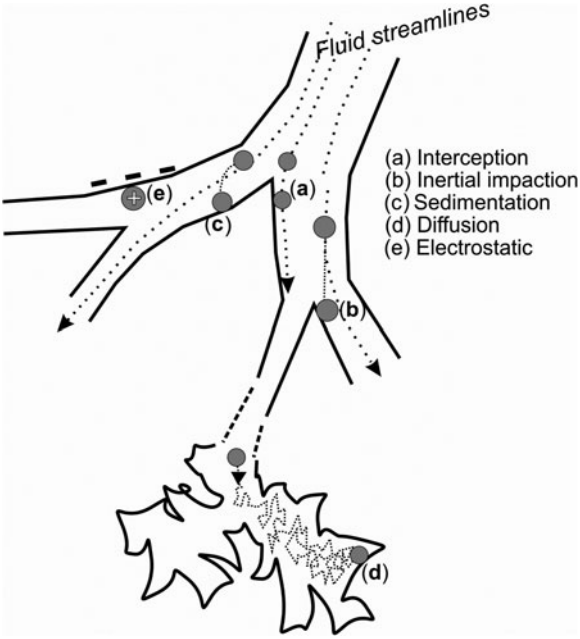

Fig. 5 Schematic representation of particle deposition onto the airway walls [37]

2. For an optimal delivery and evaluation of therapeutic effects of pharmaceutical aerosol particles by inhalation (inhalation route drug delivery) in order to reach the predetermined sites of action in the respiratory tract [35]: inhalation of drug aerosol deposited directly to airway target areas results in a reduction of the adverse reactions in the therapy of asthma, bronchitis, and other respiratory disorders [36].

The physico-chemical properties and toxicity of inhaled particles, as well as the site and magnitude of deposition in the respiratory tract, may lead to different effects. The site and magnitude of deposition is determined by the mechanisms of deposition of particles. There are five physical mechanisms (Fig. 5) due to which particle may deposit onto the airway wall [2]:

(a) Interception deposition occurs when particles that follow air streamlines touch the airway walls and become attached to them. This mechanism is especially important in the deposition of fibrous particles (particles with an elongated form) in the smaller airways.

(b) Inertial impaction deposition is characteristic of large particles, and occurs when particles are unable to adjust to the abrupt streamline changes in the neighborhood of airway walls. Therefore, inertial impaction is most effective at or near the tracheal bifurcation, and also plays a role at subsequent bifurcations. Inertial impaction is a predominant deposition mechanism for micrometric particles (>1 μm).

(c) Sedimentation is the settling of particles due to gravity. It's very effective for heavy particles transported at low velocities (i.e., at the smaller airways).
(d) Diffusion deposition is most important for submicrometric particles, especially in the airways far from the trachea, where the residence times are relatively long and the distance to airway walls relatively small.
(e) Electrostatic deposition is important only in cases with charged particles, when the airway walls are charged with an opposite charge, or when the concentration of charged particles is high enough to produce a repulsive force between particles.

4.1 Suspension Flow with Deposition in the Tracheobronchial Tree

The fraction of ingoing particles that deposit in the airway can be obtained by measuring the particle concentration upstream, C_u, and downstream, C_d, the segment

$$\Phi = 1 - \frac{C_d}{C_u} = 1 - P \tag{33}$$

Here Φ and P are the deposition and penetration efficiencies, respectively. Although important, this equation gives us little insight into the factors that affect the deposition of particles.

Particle deposition in the airway is related to the so-called characteristic deposition parameter, f (i.e., the number of particles of characteristic size d_p that get attached to the airway wall per second) and the terminal velocity of particles in the flow field u_p [38]. The deposition parameter reads as [38]

$$f = \frac{1}{D_i d_p} \tag{34}$$

Particles travelling in the fluid stream are retained at bifurcations mostly. The terminal velocity in a flow field is

$$u_p = c_0 \frac{\rho_p d_p^2 Q^2}{\rho \nu A^2 \vartheta} \tag{35}$$

where ϑ is the diameter of curvature of the bifurcation [38], ρ_p is the particle density, A is the duct section and c_0 is a constant. By invoking Buckingham's Π-theorem a dimensionless group Π can be obtained

$$\Pi = \frac{\Phi D_i \lambda f^{1/2}}{u_p} \tag{36}$$

Here Π is a constant while λ is the rate at which the airway length available for deposition changes in time. By combining Eq. 36 with Eqs. 34 and 35 yields

$$\Phi = c_{\Pi}\left(\frac{\rho\nu}{\rho_p}\right)^{1/4}\frac{Q^{3/4}}{\vartheta\lambda D_i^{3/4}}St^{5/4} \tag{38}$$

where c_{Π} (=$439c_0\Pi$) is a constant and St is the Stokes number ($\rho_p d_p^2 Q/(18\rho\nu A D_i)$. Breathing produces a cyclic airflow whose frequency depends on the metabolic demand. The inhalation flow is related with tidal volume (i.e., the volume of air exchanged per breath), V_{tidal}, and the breathing frequency, ξ, by

$$Q = 2\xi V_{tidal} \tag{39}$$

By inserting Eq. 39 into 38 one obtains

$$\Phi = 1 - P = \Lambda\left(\frac{\xi^3 V_{tidal}^3}{\vartheta^4 D_i^3}St^5\right)^{1/4} \tag{40}$$

with $\wedge = c_{\Pi}\lambda^{-1}(\rho\nu/\rho_p)^{1/4}$. Equation 40 shows that the deposition efficiency depends on the size of ducts, fluid and particles properties, as well as on tidal volume, breathing frequency and Stokes number. Besides, it indicates that the deposition efficiency increases with Stokes number, tidal volume and breathing frequency but decreases with the diameter of ducts and the curvature of the bifurcations.

4.2 Deposition of Particles in the Ttracheobronchial Tree

In evaluating the deposition of inhaled particles, it is important to consider the effect of particle size but also the breathing frequency (Eq. 40). Miguel et al. [39] studied the deposition of particles through a double bifurcation duct model made of glass fiber with the same size of the first three bifurcations of the human respiratory tree. The results, presented in terms of particle penetration, are depicted in Fig. 6 for breathing frequencies of 0.25/s and 0.42/s that match resting and light exercise breathing patterns, respectively.

Respiratory and lung diseases also influence the patterns of deposition. The effect of an obstructed airway (diameter reduction of 50% in about 20% of its length), due to chronic obstructive pulmonary diseases, on the particle penetration is depicted in Fig. 7.

The penetration of particles is found to decrease (i.e., particle deposition increase) both with the particle size and breathing frequency. Sub micrometer

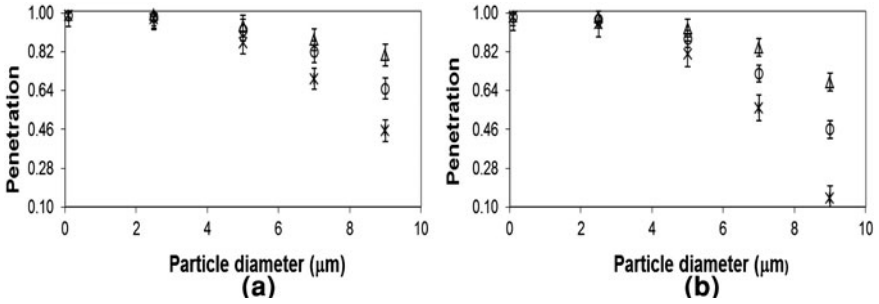

Fig. 6 Particle penetration at breathing frequencies of 0.25/s (**a**) and 0.42/s (**b**): *open circle* 1st bifurcation, *open triangle* 2nd bifurcation, *multiplication* entire bifurcation duct [39]

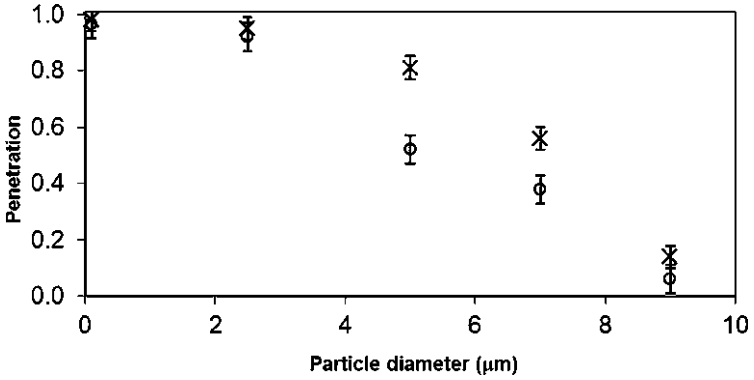

Fig. 7 Particle penetration at breathing frequency of 0.42/s in a double bifurcation duct [39]: "healthy" tract (*multiplication*) and tract with a reduction of 50% in diameter over 20% of its length a (*open circle*)

particles may penetrate deeper into the respiratory tract. Deposits are more significant at the first bifurcation and for micrometer particles and breathing frequency of 0.42/s (Fig. 6). Especially for bigger particles, deposition is considerably enhanced in respiratory tract with obstructive disease as compared to healthy tract (Fig. 7).

Estimating regional particle deposition patterns is important for the human risk assessment process and to optimize targeting of all regions of the respiratory tract in respiratory drug delivery. As a result of numerous deposition studies, the International Commission on Radiological Protection (ICRP) suggested a deposition model for regional penetration of particles.

Particle penetration in the mouth/nose-larynx (P_{mn_l}) and trachea-terminal bronchioles (P_{t_tb}), and its dependence on particle size, can be obtained from [40]

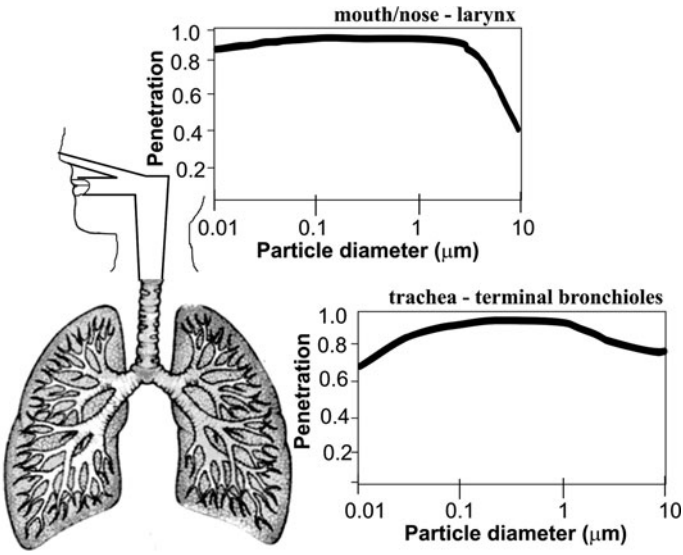

Fig. 8 Regional particle penetration inhaled orally in the human respiratory tract under resting breathing patterns

$$P_{mn-1} = 1 - \left[1 - \left(0.5 - \frac{0.5}{1 + 0.76 \times 10^{-3} d_p^{2.8}}\right)\right]\left[\frac{1}{1 + \exp\left(6.84 + 1.183 \ln(d_p)\right)} + \frac{1}{1 + \exp\left(0.924 - 1.885 \ln(d_p)\right)}\right] \tag{41}$$

$$P_{t-tb} = 1 - \left(\frac{3.52 \times 10^{-3}}{d_p}\right)\left\{\exp\left(-0.234\left(\ln(d_p) + 3.4\right)^2\right) + 63.9 \exp\left(-0.819\left(\ln(d_p) - 1.61\right)^2\right)\right\} \tag{42}$$

where d_p is the particle diameter expressed in microns. Figure 8 shows the regional deposition predicted by Eqs. 41 and 42 for particles between 0.01 and 10 micron.

4.3 Behavior of Submicrometer Particles in Periodic Alveolar Airflows

The alveolar region of the lungs is highly vascularized to permit effective gas exchange because the membrane of the alveolar lung region is very permeable [41]. Thus, particles not only can cause greater inflammation but also can be

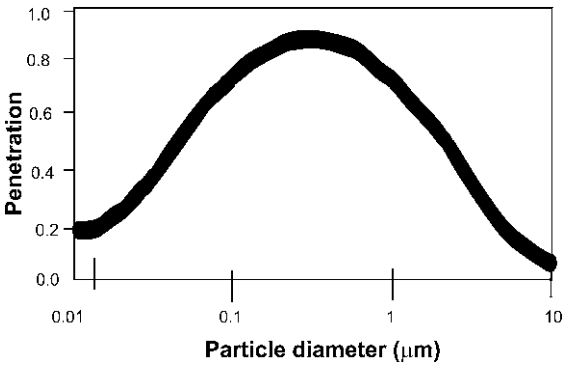

Fig. 9 Total penetration of particles inhaled orally in the human respiratory tract under resting breathing patterns

incorporated in the blood stream. There are several evidences that particles cross cell membranes and reach the blood stream [34, 42]. This can be used to deliver therapeutics aerosols into the systemic circulation but can also have hazardous consequences. For an example, inhalation anthrax follows the deposition of spore-bearing particles of ~ 1 μm into the alveolar spaces [43].

Particle penetration beyond the terminal bronchioles (P_{btb}) regions of the respiratory tract and its dependence on particle size, can be obtained from [40]

$$P_{btb} = 1 - \left(\frac{15.5 \times 10^{-3}}{d_p}\right)\left\{\exp\left(-0.416\left(\ln(d_p) + 2.84\right)^2\right) + 19.11\exp\left(-0.482\left(\ln(d_p) - 1.362\right)^2\right)\right\} \quad (43)$$

where d_p is the particle diameter expressed in microns. In the size range of 0.1–1 μm, Fig. 9 summarizes the results of the total penetration of particles (Eqs. 41–43) in the human respiratory tract at rest. According to Fig. 9, more than 50% of particles with a diameter between 0.05 and 3 microns inhaled orally have the chance of reaching the alveolar region and may be incorporated in the blood stream.

Balik et al. [44] focused on the transport of suspended submicrometer particles within the alveoli, due to periodic airflows that match breathing patterns of sedentary and light activity. This numerical study accounted for expansion and contraction of the alveolar surface and tracked the motion of particles during 30 breathing periods. It was observed that the path of the particles is independent of the breathing period (i.e., resting and light exercise breathing patterns). Particles initially tend to follow forward paths and proceed by diffusion until the far end of the alveolus. During the simulation time of 30 breathing periods, the distance traveled by the particles was practically the same for both cases.

The evolution of the mass fraction of particles in the alveolus was also compared for normal and fast breathing (Fig. 10). The results show that significant percentage of the particles that enter the alveolus are trapped there and have high probability to be deposited onto the alveolar walls. This result is consistent with

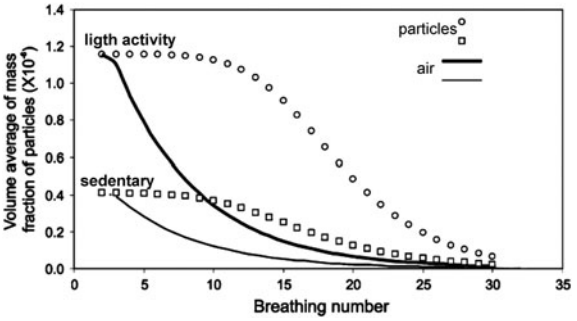

Fig. 10 Mass fraction of particles in the alveolus during 30 breathing periods [44]

the finding that sub-micrometer particle motion is out of phase with the periodic airflow in the alveolus. The numerical results also indicate that the fraction of particles trapped in the alveolus increases with breathing rate and agrees with reference values of regional sub-micrometer particle deposition in the alveolar-interstitial region of the lung [40, 45].

References

1. Nield, D.A., Bejan, A.: Convection in Porous Media. Springer, New York (1999)
2. Bejan, A., Dincer, I., Lorente, S., Miguel, A.F., Reis, A.H.: Porous and Complex Flow Structures in Modern Technologies. Springer, New York (2004)
3. Miguel, A.F.: Computational analysis of the role of permeability and inertia on fluid flow through porous media. In: Delgado, J.M.P.Q. (ed.) Current Trends in Chemical Engineering, pp. 1–19. Studium Press LLC, Houston (2010)
4. Weibel, E.R.: Morphometry of the Human Lung. Academic, New York (1963)
5. Gattuso, P., Reddy, V.B., David, O., Spitz, D.J.: Differential Diagnosis in Surgical Pathology. WB Saunders, New York (2009)
6. Horsfield, K.: Diameters, generations and orders of branches in the bronchial tree. J. Appl. Physiol. **68**, 457–461 (1990)
7. Bejan, A.: Shape and Structure—from Engineering to Nature. Cambridge University Press, Cambridge (2000)
8. Miguel, A.F.: Natural flow systems: acquiring their constructal morphology. Int. J. Des. Nat. Ecodyn. **5**, 230–241 (2010)
9. Hess, W.R.: Das prinzip des kleinsten kraftverbrauchs im dienste hämodynamischer forschung. Arch. Anat. Physiol. **2**, 1–62 (1914)
10. Murray, C.D.: The physiological principle of minimum work. Proc. Natl. Acad. Sci. U. S. A. **12**, 207–214 (1926)
11. Rashevsky, N.: The principle of adequate design. In: Rosen, R. (ed.) Foundations of Mathematical Biology, pp. 143–175. Academic, New York (1973)
12. Horsfield, K., Cumming, G.: Angles of branching and diameters of branches in the human bronchial tree. Bull. Math. Biophys. **29**, 245–259 (1967)
13. Zamir, M.: The role of shear forces in arterial branching. J. Gen. Physiol. **67**, 213–222 (1975)
14. Horsfield, K., Dart, G., Olson, D.E., Filley, G.F., Cumming, G.: Models of the human bronchial tree. J. Appl. Physiol. **31**, 202–217 (1971)
15. Koblinger, L., Hofmann, W.: Analysis of human lung morphometric data for stochastic aerosol deposition calculations. Phys. Med. Biol. **30**, 541–556 (1985)

16. Mandelbrot, B.B.: The Fractal Geometry of Nature. Freeman, San Francisco (1982)
17. Dincer, I., Rosen, M.: Exergy: Energy, Environment and Sustainable Development. Elsevier, Burlington (2007)
18. Bejan, A., Lorente, S.: Design with Constructal Theory. Wiley, New Jersey (2008)
19. West, G.B., Brown, J.H., Enquist, B.J.: A general model for the origin of allometric scaling laws in biology. Science **276**, 122–126 (1997)
20. Bejan, A.: Street network theory of organization in nature. J. Adv. Transp. **30**, 85–107 (1996)
21. Bejan, A., Lorente, S.: Constructal theory of generation of configuration in nature and engineering. J. Appl. Phy. **100**, 2006 (2006)
22. Miguel, A.F., Bejan, A.: The principle that generates dissimilar patterns inside aggregates of organisms. Physica A **388**, 727–731 (2009)
23. Bejan, A., Lorente, S.: The constructal law of design and evolution in nature. Philos. Trans. R. Soc. B **365**, 1335–1347 (2010)
24. Bejan, A., Ledezma, G.A.: Street tree networks and urban growth: optimal geometry for quickest access between a finite-size volume and one point. Physica A **255**, 211–217 (1998)
25. Miguel, A.F.: Constructal theory of pedestrian dynamics. Phys. Lett. A **373**, 1734–1738 (2009)
26. Bejan, A., Rocha, L.A.O., Lorente, S.: Thermodynamic optimization of geometry: T- and Y-shaped constructs of fluid streams. Int. J. Therm. Sci. **39**, 949–960 (2000)
27. Wechsatol, W., Lorente, S., Bejan, A.: Tree-shaped flow structures with local junction losses. Int. J. Heat Mass Tran. **49**, 2957–2964 (2006)
28. Reis, A.H., Miguel, A.F., Aydin, M.: Constructal theory of flow architecture of the lungs. Med. Phys. **31**, 1135–1140 (2004)
29. Miguel, A.F.: Dendritic structures for fluid flow: laminar, turbulent and constructal design. J. Fluid Struct. **26**, 330–335 (2010)
30. Miguel, A.F.: Fluid flow in tree-shaped constructal networks: porosity, permeability and inertial parameter. Defect Diffusion Forum **297–301**, 408–412 (2010)
31. Miguel, A.F., Reis, A.H., Melgao, M.: Urban indoor-outdoor aerosol measurements in Portugal and the global warming scenario. Int. J. Global Warming **1**, 356–367 (2009)
32. Miguel, A.F., Reis, A.H., Aydin, M.: Aerosol particle deposition and distribution in bifurcating ventilation ducts. J. Hazard. Mate. B **116**, 249–255 (2004)
33. Miguel, A.F., Aydin, M., Reis, A.H.: Indoor deposition and forced re-suspension of respirable particles. Indoor Built. Environ. **14**, 391–396 (2005)
34. Pope, C.A., Burnett, R.T., Thurston, G.D., Thun, M.J., Calle, E.E., Krewski, D., Godleski, J.J.: Cardiovascular mortality and long-term exposure to particulate air pollution: epidemiological evidence of general pathophysiological pathways of disease. Circulation **109**, 71–77 (2004)
35. Ganderton, D.: Targeted delivery of inhaled drugs: current challenges and future goals. J. Aerosol Med. **12**, S3–S8 (1999)
36. Smith, S.J., Bernstein, J.A.: Therapeutic uses of lung aerosols. In: Hickey, A.J. (ed.) Inhalation Aerosol: Physical and Biological Basis for Therapy, pp. 233–269. Dekker, New York (1996)
37. Miguel, A.F.: Porous media and filtration. In: Ingham, D.B., Mamut, E., Pop, I., Bejan, A. (eds.) Emerging Technologies and Techniques in Porous Media, pp. 419–431. Kluwer Academic, Dordrecht (2003)
38. Miguel, A.F., Reis, A.H.: Suspension flow with deposition in lung airway bifurcations in different breathing conditions. In: Bronna, O.E. (ed.) New Developments in Hazardous Materials Research, pp. 17–29. Nova Publishers, New York (2006)
39. Miguel, A.F., Reis, A.H., Aydin, M., Silva, A.M.: Particle deposition in airway bifurcations in different breathing conditions. J. Aerosol. Sci. **35**(s2), 1125–1126 (2004)
40. Hinds, W.C.: Aerosol Technology. Wiley, New York (1999)
41. Patton, J.: Mechanisms of macromolecule absorption by the lungs. Adv. Drug Del. Rev. **19**, 3–36 (1996)

42. Edwards, D.A., Hanes, J., Caponetti, G., Hrkach, J., Ben-Jebria, A., Eskew, M.L., Mintzes, J., Deaver, D., Lotan, N., Langer, R.: Large porous particles for pulmonary drug delivery. Science **20**, 1868–1872 (1997)
43. Inglesby, T., Henderson, D., Bartlett, J., Ascher, M., Eitzen, E., Friedlander, A., Hauer, J., McDade, J., Osterholm, M., O'Toole, T., Parker, G., Perl, T., Russell, P., Tonat, K.: Anthrax as a biological weapon: medical and public health management. J. Am. Med. Assoc. **281**, 1735–1745 (1999)
44. Balik, G., Reis, A.H., Aydin, M., Miguel, A.F.: Behavior of submicrometer particles in periodic alveolar airflows. Eur. J. Appl. Physiol. **102**, 677–683 (2008)
45. Valentin, J.: Guide for the practical application of the ICRP human respiratory tract model: ICRP supporting guidance. Ann. ICRP **32**, 13–14 (2002)

On Analogy Between Convective Heat and Mass Transfer Processes in a Porous Medium and a Hele-Shaw Cell

A. V. Gorin

Abstract Convective heat and mass transfer from bodies of classic geometry, a plate and a cylinder, embedded in a porous infiltrated medium and a line source located in a saturated porous medium is studied with the use of the Hele-Shaw analogy. The set of partial differential equations for steady-state, gap-averaged, two-dimensional heat and mass transfer and fluid flow with constant viscosity are identical with those for the Darcy flow regime in porous media and whose permeability K is $h^2/12$. All theoretical solutions are verified by the experimental data on processes in the Hele-Shaw cell and then compared with available experimental data on convective transfer processes in porous media. The findings indicate that convective transport phenomena in a Hele-Shaw cell share many features of those in porous media even though the phenomena in the cell are constrained to an essentially two-dimensional convection patterns. The validity of Hele-Shaw analogy for convective transport phenomena in porous media is discussed and the limits of applicability are determined where possible.

1 Introduction

Convective heat and mass transfer phenomena in fluid-saturated porous media relate to many engineering technologies such as chemical engineering, ground-water hydrology, geothermal engineering, advanced thermal methods of oil recovery, thermal insulation systems, underground nuclear and chemical waste

A. V. Gorin (✉)
School of Engineering and Science, Curtin University, Sarawak Campus,
CDT 250, 98009 Miri, Sarawak, Malaysia
e-mail: alexander.g@curtin.edu.my

J. M. P. Q. Delgado (ed.), *Heat and Mass Transfer in Porous Media*,
Advanced Structured Materials 13, DOI: 10.1007/978-3-642-21966-5_6,

disposal and many others. Due to the complex geometry of most porous media and associated irregular flow patterns, experimental studies has been focused as a rule on integral experimental measurements and correlations of test data because an accuracy of detailed direct measurements of velocity, temperature, and concentration profiles across porous media is questionable due to porous media destruction when inserting a probe. From theoretical point of view, the complexity of pore structure requires macroscopic averaging of microscopic phenomena, introducing phenomenological effective transport characteristics, for which in their turn appropriate models are to be developed [8].

Nevertheless, the quantitative evaluation of the heat and mass transfer characteristics of porous media is possible through the theoretical and experimental study of well-determined systems modelling the main features of transport phenomena in porous media. This advances physical modelling with cheap and efficient equipment to the forefront.

An example of such equipment is a fluid gap sandwiched between closely spaced parallel wall, also known as a Hele-Shaw cell. The flow of a viscous fluid in a narrow gap between parallel plates a small distance h apart had been widely used for modeling different hydraulic problems related to infiltration in percolation basin design, groundwater flow, etc. The modelling is based on the mathematical similarity between the differential filtration equations in the Darcy flow regime and those for a viscous fluid flow between parallel plates. The principles of the Hele-Shaw theory are briefly summarized in [21]. To our knowledge, Dachler [5] was the first to model groundwater flow with the Hele-Shaw cell.

Following this paper many researchers used a Hele-Shaw cell for the solution of many practical problems of ground-flow in aquifers including inhomogeneous aquifers, seepage from dams, see-water intrusion, etc. by constructing various models. More details on this analogy one can find in Bear et al. [2] where following earlier studies it was assumed that the Hele-Shaw cell was applicable as prototype for porous media flows of flow rate q for Reynolds number $Re = qh/v < 1{,}000$. Above that the analogy fails due to transition to turbulent flow. The Hele-Shaw cell applicability to turbulent filtration modeling is still an open question.

It is worth noting that the Hele-Shaw flow as an analogue of filtration in porous media has attracted considerable attention of many mathematicians and there exists a vast amount of literature concerning a single and multiphase flow into porous media and mathematical reviews of these contributions.

Surprisingly, but there is very limited number of papers concerned with the Hele-Shaw cell use for modelling of convective heat and mass transfer phenomena in saturated porous media, and they are focused primarily on stability of natural convection in the Hele-Shaw cell.

To our knowledge one of the first experiments to be carried out with this device as a model object for investigating mass transfer processes from a point source in a porous medium (the plume front velocity) was described in [27]. Some fragmentary data on temperature on a heat plume axis and a semi-width of the plume one can find in [23]. In fact, the heat plum from a heat source in a Hele-Shaw cell was exploited

by the authors to study the potential of a laser Doppler velocimeter for simultaneous measurements of velocity and temperature but not to study transfer phenomenon.

At the same time it is pertinent to note the advantage lying in the fact that for the Hele-Shaw cell we are dealing with real physical properties of fluid but not effective ones that in itself it is a problem. Further still this equipment allows the use of well developed experimental techniques for reliable and of high degree of accuracy measurements.

The modelling of convective heat and mass transfer from bodies of classic geometry, a plate and a cylinder, embedded in a porous infiltrated medium and a line source located in a saturated porous medium with the use of the Hele-Shaw analogy has become the theme of our comprehensive theoretical and experimental investigations. The set of partial differential equations for steady-state, gap-averaged, two-dimensional heat and mass transfer and fluid flow with constant viscosity are identical with those for the Darcy flow regime in porous media and whose permeability K is $h^2/12$. A wide spectrum of experimental techniques such as visualization of flow patterns, an optomechanical infra-red imaging system for thermogram production, micro-thermocouples for direct temperature profile measurements, and electrochemical diagnostics for obtaining the local and overall mass transfer rates to the surface have been exploited in experimental studies.

The problems under consideration include natural convection on a vertical wall and from a horizontal cylinder embedded in porous media, convection from a source, and forced convection heat and mass transfer from a cylinder. Analytical solutions in a boundary layer approximation were developed for boundary conditions of two types, a constant wall temperature and a uniform wall heat flux. Numerical simulation for natural convection problems was used to extend analysis and find limitations related to finite dimensions of the experimental Hele-Shaw cell.

In all experiments vertical Hele-Shaw cells were used. When studying convective heat transfer the experimental cells were formed by adiabatic walls.

All theoretical solutions were first verified by the experimental data on processes in the Hele-Shaw cell. Then, the data were compared with experimental data on the above-mentioned problems on convective transfer processes in porous media available from our data obtained in parallel and data from different authors to determine the range of validity of the Hele-Shaw analogy for the modelling of convective transfer processes in saturated porous media.

2 Natural Convection from a Vertical Plate

Consider natural convection adjacent to a narrow vertical side wall of a Hele-Shaw cell formed by thermally insulated vertical plates. In the mathematical formulation of the problem it is assumed that (1) the properties of the fluid such as viscosity μ, thermal conductivity λ, specific heats C_p and thermal expansion coefficient β are constant and (2) the Boussinesq approximation for the density $\rho = \rho_\infty[1 - \beta(T - T_\infty)]$ can be applied.

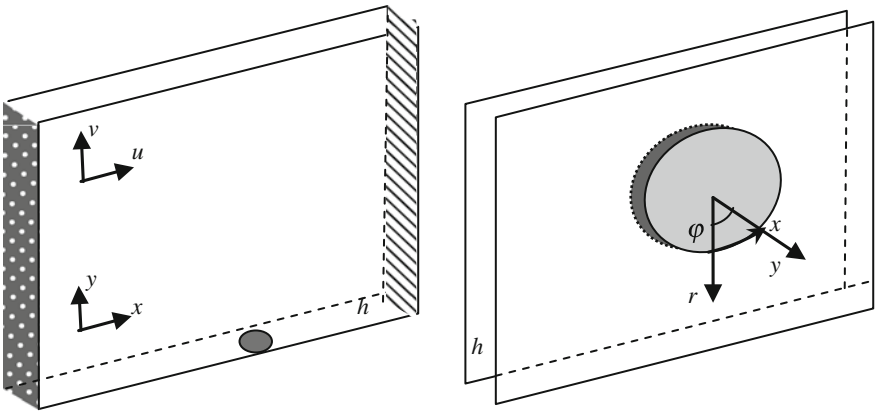

Fig. 1 Schematic of an experimental Hele-Shaw cell for study natural convection on a vertical plate or heat source (*left*) and from a cylinder (*right*)

Under these assumptions, the governing equations are given by

$$\begin{aligned} &\mathrm{div}\vec{V} = 0 \\ &\rho\left(\vec{V}\nabla\right)\vec{V} = -\nabla p + \mu\Delta\vec{V} + \rho_\infty\beta(T - T_\infty)\vec{g} \\ &\rho C_p\left(\vec{V}\nabla\right)T = \lambda\Delta T \end{aligned} \tag{1}$$

where v, p and T are the velocity, pressure and temperature of fluid; the subscript ∞ denotes the fluid parameters outside the boundary layer on the plate; the Laplace operator is $\Delta = \partial^2/\partial x^2 + \partial^2/\partial y^2 + \partial^2/\partial z^2$; $\nabla = (\partial/\partial x)\vec{i} + (\partial/\partial y)\vec{j} + (\partial/\partial z)\vec{k}$.

The directions of the axes of the Cartesian coordinate system are shown in Fig. 1, the values $z = \pm h/2$ correspond to the positions of plates. It is assumed that there is no motion anywhere in the direction of the z-axis in the cell (the velocity component $w = 0$) and that the Poiseuille profile is realized for the longitudinal and transverse velocity components

$$u = \frac{3}{2}u_0(x,y)\left[1 - 4z^2/h^2\right], \quad v = \frac{3}{2}v_0(x,y)\left[1 - 4z^2/h^2\right] \tag{2}$$

The fluid temperature is assumed to be constant in the direction of z (across the cell width), i.e.

$$T = T(x, y) \tag{3}$$

Integration of system (1), taking relations (2) and (3) into account, across the cell cross-section (from $-h/2$ to $+h/2$) [11–14]

$$\begin{aligned}
&\frac{6}{5}\rho\vec{u}_0\nabla\vec{u}_0 = -\nabla p + \mu\Delta\vec{u}_0 + \rho_\infty\beta(T - T_\infty) - \frac{12\mu}{h^2}\vec{u}_0 \\
&\vec{u}_0\nabla T = a\Delta T \\
&\nabla\vec{u}_0 = 0
\end{aligned} \tag{4}$$

It is worth noting that numerical analysis of jet flow in the Hele-Shaw cell with inertia effects (the left-hand side of the momentum equation) was represented in Zhak et al. [28] and mixed convection from a cylinder in a Hele-Shaw cell was done by Safonov [22] and Gorin et al. [15, 16].

The analysis of numerical solution of this set of equations is represented in our papers by Gorin et al. [11], Vorontsov et al. [26] for a natural convection over vertical plate, in Gorin et al. [19] for natural convection over a cylinder and in Gorin et al. [12–14] for a heat source in a Hele-Shaw cell.

Neglecting shear stress and inertia terms in the momentum equation and in the boundary layer approximation for the heat transfer equation the system (4) takes on the form [11, 26]

$$\begin{aligned}
&\frac{\partial u}{\partial x} + \frac{\partial v}{\partial y} = 0 \\
&u = \frac{g\beta(T - T_\infty)h^2}{12v} \\
&u\frac{\partial T}{\partial x} + v\frac{\partial T}{\partial y} = a\frac{\partial^2 T}{\partial y^2}
\end{aligned} \tag{5}$$

The set of Eq. 5 fully coincides with the governing equations for natural convection adjacent to a vertical plate in a saturated porous medium [3], consequently, the dimensionless heat transfer laws are valid for our problem.

The similarity solutions are given by

- for *constant wall temperature*

$$\mathrm{Nu} = 0.444\mathrm{Ra}_T^{1/2} \tag{6}$$

where $\mathrm{Nu} = \alpha x/\lambda$; $\mathrm{Ra}_T = g\beta(T–T_\infty)h^2x/(12va)$; α is the heat transfer coefficient

- for *uniform wall heat flux*

$$\mathrm{Nu} = 0.772\mathrm{Ra}_*^{1/3} \tag{7}$$

where $\mathrm{Ra}_* = g\beta q_w h^2x^2/(12va\lambda)$.

The difference lies in the form of Rayleigh number representation in the case of a porous medium $\mathrm{Ra}_T = g\beta(T–T_\infty)Kx/(va)$, and $\mathrm{Ra}_* = g\beta q_w Kx^2/(va\lambda)$ where K is the permeability of a porous medium and values v, a are physical properties, the kinematic viscosity, and thermal diffusivity, respectively, for fluid flow in a Hele-Shaw cell, which in case of porous media are assumed to have their effective constant values characteristic for porous media under consideration.

The experimental cell for studying natural convection on a vertical plate is formed by two 26 mm thick lucite plates well insulated to avoid heat transfer with surroundings (see Fig. 1, left). The cavity bottom was hermetically sealed with a rubber gasket, whereas the top was open. In some of the runs, the top was closed. The dimensions of the working cavity are: $H = 0.22$ m, $L = 0.19$ m; $h = 2 \times 10^{-3}$ m.

A dark wall represents a heated working plate for studying heat transfer and the opposite wall indicated with dash-line texture was cooled and kept at constant temperature. The study of heat transfer in a Hele-Shaw cell was carried out for a constant temperature wall and constant heat flux at the working wall.

Besides the wall temperature, the temperature profiles in the thermal boundary layer on the heated side wall were measured by scanning microthermocouples inserted from the cooling wall side at four levels along the height: 0.025, 0.046, 0.064 and 0.147 m. The water temperature in the cell was measured on the vertical symmetry axis by seven nichrome-constantan thermocouples.

Visualization of flow in the Hele-Shaw cell was carried out by injecting violet ink into the upper part of the working cavity. The filming was carried out in reflected light after a time lapse of 20 min. An optomechanical infra-red imaging system was used to visualize the temperature field of the working cavity with one lucite plate replaced by a stainless steel plate of 8×10^{-4} m thickness.

A special series of experiments were undertaken to study the effect of the aspect ratio H/W (the cell high to the cell width) $= 0.5; 1; 2$. The experimental isotherms and streamlines indicate the formation whether single-vortex or double-vortex flow structure: with Grashof number, $\mathrm{Gr} = g\beta(T–T_\infty)L^3/\nu^2$ increase (in experiments its value was as great as $\mathrm{Gr} \approx 4 \times 10^{10}$), streamlines displace towards the upper corner of the cold wall and isotherms displace towards the upper corner of the heated wall resulting in asymmetry of flow in a central part of the cell and formation of a vortex adjacent to the heated wall with ensuing development of double-vortex flow structure. Boundary layers form on the walls. It was observed that the flow structures were stable. These findings are confirmed by numerical solution of the set of equations (4) in variables stream function-vorticity with corresponding boundary conditions in the range of Grashof number $10^7 \leq \mathrm{Gr} \leq 10^9$. The experimental temperature profiles correspond well to those obtained from the similarity solution of the two-dimensional boundary layer equations (5) and which are confirmed by the experimental data for porous media [4] as well.

Figure 2 represents the comparison of the heat transfer law (6) with experimental data on natural convection about a vertical isothermal plate embedded in a porous media formed by glass beads with diameters ranging from 0.85 to 1.68 mm [4] and our experimental data on natural convection heat transfer about a vertical isothermal plate in a Hele-Shaw cell as described above. The Nusselt number scattering is observed when $\mathrm{Ra}_{\mathrm{T},\,\mathrm{x}} > 400$ for porous media.

Experimental heat transfer coefficients for natural convection about the surface with uniform heat flux embedded in a porous medium whose matrices is formed by glass beads with diameters of 1.5 mm (see Fig. 3) are in reasonably good

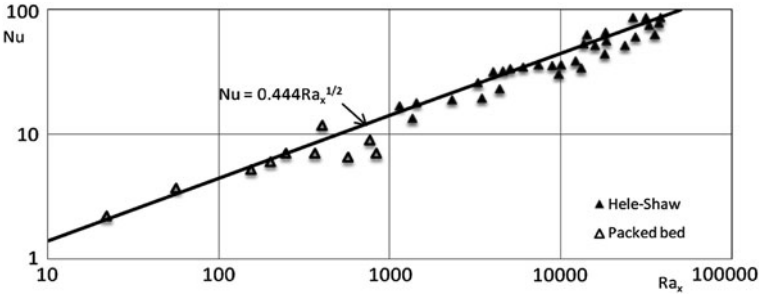

Fig. 2 Natural convection on the isothermal wall

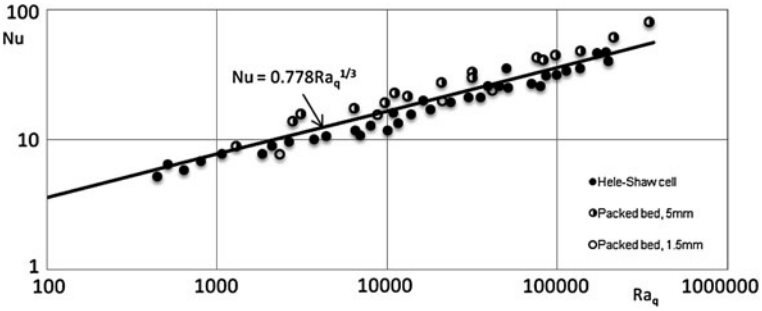

Fig. 3 Natural convection on a wall with uniform heat flux

agreement with the similarity solution for linear filtration and our data for isoflux plate in a Hele-Shaw cell, whereas the experimental values for the case of a medium with 5 mm glass beads are 20% above the theoretical ones being in accord with the trend $\mathrm{Nu} \propto \mathrm{Ra}_*^{1/3}$ (it should be noted that experimental data on porous media cited in [4] have been recalculated to represent data in the Nu-$\mathrm{Ra_q}$ coordinates instead of the incorrect Nu-Ra_T representation). The range of validity for an isoflux plate spans up to $\mathrm{Ra}_q \approx 4 \times 10^5$.

These figures confirm the validity of natural convection heat transfer modeling in a porous medium by natural convection in a Hele-Shaw cell. The theoretical and experimental results on self-similar temperature profiles and heat transfer coefficients were shown to be in a good agreement.

3 Natural Convection from a Cylinder

Detailed theoretical (self-similar solution for constant temperature wall, and integral solution for the constant flux boundary condition) and experimental study of natural convection from a cylinder has been undertaken as well. Infra-red

imaging system was used to visualize the temperature field. The effect of the cell geometrical parameters and the validity of the boundary layer approximation were checked numerically. To delineate the range of applicability of the Hele-Shaw analogy the comparison with data on natural convection from a horizontal cylinder in a porous media was undertaken.

Assuming the absence of transverse motion and the Poiseuille profile for the radial and angular velocity components

$$u(r,\varphi,z)=\frac{3}{2}u_r(r,\varphi)\left[1-4z^2/h^2\right],\quad v(r,\varphi,z)=\frac{3}{2}v_\varphi(r,\varphi)\left[1-4z^2/h^2\right] \tag{8}$$

The governing boundary layer equations for steady natural convection around a cylinder of radius R in a curvilinear system of coordinates with x aligned with the cylinder, $x = R\varphi$, and y directed radially outward the cylinder, $y = r - R$, take the form

$$\begin{aligned}&\frac{\partial u}{\partial x}+\frac{\partial v}{\partial y}=0\\ &u=\frac{g\beta(T-T_\infty)h^2}{12\nu}\sin\frac{x}{R}\\ &u\frac{\partial T}{\partial x}+v\frac{\partial T}{\partial y}=a\frac{\partial^2 T}{\partial y^2}\end{aligned} \tag{9}$$

The similarity solution for isothermal cylinder has the form as that developed by Cheng and Minkowycz [3] for a isothermal cylinder in porous medium

$$\mathrm{Nu}=0.565\mathrm{Ra}_T^{1/2} \tag{10}$$

where $\mathrm{Ra}_T = g\beta(T–T_\infty)h^2R/(12\nu a)$

For the for *uniform wall heat flux* on the cylinder surface by applying an integral method one can obtain [19]

$$\mathrm{Nu}=0.731\mathrm{Ra}_\mathrm{q}^{1/3} \tag{11}$$

where $\mathrm{Ra}_\mathrm{q} = g\beta\mathrm{q}_\mathrm{w}h^2R^2/(12\nu a\lambda)$

Numerical solutions of the full set of the nonlinear two-dimensional Equations (4) were performed for both isothermal cylinder and the cylinder with uniform heat flux at its surface [19]. Rayleigh numbers varied in the ranges $1 \le \mathrm{Ra}_T \le 10^5$ and $1 \le \mathrm{Ra}_\mathrm{q} \le 10^5$. For this problem one more parameter, the geometrical simplex, $\mathrm{D}a = \frac{h}{\sqrt{3D}}$, called by analogy with porous media the Darcy number, appears. It varied in the range of $0.001 \le \mathrm{Da} \le 0.1$.

For both types of boundary conditions, qualitatively similar temperature fields and flow patterns are observed.

At $\mathrm{Ra}_T \sim 10$, the flow is mainly uprising from the cylinder surface and the configuration of the isotherms practically corresponds to a linear heat source. With increase in Ra number, dynamic and thermal layers with distinct temperature

change and velocity gradients are formed on the cylinder surface. Their thicknesses are initially comparable with the cylinder diameter, and, hence, the boundary layer approximation will give a very great error. At $\mathrm{Ra}_T > 10$, the boundary layer thickness becomes substantially less than the cylinder diameter. In the narrow near-rear region a thermal jet forms. It is worth noting that in our calculations, as in the calculations represented in [20] there was no vortex region in the rear part of the cylinder.

At relatively small Ra numbers $\mathrm{Ra}_T \sim 10$ the variation in the Darcy number from 0.01 to 0.1 did not change the flow pattern and the temperature field qualitatively. However, with the increase in Da, the boundary layer thickness grows. The effect of the Darcy number becomes essential as the Ra number increases resulting in 20% difference in heat transfer coefficients in stagnation point at $\mathrm{Ra} = 10^3$.

A good agreement between experimental average Nusselt numbers (points) and theoretical values (solid lines) calculated by formulas (10) and (11) is demonstrated in Fig. 4. The experimental Hele-Shaw cell (see Fig. 1, right) was formed by two 60 mm thick parallel vertical plates made of foam plastic whose inner surface was glued around with glass textile. The working cylinder had a diameter of 40 mm, and the working cavity had the following dimensions: height of 760 mm, width 260 mm and thickness 2 mm.

A comparison of the flow pattern and temperature fields in natural convection near a horizontal isothermal cylinder in a Hele-Shaw cell and near a cylinder embedded at a finite depth [7] in a semi-infinite porous medium, and results of numerical simulation of the same problem for a finite porous medium [20] indicated their good qualitative agreement.

Experimental studies of natural convection from a horizontal cylinder embedded in porous medium are limited in number. These data are available for isothermal cylinders only. Fand et al. [6] recommended for the Darcy regime of filtration (they estimated the limit of applicability as $\mathrm{Ra}_T \leq 80$) for the following correlation

$$\mathrm{Nu} = 0.679\mathrm{Ra}_T^{0.646}\mathrm{Pr}^{-0.126} \tag{12}$$

The correlation was developed from experiments with a horizontal cylinder of 14.5 mm diameter embedded in a porous medium formed by glass beads of diameters 2, 3 and 4 mm with either water or silicon oil as a working fluid. At low Ra numbers, the thickness of the thermal boundary layer is of the order of the cylinder radius ($\delta/\mathrm{R} \sim \mathrm{Ra}^{-1/2}$). This means that the dimensions of the beads are comparable to the boundary layer thickness (at $\mathrm{Ra} \geq 10$ they even exceed this value). Thus, the experimental conditions in [6] do not fit the theoretical model (9) and their experimental results cannot be a criterion for the validity of Eq. 10.

Another set of experimental data is reported by Fernandez and Schrock [7], who used cylinders of diameters 76.2 and 63.5 mm embedded in a water-saturated porous media formed by sand of mean diameters of 1 and 0.15 mm. The thermal conductivity and permeability of the porous medium were measured in special experiments. The authors recommended correlation

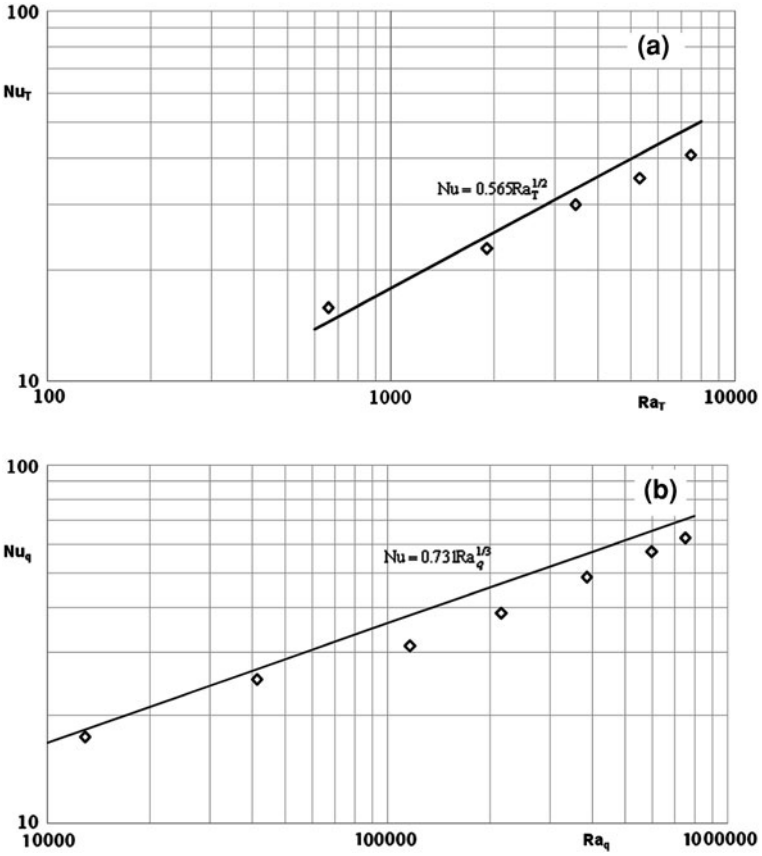

Fig. 4 Natural convection from a horizontal cylinder: **a** isothermal cylinder; **b** isoflux surface

$$\mathrm{Nu} = f(\eta)\mathrm{Ra}_F^{0.514} \tag{13}$$

where $\mathrm{Nu} = qD/(T_w - T_S)$, $\mathrm{Ra}_F = g\beta\Delta TKD\sqrt{H^2/R^2 - 1}/(2va)$, $f(\eta) = 0.015 + 1.23\exp(-0.543\eta)$, $\eta = \ln\left(H/R + \sqrt{H^2/R^2 - 1}\right)$, T_w and T_S are the temperatures on the surface of cylinder and the porous medium respectively; H is the distance from the surface of the medium to the centre of the cylinder; q is the heat flux averaged over the cylinder surface.

The convective regime studied corresponds to $\mathrm{Ra} = 15 \pm 120$. The experiments by Fernandez and Schrock [7] support the validity of Eq. 10.

Thus, the known theoretical models and experimental data confirm in general the similarity between natural convection from horizontal cylinders in porous media under the Darcy flow regime and a cylinder in a narrow gap. However, additional experimental studies are required to specify the range of applicability of this analogy.

4 Convection from a Source

Consider natural convection from a source in a Hele-Shaw cell formed by isothermally insulated vertical plates [12, 13]. In the mathematical formulation of the problem it is assumed that the properties of the fluid such as viscosity, thermal conductivity, specific heat, and thermal expansion coefficient are constant and the Boussinesq approximation can be applied. Under these assumptions, the governing equations are given by the set of Eq. 5 with the boundary conditions

$$\frac{\partial T}{\partial y} = 0 \quad \mathrm{v} = 0, \quad \mathrm{y} = 0 \tag{14}$$

$$T = T_\infty \quad y \to \infty \tag{15}$$

The total energy conservation condition across any horizontal plane in the plume is:

$$Q = 2h \int_0^\infty \rho c_P u (T - T_\infty) dy \tag{16}$$

This set of partial differential equations for steady-state, two-dimensional heat and mass transfer and fluid flow with constant viscosity coincides in its form with those for convection from a line source in a saturated porous medium with permeability ($h^2/12$) [25] and has the following analytical solution:

$$\theta = \frac{3}{8} c h^{-2} \left[\frac{1}{4} \left(\frac{A}{a^2} \right)^{1/3} \frac{y}{x^{2/3}} \right] \tag{17}$$

$$(T - T_\infty)_{y=0} = \frac{9}{2} \frac{v}{h^2 g \beta} \left(\frac{A^2}{a} \right)^{1/3} x^{-1/3} \tag{18}$$

$$Y = 4 \ln 20 \left(\frac{a^2}{A} \right)^{1/3} x^{1/3} \tag{19}$$

where $A = Qg\beta h/24\mu c_p$.

For mass sources where buoyancy forces that drive such flows arise from density differences due to variation in solute (chemical species) concentration C the governing equations in view of the apparent similarity of the transport equations for heat and constituents can be obtained from the heat-transfer-driven flow equations through the transformations $\beta \to \beta_C$, $T \to C$, $a \to D$, $Q/\to m/(\rho D)$ where β_C, D, m are the volumetric expansion coefficient, diffusivity, and mass rate respectively.

A theoretical model of convection from a virtual line source in a Hele-Shaw cell was shown to be in complete accordance with the model of line source located in a

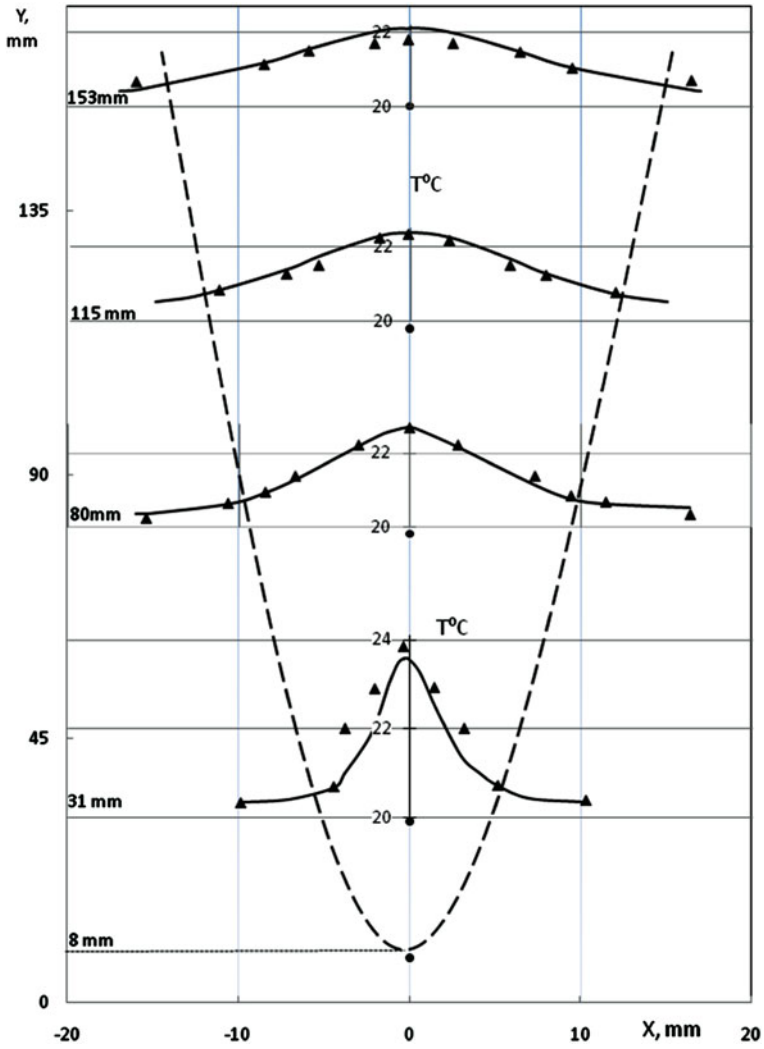

Fig. 5 Temperature profiles across the plume in physical coordinates

porous medium. The experimental temperature profiles, plume axis temperature, and the plume width are in good agreement with theoretical model and confirm the validity of the assumptions adopted in the mathematical model of process. The findings indicate that convective transport phenomena in the vertical Hele-Shaw cell share many features of those in porous media even though the phenomena in the cell are constrained to an essentially two-dimensional convection patterns. The validity of Hele-Shaw analogy for convective transport phenomena in porous media and the limits of applicability must be determined from experiment.

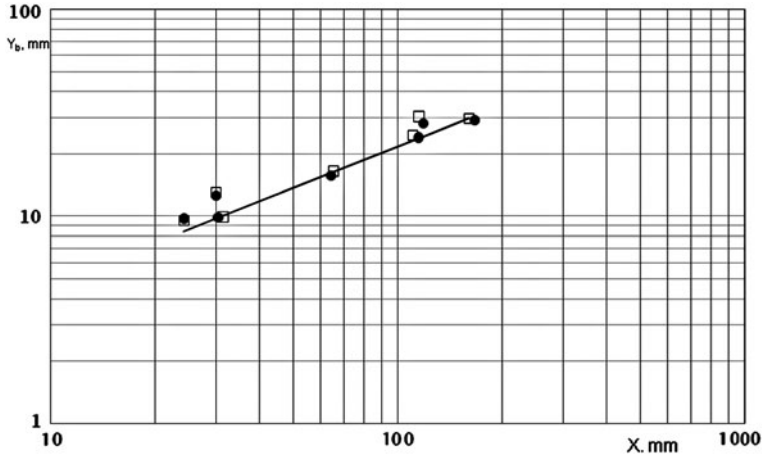

Fig. 6 Width of the plume

The experimental study of heat and mass transfer from a source [12], bearing in mind the similarity between these processes, was focused on thermal convection from a heat source. Experiments were conducted in a rectangular cavity 200×190 mm^2 with walls made from foam plastic wall whose inner surfaces were covered with water-resistant glue.

The gap width is $h = 2$ mm. The copper plate 3×1.8 mm^2 on the cell bottom served as a heat source (see the schematic in Fig. 1, left). The heating was realized by direct current from a controlled power source. The temperature profiles were measured by a scanning thermocouple at four levels along the height: 0.031, 0.080, 0.115, and 0.153 m. The measured temperature profiles across the plume at different distances from the heat source of 24 W are compared with theoretical calculations (17) and (18) in Fig. 5. The predicted border of the plume is shown in the same figure.

Figure 6 represents experimental (black dots and open rectangulars) and predicted in accordance with formula (19) (solid line) values of the half-width of the plume.

Experimental values of the temperature along the plume axis (black dots) in comparison with solution (18) represented by the solid line are shown in Fig. 7.

A satisfactory agreement in the predicted plume width, the plume axis temperature, and temperature distributions should be noted, what confirms the validity of the assumptions adopted in the mathematical model of the process. Some discrepancies between experiment and mathematical model can be assigned to the limited size of the Hele-Shaw cell (the effect of the minor secondary flow in the cell) and high sensibility of the plume to external disturbances.

Cheng [4] presented a very limited experimental data on non-dimensional temperature profiles and dimensionless temperature at the axis of a plume from a horizontal line source of heat embedded in a porous medium modelled by 3 mm

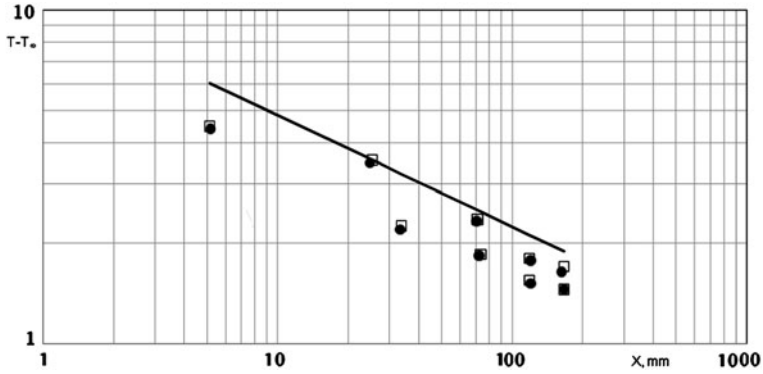

Fig. 7 The plume axis temperature

glass beads. His experimental data confirm well theoretical solution developed from two-dimensional boundary layer approximation similar to those discussed above in this section. Since many of initial data are not represented in the cited paper we are not able do make direct correlation between the data on a heat source in a Hele-Shaw cell and in a porous medium to determine the range of Rayleigh number of the analogy applicability.

Overall, these facts with our previous results on natural convection heat transfer in the Hele-Shaw cell count in favour of the Hele-Shaw cell use for quantitative study of two-dimensional heat and mass transfer in porous media.

5 Forced Convection Heat and Mass Transfer from a Cylinder

Forced convection is one of the most difficult for analytical solution problem due to non-linear character of transfer equations.

At the same time at reasonable simplifications one can find solutions predicting the main transport properties of a flow [10, 17, 18].

The next section takes care of mass transfer from a cylinder placed in a Hele-Shaw cell. The solutions to be developed will be transformed then into the form suitable to describe heat and mass transfer from a cylinder placed in porous media.

Analytical solutions for local and averaged forced convection heat and mass transfer coefficients from a cylinder in a narrow channel and heat and mass transfer in a stagnation point have been obtained for both types of boundary conditions.

Governing equations for the temperature and concentration change in a curvilinear system of coordinates are derived following the way similar to the outlined in the section on natural convection from a cylinder of radius R by assuming the absence of transverse motion and the parabolic profile for the radial and angular velocity components.

$$u(r,\theta,z)=\frac{3}{2}u_r(r,\theta)\left[1-4z^2/h^2\right],\quad v(r,\theta,z)=\frac{3}{2}v_\theta(r,\theta)\left[1-4z^2/h^2\right] \tag{2a}$$

in polar system coordinates $x = R\theta$, $y = r - R$

The transport equations in the boundary layer approximation are as follows

$$u\frac{\partial T}{\partial x}+v\frac{\partial T}{\partial y}=a\frac{\partial^2 T}{\partial y^2} \tag{20}$$

$$u\frac{\partial C}{\partial x}+v\frac{\partial C}{\partial y}=D\frac{\partial^2 C}{\partial y^2} \tag{21}$$

And continuity equation is in a standard form

$$\frac{\partial u}{\partial x}+\frac{\partial v}{\partial y}=0.$$

The problem of isothermal wall has been analysed by the example of mass transfer from a cylinder with

- constant concentration on the cylinder surface:

$$\mathrm{C}=\mathrm{C}_w \text{ at } \mathrm{y}=0 \quad \mathrm{C}=\mathrm{C}_\infty \quad \text{at y } \to \infty \tag{22}$$

- and a constant heat flux wall:

$$q=k\frac{\partial T}{\partial y}=\text{const} \quad \text{at}\, y=0; \tag{23}$$

$$T=\mathrm{T}_\infty \quad \text{at}\, y\to\infty, \tag{24}$$

In the limit of high Schmidt/Prandtl numbers in the near-wall region one can use a linear profile for the longitudinal velocity component across the thermal/diffusion boundary layer

$$u=\frac{\tau_w}{\mu}y \tag{25}$$

By using this approximation and the transverse velocity obtained from the continuity equation, the diffusion Eq. 21 can be written as [17]

$$\frac{\tau_w}{\mu}y\frac{\partial C}{\partial x}-\frac{1}{2\mu}\frac{\partial \tau_w}{\partial x}y^2\frac{\partial C}{\partial y}=D\frac{\partial^2 C}{\partial y^2} \tag{26}$$

which is to be solved with the boundary conditions presented above.

The solution for Sherwood number, $\mathrm{Sh}(\theta)=\frac{2jR}{D}$ is represented as

$$\mathrm{Sh}(\theta)=1.629\left(\mathrm{Pe}\frac{R}{h}\right)^{1/3}\Phi(\theta) \tag{27}$$

$$\text{where Pe} = \frac{2U_\infty R}{D},\ \Phi(\theta) = \sin^{1/2}\theta\left[\int_0^\theta \sin^{1/2}\theta d\theta\right]^{-1/3}.$$

In the stagnation point

$$\text{Sh}_f = 1.865\left(\text{Pe}\frac{R}{h}\right)^{1/3} \tag{28}$$

Average over the cylinder Sherwood number

$$\text{Sh}_m = 1.393\left(\text{Pe}\frac{R}{h}\right)^{1/3} \tag{29}$$

For porous media equivalent representation of these solutions is as follows

$$\text{Sh}(\theta) = 0.855\text{Pe}^{1/3}\left(\frac{m}{\text{Da}}\right)^{1/6}\Phi(\theta) \tag{30}$$

$$\text{Sh}_f = 0.978\text{Pe}^{1/3}\left(\frac{m}{\text{Da}}\right)^{1/6} \tag{31}$$

$$\text{Sh}_m = 0.731\text{Pe}^{1/3}\left(\frac{m}{\text{Da}}\right)^{1/6} \tag{32}$$

where $\text{Da} = K/(2R)^2$ is the Darcy Number, m is the porosity, K is the permeability.

The solutions are easily modified to take into account inertial terms in the momentum equation [9]:

$$\frac{\text{Sh}}{\text{Sh}_0} = \left(1 + \frac{3}{5}Re^*\right)^{1/6} \quad \text{with} \quad Re^* = Re\left(\frac{h}{R}\right)^2 \tag{33}$$

5.1 Forced Convection from an Isoflux Wall

Governing equation is represented by Eq. 20 with the boundary conditions (24) and (25)

The solution was obtained by using Laplace transform [18]. Local Nusselt number is represented as follows

$$\text{Nu}_{2h} = 9.382(\text{Pe}^*)^{1/3}\left[\int_0^\theta\left(\int_{\theta'}^\theta \sqrt{\sin\theta''}d\theta''\right)^{-2/3} d\theta'\right]^{-1} \tag{34}$$

Its value in the stagnation point is

$$\mathrm{Nu}_{2h,f} = \frac{2^{5/3}3^{5/6}}{\Gamma\left(\frac{1}{3}\right)}(\mathrm{Pe}^*)^{1/3} = 2.96(\mathrm{Pe}^*)^{1/3} \tag{35}$$

And the mean Nusselt number one can calculate from

$$\mathrm{Nu}_{2h,m} = 2.33(\mathrm{Pe}^*)^{1/3}, \quad \mathrm{Pe}^* = \frac{2U_\infty R}{a}\frac{h^2}{(2R)^2} \tag{36}$$

5.2 Experimental Verification

Theoretical study has been put in experimental test by using visualization and electrochemical technique.

The apparatus used is a closed loop with reservoir at constant level. The working section was made of two organic glass plates 470 × 200 × 24 mm. The gap width was 0.95 mm, and the diameter of experimental cylinder was $2R = 30$ mm. The working fluid was a 0.02 normal solution of potassium ferricyanide and a 0.024 normal solution of potassium ferrocyanide in a 0.6 normal aqueous NaOH solution. The electrolyte solution differed little from water in respect its physical properties.

The local mass transfer coefficients over the perimeter of the cylinder were measured by small local sensor. The streamwise dimension of the local sensor along the flow (along the circumference of the cylinder) is 1.9 mm. The total mass flux from entire surface of the cylinder could be obtained by integration of the reading of the local sensor and simultaneous measurements using the large and small sensors, which allowed the monitoring the quality of experiment.

Heat transfer was studied in a Hele-Shaw cell composed of two vertical parallel acrylic plastic plates 470 × 200 × 24 mm with the gap $h = 2$ mm. Both the isothermal cylinder and the cylinder with constant heat flux have diameter of 40 mm.

In Fig. 8 experimental data on heat transfer (black dots) in a front stagnation point are compared with theoretical values (solid line) calculated from Eq. 28 for a cylinder with constant heat flux at the surface.

The mean heat transfer coefficient for the same cylinder is represented in Fig. 9.

A comparison between experimental and theoretical values of heat and mass transfer coefficients in stagnation point of cylinders placed in porous media and in a Hele-Shaw cell for Reynolds number covering the range 0.001–10 is represented in Fig. 10. The solid line represents theoretical law, Eq. 36.

The measured local heat and mass transfer coefficients are in good agreement with the predicted ones up to $Re^* = 0.6$–0.7 [17, 18].

It is worthy of mentioning the distribution of local heat and mass transfer coefficients over a cylinder. At relatively small flow rates the maximum values of the heat and mass transfer coefficient are realized not at a front stagnation point but its location is shifted downstream (see Fig. 11).

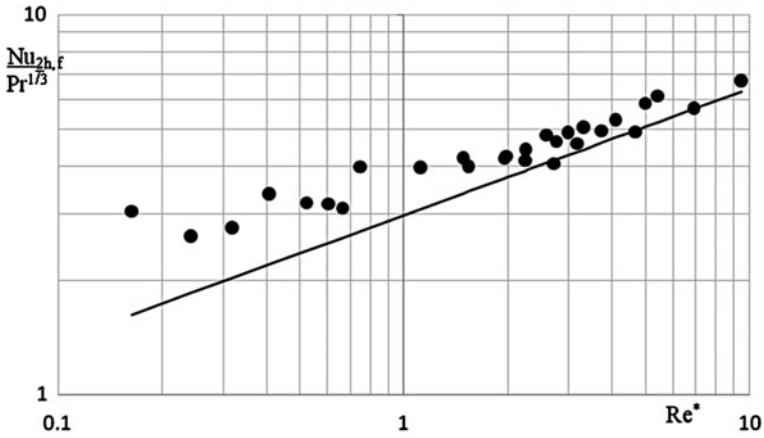

Fig. 8 Heat transfer in stagnation point of a cylinder with constant heat flux at the surface

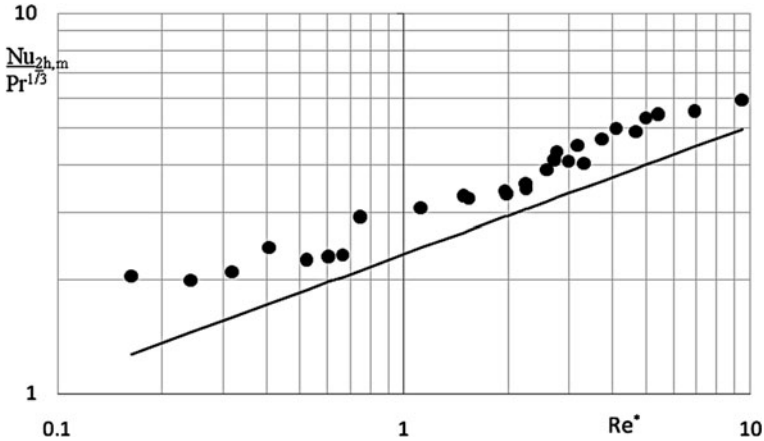

Fig. 9 Mean heat transfer for a cylinder with constant heat flux at the surface

This effect is observed in forced convection from a cylinder in a grainy layer (see Fig. 12).

This phenomenon is a manifestation of the dispersion which will make an impact on heat and mass transfer in the stagnation point area. In a Hele-Shaw cell this effect is due to non-uniform velocity profile in the cell [1, 24], whereas in a porous medium this is a result of pore-level hydrodynamic mixing which depends on the pore geometry, velocity, existence of local recirculation zones, thermophysical properties of porous material, etc.

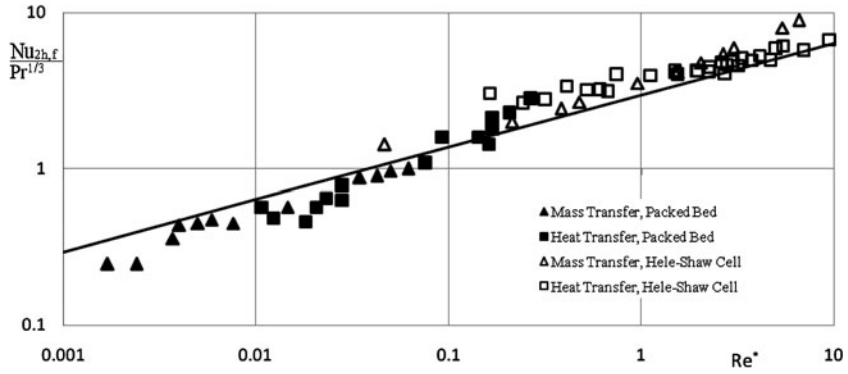

Fig. 10 Heat and mass transfer in stagnation point

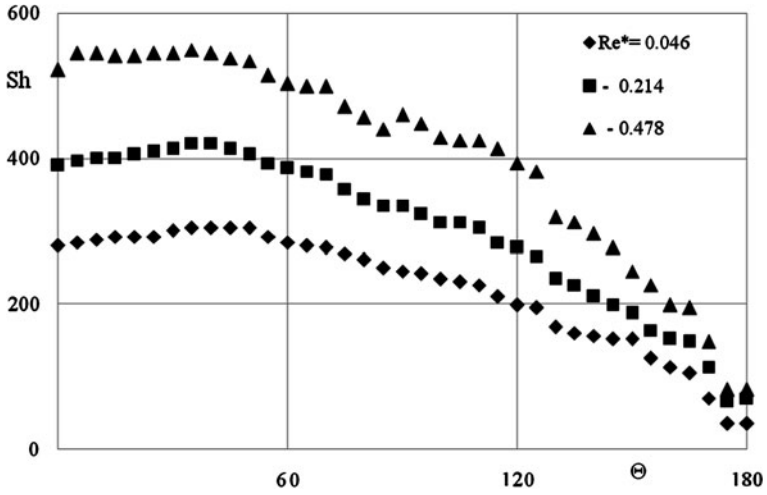

Fig. 11 Local mass transfer from a cylinder in a Hele-Shaw cell

The results of comparison between the Hele-Shaw cell data and those for a cylinder in a porous medium reveals the limits of validity of the Hele-Shaw analogy for forced convection transfer process.

6 Conclusion Remarks

The systematical theoretical and experimental studies of natural and forced convective heat and mass transfer from a classic geometry bodies placed in a Hele-Shaw cell and comparison with data on porous media available from our data obtained in

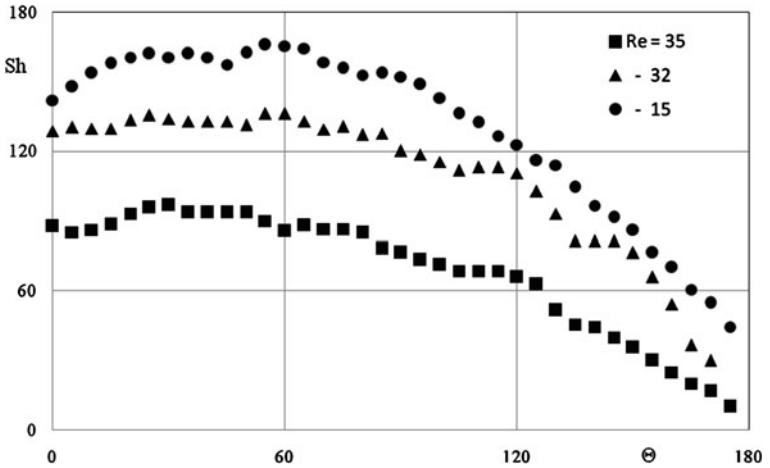

Fig. 12 Local mass transfer from a cylinder in packed bed

parallel and data from different authors clear suggest the validity of the Hele-Shaw analogy for the modelling of convective transfer processes in saturated porous media.

The available data on convective transfer processes in porous media allow to determine approximately the range of validity of the analogy.

But the data published are not enough to set more exact values of the ranges. Besides, the estimation of effective thermal conductivity and diffusivity in porous media is still a problem—more reliable experiments on dispersive coefficients accompanying the measurements of heat and mass transfer coefficients are needed.

References

1. Aris, R.: On the dispersion of a solute in a fluid flowing through a tube. Proc. R. Soc. **A235**(1200), 67–77 (1956)
2. Bear, J., Zaslavsky, D., Irmay, S.: Physical Principles of Water Percolation and Seepage. UNESCO, Firmin-Didot, Paris (1968)
3. Cheng, P., Minkowycz, W.J.: Free convection about a vertical flat plate embedded in a porous medium with application to heat transfer from a dike. J. Geophys. Res. **82**, 2040–2044 (1977)
4. Cheng, P.: Natural convection in a porous medium: external flows. In: Kakac, S., Aung, W., Viskanta, R. (eds.) Natural Convection: Fundamentals, Applications, pp. 475–513. Hemisphere, Washington, DC (1985)
5. Dachler, R.: Grundwasserströmung. Springer, Wien (1936)
6. Fand, R.M., Steinberg, T.E., Cheng, P.: Natural convection heat transfer from a horizontal cylinder embedded in a porous medium. Int. J. Heat Mass Transfer **29**, 119–133 (1986)
7. Fernandez, R.T., Schrock, V.E.: Natural convection cylinders buried in a liquid-saturated porous medium. In: Proceedings of the 7th International Heat Transfer Conference, vol. 2, pp. 335–340. Munchen (1982)

8. Gorin, A.V.: Heat transfer in packed beds. In: Proceedings of the 13th International Congress Chemical and Process Engineering (CHISA'98), Prague, Czech Republic (1998)
9. Gorin, A.V.: Convective Transfer Processes in Porous Media and Packed Beds. Institute of Thermophysics, SB RAS, Novosibirsk (1999)
10. Gorin, A.V., Sikovsky, D.Ph.: Heat and mass transfer and shear stress in a flow past cylinder in porous media and narrow slot. In: Hydrodynamics and Heat and Mass Transfer in Fixed Packed Beds, pp. 21–31. Inst Thermophysics, SB RAS, Novosibirsk (1991)
11. Gorin, A.V., Nakoryakov, V.E., Chupin, V.M.: Heat transfer under natural convection in a narrow channel. In: Proceedings of the Eurotherm Seminar Nr.16 Natural Circulation in Industrial Applications, pp. 213–218. Pisa, Italy (1990)
12. Gorin, A.V., Khoruzhenko, A.G., Chupin, V.M.: Natural convection from heat source in a narrow slot. In: Hydrodynamics and Heat and Mass Transfer in Fixed Packed Beds, pp. 128–138. Inst Thermophysics, SB RAS, Novosibirsk (1991)
13. Gorin, A.V., Nakoryakov, V.E., Khoruzhenko, A.G.: Natural convection from heat sources and surfaces in a narrow gap. In: International Seminar Evaporative Cooling Systems of Electronic Equipment, pp. 165–176. Novosibirsk (1991)
14. Gorin, A.V., Nartov, V.P., Khoruzhenko, A.G., et al.: Numerical and experimental study of natural convection in a narrow slot. In: Hydrodynamics and Heat and Mass Transfer in Fixed Packed Beds, pp. 95–127. Inst Thermophysics, SB RAS, Novosibirsk (1991)
15. Gorin, A.V., Sikovsky, D.Ph., Khoruzhenko, A.G.: Convection from a horizontal cylinder in porous media and narrow slot. In: Proceedings of the Minsk International Forum on Heat and Mass Transfer (MIF-92). Heat Transfer in Disperse Systems, vol. 5, pp. 44–47. Minsk, Belorussia (1992)
16. Gorin, A.V., Sikovsky, D.Ph., Khoruzhenko, A.G.: Convective heat transfer from a horizontal cylinder in a porous medium and a narrow slot. Heat Transfer Res. **25**, 970–974 (1993)
17. Gorin, A.V., Zarubin, A.V., Mikhailova, T.N., et al.: Friction and mass transfer in transverse flow around a cylinder in a granular bed and a narrow slot. J. Appl. Mech. Tech. Phys. **36**(1), 105–113 (1995)
18. Gorin, A.V., Sikovsky, D.Ph., Mikhailova, T.N., et al.: Forced convection heat and mass transfer from a circular cylinder in a Hele-Shaw cell. In: Proceedings of the 11th International Heat Transfer Conference, vol. 3, pp. 109–114. Kyongju, Korea (1998)
19. Gorin, A.V., Egorov, A.Yu., Nakoryakov, V.E., Chupin, V.M.: Natural convection from a cylinder in a narrow gap and in a porous medium. J. Appl. Mech. Tech. Phys. **40**(1), 120–129 (1999)
20. Ingham, D.B., Pop, I.: Natural convection about a heated cylinder in a porous medium. J. Fluid Mech. **184**, 157–181 (1987)
21. Lamb, H.: Hydrodynamics, 6th edn. Cambridge University Press, London (1932)
22. Safonov, S.A.: Mixed convection from a circular cylinder in a Hele-Shaw cell. J. Appl. Mech. Tech. Phys. **1**, 62–66 (1991)
23. Sano, O., Takaki, R.: Simultaneous measurements of velocity and temperature by the use of laser Doppler velocimeter. Phys. Fluids **28**, 818–822 (1985)
24. Taylor, G.I.: The dispersion of soluble matter in solvent flowing slowly through a pipe. Proc. R. Soc. **219**(1137), 186–203 (1953)
25. Turcotte, D.L., Schubert, G.: Geodynamics: Applications of Continuous Physics to Geological Problems. Wiley, New York (1982)
26. Vorontsov, S.S., Gorin, A.V., Nakoryakov, V.E., Khoruzhenko, A.G., et al.: Natural convection in a Hele-Shaw cell. Int. J. Heat Mass Transfer **34**, 703–709 (1991)
27. Wooding, R.A.: Convection in a saturated porous medium at large Rayleigh number and Peclet number. J. Fluid Mech. **15**, 527–544 (1963)
28. Zhak, V.D., Nakoryakov, V.E., Safonov, S.A.: Flow over a cylinder in a narrow slot at high velocities. J. Appl. Mech. Tech. Phys. **27**(3), 30–34 (1986)

Heat and Mass Transfer in Porous Materials with Complex Geometry: Fundamentals and Applications

A. G. B. de Lima, S. R. Farias Neto and W. P. Silva

Abstract This chapter provides information related to simultaneous heat and mass transfer and dimension variations in unsaturated porous bodies of arbitrary shape during transient problems. Two mathematical approaches are presented and discussed: lumped and distributed-parameters models. Here, applications have been given to some engineering processes (cooling, heating and drying). A two-dimensional distributed model written in a orthogonal curvilinear coordinate system and which assumes the pure diffusion as the sole mechanism of heat and moisture transport within the solid is applied to ellipsoidal porous bodies (prolate spheroid). A lumped-parameter model written in any coordinate system which includes effects such as shape of the body, heat and mass generation, evaporation and convection is presented, and analytical solution of the governing equations, limitations of the modeling and general theoretical results are discussed.

Notation

Bi_h	Heat transfer Biot number
Bi_m	Mass transfer Biot number
c	Specific heat, J/kg/K

A. G. B. de Lima (✉)
Department of Mechanical Engineering, Federal University of Campina Grande, Campina Grande, Brazil
e-mail: gilson@dem.ufcg.edu.br

S. R. Farias Neto
Department of Chemical Engineering, Federal University of Campina Grande, Campina Grande, Brazil
e-mail: fariasn@deq.ufcg.edu.br

W. P. Silva
Department of Physics, Federal University of Campina Grande, Campina Grande, Brazil
e-mail: wiltonps@uol.com.br

J. M. P. Q. Delgado (ed.), *Heat and Mass Transfer in Porous Media*, Advanced Structured Materials 13, DOI: 10.1007/978-3-642-21966-5_7,

D	Diffusion coefficient, m^2/s
Fo_c	Heat transfer Fourier number
Fo_m	Mass transfer Fourier number
h_c	Heat transfer coefficient, $W/m^2/K$
h_{fg}	Latent heat of vaporization of the moist solid, J/kg
h_m	Mass transfer coefficient, m/s
J	Jacobian
k, $\bar{k}$	Local and average thermal conductivity, W/m/K
L	Focal length, m
L'	Characteristic dimension, m
L_c	Characteristic length, m
L_1, L_2	Minor and major axis of the solid, m
M, $\overline{M}$	Local and average moisture content, kg/kg (d.b.)
$\dot{M}$	Mass generation per unit time, (kg/kg)/s
n	Number of experimental points
$\hat{n}$	Parameters number fitted
$\dot{q}$	Heat generation per volume unit, W/m^3
$\bar{S}^2$	Variance
S	Area, m^2
S^{Φ}	Source term
T	Air temperature, °C
t	Time, s
$\hat{U}$, $\hat{V}$, $\hat{W}$	Metric coefficients
UR	Air relative humidity
v	Air velocity, m/s
V	Volume, m^3
x, y, z	Cartesian coordinates, m

Subscripts

Exp	Experimental
fn	Final
0	Initial
Num	Numerical
p	Product
s	Dry solid
t	Time
v	Vapor
∞	Equilibrium

Greek letters

α	Thermal diffusivity, m^2/s
$\overline{\beta}_1$, $\overline{\beta}_2$	Shrinkage coefficient

Δ	Variation
Φ	Function
Φ''	Potential Φ per area unit
Φ'''	Potential Φ per volume unit
Γ^{Φ}, Ψ	Transport property of material
μ, ϕ, ω	Prolate spheroidal coordinates
η, ξ, ζ	Orthogonal curvilinear coordinates
θ, $\overline{\theta}$	Local and mean temperature of solid, °C
∇	Del operator
ρ	Density, kg/m^3

1 Introduction

In the microscopic scale, a porous material is a body consisting of a solid matrix having void spaces (pores) with irregular shape, different size and random distribution that are filled with one or more fluids. In the usual situation, some pores are interconnected and another disconnected. The interconnectedness of the pores allows the heat and mass transfer and fluid flow through itself that is accompanied with heat transfer into the solid matrix. Depending on the physical problem, the following phenomena may occur between the phases into the solid at the pore level: (1) heat transfer by convection, diffusion and radiation, (2) mass transfer by convection and diffusion, (3) phase change by melting, solidification and evaporation, and (4) chemical reactions (exothermic and endothermic) [28]. The size of pores can be classified as macropores (large pores) and micro and nanopores (small pores). When the equivalent pore diameter is less than 10^{-7} m, capillary forces within the pores are higher than gravitational forces, and the material is defined as capillary-porous material [13, 30]. Examples of these materials include wood, clay, grains, fruits and vegetables. Based in the states of moisture within the porous bodies they are classified still as hygroscopic and non-hygroscopic. In non-hygroscopic materials the pores are filled with liquid when it is completely saturated and with air when it is completely dry, very little amount physically bound water is found within itself, and there is not dimension variation during drying process, i.e., the body does not shrink. In contrast, in hygroscopic materials, there is very large bound water and very large dimensions variations during drying process are found [13, 45]. Unbound water in a hygroscopic material is the water in excess which can be removed by drying. On the other hand, during firing, the green clay loses chemically and mechanically bound water. Figure 1 illustrate scheme of a packed bed of porous particles (porous material) and details into these particles.

Diffusive and convective transport phenomena in porous bodies had been subject of the investigation for many years, because of their wide variety of

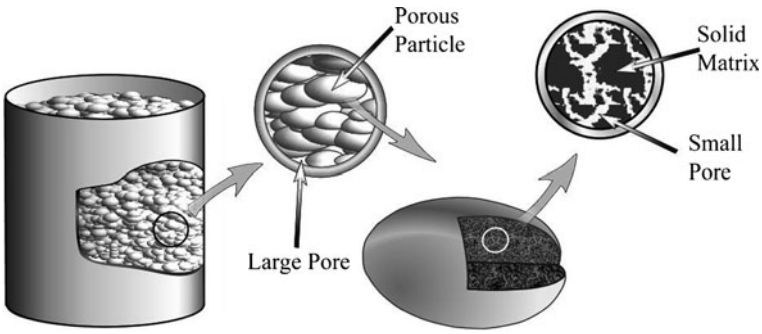

Fig. 1 Schematic of a packed bed of porous particles

industrial applications mainly in the mechanical, agricultural and chemical areas. The following books related to transport phenomena in porous media can be cited: [15, 25–27, 30, 46, 61, 65, 66].

For best understanding, consider a moist porous body with complex geometry at low temperature that is immersed suddenly in a heated unsaturated fluid (air) at a different temperature. When this moist porous body is being heated by the fluid surrounding it heat penetrates into the solid (as results of a temperature difference) and moisture is removed by evaporation and convection at the surface. Heat and mass transfer creates temperature and moisture gradients inside the solid, which in general, depends on the internal and external conditions of the porous body. Sometimes, internal diffusion occurs so quickly (i.e., there is small resistance inside the porous solid) which temperature and moisture gradients are neglected. Therefore, based in these information, in this chapter two different analyses will be given to describe heat and mass transfer in porous body with arbitrary shape: lumped and distributed system analyses.

2 Mathematical Modeling in Porous Bodies: Macroscopic Analysis

Transport phenomena in porous bodies with arbitrary shape is very complex involving heat and mass transfer and sometimes phase change into the solid. A theoretical treatment for this problem is based upon the traditional method and start with a potential balance in a differential control volume with arbitrary shape in macroscopic scale (i.e. porous material is represented as a fictitious continuum). Another way is to derive the macroscopic formulation from microscopic balance equations by means of volume averaging at level of pores [53]. Figure 2 illustrate an elementary control volume in the orthogonal coordinate system at macroscopic scale. In the next section will be presented the lumped and distributed mathematical models for predict heat and mass transport within the porous bodies.

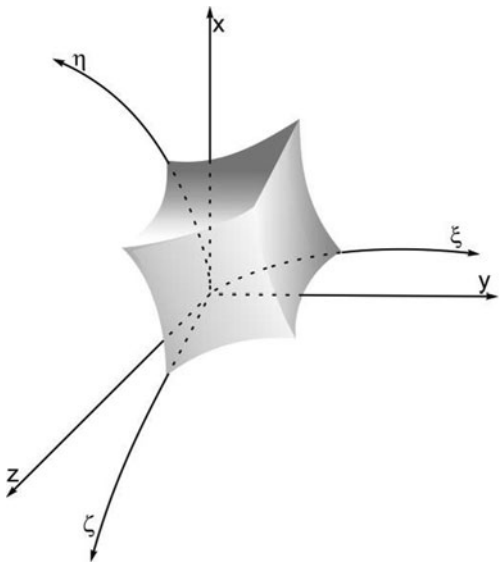

Fig. 2 Orthogonal curvilinear volume within the porous body

2.1 Distributed System Analysis

2.1.1 General Modeling

Distributed system analysis is the more actual method to study diffusion and convection transient problems. This method is used when internal gradients of the potential into the solid are significant. To help us better understand this physical problem kindly consider the Fig. 3 where the cool and moist porous body with arbitrary shape is surrounded by a flowing (or stagnant) unsaturated fluid (gas) at different thermodynamic conditions. So, we have heat flux from the external fluid to the body and mass flux from itself to the external fluid surrounding it. Under assumptions of a local equilibrium between fluid and solid phases into the body (potential reach equilibrium between the phases instantaneously) transport of the potential (heat or mass) into itself can be predicted by mixture model (pure diffusion). The validate of the assumption of local equilibrium remains in discussion, especially when the timescale of transient diffusion is short and the transport properties ratio between the fluid and solid matrix is very different from unity [23]. Kaviany [28] reports that for very fast transients and when significant internal generation exists in the solid or fluid phases local equilibrium condition may not be satisfied.

Then, under local equilibrium macroscopic condition, we can describe heat and mass transfer within an arbitrary shape porous body including volumetric generation term, by using the following general conservation equation (written in an orthogonal generalized coordinates):

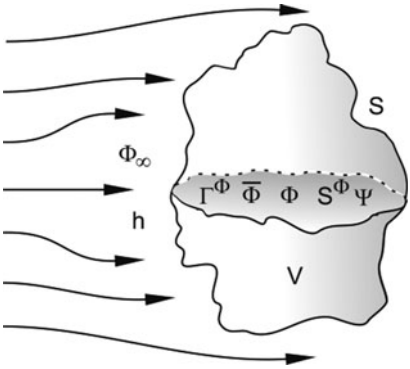

Fig. 3 Schematic of the moist capillary-porous body with an arbitrary shape surrounded by an unsaturated fluid

$$\frac{\partial}{\partial t}\left(\frac{\Psi\Phi}{J}\right) = \nabla\cdot(\Gamma^{\Phi}\nabla\Phi) + \frac{S^{\Phi}}{J} \tag{1}$$

where Ψ and Γ^{Φ} represent effective transport properties, t is the time and Φ is the potential of transport. In the last term, S^{Φ} is the source term and J is the Jacobian of the transformation given by $J = \hat{U}\hat{V}\hat{W}$, being $\hat{U}$, $\hat{V}$ and $\hat{W}$ metric coefficients. The metric coefficients, Laplacian, gradient of the potential Φ, differential volume and differential areas of the control volume are given as follows [2, 42]:

- Metric coefficients of the transformation:

$$\frac{1}{\hat{U}^2} = \left(\frac{\partial x}{\partial \xi}\right)^2 + \left(\frac{\partial y}{\partial \xi}\right)^2 + \left(\frac{\partial z}{\partial \xi}\right)^2 \tag{2}$$

$$\frac{1}{\hat{V}^2} = \left(\frac{\partial x}{\partial \eta}\right)^2 + \left(\frac{\partial y}{\partial \eta}\right)^2 + \left(\frac{\partial z}{\partial \eta}\right)^2 \tag{3}$$

$$\frac{1}{\hat{W}^2} = \left(\frac{\partial x}{\partial \zeta}\right)^2 + \left(\frac{\partial y}{\partial \zeta}\right)^2 + \left(\frac{\partial z}{\partial \zeta}\right)^2 \tag{4}$$

  where $x = f_1(\xi, \eta, \zeta)$, $y = f_2(\xi, \eta, \zeta)$ and $z = f_3(\xi, \eta, \zeta)$ are Cartesian coordinates and ξ, η and ζ are coordinates of the new orthogonal coordinates system.
- Laplacian of the potential Φ:

$$\nabla\cdot(\Gamma^{\Phi}\nabla\Phi) = \left\{\frac{\partial}{\partial\xi}\left[\left(\frac{\hat{U}}{\hat{V}\hat{W}}\right)\Gamma^{\Phi}\frac{\partial\Phi}{\partial\xi}\right] + \frac{\partial}{\partial\eta}\left[\left(\frac{\hat{V}}{\hat{U}\hat{W}}\right)\Gamma^{\Phi}\frac{\partial\Phi}{\partial\eta}\right] + \frac{\partial}{\partial\zeta}\left[\left(\frac{\hat{W}}{\hat{U}\hat{V}}\right)\Gamma^{\Phi}\frac{\partial\Phi}{\partial\zeta}\right]\right\} \tag{5}$$

- Gradient of the potential Φ:

$$\nabla\Phi = \text{Grad}\,\Phi = \hat{U}\frac{\partial\Phi}{\partial\xi}\vec{i}_{\xi} + \hat{V}\frac{\partial\Phi}{\partial\eta}\vec{i}_{\eta} + \hat{W}\frac{\partial\Phi}{\partial\zeta}\vec{i}_{\zeta} \tag{6}$$

where $\vec{i}_{\xi}, \vec{i}_{\eta}$ and $\vec{i}_{\zeta}$ are unit vectors in the directions of ξ, η and ζ, respectively.

- Differential volume:

$$dV = \frac{1}{\hat{U}\hat{V}\hat{W}}d\xi\,d\eta\,d\zeta \tag{7}$$

To solve the diffusion partial differential equation (Eq. 1) in conjunction with appropriate considerations and boundary conditions different analytical (for example, separation of variables and Galerkin-based integral method) and numerical (for example, finite-difference, finite-element, boundary-element and finite-volume) techniques can be used.

Based on a review of the technical literature, it can be noted that some works have been directed to analytically solve the diffusion problems with specified boundary conditions and constant thermo-physical properties. These works are applied to few geometric bodies only, specifically: parallelepipeds, cylinders, spheres and plates [11, 19, 39, 59, 60] and for prolate and oblate spheroidal bodies [3, 7, 12, 20–22, 35, 38, 47].

Products of infinite series and complex integrals give the analytical solution for diffusion problems inside prolate spheroidal bodies. Depending on the initial and boundary conditions, the series are, for example, in Bessel functions and Legendre polynomials, both of high order. Each series is formed by coefficients that are very complex to obtain. Therefore, to obtain an analytical solution of a partial differential equation with a high level of complexity is sometimes difficult, in this case a numerical solution may be used to model the phenomenon, especially when variable thermo-physical properties are used. In this section, the focus will be given to heat and mass transfer (drying) in spheroidal porous bodies including change dimensions.

2.1.2 Modeling Applied to Prolate Spheroids

During drying of capillary-porous materials such as fruits and vegetables, moisture migration (in liquid and vapor phases) inside the solid can occurs by various mechanisms such as diffusion by concentration gradients, capillary forces, shrinkage, pressure gradients and temperature gradients. Vapor phase is expected to be significant for high-intensity drying (for example, in high temperature, typically higher than the 100°C) [53] and for moderate drying but close to end of process where lower moisture content is found (typically, moisture content lower than the 20% dry basis) [17, 48]. Because of the complexities of the mechanism

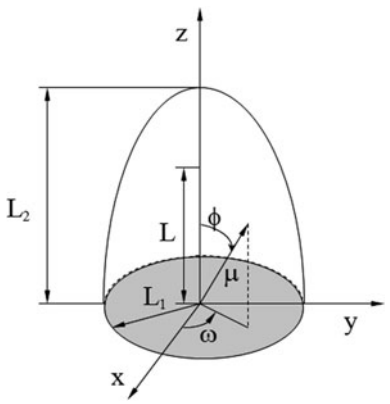

Fig. 4 Geometrical parameters of a prolate spheroidal solid

involved in the process through the irregular void configuration many theories has been proposed to predict moisture movements into the porous solids. Details this topic can be found, for example, in [9, 10, 14, 18, 30, 40, 41, 56, 58, 62].

In many physical problems, depending on the shape of the body it is better to use a new orthogonal coordinate system ξ, η and ζ instead of the Cartesian coordinate system x, y and z. In the case of the body with ellipsoidal geometric shape, the prolate spheroidal coordinate system is adequate. The relationships between Cartesian and prolate spheroidal coordinate systems are given by [2, 16, 42, 67]:

$$x = L\sqrt{(1-\xi^2)(\eta^2-1)}\,\zeta \tag{8}$$

$$y = L\sqrt{(1-\xi^2)(\eta^2-1)}\sqrt{(1-\zeta^2)} \tag{9}$$

$$z = L\,\xi\,\eta \tag{10}$$

where $\xi = \cosh\,\mu$; $\eta = \cos\,\phi$; $\zeta = \cos\,\omega$ and $L = (L_2^2 – L_1^2)^{1/2}$ (see Fig. 4). It is important to note that in the limit when L becomes zero, the prolate spheroidal solid reduces to sphere and when L becomes to L_2, the prolate spheroid assumes the shape of the infinite cylinder. So, it is true that, the cylindrical and spherical coordinate systems are particular cases of the prolate spheroidal coordinate system.

For simplicity, Lima et al. [37] developed a model that assumes which water migrates from the center of the solid to external surrounding by only liquid diffusion. So, gravity, capillary or another effect are neglected. Besides, the following considerations were made: the porous solid is homogeneous, deformable, and does not interact chemically with the fluid phase into itself; the porous body is axially symmetric around z-axis; the shape of solid is approached to an ellipsoid of revolution; the solid is composed of water in liquid phase and solid material; the mechanisms of drying (moisture migration) are diffusion and shrinkage; the shrinkage of the solid is equal to the volume of water evaporated and it is axi-

symmetric around the z-axis; the moisture content and temperature field is considered symmetric around z-axis in any time and uniform in the beginning of the process; the phenomenon occurs under evaporative and convective boundary conditions including heating of vapor produced at the surface. No energy and mass generation occurs; diffusion phenomenon occurs under falling rate; thermophysical properties are variables during drying process.

Then, calculating the metric coefficients $\hat{U}, \hat{V}$ and $\hat{W}$, the volume of the body and the Laplacian for the new coordinate system, utilizing the symmetry around the z-axis, $\partial/\partial\omega = 0 \Rightarrow \partial/\partial\zeta = 0$ and using the considerations presented, the governing mathematical equations can be formulated in the prolate spheroidal coordinate system, see [37], as follows.

Mass Transfer Model

For mass transfer process, the variables $\Phi = M$, $\Gamma^{\Phi} = \rho_s D$ and $\Psi = \rho_s$. Then, when no mass source exists, Eq. 1 may be written in the short form as follows:

$$\frac{\partial M}{\partial t} = \frac{1}{L^2\left(\xi^2 - \eta^2\right)}\left\{\frac{\partial}{\partial \xi}\left[D\left(\xi^2 - 1\right)\frac{\partial M}{\partial \xi}\right] + \frac{\partial}{\partial \eta}\left[D\left(1 - \eta^2\right)\frac{\partial M}{\partial \eta}\right]\right\} \tag{11}$$

To solve Eq. 11, the following initial and boundary conditions are used:

$$M(\xi, \eta, t = 0) = M_0 \tag{12}$$

$$\frac{D}{L}\sqrt{\frac{\left(\xi^2 - 1\right)}{\left(\xi^2 - \eta^2\right)}}\left.\frac{\partial M}{\partial \xi}\right|_{\xi = \xi_f} + h_m[M(\xi = \xi_f, \eta, t) - M_\infty] = 0 \tag{13}$$

where $\xi_f = L_2/L$ at the surface, M is the moisture content in dry basis, M_∞ represents equilibrium moisture content, D is the mass diffusion coefficient, h_m is the convective mass transfer coefficient and ρ_s represents density of the dry solid.

The mean moisture content of the porous body in every instant can be calculated as follows:

$$\overline{M} = \frac{1}{V}\int_V M dV \tag{14}$$

where V is the volume of the solid.

Heat Transfer Model

For heat transfer process, we have replaced $\Phi = \theta$, $\Gamma^{\Phi} = k_p$ and $\Psi = \rho_p c_p$ in the Eq. 1. In this case the transient heat conduction equation is given by:

$$\frac{\partial(\rho_p c_p \theta)}{\partial t} = \frac{1}{L^2(\xi^2 - \eta^2)} \left\{ \frac{\partial}{\partial \xi} \left[k_p (\xi^2 - 1) \frac{\partial \theta}{\partial \xi} \right] + \frac{\partial}{\partial \eta} \left[k_p (1 - \eta^2) \frac{\partial \theta}{\partial \eta} \right] \right\} \quad (15)$$

To solve Eq. 15, the following initial and boundary conditions can be used:

$$\frac{k_p}{L} \sqrt{\frac{(\xi^2 - 1)}{(\xi^2 - \eta^2)}} \frac{\partial \theta}{\partial \xi}\bigg|_{\xi=\xi_f} + h_c[\theta_\infty - \theta(\xi = \xi_f, \eta, t)] + \frac{\rho_s V}{S} \frac{\partial \overline{M}}{\partial t} \{h_{fg} + c_v[\theta_\infty - \theta(\xi = \xi_f, \eta, t)]\} = 0 \quad (16)$$

$$\theta(\xi, \eta, t = 0) = \theta_0 \quad (17)$$

where θ is the temperature, θ_∞ represents equilibrium temperature, k_p is the thermal conductivity of the moist solid, S is the surface area, h_c is the convective heat transfer coefficient, ρ_p represents density of the moist solid, c_v and c_p are specific heat of the vapor and moist solid, respectively, and h_{fg} is the latent heat of vaporization of water within the moist solid.

The mean temperature of the porous body during diffusion phenomenon can be calculated as presented to mass transfer process. So, Eq. 14 can be rewritten as follows:

$$\overline{\theta} = \frac{1}{V} \int_V \theta dV \quad (18)$$

Shrinkage Model

During drying process, the porous body changes dimensions by heating (dilatation) and loss of water (contraction, well-known as shrinkage). Dilatation phenomenon is insignificant as compared with shrinkage, because the volumetric dilatation coefficient is smallest that the shrinkage coefficient, especially for fruits and vegetables. However, when moisture migration is stopped, dimension variation due to heating is very important phenomenon, and it provokes large thermal stress within the solid, especially for clay materials. A fundamental point in the shrinkage model (dimension variation by moisture migration) is the inclusion of an equation that relates both volume and mean moisture content. According to Fig. 5, the following mathematical relation for linear shrinkage was proposed by [34, 36, 37]:

$$(V)_t = V_o(\overline{\beta}_1 + \overline{\beta}_2 \overline{M}) \quad (19)$$

Since $t = 0$ implies $\overline{M} = M_o$ and $(V)_{t=0} = V_o$, so Eq. 19 can be written as follows:

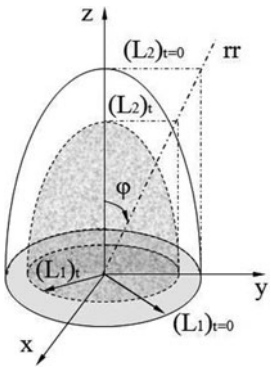

Fig. 5 Shrinkage of the prolate spheroidal solid during diffusion process

$$\frac{(V)_t}{V_o} = 1 - \overline{\beta}_2(M_o - \overline{M}) \tag{20}$$

where $\overline{\beta}_1$ and $\overline{\beta}_2$ are the shrinkage coefficients of the moist solid. From Fig. 5, it can be verified that:

$$\left(\frac{L_2}{L_1}\right)_t = \left(\frac{L_2}{L_1}\right)_{t=0} = \tan(\varphi) \tag{21}$$

2.1.3 Application to Drying of Banana

Numerical solution of these formulations were made by [34, 36, 37] to predict heat and mass transfer within the peeled banana (Musa acuminata, Cavendish subgroup, "Nanicão" variety) by using experimental data reported by [52, 54, 55]. Transport properties [31, 32, 63] were obtained as follows:

$$\rho_p = \frac{\left[1 + \left(\frac{\overline{M}}{1+\overline{M}}\right)\right]}{\left[\frac{1}{1810} + \frac{1.04\left(\frac{\overline{M}}{1+\overline{M}}\right)}{1020}\right]} \tag{22}$$

$$c_p = 0.837 + 3.349\left(\frac{\overline{M}}{1+\overline{M}}\right) \tag{23}$$

$$\bar{k}_p = 0.148 + 0.493\left(\frac{\overline{M}}{1+\overline{M}}\right) \tag{24}$$

The heat of vaporization of pure water was used instead of the heat of vaporization of the moisture within of the banana, at particular moisture content, in the same air drying condition. The estimate value of the shrinkage coefficient in Eq. 20 applied to the banana was $\overline{\beta}_2 = 0.269$, computed for moisture contents ranging from 3.16 to 0.34 kg/kg dry basis.

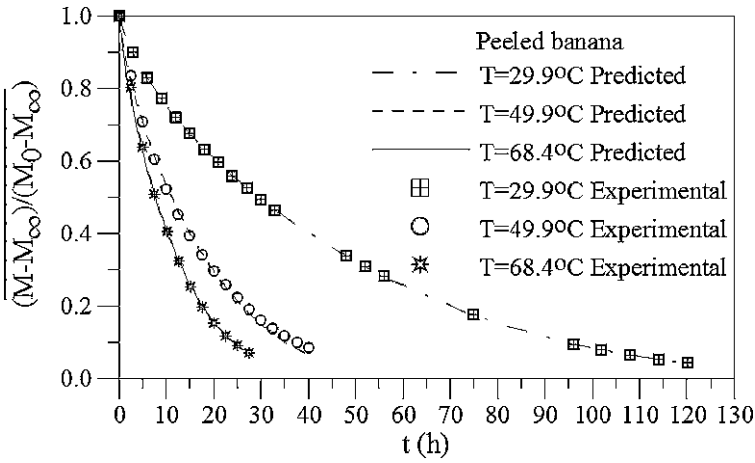

Fig. 6 Comparison between predicted and experimental dimensionless mean moisture content during the drying of peeled banana

Besides, based on the behavior of the temperature in the center of the banana during the experimental drying process, the authors have proposed the following equation for thermal diffusivity:

$$\alpha = \frac{A_1}{\left[A_2\left(1 - M^{*A_3}\right) + A_4\right]} \tag{25}$$

where $M^* = (M - M_\infty)/(M_0 - M_\infty)$ and $\alpha = k_p/\rho_p c_p$ is the thermal diffusivity. Note that k_p vary as a function of the position and time while ρ_p, $\bar{k}_p$ and c_p varies as a function of the mean moisture content.

Based on the works of the Pasternak and Gauvin [51] and Sehlin, cited by [34, 36, 37, 43] have proposed the following equation for the heat transfer coefficient:

$$h_c = \frac{A_5}{\left[(L')^{2/3}\right]} \tag{26}$$

The characteristic length L' can be obtained by the total surface area of the particle divided by the perimeter of the maximum projected area perpendicular to flow $[2\pi(L_1)_t]$. It is noted that heat transfer coefficient is variable with the time because L' and shape of the body changes during the process. Constants A_i were obtained fitting Eqs. 25 and 26 to experimental data.

Numerical results were compared with experimental data of the moisture content and center temperature obtained during the drying of bananas, as illustrated in the Figs. 6 and 7, and transport coefficients (D, h_m, α and h_c) estimated by using the least square error technique. It can be seen in these figures that a good agreement was obtained. Some discrepancies appear at lower moisture contents

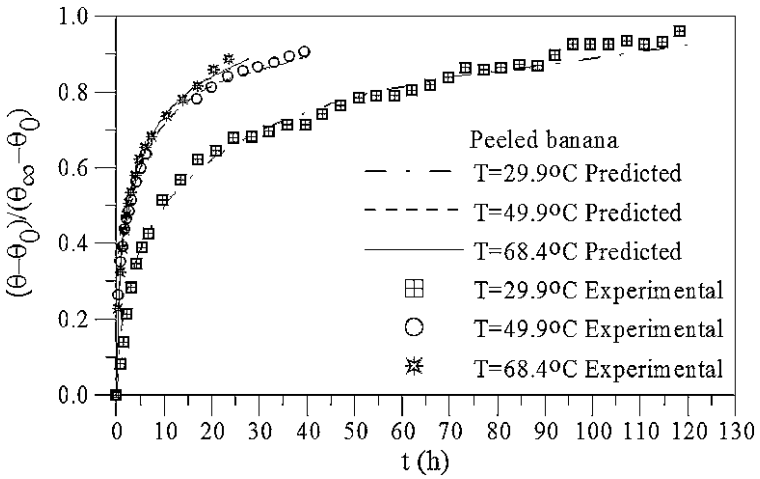

Fig. 7 Comparison between predicted and experimental dimensionless center temperature of the peeled banana during the drying process

Table 1 Air and banana experimental conditions

Air	Peeled banana						Drying time			
T (°C)	UR (%)	v (m/s)	M_0 (d.b.)	M_{fn} (d.b.)	M_∞ (d.b.)	θ_0 (°C)	θ_{fn} (°C)	L_2 (m)	L_1 (m)	t (h)
29.9	35.7	0.38	3.43	0.32	0.143	19.1	29.7	0.0586	0.0161	121.8
49.9	19.2	0.37	3.21	0.32	0.058	20.3	47.1	0.0590	0.0152	40.8
68.4	7.3	0.39	2.95	0.22	0.012	25.3	64.2	0.0589	0.01545	27.6

and higher center temperatures due to the fact that for longer drying times the assumption of linear shrinkage is probably not valid, like was assumed in Eq. 20. Table 1 shows the air and porous material conditions.

The moisture content distribution inside the solid is important in order to study the evolution of mechanical stress, developed into the body due to high moisture gradients. Figures 8 and 9 show the simulated moisture content and temperature inside the peeled banana exposed to drying for 1.11, 5.00 and 15.00 h, respectively, for T = 68.4°C. In both results it can be seen that the highest moisture gradients occur near the surface. There is strong drying also close to the focal point (y = 0, z = L) and consequently the highest shrinkage velocity is found in this region. Therefore, these areas must be more susceptible to having problems such as cracks and fissures, due to higher thermal and moisture gradients and shrinkage velocity which provokes thermal and hydrical stresses within the capillary-porous body, having possibility of altering the color, texture and flavor, reducing in this way, the quality of the fruit.

Tables 2 and 3 present the transport coefficients as well as the variance obtained for all experiments. The small variance indicates that the model proposed presents

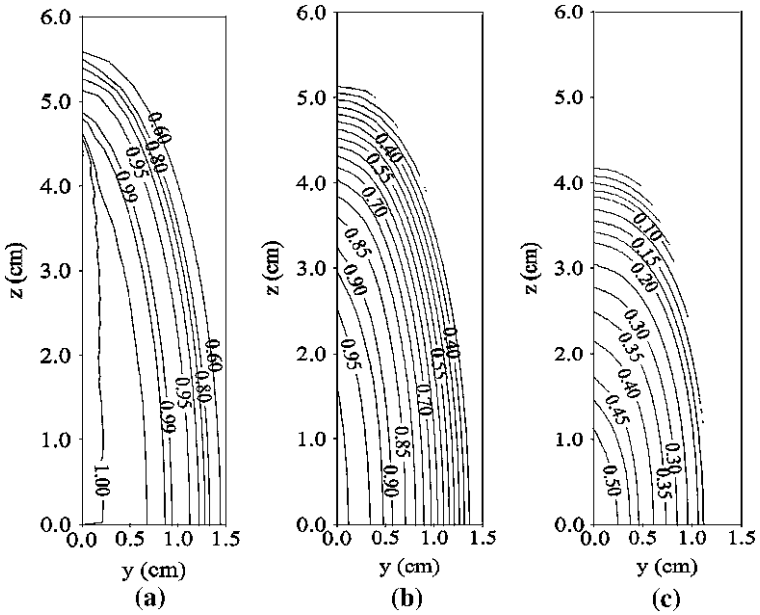

Fig. 8 Dimensionless moisture content distribution (M*) within the peeled banana (T = 68.4°C). **a** t = 1.11 h, **b** t = 5.00 h, **c** t = 15.00 h

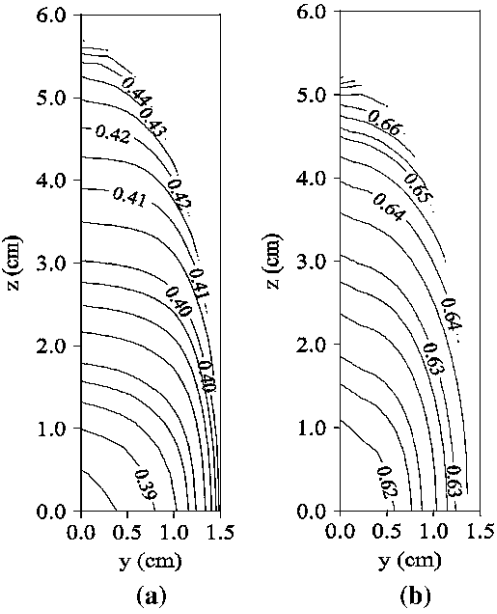

Fig. 9 Dimensionless temperature distribution ($1-\theta^*$) within the peeled banana during drying process (T = 68.4°C). **a** t = 1.11 h, **b** t = 5.00 h

Table 2 Convective mass transfer and mass diffusion coefficients and variance estimated for all drying experiments

T (°C)	D × 10^{+10} (m^2/s)	h_m × 10^{+8} (m/s)	$\bar{S}^2 = \frac{\sum_{i=1}^{n}\left(\Phi^*_{i,Num}-\Phi^*_{i,Exp}\right)^2}{(n-\hat{n})}$ (×10^{+4})
29.9	1.65	10.10	0.96
49.9	4.57	21.35	0.91
68.4	8.63	26.56	1.42

Table 3 Coefficients A_i of Eqs. 25 and 26 and variance obtained in each experiment

T (°C)	α (m^2/s)				h_c (W/m^2K)	$\bar{S}^2 = \frac{\sum_{i=1}^{n}\left(\Phi^*_{i,Num}-\Phi^*_{i,Exp}\right)^2}{(n-\hat{n})}$ (×10^{+4})
	A_1 × 10^{+9}	A_2	A_3	A_4	A_5	
29.9	0.88	0.60	2.46	0.01	57.04	2.37
49.9	2.38	0.60	2.46	0.01	58.49	0.89
68.4	2.70	0.54	2.93	0.01	63.56	1.48

good agreement with the experimental data. The lowest temperature gives the highest internal resistance to the moisture migration and heat flux. As expected, all the transport coefficients increase strongly with the temperature.

The heat transfer coefficient is not a property of a material. It is used to quantify the rate of heat transfer at the surface of the body. It is dependent on the fluid velocity, fluid properties, roughness of the surface and shape of the body, as well as of the temperature difference between the surface and the fluid surround it.

In practice, heat flux and temperature on the surface of a material are very difficult to measure without disturbing the heat transfer. In food with high moisture content, mass transfer accompanies heat transfer; this fact is still an additional complication in the measurement of the heat transfer coefficient.

During drying process banana shrinks. This modifies the shape of the body, decreases the area of heat transfer and increases the superficial roughness of the material. This last characteristic provides an increase of the turbulence level in the boundary layer, favoring therefore, the change of energy between air and material. The heat transfer coefficient is also dependent on the air velocity, however this effect is not visible in Eq. 26, due to the fact that the air velocity was practically constant in all of the experiments, so, this effect is incorporate in the constant A_1, as well as the effects of the properties of air, see [36, 37].

2.2 Lumped System Analysis

2.2.1 General Formulation

In the distributed system analysis significant temperature and moisture gradients occurs inside the solid in every time. So, moisture and temperature are functions of

the position inside the solid and time. However, when internal resistance to heat and mass fluxes is very small, heat and mass transfer takes place at the surface of the solid and uniform temperature and moisture distribution through the porous body is verified. This situation occurs when the transport property Γ^{Φ} is infinite. For this situation, no such material is known to exist.

Lumped system analysis is a simplest approach in diffusion and convection transient problems which may be used whenever diffusion inside the material is much faster than the diffusion across the boundary of the solid. In this approach, lumped parameters typically combine aspects of several different physical phenomena such as shrinkage, heterogeneity and shape of the body, and under appropriate situation may actually give a better result than a more complex formulation, for example, a distributed model. Besides require less input data to theoretically study the physical problem.

For best understanding, consider again the moist porous body with arbitrary shape as illustrated in the Fig. 3 where the potential Φ is spatially uniform within the body in any time, so, we have $\Phi(x, y, z, t) = \overline{\Phi}(t)$. This way, we can write the Eq. 1 as follows:

$$\frac{\partial}{\partial t}\left(\frac{\Psi\Phi}{J}\right) = -\Phi'' dS + \frac{S^{\Phi}}{J} \tag{27}$$

where Φ'' is the flux of the potential Φ per area unit and dS is the differential surface area of the solid.

After the integration of Eq. 27 over the solid, we obtain

$$\Psi V \frac{d\overline{\Phi}}{dt} = -\Phi'' S + \Phi''' V \tag{28}$$

being S and V the surface area and volume of the solid, respectively, and Φ''' is the generation term per volume unit. The quantities Φ'' and Φ''' can be positive or negative, or can be still constant or variable in the time.

2.2.2 Mass Balance

For a body of volume V, mass balance requires that the mass transferred into the porous body that across the surface plus mass generation within itself equals the mass variation of the body in any time. This way, we can write:

$$V \frac{d\overline{M}}{dt} = -h_m S\left(\overline{M} - \overline{M}_{\infty}\right) + \dot{M} V \tag{29}$$

Separating variables and integrating since $t = 0$ (where $\overline{M} = \overline{M}_0$) until $t = t$ (where $\overline{M} = \overline{M}(t)$) as limits, we then obtain:

$$(\overline{M} - \overline{M}_\infty) = \left[(\overline{M}_0 - \overline{M}_\infty) - \frac{\dot{M}V}{h_m S}\right] \exp\left[\left(-\frac{h_m S}{V}\right) t\right] + \frac{\dot{M}V}{h_m S} \tag{30}$$

Now, defining the following dimensionless parameters,

$$\overline{M}^* = \frac{\overline{M} - \overline{M}_\infty}{\overline{M}_0 - \overline{M}_\infty} \tag{31}$$

$$S^* = \frac{SL_c}{V} \tag{32}$$

$$Bi_m = \frac{h_m L_c}{D} \tag{33}$$

$$Fo_m = \frac{Dt}{L_c^2} \tag{34}$$

$$P^* = \frac{\dot{M}L_c}{h_m S^* (\overline{M}_0 - \overline{M}_\infty)} \tag{35}$$

We write Eq. 30 shortly as:

$$\overline{M}^* = P^* + (1 - P^*)\exp(-S^* Bi_m Fo_m) \tag{36}$$

In dehydration problems, the parameter $\overline{M}_\infty$ is so-called equilibrium moisture content and correspond to maximum moisture content reached by the porous body when is in equilibrium condition with the fluid that surround it at constant thermodynamic condition (residual bound moisture). The value of the moisture content depends on the relative humidity (water activity), temperature of the drying air and composition of the material. It is determined experimentally, and it is usually presented as the moisture sorption isotherms of the material. In general, for hygroscopic materials residual bound moisture appear like water trapped in closed capillaries, the water component of juices and water absorbed by surface forces [6].

The sorption phenomena by solid, mainly fruits, it has received much attention because of its role in packaging, and in quality changes during drying and storage. Changes in food materials, for example, includes microbial changes, enzymatic chemical reactions, physical and structural changes, and aroma retentions (loss of flavor). Detailed discussion about this topic can be found in [9, 56, 57].

2.2.3 Energy Balance

From the analysis of the Fig. 3 heat is transferred from the surrounding to the body and it is used to evaporate the water at the surface of the body, to heat the vapor since saturation temperature until air drying temperature, and to heat the body. So, the temperature of the body will increase with the time because of this heat flux

and heat generation within itself. Therefore, we can write an energy balance as follows:

$$\rho_p V \frac{d\overline{\theta}}{dt} = \frac{h_c\left(\overline{\theta}_\infty - \overline{\theta}\right) + \frac{\rho_s V}{S}\frac{d\overline{M}}{dt}\left[h_{fg} + c_v\left(\overline{\theta}_\infty - \overline{\theta}\right)\right]}{c_p} S + \frac{\dot{q} V}{c_p} \tag{37}$$

Since the term $c_v(\overline{\theta}_\infty - \overline{\theta}) \ll h_{fg}$, it will be neglected. By introducing Eqs. 29 and 30 into the Eq. 37, we can write one in the short form as

$$\begin{aligned}\frac{d\overline{\theta}}{dt} = &\left\{\left[-\rho_s h_m\left(\overline{M}_0 - \overline{M}_\infty\right) + \frac{\rho_s V \dot{M}}{S}\right]\frac{h_{fg} S}{\rho_p V c_p}\right\}\exp\left[-\left(\frac{h_m S}{V}\right)t\right] \\ &+ \frac{h_c S}{\rho_p c_p V}\left(\overline{\theta}_\infty - \overline{\theta}\right) + \frac{\dot{q}}{\rho_p c_p}\end{aligned} \tag{38}$$

Therefore, solving the ordinary differential equation by using the initial condition $t = 0$ where $\overline{\theta} = \overline{\theta}_0$, we then obtain

$$\begin{aligned}\left(\overline{\theta} - \overline{\theta}_\infty\right) = &\left[\left(\overline{\theta}_0 - \overline{\theta}_\infty\right) - \frac{\dot{q} V}{h_c S}\right]\exp\left[-\left(\frac{h_c S}{\rho_p c_p V}\right)t\right] + \frac{\dot{q}}{\rho_p c_p} \\ &+ \frac{\left[\frac{-\rho_s h_m S\left(\overline{M}_0 - \overline{M}_\infty\right)}{V} + \rho_s \dot{M}\right]\frac{h_{fg}}{\rho_p c_p}}{\left(\frac{h_c}{\rho_p c_p} - h_m\right)\frac{S}{V}} \times \left\{\exp\left[-\left(\frac{h_m S}{V}\right)t\right] - \exp\left[-\left(\frac{h_c S}{\rho_p c_p V}\right)t\right]\right\}\end{aligned} \tag{39}$$

Now, consider the following dimensionless parameters,

$$V^* = \frac{h_c\left(\overline{\theta}_\infty - \overline{\theta}_0\right)}{h_{fg}\, h_m\, \rho_s\left(\overline{M}_0 - \overline{M}_\infty\right)} \tag{40}$$

$$Q^* = \frac{\dot{q} L_c}{S^*\, h_c\left(\overline{\theta}_\infty - \overline{\theta}_0\right)} \tag{41}$$

$$R^* = \frac{\rho_p\, c_p\left(\overline{\theta}_\infty - \overline{\theta}_0\right)}{h_{fg}\, \rho_s\left(\overline{M}_0 - \overline{M}_\infty\right)} \tag{42}$$

$$Fo_h = \frac{\alpha t}{L_c^2} \tag{43}$$

$$\overline{\theta}^* = \frac{\overline{\theta} - \overline{\theta}_\infty}{\overline{\theta}_0 - \overline{\theta}_\infty} \tag{44}$$

$$Bi_h = \frac{h_c L_c}{k_p} \tag{45}$$

By using the non-dimensional groups defined above, substituting into Eq. 39 and rearranging the terms yields

$$\overline{\theta}^{*} = \left[\left(\frac{P^{*}-1}{V^{*}-R^{*}}\right)+Q^{*}+1\right]\exp\left(-S^{*}Bi_{h}Fo_{h}\right) - \left(\frac{P^{*}-1}{V^{*}-R^{*}}\right)\exp\left(-S^{*}Bi_{m}Fo_{m}\right)-Q^{*} \quad (46)$$

Most lumped models are derived by simplifying the distributed models. By analyzing the Eqs. 30, 36, 39 and 46 some information we can obtain. For example: (1) When the third term is null, Eq. 39 is similar to Eq. 30 (i.e., no coupling between heat and mass transfer exists), (2) If thermal equilibrium is considered between the porous particles and fluid surrounding it, only Eq. 30 or 36 is used to predict the wetting or drying process. When $\dot{M}=0$ and thermal equilibrium exist, the resultant equation (Eq. 30) is well-known as Lewis model [1, 9, 33, 49, 50], and (3) If no heat and mass generation and $h_m \rightarrow 0$ are assumed (i.e., moisture content remain constant along the process), only Eq. 39 or 46 is used to predict heating or cooling of the porous particles during the transient process. Under these assumptions, the simplified equation is well-known as Newton's law of cooling [44].

2.2.4 Criteria for Lumped System Analysis

Lumped system analysis is the simplest and most convenient method that can be used to solve transient diffusion problems because the governing equations are solved easily by using analytical techniques. Then, it is evident that is necessary to establish conditions for the applicability of this technique with reasonable accuracy. This method assumes uniform moisture and temperature gradients within the individual particles, which occurs when the internal resistance of diffusion approximate to zero. So, convection at the surface of the solid is lower than the diffusion within the solid, and the process is controlled by external convection.

According to literature, it is accepted that lumped system analysis is applicable if [4, 24, 29]

$$Bi = \frac{hL_{c}}{\Gamma^{\Phi}} < 0.1 \quad (47)$$

where $L_c = V/S$ is a characteristic length for bodies with arbitrary shape, and h and Bi are the convective transfer coefficient and Biot number, respectively, for heat or mass transfer. If the volume or surface area of the solid cannot be determined, we can use another characteristic length, for example, one dimension of the body or one spatial scale corresponding to the desirable maximum temperature difference within the body.

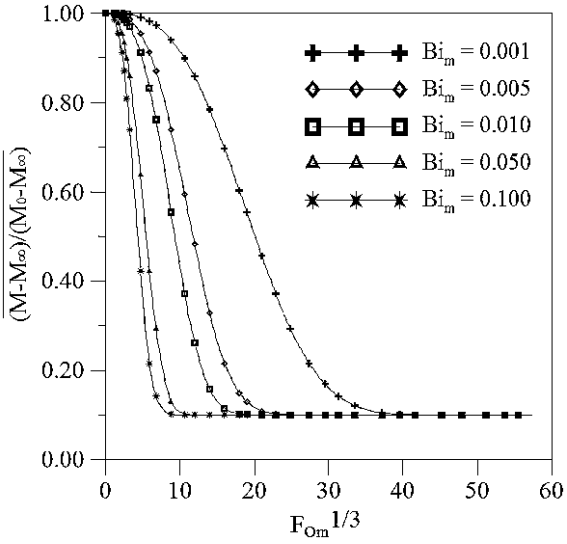

Fig. 10 Effect of the parameter Bi_m on the dimensionless mean moisture content as a function of the Fo_m ($P^* = 0.10$ and $S^* = 0.10$)

Based in the Eq. 47, if the diffusion resistance of the body is less that 10% of the convective resistance at its surface, the moisture and temperature distribution will be uniform within an error of 5%, during transient conditions. Since: (1) 20% uncertainty in the convective transfer coefficient (heat or mass) in most cases is acceptable, (2) to consider h to be constant and uniform at the surface of the body is also an approach questionable, especially for arbitrary shape, and (3) few experimental data for bodies with arbitrary shape are reported in the literature, an error of 5% is perfectly acceptable.

2.2.5 Application to Drying of Irregularly-Shaped Solid

As general application and independent of the nature (fruit, vegetable, clay, etc.), chemical composition, chemical reaction and shape of the porous body, and external conditions of the fluid surrounding it, results of the dimensionless temperature and moisture content are shown, for fixed values of the non-dimensional groups defined before.

Figures 10, 11, 12 and 13 illustrate the effect of the parameters Bi_m, Bi_h and S^* on the heating and loss of water of the porous body. After analysis of the curves we can note a strong influence of these parameters on the process. The dimensionless parameter S^* is mainly related to surface are and volume relationships (shape factor) of the solid. So, to consider a solid with arbitrary shape like sphere with equivalent diameter (diameter of the sphere having the equivalent volume as the irregularly-shaped porous body) as reported in the literature [64] is a strong approach and error in the prediction of the transient process must be expected.

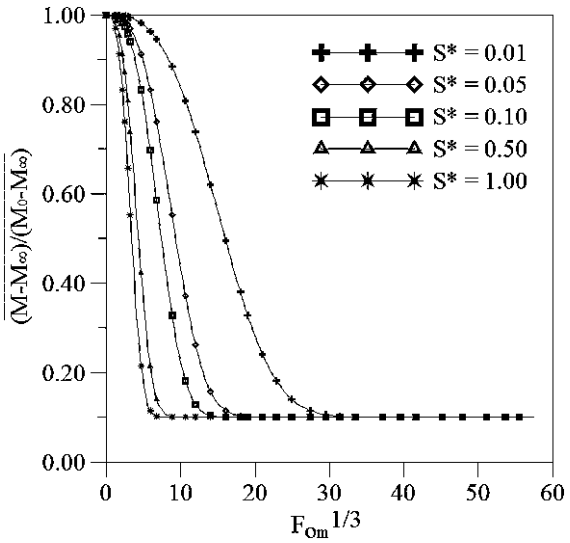

Fig. 11 Effect of the S^* in the dimensionless mean moisture content as a function of the Fo_m ($P^* = 0.10$ and $Bi_m = 0.02$)

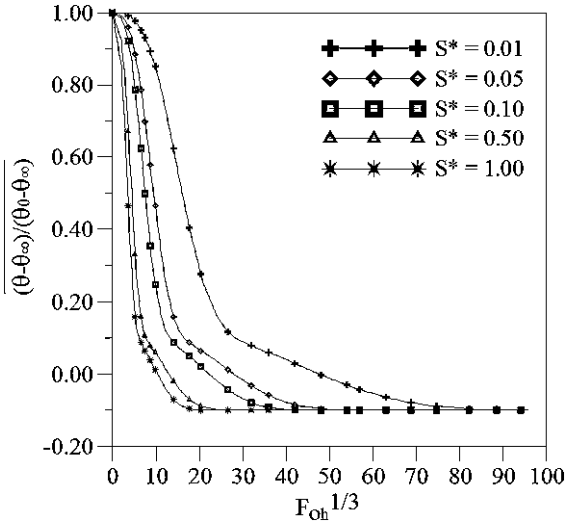

Fig. 12 Effect of the parameter S^* on the dimensionless mean temperature as a function of the Fo_h ($P^* = 0.10$, $V^* = 5.00$, $R^* = 1.00$, $Q^* = 0.10$, $Bi_h = 0.02$ and $Bi_m = 0.02$)

It can be noted that until the instant where $\overline{\theta}^* = P^*$, the process is dominate by heat transfer and mass transfer presents few contribution to modify the temperature of the porous solid. After this point until $\overline{\theta}^* = -Q^*$, the heat rate is influenced by heat generation and mass transfer. Following, hydrothermal equilibrium condition into the solid is reached and the process is controlled by heat and mass source terms.

From the practical view point, in fresh biological products (for example, grains, fruits and vegetables) the moist predominant constituent is water (in the liquid phase mainly) which significantly affect the physical properties of these capillary-

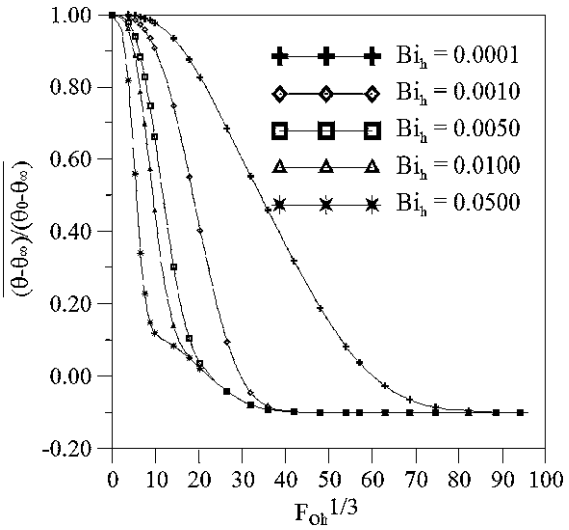

Fig. 13 Effect of the parameter Bi_h on the dimensionless mean temperature as a function of the Fo_h ($P^* = 0.10$, $V^* = 5.00$, $R^* = 1.00$, $Q^* = 0.10$, $S^* = 0.10$ and $Bi_m = 0.02$)

porous bodies. Because of the water content different phenomena occurs itself such as: transpiration, respiration and evaporation.

Transpiration is one process by which biological product loses water by transport of moisture through the skin which evaporates at the surface of the solid. This vapor is removed by convection to the surroundings [8]. This is a very slow mass transfer process. For the other side, all biological products respire after harvest and the normal life process continue. In this process, the following chemical reaction within the porous bodies occurs: sugar and oxygen are combined to give like reaction products Carbon dioxide, water and heat (enthalpy of reaction) [5]. The produced heat (heat generation term) affects the temperature distribution inside the solid and tends to increase the local and mean temperatures. The respiratory heat generation varies with the type and temperature of the porous body. The properties associated with this phenomenon are called thermogenic properties [44].

Evaporation that occurs at the surface of the solid is an endothermic process that cools the surface. As water changes from the liquid to vapor, it absorbs heat from the fluid (air) surrounding it, thereby lowering the produce temperature and vapor pressure at the surface and reducing water loss by transpiration [5].

As final comment, because of the fresh produce starts to deteriorate much faster after harvest, water loss and heat generation must be minimum, thus substantially to prolong the storage life of these products. Postharvest produce quality cannot be improved, only maintained, therefore is very important to maintain freshly harvested produce quality, especially those types with high respiration rates. So, under the theoretical and experimental aspects to study heat and mass transfer in fresh biological products is very important to retards the physiological process of respiration, for example, by using cooling, which slows ripening and the bacteriological process of decay caused by microorganisms [44].

Acknowledgments The authors would like to express their thanks to CAPES (Coordenação de Aperfeiçoamento de Pessoal de Nível Superior, Brazil) and CNPq (Conselho Nacional de Desenvolvimento Científico e Tecnológico, Brazil) for supporting this work, and are also grateful to the authors of the references in this paper that helped in the improvement of quality.

References

1. Abe, T., Afzal, T.M.: Thin-layer infrared radiation drying of rough rice. J. Agric. Eng. Res. **67**, 289–297 (1997)
2. Abramowitz, M., Stegun, I.A.: Handbook of Mathematical Functions. Dover Publications Inc, New York (1972)
3. Alassar, R.S.: Heat conduction from spheroids. J. Heat Transf. **121**, 497–499 (1999)
4. ASHRAE Refrigeration Handbook. American Society of Heating, Refrigeration and Air-Conditioning Engineers, Inc., Chapter 9: Cooling and freezing times of foods, Atlanta (1998a)
5. ASHRAE Refrigeration Handbook. American Society of Heating, Refrigeration and Air-Conditioning Engineers, Inc., Chapter 8: Thermal properties of foods, Atlanta (1998b)
6. Bansal, N.K., Garg, H.P.: Solar crop drying. In: Mujumdar, A.S. (ed.) Advances in Drying. Hemisphere Publishing Corporation, New York (1987)
7. Beck, J.V., Cole, K.D., Haji-Sheikh, A., Litkouhi, B.: Heat Conduction Using Green's Functions. Hemispheric Publishing Corporation, New York (1992)
8. Becker, B.R., Misra, A., Fricke, B.A.: Bulk refrigeration of fruits and vegetables Part I: theoretical considerations of heat and mass transfer. Int. J. Heat. Ventil. Air Cond. Refrig. Res. **2**, 122–134 (1996)
9. Brooker, D.B., Bakker-Arkema, F.W., Hall, C.W.: Drying and Storage of Grains and Oilseeds. AVI Book, New York (1992)
10. Bruin, S., Luyben, K.Ch.A.M: Drying of food materials. a review of recent developments. In: Mujumdar, A.S. (ed.) Advances in Drying. Hemisphere Publishing Corporation, New York (1980)
11. Carslaw, H.S., Jaeger, J.C.: Conduction of Heat in Solids. University Press, New York (1959)
12. Cihan, A., Kahveci, K., Hacihafizoğlu, O., Lima, A.G.B.: A diffusion based model for intermittent drying of rough rice. Heat Mass Transf. **44**, 905–911 (2008)
13. Datta, A.K.: Porous media approaches to studying simultaneous heat and mass transfer in food processes. I: problem formulations. J. Food Eng. **80**, 80–95 (2007)
14. De Groot, S.R., Mazur, P.: Non-Equilibrium Thermodynamics. Dover Publications Inc, New York (1984)
15. de Lemos, M.J.S.: Turbulence in Porous Media: Modeling and Applications. Elsevier, Amsterdan (2006)
16. Flammer, C.: Spheroidal Wave Functions. Stanford University Press, Stanford (1957)
17. Fortes, M.: A Non-equilibrium thermodynamics approach to transport phenomena in capillary-porous media with special reference to drying of grains and foods. Ph.D. Thesis, Faculty of Purdue University, United States of America (1978)
18. Fortes, M., Okos, M.R.: Drying theories: their bases and limitations as applied to foods and grains. In: Mujumdar, A.S. (ed.) Advances in Drying. Hemisphere Publishing Corporation, Washington (1980)
19. Gebhart, B.: Heat Conduction and Mass Diffusion. McGraw-Hill Inc, New York (1993)
20. Hacihafizoğlu, O., Cihan, A., Kahveci, K., Lima, A.G.B.: A liquid diffusion model for thin-layer drying of rough rice. Eur. Food Res. Technol. **226**, 787–793 (2008)
21. Haji-Sheikh, A., Sparrow, E.M.: Transient heat conduction in a prolate spheroidal solid. Trans. ASME J. Heat Transf. **88**, 331–333 (1966)
22. Haji-Sheikh, A., Sparrow, E.M.: The solution of heat conduction problems by probability methods. Trans. ASAE J. Heat Transf. **89**, 121–131 (1967)

23. Hsu, C.-T.: Dynamic modeling of convective heat transfer in porous media. In: Vafai, K. (ed.) Handbook of Porous Media, 2nd edn. CRC Press, Boca Raton (2005)
24. Incropera, F.P., DeWitt, D.P.: Fundamentals of Heat and Mass Transfer. Wiley, New York (2002)
25. Ingham, D.B., Pop, I.: Transport phenomena in Porous Media. Elsevier, Oxford (1998)
26. Ingham, D.B., Pop, I.: Transport Phenomena in Porous Media II. Elsevier, Oxford (2002)
27. Ingham, D.B., Pop, I.: Transport Phenomena in Porous Media III. Elsevier, Oxford (2005)
28. Kaviany, M.: Heat transfer in porous media. In: Rohsenow, W.M., Hartnett, J.P., Cho, Y.I. (eds.) Handbook of Heat Transfer. McGraw Hill, Boston (1998)
29. Kaviany, M.: Principles of Heat Transfer. John Wiley and Sons Inc, New York (2002)
30. Kowaslski, S.J.: Thermomechanics of Drying Process. Springer, New York (2003)
31. Krokida, M.K., Maroulis, Z.B.: Effect of drying method on shrinkage and porosity. Drying Tech. **15**, 2441–2458 (1997)
32. Krokida, MK., Maroulis, ZB., Marinos-Kouris, D.: Effect of drying methods on physical properties of dehydrated products. In: Proceedings of the International Drying Symposium (IDS'98), Halkidiki, vol. A, pp. 809–816. (1998)
33. Lewis, W.K.: The rate of drying of solid materials. J. Ind. Eng. Chem. **13**, 427–432 (1921)
34. Lima, A.G.B.: Diffusion phenomenon in prolate spheroidal solids. Case studies: drying of banana. Doctor Thesis, State University of Campinas, Campinas, Brazil (In portuguese) (1999)
35. Lima, A.G.B., Nebra, S.A.: Theoretical analysis of the diffusion process inside prolate spheroidal solids. Drying Tech. **18**, 21–48 (2000)
36. Lima, A.G.B., Queiroz, M.R., Nebra, S.A.: Simultaneous moisture transport and shrinkage during drying of solids with ellipsoidal configuration. Chem. Eng. J **86**, 85–93 (2002)
37. Lima, A.G.B., Queiroz, M.R., Nebra, S.A.: Heat and mass transfer model including shrinkage applied to ellipsoidal products: case study for drying of bananas. Develop. Chem. Eng. Miner. Process. **10**, 281–304 (2002)
38. Lima, D.R., Farias, S.N., Lima, A.B.G.: Mass transport in spheroids using the Galerkin method. Braz. J. Chem. Eng. **21**, 667–680 (2004)
39. Luikov, A.V.: Analytical Heat Diffusion Theory. Academic Press Inc Ltd, London (1968)
40. Luikov, A.V., Mikhailov, Y.A.: Theory of Energy and Mass Transfer. Pergamon Press Ltd, Oxford (1965)
41. Luikov, A.V.: Heat and Mass Transfer in Capillary Porous Bodies. Pergamon Press, New York (1966)
42. Magnus, W., Oberhettinger, F., Soni, R.P.: Formulas and Theorems for the Special Functions of Mathematical Physics. Springer, New York (1966)
43. Masliyah, J.H., Epstein, N.: Numerical solution of heat and mass transfer from spheroids in steady axisymmetric flow. In: Hetsroni, G., Sideman, S., Hartnett, J.P. (eds.) Progress in heat and mass transfer. International Symposium on Two-phase System. Pergamon Press, Oxford (1972)
44. Mohsenin, N.N.: Thermal Properties of Foods and Agricultural Materials. Gordon and Breach Science Publishers, New York (1980)
45. Mujumdar, A.S., Menon, A.S.: Drying of solids: principles, classification and selection of dryers. In: Mujumdar, A.S. (ed.) Handbook of Industrial Drying. Marcel Dekker Inc, New York (1995)
46. Nield, D.A., Bejan, A.: Convection in Porous Media. Springer, New York (1992)
47. Oliveira, V.A.B., Lima, A.G.B.: Mass diffusion inside prolate spherical solids: an analytical solution. Braz. J. Agri-ind. Prod. **4**, 41–50 (2002)
48. Oliveira, V.A.B., Lima, A.G.B.: Drying of wheat based on the non-equilibrium thermodynamics: a numerical study. Drying Tech. **27**, 306–313 (2009)
49. Parry, J.L.: Mathematical modeling and computer simulation of heat and mass transfer in agricultural grain drying. A review. J. Agric. Eng. Res. **32**, 1–29 (1985)
50. Parti, M.: Selection of mathematical models for drying grain in thin-layers. J. Agric. Eng. Res. **54**, 339–352 (1993)

51. Pasternak, I.S., Gauvin, W.H.: Turbulent heat and mass transfer from stationary particles. Can. J. Chem. Eng. **38**, 35–42 (1960)
52. Pérez, V.H.: Study of the behavior of temperatura of banana during the drying process. Master Thesis, State University of Campinas, Campinas, Brazil (1998)
53. Perré, P., Rémond, R., Turner, I.W.: Comprehensive drying models based on volume averaging: background, application and perspective. In: Tsotsas, E., Mujumdar, A.S. (eds.) Modern Drying Technology: Computational Tools at Different Scales. Wiley-VHC, Weinheim (2007)
54. Queiroz, M.R.: Theoretical and experimental study of the drying kinetics of banana. Doctor Thesis, State University of Campinas, Campinas, Brazil (In portuguese) (1994)
55. Queiroz, M.R., Nebra, S.A.: Theoretical and experimental analysis of the drying kinetics of bananas. J. Food Eng. **47**, 127–132 (2001)
56. Rizvi, S.S.H.: Thermodynamic properties of foods in dehydration. In: Rao, M.A., Rizvi, S.S.H. (eds.) Engineering Properties of Foods, 2nd edn. Marcel Dekker Inc, New York (1995)
57. Saravacos, G.D.: Mass transfer properties of foods. In: Rao, M.A., Rizvi, S.S.H. (eds.) Engineering Properties of Foods, 2nd edn. Marcel Dekker Inc, New York (1995)
58. Shukla, K.N.: Diffusion Processes During Drying of Solids. World Scientific, Singapore (1990)
59. Silva, W.P., Precker, J.W., Silva, C.M.D.P.S., Gomes, J.P.: Determination of effective diffusivity and convective mass transfer coefficient for cylindrical solids via analytical solution and inverse method: application to the drying of rough rice. J. Food Eng. **98**, 302–308 (2010)
60. Silva, W.P., Precker, J.W., Silva, C.M.D.P.S., Silva, D.D.P.S.: Determination of effective diffusivity via minimization of the objective function by scanning: application to drying of cowpea. J. Food Eng. **95**, 298–304 (2009)
61. Spanos, T.J.T.: The thermophysics of porous media. Chapman and Hall/CRC, Boca Raton (2002)
62. Strumillo, C., Kudra, T.: Drying: Principles, Science and Design. Gordon and Breach Science Publishers, New York (1986)
63. Sweat, V.E.: Experimental values of the thermal conductivity of selected fruits and vegetables. J. Food Sci. **39**, 1080–1083 (1974)
64. Tolaba, M.P., Aguerre, R.J., Suarez, C.: Shape characterization for diffusional analysis of corn drying. Drying Tech. **7**, 205–217 (1989)
65. Vadász, P.: Emerging Topics in Heat and Mass Transfer in Porous Media from Bioengineering and Microelectronics to Nanotechnology. Springer, Dordrecht (2008)
66. Vafai, K.: Handbook of Porous Media, 2nd edn. CRC Press/Taylor and Francis, Boca Raton (2005)
67. Yovanovich, M.M.: Conduction and thermal contact resisteances (conductances). In: Rohsenow, W.M., Hartnett, J.P., Cho, Y.I. (eds.) Handbook of Heat Transfer. McGraw Hill, Boston (1998)

Contribution to Thermal Properties of Multi-Component Porous Ceramic Materials Used in High-Temperature Processes in the Foundry Industry

Z. Ignaszak and P. Popielarski

Abstract This chapter presents a practical approach to the identification and interpretation of phenomena in multi-component ceramic granular porous materials (called mould sands) used as the moulds to cast metal alloys at temperatures above 1,300°C. The methodologies chosen for experimental (using artificial and technological heat sources) and numerical studies (using the inverse solution) of these materials and their application in database of simulation systems for virtualization of casting processes are described. The essence of substitute coefficients of mould thermal parameters and the notion of thermal history of heating are explained. The experiment shows the sensitivity of the simulation results to changes in the materials' coefficients and also that validation is required for the proper use of simulation systems in foundries. Examples of estimating thermal characteristic for the materials chosen with—middle and high thermal instability are presented. Furthermore, the thermo-mechanical parameters of these porous thermolabile materials in original Hot Distortion® tests are signalled.

Z. Ignaszak (✉) · P. Popielarski
CAD/CAE Laboratory of Materials Technology, Poznan University of Technology, Poznan, Poland
e-mail: zenon.ignaszak@put.poznan.pl

P. Popielarski
e-mail: pawel.popielarski@put.poznan.pl

J. M. P. Q. Delgado (ed.), *Heat and Mass Transfer in Porous Media*,
Advanced Structured Materials 13, DOI: 10.1007/978-3-642-21966-5_8,

1 Introduction: Specificity of High Temperature Use of Porous Materials in Foundry Applications

The porous ceramic materials described here are used in the manufacture of sand moulds widely used in foundries as disposable tools for casting different metal alloys. Operating as such a tool the sand mould fulfils a subsidiary yet important role with regard to the quality of the final casting.

On the example of granular material (as quartz sand bonded by different resin/clay used for mould production in metallic alloy casting—in foundry industry), the complexity level of the phenomenon in a such porous multicomponent porous material during high temperature heat transfer is presented, as is its identification and interpretation Accurate and mathematical modelling of these phenomena (also their superposition) is of limited value, due to the incomplete material databases that are needed for this purpose. The practical solution is based on the application of simplified models for non-porous, homogenous, solid materials.

This fact is important for the pure heat transfer model, for example, as it requires knowledge of the substitute thermal conductivity coefficient ($\lambda_{substit}$) combined with other fundamental coefficients for heat transfer (c—specific heat, ρ—bulk density and in exo/endo reactions cases: Q—latent heat source productivity). For the majority of mould sands the $\lambda_{substit}$ coefficient depends on the local temperature and on the time of various factors influencing temperature in the same place of material (a highly non-stationary process typical for thermolabile materials). These thermal problems and also practical solutions are presented by the author in [1].

When we want to solve them by modelling the thermo-mechanical phenomena to predict the porous mould material's influence on the quality of the castings (stress in the casting), the supplementary parameters will be applied in these thermo-mechanical models (E—Young's modulus, v—Poisson's ratio, σ—Yield stress). Their variations with temperature are not really known for thermally unstable mould material. There is no adapted method in the literature nor a description of such total investigations of both parameter groups: thermo-physical and thermo-mechanical. In the final part of this paper the author's original method, called Hot Distortion Plus® and consisting in acquisition of temperature curves of a heated sample of material and correlation with curves of their dilatation, will be presented. Following the simulation, an inverse method was applied in order to reproduce measured parameters with experiment.

2 Thermal Phenomena in Porous Multi-Component Ceramic Materials at High Temperatures

Multi-component ceramic composite material contains a granular and/or fibrous matrix and also other, materials including a material called the binder. These components are often characterized by diverse fire-resistance and influence

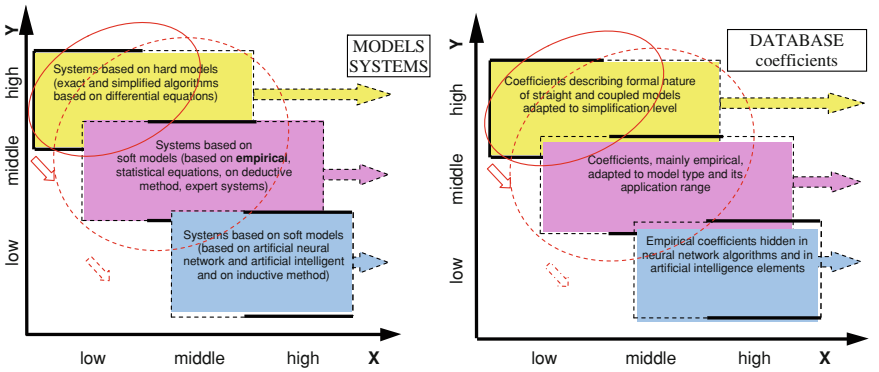

Fig. 1 Schemes of phenomena modelling principles in process engineering according to: model/system and coefficient databases (*arrows* indicate the current development trends) *Y*—knowledge level about phenomena—possibilities of their description using physical-mathematics equations, *X*—level of problem complexity (phenomena, processes) [4]

heat parameters. In high temperature conditions, for example, more than 1,000°C, the space structure, internal/external porosity and chemical composition are significantly modified. Moreover, new phases occur as a result of endo- or exothermic transformations. Together with these transformations the mechanical and thermal properties are modified and that depends on the time (intensity) of heating. This process is significantly non-stationary [2, 3].

To forecast the casting quality by virtual means, the Computer Aided Design systems applied in foundry and mould technology are more effective, when the thermophysical mould characteristics better correspond to reality with regard to the numerous simplifications of the mathematical model.

Comparing the scheme concerning the knowledge level with that of the level of problem complexity is shown in Fig. 1. The intention is to conduct an analysis of the complexity level and variety of mould materials with regard to the physical and chemical phenomena, considering the possibility of experimenting, forecasting, modelling and mathematical description of phenomena and physical data connected with heat transfer.

The mould sand, which consists of at least two phases, separated by strongly developed surfaces, is of the porous type (called also dispersed or distracted) in the meaning of macro. However, the micro-scale concerns the crystalline mesh defects, micro-cracks, dislocations, inclusions in non-metallic solids (semi-conductors, ceramic-metals, minerals, ceramics). This micro-scale is absent in effective heat macro modelling and can be used only for selected singular grain studies. At the present time this method is of limited usefulness in s premature to integrating the micro and macro scale to modelling the heat transfer in the casting moulds.

The testing and solution of thermal processes carried out in multi-component macro-porous materials can be conducted using a two-way method [3]:

1. The coupled model—formulation of heat and mass transfer equations solved by available methods, on condition that the thermal and diffusion characteristics are known as a function of unclear specific conditions and the structure type of material.
2. The porous body is considered as quasi-homogenous and one thermal transfer equation is formulated (alternatively taking into consideration the internal heat sources, positive or negative). The material characteristics used in this model reflect all phenomena accompanying heat transfer (conduction, radiation, convection and also the mass transfer). These coefficients, called thermo-physical or substitute, require detailed analysis.

If a three-phase aggregation state as the set of solid particles with varied shape and size, separated by complex micro-spaces filled with liquid or/and gaseous phase, is recognised as generally being the case, then the successive fundamental mechanisms and phenomena will be responsible for heat transfer:

- conduction by each separated solid particle, creating a frame of porous body or performing the role of a binder or special component,
- conduction by the area of direct contact between the particles mentioned,
- molecular conduction in components of liquid existing in the pores,
- heat exchange between the solid particles and pore components,
- radiation between the solid particles,
- radiation through the semi- and transparent solid particles,
- convection in the fluids (liquid or/and gas), in the pores.

In principle, while solving the practical problems of heat transfer for porous materials it is not necessary to improve the physical nature of phenomena described e.g. considering the molecular–atomic structure.

The Fourier–Kirchhoff equation, which describes the temperature field and the porous space, can be considered as quasi-homogenous, and thermal conductivity coefficient expresses the effects of all heat transfer phenomena. It may be an obvious simplification but the form of Fourier–Kirchhoff equation, where the effective conductivity components are present, (conduction—λ_{cond}, convection—λ_{conv}, radiation—λ_{rad}), becomes more complicated (bottom for 1D)

$$C(T)\frac{\partial T}{\partial \tau} = \frac{\partial}{\partial x}\left(\lambda_{\text{cond},x}(T)\frac{\partial T}{\partial x}\right) + \frac{\partial}{\partial x}\left(\lambda_{\text{conv},x}(T)\frac{\partial T}{\partial x}\right) + \frac{\partial}{\partial x}\left(\lambda_{\text{rad},x}(T)\frac{\partial T}{\partial x}\right) \quad (1)$$

The sense of this model formulation is not neglected but the difficulties in solving the models do not take into account the necessity of knowledge of the components of heat transfer that are changed with temperature, time and space coordinates. In [5] authors show an example expressing in detail the new proposition to estimate the effective thermal conductivity of multi-phase materials using a novel thermal analysis technique, the so-called Lattice Monte Carlo (LMC) method. This coupled modelling concerns the simplified cases singled out from the macro-porous structure but application of this methodology in simulation in macro-scale heat transfer problem described in this paper is still premature.

These difficulties are the result of a global interpretation toward substitute thermal conductivity $\lambda_{substit}$, with local time and space coordinates. Additional phenomena resulting from phase transformations and internal heat sources even with a medium or high calorific effect may also be considered by $\lambda_{substit}$ under certain conditions.

3 Specificity of Data Bases of Mould Materials for Virtualization of Heat Transfer and Thermomechanical Behaviour During Casting Processes

The quality of calculation results that are obtained in modelling foundry process courses by means of simulation codes (systems), depends greatly on the database accuracy for both the cast and mould material.

Only data which characterize the materials and phenomena that are in good relation to the process guarantee the correct conclusions and that a valuable prediction of the real casting-mould-set behavior will be obtained. In these simulation codes the physical models reflect particular stages of the casting development (filling the mould, solidification and cooling of metal, the mould heating and development of stresses). The problem of material data is relevant at each of these stages. All these processes are based on, or at least are coupled with the Fourier–Kirchhoff model, in which the thermophysical coefficients of heat transfer play an important role.

Furthermore, the thermomechanical interactions between casting and mould at high temperature intervals are known mainly intuitively. It is well known that these phenomena determine the intermediate and final state of stresses in casting. In individual cases deformation or even cracks in the casting may occur. Non-permanent moulds (sand moulds) are characterized by diverse flexibility, depending on the kind of mould material (moulding sand), and are made by use of compacted (and hardened) mould sand. The literature only contains citations from classical sources where the description of rigidity is not quantified (range from very low to very high). No numerical values are quoted.

The behavior of the mould material depends on the changeability of the properties of its components with temperature and applied load. It is known that foundry sand parameters as sintering temperature, refractoriness coefficient, roasting losses, permeability in conditions of hot air flow and heat radiation on the mould surface, which are ‘partially normalized’ (sometimes standardized) measures at increased and at high temperatures. They do not allow the thermomechanical values and characteristics searched for and enumerated above to be estimated.

In fact, reconstruction of the thermomechanical conditions applied to moulds (heated by a liquid alloy) and the study of the assumptions to construct suitable apparatus must be based on a series of simplifications, together with a simultaneous test for the standardization and repeatability of the tests [6].

Another kind of problem regarding the dynamics of heat phenomena is presented in the materials for riser lagging (sleeves and riser powders) a particular group of porous mould structure materials. On one hand, they are responsible for the correct slowing of heat exchange with the environment and, on the other, they must meet the conditions related to fire resistance and give no rise to unwanted or even dangerous situations during mould pouring and cast solidification [7].

Research into insulating and insulating-exothermic materials for metallurgy and foundries is carried out in laboratories on relatively small samples, in a loose or ready-to-use form (finished sleeve), and often in conditions different from those existing in a real mould.

Failure to comply with time–temperature conditions may result in:

- mismatch of the temperature range of the real material use,
- incompatibility of the duration of the thermal effect exerted on the material sample, aimed at determining a required coefficient,
- the lack of thermal shock accompanying e.g. the sudden contact with liquid metal.

As a source of the thermophysical data necessary for the simulation calculation, coefficient specifications in manuals and handbooks are used or, less commonly, specialist elaborations made for the purpose of the simulation systems. Valuable data of insulation or, in particular, exothermic materials simply do not exist or are not made available by industrial groups acquiring such information.

It should be mentioned that the use of the λ, c, ρ—thermal coefficients instead taken from the sources that disclose no inverse model or method of their determination is not recommended.

What concerns the heat source in the material, i.e. the exothermic reaction heat [Power or Q (W/m^3)] may be expressed, according to the type of the simulation system, in the form of the:

- constant value (Power = const. or Q = const., no depending on time and temperature),
- variable function of temperature: Power = f(T) or Q = f(T),
- variable function of time: Power = f(t), Q = f(t).

In case of the Magmasoft and NovaFlow&Solid simulation systems [8, 9] the user, apart from λ, c, ρ, may make use of the following sleeve parameters:

- ignition temperature of the exo-mixture (ignition temperature in Magmasoft system or burning temperature in NovaFlow&Solid system) (°C),
- duration of the exo-reaction (burn time) (s),
- latent heat of the exo-reaction (heat generation in Magmasoft or burning heat in NovaFlow&Solid) (kJ/kg).

Another approach is proposed in the Pam-QuikCast system. The user may define the exothermic material by means of their own thermal sleeve parameters (λ, c, ρ) and the heat source function (Ignaszak, 2002–2007, Essais comparatifs des materiaux et poudres iso- et exothermiques. Ferry-Capitain Metallurgical Group,

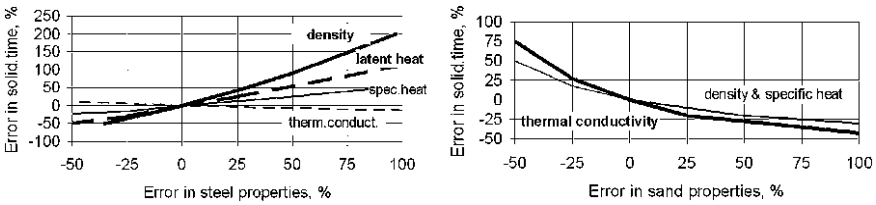

Fig. 2 Percentage errors in simulated solidification time of steel plate test-casting (selected point) due to errors in steel and sand properties [14]

"unpublished research reports, Joinville-France") [10, 11, 40]. The greatest possibility of defining the exothermic material parameters is provided by the Calcosoft system. The user may define, on the basis of available knowledge, the heat source function of the material (named the FFORCE algorithm [12]).

4 Sensitivity Tests of Simulation Models Used in Chosen Calculation Codes on Uncertainty of Thermophysical Parameters

Sciama [13] summarises the results of the simulation calculations of a test cylindrical casting (ϕ100/ϕ200 mm) cast in a sand mould and die. Overfeld [14] performed similar simulation research for a 25 mm thick cast steel plate (the experiment was conducted in the 50s by Bishop and Pellini), on the grounds of material data obtained from the literature [15]. Initially achieving good conformity with the experiment, he then deviated the values of thermophysical coefficients: λ, λ'—thermal conductivity, c, c′—specific heat, ρ, ρ'—density, L—latent heat, in the range from +100 to −50%. Figure 2 presents the results of the influence of such significant interference on solidification time at a selected point on the thermal axis of the plate.

In [3, 15] a comprehensive study of the reasons for changes of the λ' and c′ values are presented, showing their influence on the variability of the parameters calculated from the simulations, namely: the time and volumetric rate of solidification (Fig. 3). These calculations were experimentally verified and the specified error is related to the real experimental value.

The procedure presented above encouraged a deeper analysis of the *real variability* of the casting data. Taking into account the data analysis and the experiments effected in their own laboratories [1, 3], the author presents in the following table the estimated errors of thermophysical coefficients of cast steel and chemical (resin) bonds quartz sand.

As can be seen in Table 1, particular coefficients are charged with various possible errors. In order to appreciate the possible errors included in simulation calculations, a comparative analysis with the results of [14] was performed.

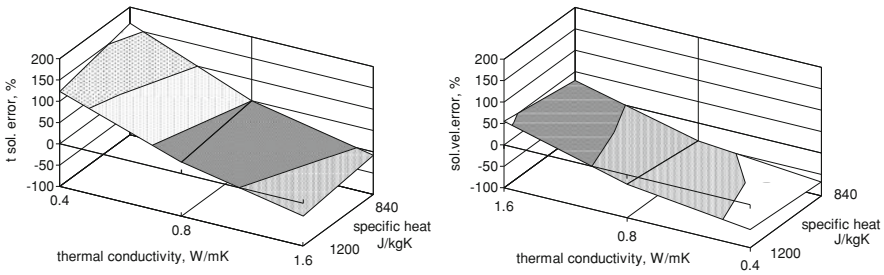

Fig. 3 Percentage error in simulated: solidification time and volumic solidification velocity of grey iron share-test-casting with thermal parameters real uncertainty of sand [3]

Table 1 Range of estimated error on thermophysical properties

Material	Properties	Estimation error %
Steel	Thermal conductivity λ	±20
(Low %C)	Specific heat c	±15
	Latent heat L	±7
Sand	Density ρ	±3
(Resin)	Thermal conductivity λ'	±30 (50)
	Specific heat and density ($c' \cdot \rho'$)	±25

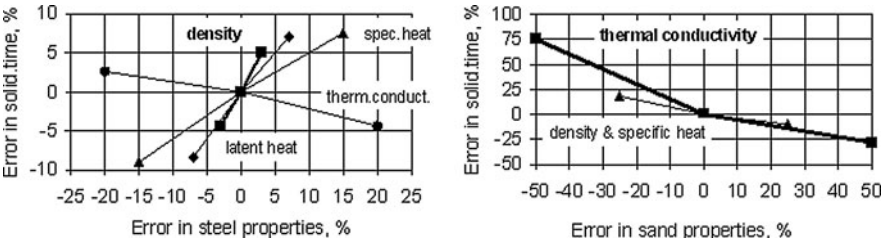

Fig. 4 Study of the influence of real steel and sand property errors on the percentage errors in simulated solidification time of steel plate test-casting [16]

Figure 4 shows the values of solidification time errors, corresponding to the limit values of thermophysical coefficients from Table 1.

According to new research [16] concerning the sensitivity problems of simulation calculation results on the quality of material data, the importance of mould thermal coefficients has been proved and the *new* sequence of the influence would be then as follows (other than that provided in the works mentioned above [13, 14]: $\lambda' > (c' \cdot \rho') > c > L > \rho > \lambda$, where: λ, λ'—thermal conductivity, c, c′—specific heat, ρ, ρ'—density, L—latent heat, and where $'$ signifies a sand mould.

The quality of simulation results (in the example of cast steel cast to sand moulds) depends most on the thermophysical parameters of moulding sand. This is due to its components, its thermal instability and the relations of the moulding sand

state with the conditions of its preparation and use. This was confirmed recently by Farre [17].

5 Thermal Parameters as Substitute Coefficients: Thermal History of Heating Process—New Notion for Thermolabile Materials

In order to determine the substitute thermal conductivity coefficient, the simplified Fourier–Kirchhoff model, without internal sources [3, 10], was applied. It was assumed that the values of thermal capacity $c \cdot \rho = f(T)$ are known from the test conducted in the stationary regime heat and that the bulk density of porous material is not-dependent on the process parameters. This assumption is equivalent to the hypothesis that all effects influence the $\lambda_{substit}$, including the internal source effects (for example, the peaks on the DTA curve).

In connection with these remarks the boundary-initial model is given as:

$$\begin{aligned} \frac{1}{x^{\beta}}\frac{\partial}{\partial x}\left(\lambda_{sub} x^{\beta}\frac{\partial T}{\partial x}\right) - c\rho\frac{\partial T}{\partial \tau} &= 0 \\ \lambda_{sub}\frac{\partial T}{\partial x}\bigg|_{x=x_a} &= -q \\ \lambda_{sub}\frac{\partial T}{\partial x} + \alpha_b \cdot \left(T - T_b^*\right)|_{x=x_b} &= 0 \\ T|_{\tau=0} &= 0 \end{aligned} \tag{2}$$

where:

T	temperature in the tested sample dependent on the x coordinate and τ time,
x_a, x_b	a and b boundary coordinates,
c	specific heat dependent on temperature,
ρ	bulk density (constant),
$\lambda_{substit}$	substitute thermal conductivity dependent on temperature (x coordinate) and on the time,
β	shape coefficient: $\beta = 0$ for plate layer (plate source, $\beta = 1$ for cylindrical layer (linear source), $\beta = 2$ for spherical layer (point source),
q	heat flux on the boundary $x = x_a$,
T_b*	ambient temperature on the boundary $x = x_b$.

For the second type boundary condition (known heat flux on the boundary $x = x_a$), the final formula is given below:

$$\lambda_{sub}|_{x=x_p} = \frac{-qx_a^{\beta} + \int_{x_a}^{x_p} c\rho\frac{\partial T}{\partial \tau}x^{\beta}dx}{x^{\beta}\frac{\partial T}{\partial x}}. \tag{3}$$

The formula presented above is fundamental to calculating the $\lambda_{substit}$ values at the defined point $x = x_p$ in which for the moment $t = t_i$ the temperature is $T(x_p, T_i)$.

The calculating procedure includes numerical approximate methods to determinate the derivative $\partial T/\partial t$ and gradient $\partial T/\partial x$ for a limited number of temperature measurement points.

Comparison of the experimental tests with the reality of the thermal shock between melted-metal and multi-component mould sand allows us to define the procedure for heating the sample sub-spaces. These samples were submitted to the varied thermal treatment as a function of time and temperature changes.

It was assumed that the thermal stability of the micro-area temporary state of the tested material around the thermocouple remains in the relations with the following formula named "thermal history" [3, 10]

$$th = \int_{\tau_{ON}}^{\tau} T_N(\tau) d\tau. \tag{4}$$

This dependence is expressed by the field below the x dependent temperature versus time. In the case of numerical computations, the above integral is calculated by a trapezium method from experimental curves T = f(time, position of thermocouple).

The data measured were numerically approximated, with a minimization of the absolute square deviation of variable temperature, which depends on the time and space coordinates. The formula was drawn up by use of a functional description $T = f(X,\tau)$, and consequently knowing the stream on the boundary $q = f(t)$, iteration procedures can be avoided. Thus the values of thermal conductivity substitute coefficients were defined for many sand moulds, and then expressed in the form of the relation

$$\lambda_{substit} = f(T, th) \tag{5}$$

where *th* is thermal history (in the region x), which permanently increases during the process (it is a definite integral under the heating curve of the sand mould) [3, 10], Fig. 5.

The use of the boundary condition $q = f(\tau)$ in the model is not always feasible (because of the difficulties involved in measuring). In Hueber (1993, "Not published work, LM3-ENSAM, Paris") it is shown that temperature, which is easier to measure (the $T = f(t)$ boundary condition), requires a full optimisation method in order to determine the λ of mould sand. In Hueber (1993, "Not published work, LM3-ENSAM, Paris") the thermal conductivity results of furan sand are presented. This characterisation shows that in times shorter then the solidification time of a 20 kg cylindrical steel casting, the use of a $\lambda = f(T)$ curve, not taking into account the thermal history *th*, must be sufficient. The classic form of this $\lambda = f(T)$ curve was found by the optimisation method. After this short period (1,200 s), fitting problems appeared when this simple formula $\lambda = f(T)$ was applied.

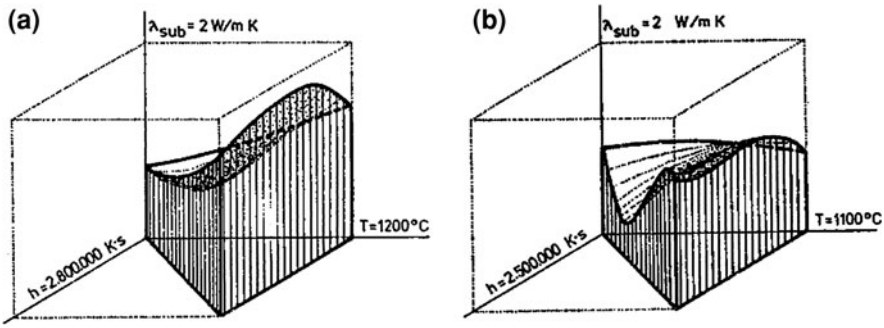

Fig. 5 Substitute thermal conductivity versus temperature T and thermal history th, determinated by simple numerical identification (the axis maximal values of λ, T, and th are shown). Quartz sand AFS 30 bonded by silicate—7.5% (**a**), and by furan resin—3% (**b**)

Optimisation is one of the numerical solutions of inverse problems and has been appreciated for many years by the specialists who seek effective methods for identifying boundary conditions and material data [18, 19].

Recently, the use of simulation code procedures as a solution for inverse problems was shown in [20], as an example of boundary conditions determining ingot cooling and for determining the thermal conductivity coefficient of one alloy. The possibility of determining many parameters from one data package with the use of inverse calculating method presented there can be commented on as follows:

- inverse problems belong to the group of what are known as badly conditioned problems, which often lead to considerable errors in the values of the coefficients sought, in spite of the fact that these phenomena are suitably separated and matched to the physical model, cf. [3, 11]. The reason for such a situation usually arises from systematic measuring errors and/or model simplifications;
- even with the proper separation of the phenomenon, the realisation of the numerical solution in full 3D geometry implies an important CPU time, due to the convergence of the solution and the number of iterations. This problem is also noticed in [20].

The effectiveness of $\lambda_{substit}$, using to the computer simulation of heat chock in the material described, is more efficient than modelling granular system geometry and the superposition of conductivity, convection and radiation phenomena, which require a specific material database. Also, the knowledge relating to the latent heat calorific effect of existing internal heat sources is not sufficient to correct the estimation in the components of mould sands. This original idea and formula of $\lambda_{substit}$ for the materials under discussion, characterized by low thermal stability or/and refractority, shows that $\lambda_{substit} = f(T,th)$ is of a different shape than the parabolic curve $\lambda = f(T)$ obtained from heat stationary test. The $\lambda_{substit}$ is an original proposition for modelling heat transfer in these materials.

6 Methodologies of Experimental (Using Artificial and Technological Heat Sources) and Numerical Studies (Using Inverse Solution)

The validation of the model, understood as the physic–mathematical engineering problem solved by means of numerical methods, can concern the preparatory stage, called pre-processing, as well as the procedures which serve for analysis of computation results, known as post-processing. This validation is based on the effective adjustment of model components with parameters of processes occurring in reality and connected with the tests of different variants, which allows the margin of error [21] to be determined.

Once simulation computations are complete (or as partial results are obtained—interactively), it is necessary to estimate the state of phenomena in casting. For the solidification period this requires the interpretation of thermal process effects with reference to temperature fields (local in the time-space coordinates). The final comparison of the "calculated" state to an experimentally identified "real" state, and with the possible correction of the model, is simply called validation. This validation determines the usefulness of applying the simulation system for solving models and for optimising casting technology. Only then can it be said that our simulation tool is ready to optimize the process in real manufacturing conditions. The condition absolutely required and necessary in view of the diversity of materials used for mould manufacturing is energetic validation of the model i.e. receiving, for example, the conformity between real and simulated solidification time of chosen casting walls [22]. Only this satisfactory conformity authorizes us to draw conclusions about the virtual solidification and feeding phenomena in the casting. The scheme of classification of information sources is shown in Fig. 6.

It is supposed that the uncertainty of thermophysical material data (in pre-processing) is associated with a lack of sufficient experimental data (sources of the first group, Fig. 6). This fact makes energetic validation difficult. In this case it is inferred that only one possible estimation of simulation quality results from the second set of data (Fig. 6).

In [1] it was shown that it is possible to obtain precious I group information using low cost methods of measurement applied to the Casting–Mould system.

In [1, 21] the authors proposed a scheme of connections between measuring-calculating procedures related to the obtainment of material data, generally performed in laboratory conditions using procedures with a transformed formula of direct methods (Fig. 7). In the case of thermal casting processes, such a procedure may be called a numerical identification of thermophysical data. In the procedure of simplifying the physical model, it is important to take temperature–time conditions, simplifications of geometrical model and mesh design into account. The numerical method of identification is an optimization realized by means of iteration loops, providing minimization of the objective function. Validation of material data determined in this way would necessitate simultaneous validation of the whole model (comparison of the results of simulation of real casting, Fig. 7).

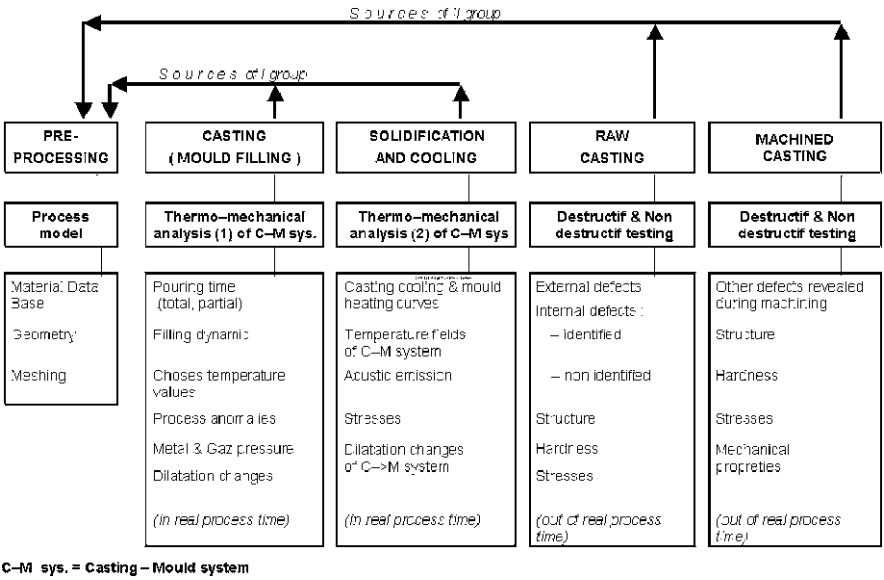

Fig. 6 Scheme of casting model validation. Sources and information transfer in casting production

The inverse problems which are most frequently discussed and have generated the richest bibliography related to foundry problems are: (1) boundary problems called also *temperature identification problems*, (2) coefficient and boundary problems called *material characteristic identification and conditions on the domain border* [1].

A very important stage of numerical identification is the proper separation of the phenomenon, which affects the values of the determined coefficient (in the research sense) and remains numerically coherent. Examples of such procedures may be found in reference works [3, 15].

7 Examples of Thermal Characteristic Estimation for Chosen Materials

7.1 Resin Bonded Sand: Material with Middle Thermal Instability

The use of procedures of simulation code as a solution for inverse problems was shown for example in [23, 24], namely a case of boundary conditions reproduction of ingot cooling and of the determination of the thermal conductivity coefficient of one alloy. The possibility of estimating many parameters from one data package

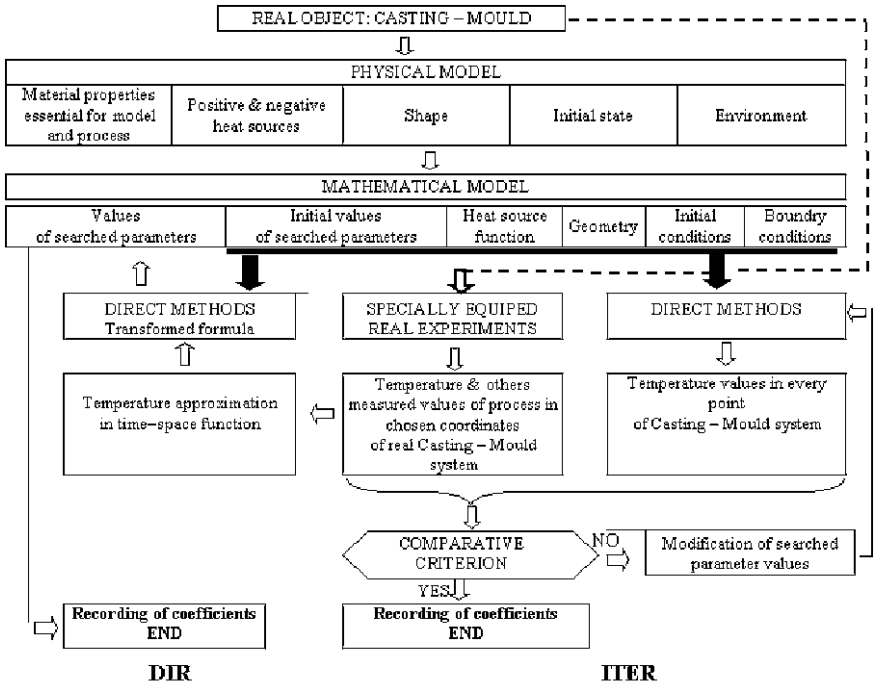

Fig. 7 Scheme of direct and iterative method of coefficient inverse problem solution

with the use of the inverse calculating method presented there can be commented on as follows:

- inverse problems belong to the group known as badly conditioned problems, which often lead to considerable errors in the values of the coefficients sought, in spite of the fact that these phenomena are suitably separated and matched to the physical model, cf. [21, 25]. The reason for such a situation usually arises from systematic measuring errors and/or model simplifications;
- even with the proper separation of the phenomenon the realisation of the numerical solution in full 3D geometry implies an important CPU time, due to the convergence of the solution and the number of iterations.

An absolute condition which is required due to the diversity of materials used for mould production is *energy balance model validation* [15]. This requires us to obtain conformity of solidification times for real casting walls and walls calculated by simulation. If the energy balance validation of the model is fulfilled, it would appear that any number of λ_i, c_i and ρ_i sets could perform a condition of obtaining the conformity of solidification time in real and virtual casting. For this reason, the condition for obtaining satisfactory conformity of temperature changes in both the tested and the virtual material should be considered. *Dynamic temperature*

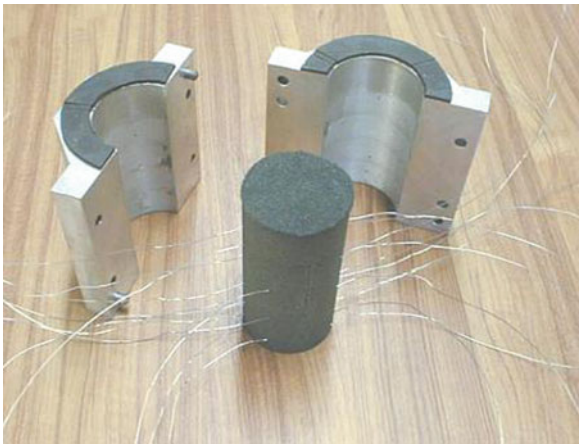

Fig. 8 Special equipment for measurement core (MC) preparation

validation requires references of recorded results derived from experiment (curves of cooling/heating) to curves built of simulated values.

The example of the inverse problem solution for cast iron solidification experiments in two kinds of furanic moulds with mould equipment and methodology of inverse solution is presented in Figs. 8, 9 and 10 (Ignaszak, 2002, Thermophysical parameters of materials needed to computer simulation systems in the foundry. Studies, validation, optimisation, "Nonpublished work sponsored by KBN: grant no T08B 041 19 (Polish National Research Committee) Poznan ").

Very satisfactory conformity of temperature T (°C) is obtained between the measured and virtual (optimised using Calcosoft–2D system) curves T = f(time) obtained by the inverse problem solution for these two kinds of mould, poured by sheroidal cast iron (thickness of plate castings: 100 mm).

7.2 Clay-Water Bonded Sand: Material with Middle Thermal Instability

The water evaporation from the mould sand gains heat energy and next the same steam condensing in the colder areas of the mould gives up this heat.

This is connected with the formation of the temperature arrest at 100°C (Fig. 11a) and with the changing range the dimension of the highly humidified zone. The example curves in Fig. 11a illustrate the temperature arrests corresponding to the duration of the over-moisture zone in the three selected points for the bentonite bonded green sand mould. The phenomena occurring in the over-moist zone is connected with changes in the thermophysical parameters of this mould zone. With some approximations we can assume that they apply particularly to the conventional (apparent) specific heat coefficient, taking into consideration its increase caused by evaporation (condensation) latent heat of water in a

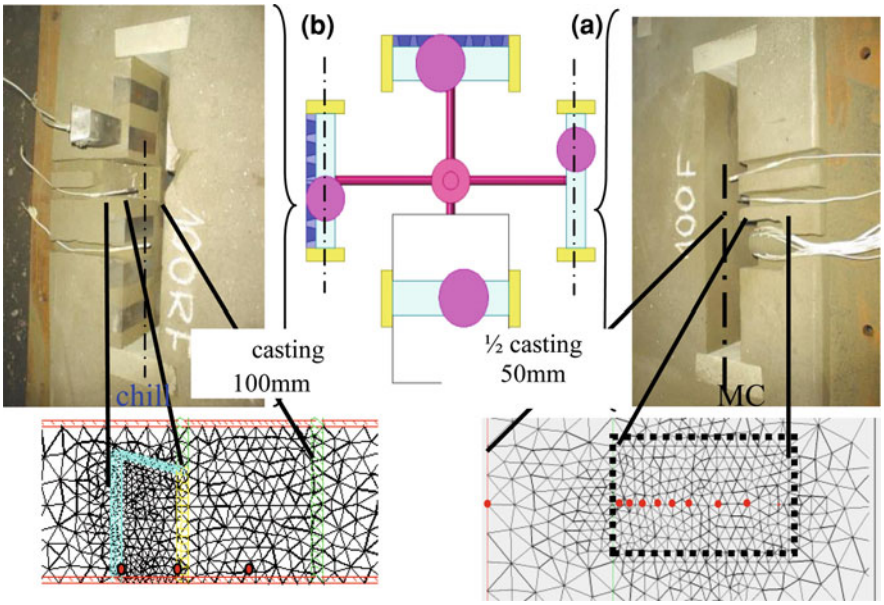

Fig. 9 Scheme of plate casting–mould system and details of mould instrumentation: **a** furanic mould, **b** furanic mould with chills (below: o positions of thermocouples in 2D finite elements mesh for inverse problem solution by Calcosoft 2D)

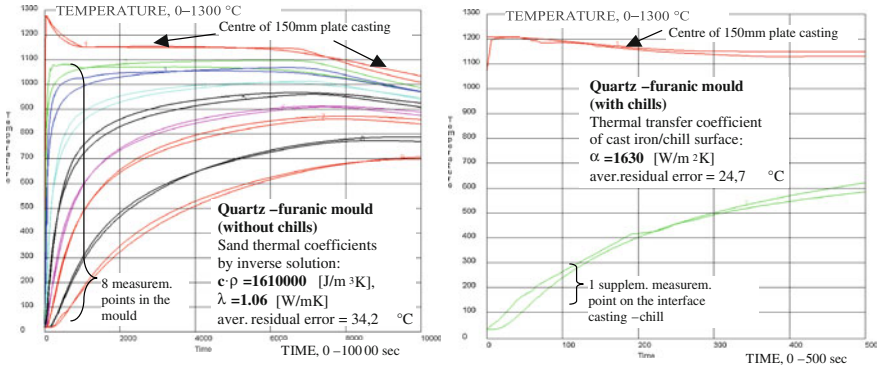

Fig. 10 Comparison of real (from measurement) and virtual (by inverse solution) temperature curves (two examples) (Ignaszak, 2002, Thermophysical parameters of materials needed to computer simulation systems in the foundry. Studies, validation, optimisation, "Nonpublished work sponsored by KBN: grant no T08B 041 19 (Polish National Research Committee) Poznan")

defined range of temperature (2,257 kJ/kg). In [26] the analysis regarding changes in the apparent specific heat of bentonite-bonded green sand mould is presented (Fig. 11b).

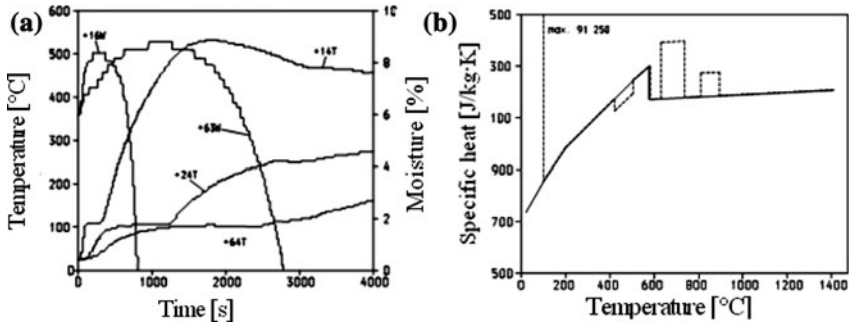

Fig. 11 **a** Temperature (T) and moisture (W) measured in bentonite-bonded moulding sand (distance in mm from casing–mould interface are marked) [26], **b** Specific thermal capacity cp of bentonite-bonded moulding sand (4% water), for increasing and decreasing of temperature [26]

Generally, with the changes of apparent specific heat the following phenomena in sand moulds are interrelated [26]:

- from 100°C intensive water evaporation,
- from 300 to 600°C the progressive decomposition of the resin (mainly with exothermic effect),
- at about 573°C reversible transformation of transformation of β quartz (low temperature) in the quartz α (high temperature),
- between 600 and 900°C endothermic transformation of resin or bentonite is possible.

In Fig. 11b for an interval around 100°C a significant change in substituted (average) specific heat is shown—heat—this is the cp value associated with the latent heat of water vaporization, taken into consideration in a very narrow temperature interval.

It is also worth noting that in the over-moist zone the presence of water under different physical states and the increase in water quantity is responsible for an increase in the substitute thermal conductivity in this zone.

Our studies consisted of two parts the experiment and the simulation.

The implementation of the experiment consisted in measuring and acquiring a temperature field in a mould and in casting of high chromium cast iron as the heat source using appropriate thermocouples. The mould material tested during the experiment was quartz sand with the addition of iron shot (up to 2 mm) bonded by water glass i.e. sodium silicate (6%) [27].

In view of the occurrence of free and constitutional water content in the water glass binder this moulding sand is characterized by similar phenomena to those in bentonite + water bonded green sand. In the second part of study a simulation using 2D Calcosoft system was performed.

In order to conduct experimental research it was necessary to make a special measurement core manufactured of tested moulding sand with water glass. Chromel–alumel thermocouples were placed at distances of 5, 7 and 12 mm from

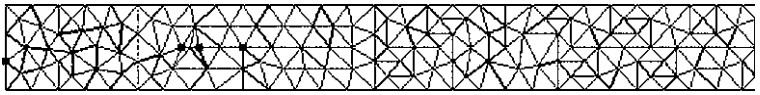

Fig. 12 Cast/mould geometry with FEM mesh and thermocouples positions

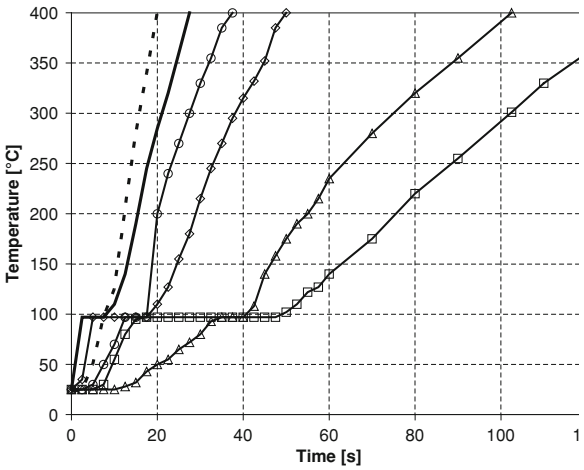

Fig. 13 Result of one of first simulation–comparison of results with experiment [26]

the casting–mould interface and in the center of the casting. The casting (as heat source) of the high chromium cast iron plate was used (size 300 × 300 × 30 mm).

Data was obtained using CASTOR 2 computerized measurement and recording equipment. The measurement results are saved as a text file, and having been analysed, were transferred to the Calcosoft 2D system in order to perform the simulation studies. Taking into consideration that the thickness of the plate is ten times smaller than its overall dimensions, it can be assumed that heat flow occurs only in the 1D (one dimension). The geometry with the FEM mesh and the thermocouple positions is shown in Fig. 12.

For numerical simulations the following primary chosen material parameters of the mould are assumed: volumetric heat capacity $c \cdot \rho = 2.2$ MJ/m^{3}K and thermal conductivity $\lambda = 2.6$ W/m K. The "heat source function" is initialized by the algorithm from the user function at 100°C. The preliminary simulations were performed at the assumed parameters. The result expressed as the temperature variation at the locations of thermocouples is shown in Fig. 13.

It should be noted that in each case temperature validation of the local mould was implemented with the restriction that conformity of real and calculated casting solidification times (the procedure called energy balance validation is satisfactory [1]). A comparison of the temperature curves at particular measurement points

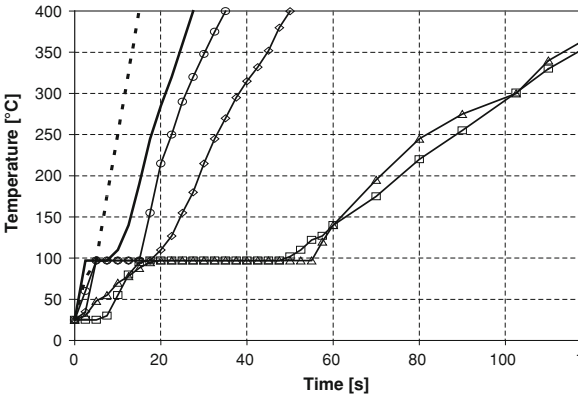

Fig. 14 Result of simulation for mould–comparison of results with experiment [28]

extracted from the simulation results indicates differences in relation to the experimental results, especially concerning the duration of the temperature arrest of 100°C. An attempt to validate the model of the heat and mass transfer phenomena consists here in matching the temperature curves obtained from the simulation to the experiment (real). For this reason, the mould was artificial divided into sub-areas—i.e. seven layers at a thickness of 2–2–2–2–1.5–5 and 120.5 mm. Each sub-area was assumed to have an increasing moisture content, thus the further from the casting–mould interface, the higher the moisture. In each sub-area it was assumed that.

In carrying out further simulations adjustments were made in order to approximate the simulation results with the results of the experiment, which were obtained for the following parameters:

- moisture in the subsequent sub-area (1–7), respectively: 16, 22, 28, 34, 40, 40 and 40%,
- substitute volumetric heat capacity 0.7 MJ/m^{3}K (constant),
- substitute thermal conductivity 3 W/(m K) (constant).

It was clear that the introduced moisture values deviate from the homogeneous initial moisture resulting from the sufficiently uniform content distribution of water glass in the mould sand. The assumed moisture distribution was obtained on the basis of numerous simulations (energy and temperature validations) [28].

A comparison of the two sets of results is shown in Fig. 14.

From the above comparison we can to conclude that the agreement of simulated results with the experiment ones is the best for the node corresponding to the thermocouple placed at distances of 12 mm from the casting–mould interface. Discrepancies in the first two temperature curves (position thermocouples, respectively: 5 and 7 mm from the casting–mould interface) may result from an incorrect estimation of the moisture quantity in the corresponding sub-area. It is necessary to emphasise that the conformity of real solidification time of casting

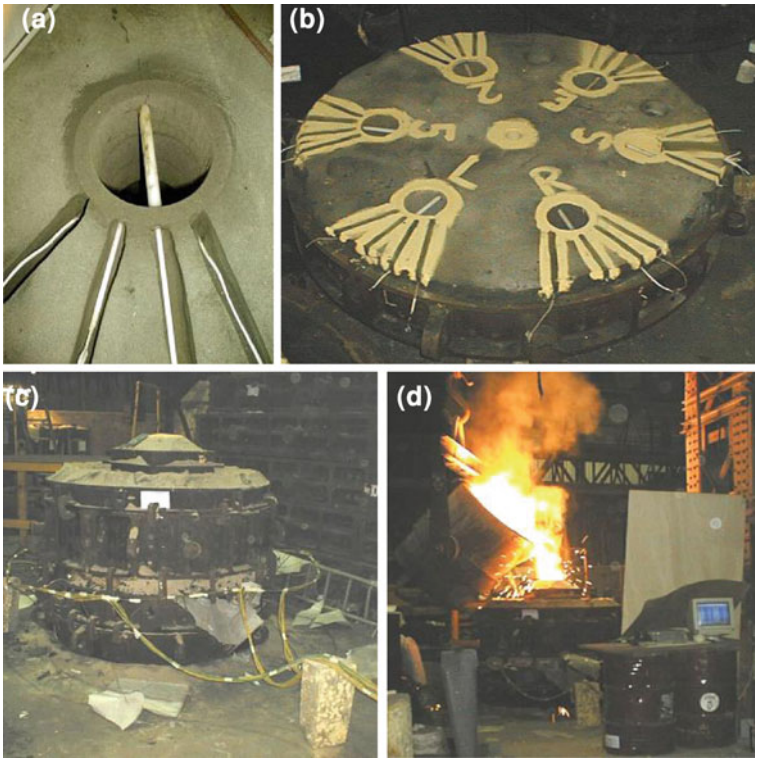

Fig. 15 The course of the experimental tests—sleeves: **a** thermocouples in mould cavity, **b** view of the middle part of the mould, **c** view of assembled mould (with the thermocouples connections), **d** pouring the mould with cast steel (with data acquisition stand)

and that calculated by simulation was perfect in this case. The complete results of these studies are presented in [28].

7.3 Insulation and Exothermic Materials: Materials with Strong Thermal Instability

The first group of the experiments consisted in simultaneous casting of cast steel of known overheating degree into a mould with the cavities of identical geometric dimensions made of the sleeves of the tested materials [29].

Each of the casts, except for the reference one (in quartz furan sand), was lagged with another kind of insulating- or insulating-exothermic sleeves of average thickness 25 mm. The experiment aimed to define the solidification time of cylindrical castings located in the sleeves, based on the shape of cooling curves and their derivatives, and to determine the temperature variation at the back of a

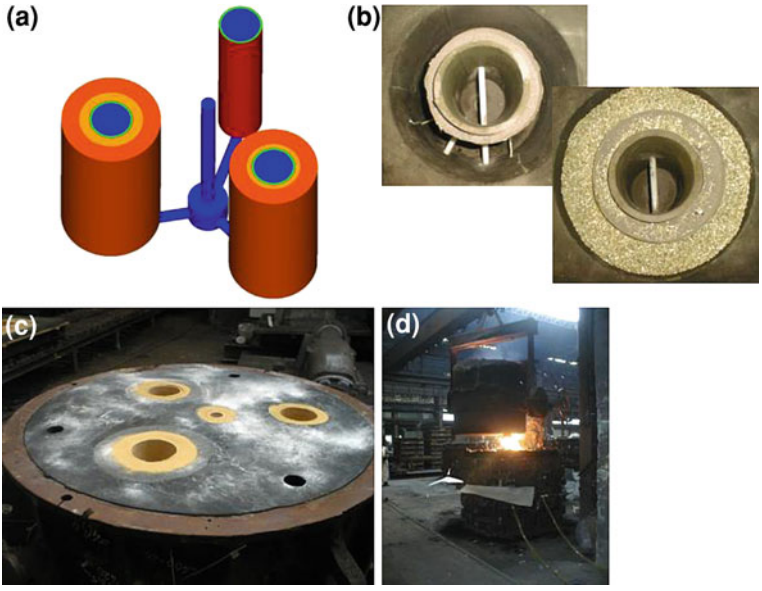

Fig. 16 The course of the experimental tests—powders: **a** principle of forming the mould and its cavity tooling, **b** view of division surface of a complete mould, **c** a CAD drawing (I-deas), **d** view of assembled mould, mould pouring with cast steel (with the connections)

particular sleeve. The mould and its thermocouple tooling is shown in Fig. 15. The temperature curves recorded in the geometric centers of the castings and at the back of sleeve were then considered as files of experimental data implemented into the system carrying out the inverse calculation.

Similar tests were performed with the use of cast iron (the second set of experiments) for various diameters of cast samples (60 and 200 mm). This aimed to investigate one of the insulating materials lagging the casting with the layer of about 25 mm, in order to test its thermal effect on the castings in two remarkably different periods (from pouring until total solidification).

Difficulties in defining the thermophysical parameters of the insulating and exothermic powders used without a binder were conducive to searching for and testing several methods. This resulted in a method being chosen consisting in making cylindrical sleeves of loose materials in the form of sample mould cavities (the exothermic material from the casting side—an exothermicl powder, and the insulation material—vermiculite, at its back). Figure 16 shows the course of the test. The mould was poured with cast steel (the third set of experiments).

7.3.1 Simulation Tests: Solution of the Inverse Problems

The course of the simulation test [29] related to the first set of experiments is shown below with the example of selected insulation-exothermal sleeves, for

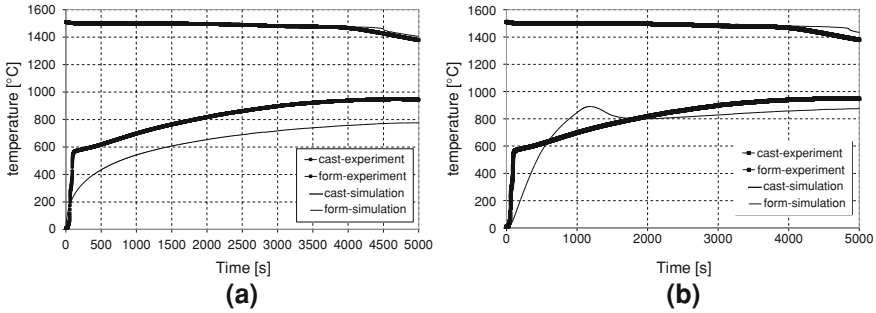

Fig. 17 Cases A and B—temperature variation in the casting-sleeve system: comparison of the best approximations to the experiment. The numbers in all the plots denote temperature curves generated by use of the coefficients identified with the help of Calcosoft Inverse Solution. **a** solidification times t exp = 4,660 s and t sim = 4,492 s [the identified values $c{\cdot}\rho = 1$ (J/m^3 K) and and $\lambda = 0.65$ (W/m K)], **b** solidification times t exp = 4660 s and t sym = 4844 s. Tz (ignition) = 500 (°C), t reaction time = 1,000 (s), reaction heat = 2,176 (kJ/kg), (the identified values $c{\cdot}\rho$ = 0.8E+06 (J/m^{3}K) and $\lambda = 0.8$ (W/m K)]

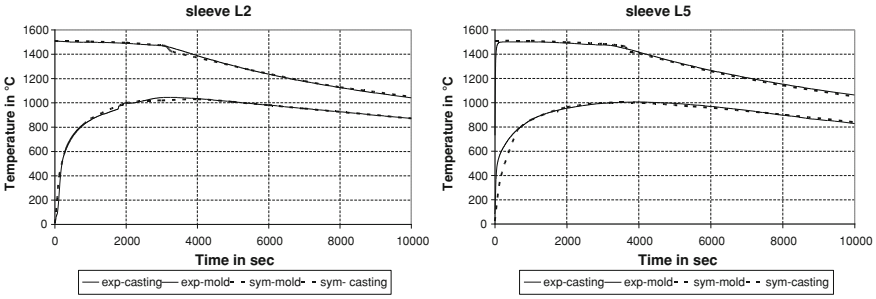

Fig. 18 The case of description of an exothermic source with the help of an exp function—temperature variations in the casting-sleeve system: comparison of two kinds of insulating-exothermic sleeves to the experiment (very good agreement of experimental and simulation curves)

which three approaches of the thermophysical parameters are proposed (cf. Figs. 17 and 18):

A—in cases when the heat source function cannot be implemented into the simulation system, the thermal interaction of the sleeve is expressed with substitute coefficients λ, c, and ρ,

B—in cases when the sleeve heat source function may be implemented but the source is of constant intensity within the whole reaction time (cf. Magmasoft and NovaFlow&Solid simulation systems),

C—in cases when the sleeve heat source function may be implemented but the source is of varying intensity within the whole reaction time.

In all the simulation trials the material was cast steel of the following properties:

- specific heat $c \cdot \rho$: 100°C–3.51e6; 1,100°C–5.21e6; 1,600°C–5.68e6 (J/m^{3}K),
- conductivity λ: 100°C–52.0; 800°C–26.4; 1,200°C–30.3; 1,550°C–30.6 (W/m K),
- latent heat of solidification L: 1.967E+09 (J/m^3),
- solid phase fraction curve: 1,463°C–1.00; (1,486.5)C–0.50; 1,510°C–0.00,
- density ρ: 20°C–7,850; 1100°C–7,500; 1,460°C–7,288; 1,520°C–6,982 (kg/m^3),
- the furan sand as a mould—$c \cdot \rho$ = 1.7E+06 (J/m^{3}K) and λ = 1.07 (W/m K).

The works [12] provide a proposal of the authors comprising a functional approach to the value of exothermic reaction intensity.

The degree of advancement of the chemical reaction, including the exothermic one, is related to the quantity (concentration) of the substrate selected [30]. The rate of any chemical reaction with respect to a given substrate is defined as the rate of concentration decrease (c) of the substrate in the time.

$$V = -\frac{dc}{dt} \tag{6}$$

During the reaction some factors considered as disturbing may arise—e.g. unsuitable temperature, oxygen deficit and lack of catalyst. In the simplest case, namely analyzing only one substrate (the progress of the reaction depends on its concentration), the reaction rate is proportional to the decreasing concentration of the substrate. The reaction rate depending on time is determined by solving the following differential equation.

$$V = -\frac{dc}{dt} = k \cdot c^n \tag{7}$$

In this equation n stands for the reaction order, k is the coefficient of proportionality. The reaction order may also be fractional. If $n = 0$ (zero-order reaction), the reaction rate is determined in the process independent of the concentration. The solution of the above differential equation for the first–order reaction gives the reaction rate depending on time and is expressed by the function of exponential type.

$$V = kA \exp(-kt) \tag{8}$$

where A is the constant resulting from integral calculation of Eq. 7.

As mentioned before, the progress of any chemical reaction is determined by the quantity (concentration) of one of the substrates of the reaction—in this case it will be the deficit of the *exo*-material in the process of its burning out. The reaction progress will affect the quantity of heat released, proportional to the rate of the *exo*–substrate decrement. This allows us to adopt the following form of the function of the heat source released as a result of the exothermic reaction:

Table 2 The coefficients of two insulating-exothermic (L2 and L5) sleeves

Sleeve	$c\rho$ (10^6 J/m^{3}K)	λ (W/mK)	Tz (°C)	Q (W/m^3) *10^6	τ (s)	Q_{total} (kJ/kg)
L2	0.56	1.09	150	0.45	3,500	2,257
L5	0.50	0.98	150	1.00	1,300	1,857

$$P(t) = Q\exp\left(-\frac{t}{\tau}\right) \tag{9}$$

where t is the time elapsed from the ignition moment in a given location of the sleeve (that is from reaching the ignition temperature, i.e. initiation of the exothermic reaction), τ—the value of a time-constant in the mathematical formulation of the exothermic reaction, while P(t) is thermal power per unit volume of the sleeve. Once the sleeve is poured with liquid metal, its successive layers reach the ignition temperature as a result of the heat transferred from the casting (exponential function describing the heat source).

The assumption of the heat source function in the form of the formula (9) leads to the following consequences:

1. Total heat quantity released from unit volume of the sleeve (Q_{exo}) shall be expressed as a product of Q and τ coefficients. In order to prove this, the heat source function should be integrated in time.

$$Q_{exo} = \int_0^\infty P(t)dt = \int_0^\infty Q\exp\left(-\frac{t}{\tau}\right)dt = Q\tau \tag{10}$$

2. The quantity of heat released from unit volume within the time from ignition is expressed by the following function

$$\begin{aligned} Q_t &= \int_0^t P(t)dt = \int_0^t Q\ \exp\left(-\frac{t}{\tau}\right)dt = -Q\tau\ \exp\left(-\frac{t}{\tau}\right)dt + Q\tau \\ &= Q\tau\left(1 - \exp\left(-\frac{t}{\tau}\right)\right) \end{aligned} \tag{11}$$

Total heat quantity emitted until the end of the reaction is expressed as a product of Q and τ. The coefficients related to the source functions of two insulating-exothermic (L2 and L5) sleeves determined in the above indicated manner are specified in Table 2 and in the diagrams shown in Fig. 18.

Finally, the thermophysical parameters of the sleeve determined in this way are the effect of the simulation process in which the characteristics T = T(f) from the experiment and from the simulation have the best conformity (the least residual). This method allows us to carry out the energy and temperature validation simultaneously.

8 Thermomechanical Parameters of Porous Thermolabile Materials Studied by Hot Distortion Tests

Modern technologies require new materials with special properties. One of the reasons for interest in materials of non-classic mechanical properties comes from the fact that they can be used (either as reinforcing inclusions, binding phases or as matrices) to form composite materials with special properties.

There are a number of physical properties of these new materials that we implicitly assume to be temperature-independent. However, one may be surprised to discover that they can also change in time or due to temperature variation. In many cases, the relations between properties and temperature are unknown for users. One can try to describe this formula using an experimental method and an inverse solution method. Another way which we can use is optimization e.g. to develop the mathematical formula describing temperature dependent properties using data measured by experiments.

In this chapter the thermo-mechanical phenomena which occur in thermal shocked thermolabile porous ceramic material were described. Such materials are applied in foundry industry for mould making. They are characterized by low thermal stability and lose strength above 400°C. In [31] the usefulness of Hot Distortion Plus® to estimate the thermo-physical parameters (apparent thermal conductivity and heat capacity) was discussed. These parameters are necessary in the database of foundry simulation codes, which permit the phenomena in casting-mould system to be simulated.

The aim of these tests is to estimate the mould material phenomena's influence on casting quality. Nowadays the models applied in simulation systems also contain the mould dilatation problem under high temperature. Parameters applied in these thermo-mechanical models (Young's modulus, Poisson's ratio, Yield stress) and their variations with temperature are not really known for thermal unstable mould material. There is no adopted method in literature and in descriptions of such total investigations of both groups of parameters: thermo-physical and thermo-mechanical. The authors adapted the apparatus based on the BCIRA method [32], which allowed them to conduct the investigations into a classic parameter called Hot Distortion. The authors' method, called Hot Distortion Plus®, consists of obtaining temperature curves of a heated sample of material and of their dilatation in relation to calculated curves.

The method developed by the British Cast Iron Research Association (BCIRA) consists in heating the material specimen with a Bunsen burner. The items [33, 34] outline the methodical foundations and interpretation of the Hot Distortion Test. The advantage of gas burner heating is due to the high heat exchange coefficient between the flame and the sample. The BCIRA Test principle has been applied for the purposes of designing a Polish professional DMA Device, which its designers have named a device for testing the high-temperature phenomena in casting cores [35, 36].

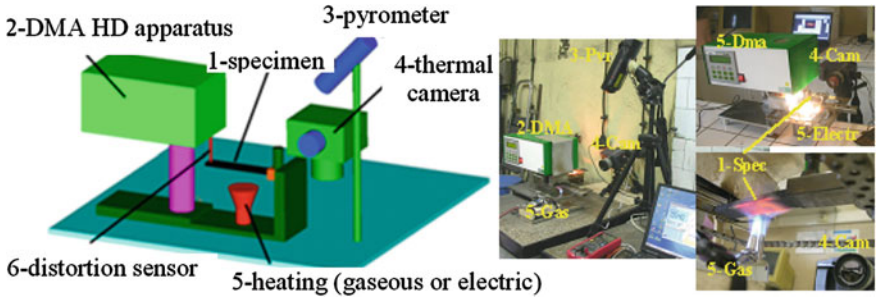

Fig. 19 Modified measuring stand. Diagram of the measuring stand (*left*), photographs made during the tests (*right*)

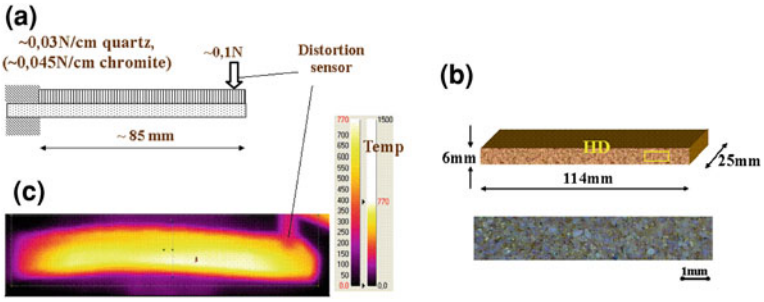

Fig. 20 Scheme of HD specimen (**a**), view of real specimen (**b**), and his temperature map during a HD test recorded by thermal camera (**c**)

This is an innovatory solution, fulfilling the complex functions of a measuring automatic device. Its components include a microprocessor programming system of heating parameters, an automatic drive of the sample approach with a self-adjusting position, and a super-accurate position converter (up to 1 μm). The whole device is computer-controlled. Initially, a heat source in the form of a 1 kW halogen radiator was used. For the studies described in this paper, the DMA—Hot Distortion apparatus modified by Ignaszak (with supplementary devices) was applied. Necessary modifications to the DMA apparatus were introduced: i.e. additional gas heating, the Raytek pyrometer and the V50 thermovision camera provided with its own recording systems enabling the variable temperature field of the specimen to be analysed. The modified measuring stand is shown in Fig. 19. Gas and halogen lamp radiation heating were used interchangeably. The pyrometer recorded the specimen temperature on the side opposite to the heated surface. The temperatures of the heated and side surfaces were recorded by means of the thermovision camera. The sample deformation was also recorded. A diagram of the measuring stand and the photographs made during the tests is shown in Fig. 20. The tests were carried out for the reclaimed and new quartz sand. The specimen dimensions were 114 × 25 × 6 and 120 × 22.4 × 22.4 mm.

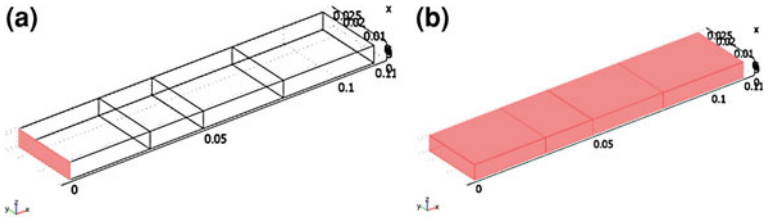

Fig. 21 Definition of boundaries for stress–strain Navier's equation: **a** fixed boundary, **b** free boundaries (with practical simplifications)

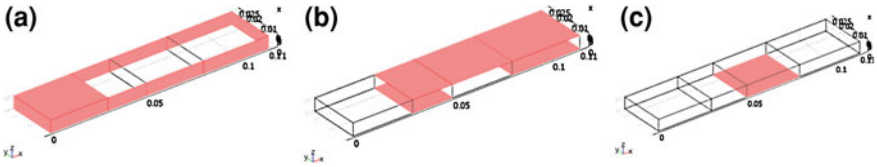

Fig. 22 Definition of boundaries for heat transfer equation: **a** boundaries with thermal insulation, **b** boundaries with smaller heat flux, **c** boundary with greater heat flux

All thermo-mechanical problems considered in this work are governed by selected partial differential equations (PDEs) with appropriate boundary and initial conditions. The numerical results for 3D systems are obtained using standard computational code COMSOL Multiphysics [37]. COMSOL Multiphysics is a powerful interactive environment for modelling and solving the majority kinds of scientific and engineering problems based on coupled partial differential equations (PDEs) using the finite element method (FEM) [38].

The authors show how to estimate the mechanical parameters—Young's (elastic) modulus and thermal expansion coefficient—for a rectangular prism sample to achieve satisfactory agreement between experimental and computational results. There is a number of physical properties that are temperature independent. In this paper, the Young's modulus, $E = E(T)$, and thermal expansion coefficient, $\alpha = \alpha(T)$, are considered as temperature- dependent as well. The principle of homogenization used in this model of porous and multiphase material permits us to simplify the volumic characterization of its properties. These temperature-dependent relations have a great influence on material behaviour and deformation during heating.

Tests were carried out for the new quartz sand bonded by two resins: chemically and thermally hardened binders (about 1%). The specimens (dimensions 114 × 25 × 6 mm, length × width × height) were made with a special core-box using a binder-sand mixture. The material parameters are: $c \cdot \rho = 840 \times 1500$ (J/m^3K), $k = 0.55$ (W/mK), $\nu = 0.25$. Young's modulus and the thermal expansion coefficient were first assumed constant $E = 1e{+}10$ (Pa) and $\alpha = 2.2e{-}5$ (K^{-1}) and finally temperature-dependent, $E = E(T)$ and $\alpha = \alpha(T)$ (see Fig. 23a).

8.1 Boundary and Initial Conditions

The following boundary conditions for Navier's equation are assumed [37]: boundaries A (see Fig. 21a): fixed boundary, $u = 0$ boundaries B (see Fig. 21b): free boundaries. Following boundary conditions for heat equation are assumed: boundaries A (see Fig. 22a): thermal insulation, $-n\cdot(\lambda\nabla T) = 0$ boundaries B (see Fig. 22b): heat flux, $-n\cdot(\lambda\nabla T) = h(T_{inf} - T)$ with heat coefficient $h = 45$ (W/m^{2}K) and $T_{inf} = 293$ (K); boundaries C (see Fig. 22c): heat flux, $n\cdot(\lambda\nabla T) = h(T_{inf} - T)$ with heat transfer coefficient $h = 150$ (W/m^{2}K) and $T_{inf} = 1223$ (K).

Constant initial condition temperature in the domain being considered is assumed: for $t_0 = 0$ $T = 293$ (K). No stress and strain is assumed. Time-dependent problems are considered for time t from 0 to 120 s. These problems are solved with COMSOL code using direct SPOOLES or a UMFPACK linear system solver. Relative and absolute tolerance used in the calculations are 0.01 and 0.001, respectively. A Quadratic Lagrange shape function with a tetrahedral element is used for the solid stress–strain mode and a linear Lagrange shape function with a tetrahedral element is used for the heat transfer mode.

The results show very good agreement concerning temperature variations [39].

An anaslysis was made of the intuitive temperature variations of $E = f(T)$ and $\alpha = \alpha(T)$ resulting from our experiments on thermo-mechanical behaviours in the material being considered in contact with high temperature. Many numerical tests were done using a wide range of parameter values resulting from $E = f(T)$ and $\alpha = \alpha(T)$ formulas. A good agreement between the real (measured by HD Plus test) and simulated distortion curves was assumed as the goal criterion.

The final estimation of temperature-dependent $E = f(T)$ and $\alpha = \alpha(T)$ is proposed in Fig. 23. The applied formulas allow us to obtain the expected agreement for measured and simulated distortions (see Fig. 24).

It turned out that application of the simplest type of mechanical model (elastic) [41] and temperature dependent parameters (E and α) allow expected agreement of measured and simulated distortions to be obtained.

9 Summary

The review presented above is based on the experience of our CAD/CAE Laboratory specializing in materials technologies, especially in virtualization of metallurgy and foundry phenomena and in prognosis of the quality of industrial casting.

According to the results obtained by our studies, good agreement of simulation results with reality for the casting made in the sand mould depends mostly on the thermophysical parameters of the mould sand. The influence of numerous factors resulting from its components, its thermal instability and the relations with the conditions of its preparation and use in mould is observed.

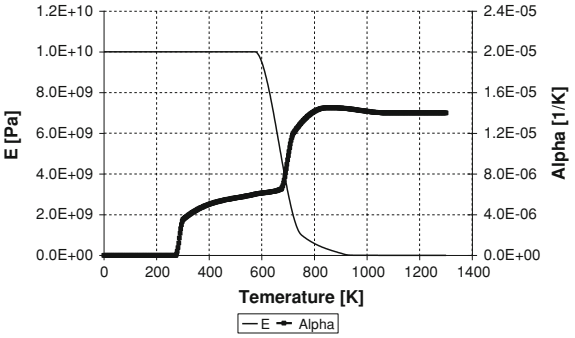

Fig. 23 Estimated final formulas E = f(T) and $\alpha = \alpha(T)$ for quartz sand bonded by 1% of chemically hardened resin [39]

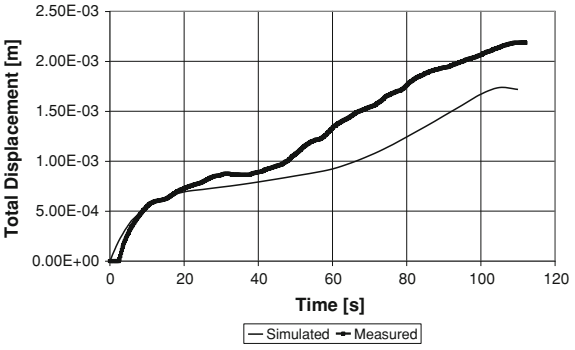

Fig. 24 Comparison of measured and simulated distortion curves [39]

The model of virtual phenomena occurring in sand mould material used in cast simulation systems (simulation codes) is extremely simplified.

But the necessary condition required here is energy (thermal) balance in model validation. If the energy balance validation of the model is fulfilled, it would appear that any number of λ_i, c_i and ρ_i sets could perform the function of obtaining the conformity of solidification time in real and virtual casting. For this reason, conditions necessary for obtaining the satisfied conformity of temperature changes in the tested and virtual material should be considered. Dynamic temperature validation requires references of recorded results obtained from experiments (curves of cooling/heating) to curves built of simulated values.

For solving this important and difficult inverse problem it is necessary to have the results of carefully prepared and original experiments, not only in laboratories but also mainly in industry conditions, wellplanned, with a high level of measurement equipment (data acquisition computer unit) compared with virtual reality, for example, by iterative methods.

Some risks are indicated, which result from the use of numerical optimization to solve inverse problems. The complex approach to the identification of material data and boundary conditions, which was discussed, must be always connected with the model validation, with reference to full casting experiment procedure.

Also the introduction of a new mould sand for making a casting mould of unknown thermomechanical features (new matrix, new resin) requires at least estimative testing of its thermal and thermomechanical parameters (hot distortion caused by heating).

This allows us to answer the question of assessing the new material with respect to the values of the aforementioned parameters in the materials formerly used for the moulds, with characteristics identified earlier.

The combined analysis of thermal parameters and the Hot Distortion parameter shows that the rates of the loss of mechanical properties are different, depending on the destruction of the resin bonds. Destruction of the system thermal bridges affects local thermal and thermomechanical coefficients. On the other hand, the specifications $T = f(T)$ and $\Delta x = f(t)$ shown in the summary diagrams reflect the first such trial performed for the mould materials, followed by estimation of equivalent values of the λ and c parameters. Positive validation of the coupled model describing the thermo-mechanical phenomena in porous thermolabile materials allows the estimated thermo-physical parameters to be used successfully as a database item in casting simulation systems i.e. casting—non-permanent moulds from a quartz sand bonded e.g. by chemically hardened resin).

The satisfactory validation of the coupled models describing the thermal (thermophysical and thermomechanical) phenomena in porous thermolabile materials allows the estimated thermo-physical parameters to be successfully used as a database item in casting simulation systems i.e. for castings poured into non-permanent moulds from a quartz sand bonded e.g. by chemically hardened resin.

References

1. Ignaszak, Z.: Virtual Prototyping in the Foundry. Data Bases and Validation (in Polish). Edition of Poznan University of Technology, Poznan (2002)
2. Handbook of Thermophysical Properties (ed.) Macmillan Comp., New York (1961)
3. Ignaszak, Z.: Thermophysical Properties of Mould Materials in Aspect of Solidification Control of Simulation Process (in Polish). Poznan University of Technology, Rozprawy nr 211, Poznan (1989)
4. Ignaszak, Z.: Study on Data Base of Modeling Concerning Casting Phenomena in Cast-Iron-Mould Simulation Systems, Engineering Materials, vol. 457, pp. 305–311. Trans Tech Publications, Zürich (2011)
5. Fiedler, T., Belova, I.V., Öchsner, A., Murch, G.E.: Application of the LMC Method to Heat Conduction Problems: Overview on Recent Developments DSL (2010)
6. Ignaszak, Z., Popielarski, P.: Heat Transfer During Hot Distortion Test of Ceramic Porous Material Bonded by Various Resins, Defect and Diffusion Forum, vols. 283–286, pp. 382–387, Trans Tech Publications, Zürich (2009)
7. Ignaszak, Z., Popielarski, P.: Problem of the Variability of Substitute Thermo-Physical Properties for Heat Transfer Modelling in Iso-exo Porous Materials, Defect and Diffusion Forum, vols. 283–286 pp. 376–381 Trans Tech Publications, Zürich (2009)
8. Magmasoft user's manual, www.magmasoft.de
9. NovaFlow&Solid user's manual, www.novacast.se

10. Ignaszak, Z.: La conductivité thermique substitutive du moule. Une nouvelle méthode de mesure pour la simulation de la solidification des pieces. Proceedings of 58th World Foundry Congress, Official Exchange paper, Krakow, (1991) and Fonderie—Fondeur d'Aujourd'hui 121, janvier 1993
11. Schmidt, P.: Materials Science and Engineering, Al 73 (1993)
12. Calcosoft user's manual, www.esi-group.com
13. Sciama, G.: Sensibilité des résultats des simulations de solidification aux variations de caractéristiques thermiques, Fonderie Fondeur d'Aujourd'hui, 133, mars 1994
14. Overfeld, T.: Sensitivity of a steel plate solidification model to uncertainties in thermophysical properties. Conference on Modeling of Casting, Welding and Advanced Solidification Processes, VI, Floride, USA (1993)
15. Minikawa, S., et al.: Metall. Trans. B, 16B (1985)
16. Ignaszak, Z.: Simulation model sensivity to quality of material properties. Solidif. Metals Alloys **1**, 25–36 (1999). Book no 40
17. Farre, S.: Private communication during Symposium Computer Aided Design (Virtual Prototyping) in the Foundry Using NovaFlow & Solid System, Poznan, 2 April 2003
18. Kubo, K., et al.: Proceedings of 50th World Foundry Congress, Official Exchange paper, Cairo (1983)
19. Zak, E.M.: Liteinoe proizvodstvo (russish Foundry J.), 1 (1986)
20. Rappaz, M., et al.: Proceedings of Conference Casting, Welding and Advanced Solidification Processes, London (1995)
21. Hueber, N., Ignaszak, Z.: Water effects and thermal behavior of a sand, thermal properties identification by optimization tools. Proceedings of 8th Conference Modelling of Casting, Welding and Advanced Solidification Processes, San Diego (USA) (1998)
22. Ignaszak, Z.: Thermophysical parameters of insulating materials applied to design of casting feeding and to simulation of its solidification (in Polish). Solidif. Metals Alloys **1**, 125–131 (1999). Book No. 40
23. Drezet, J.M., Rappaz, M., Grün, G., Gremaud, M.: Determination of thermophysical properties and boundry conditions of direct chill-cast aluminium alloys using inverse methods. Metall. Mater. Trans. **31A**, 1627–1634 (2000)
24. Rappaz, M., Desbiolles, J.L., Drezet, J.M., Gandin, Ch.A., Jacot, A., Thévoz, Ph.: Application of inverse methods to the estimation of boundary conditions and properties. Proceedings 7th International Conference Modelling of Casting, Welding and Advanced Solidification Processes, The Minerals, London, Metals & Materials Society (1995)
25. Ignaszak, Z.: Energetic and dynamic validation of thermal models in practice of casting technology simulation. Proceedings of the International Conference on Advances in Materials and Processing Technologies (AMPT2003), Dublin, 8–11 July 2003
26. Wolff, H., Engler, S., Schrey, A., Wolf, G.: Wärmetransport I Formen bei der Erstarrung und Abkühlung von Mittel- und Grossguss aus Gusseisen, Giessereiforschung, no 4 (2002)
27. Drotlew, A., Ignaszak, Z., Bieńko, G., Popielarski, P.: Identyfication of thermo phisical properties of moulding Sand with micro-cobler addition. Arch. Founry **4**(14), 132–137 (2004)
28. Ignaszak, Z., Graczyk, L., Popielarski, P.: Experimental—Simulating method of over most zone identification in the mould. Arch. Founry **6**(22), 216–223 (2006)
29. Ignaszak, Z., Popielarski, P.: Problem of the Variability of Substitute Thermo-Physical Properties for Heat Transfer Modelling in Iso-exo Porous Materials, Defect and Diffusion Forum, vols. 283–286, pp. 376–381. Trans Tech Publications, Zürich (2009)
30. Ignaszak, Z., Popielarski, P.: Problems of Heat Source Modeling In Iso–exothermic Materials Used as Riser Sleeves in Foundry. Materials Science Forum, vols. 514-516, pp. s1438–1442 May 2006, Trans Tech Publications (2006)
31. Ignaszak, Z., Popielarski, P.: Heat Transfer During Hot Distortion Test of Ceramic Porous Material Bonded by Various Resins, Defect and Diffusion Forum, vols. 283–286, pp. 382–387, Trans Tech Publications, Zürich (2009)
32. Ramrattan S.N., et al.: Thermal Distortion in Process Control of Chemically-Bondes Sands, AFS Transactions, paper no 152, pp.152–165 (1997)

33. BCIRA Hot distortion tester. Operating instructions (1975)
34. Morgan, A.D., Fasham, E.W.: A new hot distortion tester for chemically bonded sands. Report of BCIRA (1974)
35. Information on http://www.multiserw-morek.pl/pl/indexpl.htm
36. Jakubski, J., Dobosz, St.M.: Analysis of thermal deformation of core sands using apparatus DMA, Archives of Foundry. Nr 9 vol. 3, pp. 246–251 (2003)
37. Comsol, Comsol Multiphisycs 3.4 User's Guide, Comsol AB (2007)
38. Zienkiewicz, O.C., Taylor, R.L.: The Finite Element Method, vols. 1–3, 5th edn. Butterworth-Heinemann, Oxford (2000)
39. Ignaszak, Z., Popielarski, P., Strek, T.: Estimation of coupled thermo-physical and thermo-mechanical properties of porous thermolabile ceramic material using Hot Distortion Plus® test. Proceedings of 6th DSL Conference, Paris, 5–7 July 2010
40. Ignaszak, Z.: Substitute thermal conductivity coefficient for multi-component ceramic materials. Proceedings of International Conference on Advances in Materials and Processing Technologies, AMPT'01 Madrid, September 2001
41. Landau, L.D., Lifshits, E.M.: Theory of Elasticity. Pergamon Press, London (1986)

Metal Foams Design for Heat Exchangers: Structure and Effectives Transport Properties

Jean-Michel Hugo and Frédéric Topin

Abstract This chapter deals with metal foams heat exchangers design. We present effective properties of metal foams such as (a) thermal conductivity and heat transfer coefficient used to model heat transfer, (b) permeability and inertial coefficient used to model flow pattern through foams. All these properties constitute basic inputs for homogeneous equivalent porous media approach widely used to design heat exchanger. We present methods which will allow one to determine thermo-physical and geometrical properties of foams. A numerical approach is used to get better understanding of solid matrix geometry influence on transport properties.

1 Introduction

Solid foams are relatively new class of multifunctional materials that possess attractive thermal, mechanical, electrical and acoustic properties. Moreover, they also promote mixing and have excellent mechanical properties. They are widely quoted to present a random topology, high open porosity, low relative density and high thermal conductivity of the cell edges, large accessible surface area per unit volume [1]. Usually, geometric properties such as high tortuosity and high specific

J.-M. Hugo (✉) · F. Topin
IUSTI Lab, CNRS UMR 6595, Polytech, Marseille, France
e-mail: Jean-Michel.Hugo@Polytech.univ-mrs.fr

J.-M. Hugo
MOTA S.A. Cooling System, ZI les Paluds, Aubagne, France

F. Topin
e-mail: frederic.topin@Polytech.univ-mrs.fr

J. M. P. Q. Delgado (ed.), *Heat and Mass Transfer in Porous Media*,
Advanced Structured Materials 13, DOI: 10.1007/978-3-642-21966-5_9,

surface are proposed to explain their properties, although pore space tortuosity is low (i.e. <1.1) and specific surface range from 200 up to 5,000 m^2/m^3 for commercially available samples [2]. They are, nowadays, proposed for use in numerous applications such as compact heat exchangers, reformers, biphasic cooling systems and spreaders. They are also used in high-power batteries for lightweight cordless electronics, and catalytic field application such as fuel cells systems [3–6].

Compact heat exchangers are employed in a wide variety of engineering applications, such as geothermal processes, air conditioning, cooling system, and so on. Heat exchangers are selected for a process considering the following factors: Heat-transfer requirements, cost, physical size and pressure-drop characteristics [7]. Metallic foams are used in this field to increase heat transfer at the cost of an additional pressure drop [8, 9]. However, their use permit substantially to reduce the physical size of heat exchanger, and thus fabrication costs and they present many other favorable characteristics (vibration damper, rigidity, etc.).

A synthesis of correlations for heat exchanger design is made by Mahjoob and Vafai [4]. They gathered heat transfer coefficient and friction factor laws from experimental, analytical and numerical studies.

Yet, solid foam structure and its properties are still incompletely characterized although accurate evaluation of these properties becomes critical for various uses.

Thermo-physical and flow properties greatly depend on the local morphology of both pores and solid matrix [10, 11]. Local changes (e.g. constriction, strut cross section, surface roughness, etc.) in the structure can influence the properties. Literature models of effective thermal properties, widely used in low porosity media, can no longer be applied to high porosity materials [12]. Most of the modeling approaches are based on arbitrary periodic structures that represent the foam. There is a lack of morphological tools to characterize the real microstructures of these foams and very few works use the real geometry (usually obtained by 3D X-ray tomography) to determine physical properties [13, 14].

If overall heat transfer coefficient is known, NTU method allows predicting the thermal performance of heat exchangers. The pressure drop then can be deduced from global friction factor. However, for complex and relatively new structures, it is more difficult to get values for these parameters. Thus, two ways can be followed to design metal foam or classical heat exchangers (fins and tubes, plate, etc.): concept and produce several prototypes (along with their technical problems, cost and time consuming realization) or use of numerical simulation tool. Direct numerical simulation on whole device needs high performance computers and time. It's thus necessary to model heat exchangers using porous media approaches that reduce drastically computational time but require prior knowledge of effective properties.

In the present paper, we propose to define useful properties of metal foam for heat exchangers design. We also propose a method to determine foam structure and global geometry of the device for given thermal performance. Finally we present some numerical or experimental method of determination of geometric and transport properties.

2 Foam Properties for Heat Exchanger Design

To model metal foam crossed by a single phase flow as a homogeneous continuum, macroscale fluid flow, heat exchange and thermal diffusion laws are necessary. The knowledge of following properties is essential for this design: a mean volume heat transfer coefficient between solid and fluid phase, solid and fluid effective diffusivities, foam inertia coefficient and permeability.

2.1 Fluid Flow Law

It is classically considered that a porous medium can be assimilated to an equivalent homogeneous medium [15]. For our foam samples, we have considered that a minimum volume of ten pores is necessary to satisfy this condition.

Considering the three classical laws on flow through porous media, the only way to decide which one applies best to flow through metallic foams is to test them against experimental data [10, 11].

It is well known that flow at very low flow rate through a porous medium is governed by Darcy's law (Darcy 1856).

$$-\nabla P = \frac{\mu}{k} \cdot U \tag{1}$$

where $\nabla P = \mathrm{d}P/\mathrm{d}z$ is the pressure gradient along the main flow in z-direction, μ the dynamic viscosity, u is Darcy's velocity, and K (m2) is the permeability of the medium.

In homogeneous porous media, a nonlinear relationship between the pressure drop and the flow rate characterizes a "high-velocity" flow. For high Reynolds numbers (strong inertia regime), the empirical Forchheimer equation is used to account for the deviation from Darcy's law. Expressed as a function of the mass flow rate, this equation is written (incompressible fluid):

$$-\nabla P = \frac{\mu}{k} \cdot U + \rho \cdot \beta \cdot U^2 \tag{2}$$

where ρ (kg m^{-3}) is the fluid density and β (m^{-1}) the inertia factor or the non-Darcy flow coefficient. In this formulation, the Brinkman correction is neglected. The pressure drop is considered as the sum of two terms: a viscous (u, Darcy law) term and an inertia (u^2) term.

Since the Forchheimer equation applies to high flow velocities, it is important in the case of a gas flow to take into account the compressibility [16]. Considering the fluid as a perfect gas, velocity and density are position functions. Mass conservation implies that $\eta = \rho(z) \cdot u(z)$ is constant along the main flow axis for a fixed flow rate. Considering that advection contribution is negligible compared to pressure gradient, we write the Forchheimer equation:

$$-\nabla \rho P = 2 \cdot \rho \cdot \left(\frac{\mu}{k} \cdot U + \rho \cdot \beta \cdot U^2 \right) \tag{3}$$

Expression (3) implies that the profiles of the product "density × pressure" (called "ρP" in the rest of the text) along the main flow axis are linear at all tested velocities for both fluids.

Several authors have shown that the onset of the non-linear behavior (which is sometimes called the weak inertia regime) can be described by a cubic law [17–19]:

$$-\nabla P = \frac{\mu}{k} \cdot U + \gamma \cdot \frac{\rho \cdot U}{\mu} \rho \cdot U^2 \tag{4}$$

where γ is a dimensionless parameter for the non-linear term. $\beta(u) = \gamma \rho \, \mu \, u$ can be described as a velocity-dependent inertia coefficient.

In spite of the numerous attempts to clarify the physical reasons for the non-linear behavior described above, neither the Forchheimer equation 3 nor the weak inertia equation 4 have received any physical justification [20].

For all three formulations of the pressure gradient through a porous medium, K, β and γ are intrinsic characteristics of the solid matrix alone, and are thus independent of the fluid nature.

Usually, the Reynolds number, Re, is defined as:

$$Re = \frac{\rho \cdot U \cdot L}{\mu} \tag{5}$$

where L is the characteristic length of the flow zone and η the mass flux density.

In the case of porous media, it is difficult to define a characteristic length "L". Literature shows some ambiguity (arbitrary choice that introduces a numerical factor) in the definition of the Reynolds number may impede the interpretation or comparison of the different experiments.

Many expressions have been proposed for the Reynolds number [15, 21, 22]. The most widely used characteristic length is the pore diameter. The strut size and the hydraulic diameter of the channel containing the porous medium are also often quoted. It has been proposed to use the value $\sqrt{K}$ or $\sqrt{K/\varepsilon}$, which has the dimension of a length and contains information about the viscous part of flow law. Thus, this expression can only be used in the case of Darcy flows. When the Forchheimer model is used, some authors propose $K \times \beta$ as a characteristic length [23]. These two formulations make it possible to evaluate the characteristic size from flow experiments, but cannot be used to quantify the structural influence of the solid matrix on the flow parameters.

In the present work, we used as characteristic size, the pore diameter—measured independently using X-ray tomography [24]. Even though a slight anisotropy of the geometrical parameters was observed, this effect was neglected in our work [25]. Bonnet et al. proposed experimental method to determine Forchheimer parameters for several foams. In the following paragraph, we present a method to determine permeability and inertia coefficient based on foam real 3D structure and CFD calculation at pore scale.

Fig. 1 Foam matrix surface mesh. Sample size: 15 × 15 × 15 mm. Volume mesh: about 10 million polyhedral cells

2.1.1 Computational Domain

The studied system is a rectangular domain representative of a heat exchanger section. The sample size (15 mm in all directions) is sufficient to define macroscopic parameter as the Representative Elementary Volume (REV) characteristic length is about three pore diameter [26]. The computational domain is divided in three sections parts: Inlet zone, test section and outlet zone to avoid bias product by back conduction and fluid recirculation.

Volume mesh (∼1–10 million cells with a mean size of about 0.2 mm and a minimal one of 0.01 mm) is generated from actual solid surface using StarCCM4 + mesher. It is composed from core polyhedral meshes in both solid and fluid phases with additional prism layers mesh in fluid phase in the vicinity of solid surfaces. Boundary conditions are defined as: imposed temperature on one lateral wall and adiabatic on the other walls. Inlet temperature and pressure are imposed. Other walls are symmetry planes (Fig. 1).

2.1.2 Results

The Navier–Stokes equations and energy balance equation are solved using a finite volumes method (StarCCM+). These equations are solved at the pore scale and give access to velocity and pressure fields in the fluid phase and temperature in both, solid and fluid phases. Local heat fluxes across the solid matrix surface are

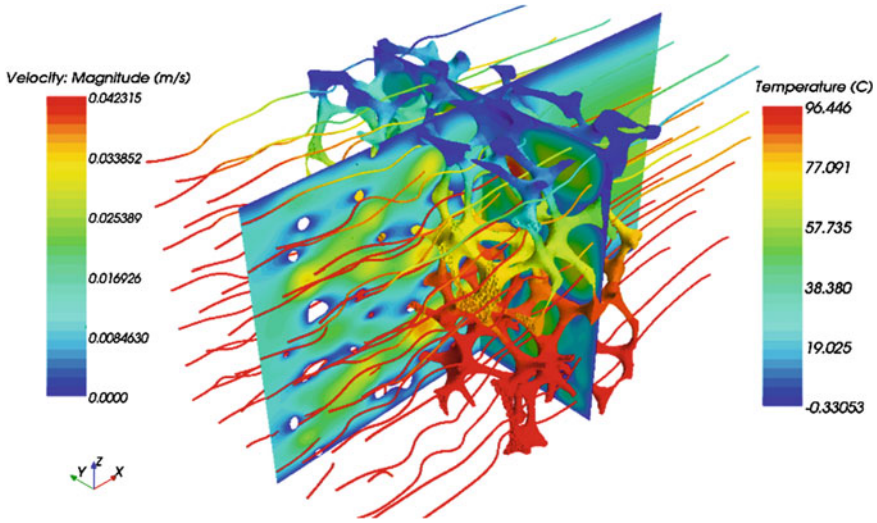

Fig. 2 Simulation of heat and mass transfer in a real metal foam: both plane sections show velocity magnitude. Solid matrix surface and streamlines are colored by respectively solid and fluid temperature

also determined. Numerical simulation are performed for wide Reynolds number range (10^{-2}–10^{4}).

On Fig. 2 the two plane sections show velocity magnitude. Important velocity gradient could be observed locally while a constant averaged value is obtained in a cross section normal to the principal fluid flow direction. Solid surface is colored with its temperature. A sharp gradient exists near the cooled wall while near the other side, fluid and solid temperature are roughly identical. This indicates that solid to fluid heat transfer occurs mainly in the vicinity of the heated wall. Finally, some streamlines illustrate the tortuous path followed by the fluid. This indicates that boundary layers will not develop near wall channel. Also, some eddies could be located in the wake of struts. These phenomena govern heat transfer enhancement and pressure drop increase.

At macroscopic scale, mean velocities are indeed representative of global fluid behavior. Nevertheless, according to Reynolds number values, velocity gradients and preferential paths may appear. For Reynolds near unity, velocity field is very homogeneous, and struts wakes are very small (similar to Stokes regimes around cylinders). For higher Reynolds, large eddies and recirculations are observed in the struts wakes (Fig. 3). The flow may become un-stationary and wake interactions between struts may appear. A strut in the wake of a previous one will exhibit poor heat performance. Preferential high velocity path will cause rather important pressure gradient. On Fig. 3 some high velocity vectors exist just upstream of struts. This is a typical 3D effect, the flow gets around the struts in the third dimension. Global heat exchange limitation and strong inertia effects intensity at high Reynolds can be explained by these phenomena. On the other hand, low

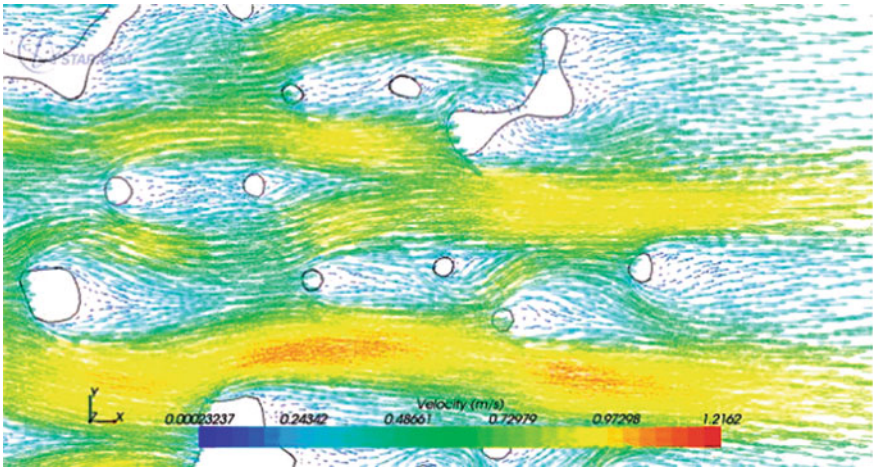

Fig. 3 3D velocity vectors ($Re = 80$) extracted from a single plane parallel to the main flow axis. Sharp velocity gradient and eddies in the wake of each struts are observed

toruosity of pore space associated to the relatively small specific surface of the solid matrix could not explain heat transfer perfomance and inertia effect intensity.

Brun [26] shows that commercial foam, such as ERG ones, are homothetic. These properties is used in the present study to change the mean pore diameter (from 1.125 up to 18 mm) by scaling the computational domain.

2.1.3 Fluid Flow

To establish parameters K and β numerically, simulations must be performed for several values of Reynolds. K and β are then computed by fitting pressure gradient versus superficial velocity data with the Forchheimer model. Results are then compared to those obtained experimentally. References [6, 27] give experimental data for pressure losses in similar metal foam (ERG) for liquid and gas flows (Table 1 and Fig. 4).

$$f = \frac{\Delta P}{l}\frac{D_p}{0.5\rho U^2} = \frac{2{D_p}^2}{K \cdot Re} + 2\beta D_p \tag{6}$$

On Fig. 4, experimental data from [6] for two pores diameters (3 and 4.5 mm) are compared to numerical results. A good agreement is found. For clarity, data are presented as friction factor (6) versus the Reynolds number based on pore diameter. For all pore diameters, there is a unique curve of friction factor determined by numerical simulation in the present study (Fig. 4). Equation 6 associated to these results demonstrates that both permeability and inertia coefficient evolve with the pore diameter only. For a given Reynolds, to conserve a constant friction factor, permeability should be proportional to the squared pore diameter and to the

Table 1 Summary of experimental and numerical results

	Grade (PPI)	Dp (mm)	K (m²)	β (m^{-1})
Hugo et al. [28]	80	1.125	1.89E-08	1208
	40	2.25	7.48E-08	612.1
	20	4.5	2.97E-07	266.1
	10	9	1.30E-06	111.5
	5	18	4.80E-06	53.2
Tadrist et al. [6]	40	3	6.60E-08	389
	20	4.5	2.50E-07	244
Kim et al. [27]	40	0.635	5.10E-08	442
	20	1.27	7.80E-08	362
	10	2.54	1.04E-07	308

Greyed valued are estimated from grade definition (PPI = $25.4/D_p$)

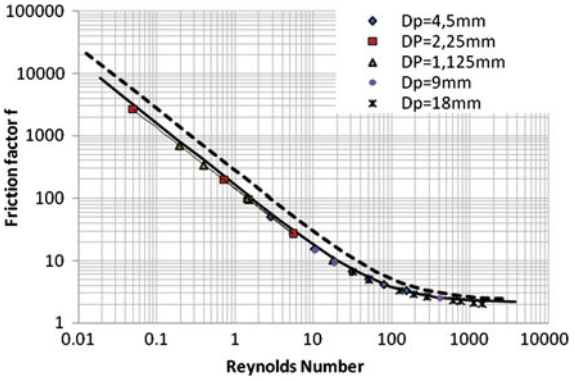

Fig. 4 Friction factor versus Reynolds (characteristic length: pore diameter) compared with experimental results from [6]

inverse of the pore diameter as [10] has shown experimentally on several metal foams. The friction factor versus Reynolds curve exhibits two behaviors separated by a transition zone. For Reynolds smaller than 50, viscous effects are predominant. Pressure drop increases linearly with the velocity. For high Reynolds (greater than 2,000), the flow behavior is dominated by inertial effects. The pressure drop increases as the square of velocity. For Reynolds between 50 and 2,000, there is a transition zone where, both, viscous and inertial effects govern pressure losses. Friction law is well described by the Forchheimer model.

Inertia coefficients and permeability obtained from numerical simulations are summarized in Table 1 and compared to experimental data. Foam pore diameter for [6] study have been determined latter by [26]. Kim et al. [27] just gives foam grade; pore diameter are not exactly determined. However, flow law parameters for 40PPI foam given in both experimental studies are quite close. This indicates

that grade is clearly not relevant as pore size estimator. Several authors have proposed to use K as pore size estimator but K is usually difficult to obtain accurately using available experimental data. This is particularly true in case of high pore size foam (e.g. 5 up to 20 mm).

2.2 Heat Exchange Law

Many experimental, theoretical and numerical works were carried out to describe heat transfer in porous media. Two theoretical approaches are used to model heat transfer in metal foam: "one temperature model" (local thermal equilibrium between each phases) and "two temperature model" (non equilibrium). Both models need to know effective properties: thermal effective conductivities of each phases and mean local heat transfer coefficient between solid and fluid phase.

2.2.1 One Temperature Model (Thermal Equilibrium)

In this model, a local thermal equilibrium is considered between solid and fluid phases [29]. It means that locally, the fluid and solid temperature reach the same value or the convective heat transfer coefficient between fluid solid matrix is infinite. This model is described by the following equation:

$$\left[\left(\rho\, C_p\right)_s (1-\varepsilon) + \left(\rho\, C_p\right)_f \varepsilon\right] \frac{\partial T}{\partial t} + \left(\rho\, C_p\right)_f \boldsymbol{U} \cdot \nabla T = \nabla \cdot \left(K_{eff}\, \nabla T\right) \tag{7}$$

This model is valid for the following hypothesis: homogeneous porous continuum, no heat transfer between each phases, very low velocity flow and an important thermal dispersion. In this model, the knowledge of foam properties is needed: porosity, density, heat capacity and effective thermal conductivity of both phases.

2.2.2 Two Temperatures Model (Thermal Non-Equilibrium)

The "two temperatures model", also called local thermal non-equilibrium, is used for stationary and non stationary flow to model convective heat transfer. In this model, each phase is considered as a homogeneous continuum. Locally, temperature of each phase can be different. In this model, we introduce effective thermal conductivity of each phase and a mean volume heat transfer coefficient between foam struts and fluid flow [30]:

$$\varepsilon\left(\rho\, C_p\right)_f \frac{\partial T_f}{\partial t} + \left(\rho\, C_p\right)_f \boldsymbol{U} \cdot \nabla T_f = \nabla \cdot \left(k_{f\,eff} \nabla T_f\right) + h \cdot \left(T_s - T_f\right) \tag{8}$$

$$(1-\varepsilon)\left(\rho\, C_p\right)_s \frac{\partial T_s}{\partial t} = \nabla \cdot \left(k_{s\,eff} \nabla T_s\right) - h\left(T_s - T_f\right) \tag{9}$$

This model can be used for the design of heat exchanger with metal foam field. For this, the knowledge of local heat transfer coefficient effective thermal properties is needed. There are only few works dealing with the experimental determination of the local heat transfer coefficient [31]. Effective thermal conductivities can be determined for the solid phase [32, 33] but it's a scientific challenge to determine the one of the fluid phase because of the macroscopic thermal dispersion, due to the fluid flow behavior in the porous media.

2.2.3 Determination of Local Heat Transfer Coefficient

Viskanta et al. proposed an experimental method to determine the volume heat transfer coefficient for ceramic foams [34]. The volume heat transfer coefficient is equal to the local heat transfer coefficient times the foam specific surface. They used the single blow transient experimental technique in conjunction with an inverse analysis. Serret et al. also proposed an experimental technique based on measurement of attenuation and phase shift of a sinusoidal temperature signal transported by constant velocity flow across foam slab [31].

In order to gain a better interpretation of global heat transfer performance, a local heat transfer coefficient between fluid and struts surfaces is determined numerically on the real metal foam structure by Hugo et al. [28]. It is defined with heat flux through the solid matrix surface and a mean logarithmic temperature difference between solid and fluid phases. The mean solid temperature is averaged on the whole foam developed surface. The characteristic length used to calculate the Nusselt and Reynolds numbers is the mean strut diameter.

Results obtained with all pore size gather on a single curve (Fig. 4). For Reynolds smaller than the unity, Nusselt number follows quite well a power law. Then, for Reynolds up to 100, Nusselt is inflecting towards logarithmic law. Numerical results are compared with a good agreement to Lu et al. [35] numerical model for Reynolds smaller than 1. For low Reynolds, the curve shape is as we expected. In the vicinity of all struts, velocity fields are homogeneous. Whereas, for high Reynolds, there is a decrease of foam efficiency (as fin efficiency) and velocity field shows sharp gradient and preferential paths. This phenomenon is also observed with staggered multirow heat exchangers (Fig. 5).

A local Nusselt (and heat transfer coefficient) along the fluid flow is deduced from the simulation by dividing the test zone in numerous thin boxes perpendicular to the main flow axis. In each box, mean temperatures of both fluid and solid phases as well as exchanged heat flux are determined.

Figure 6 shows local and integrated Nusselt number variations along the main flow axis. Nusselt number decreases slightly along the flow direction and its averaging reaches a quasi-constant value after three pores diameters. But its behaviour differs from the empty channel case. No clear entrance zone is observed. High amplitude periodic oscillations around the global decreasing trend are observed with a one pore period. Locally, the Nusselt number reaches high and low values. Local maxima and a minima are located every half pore diameter.

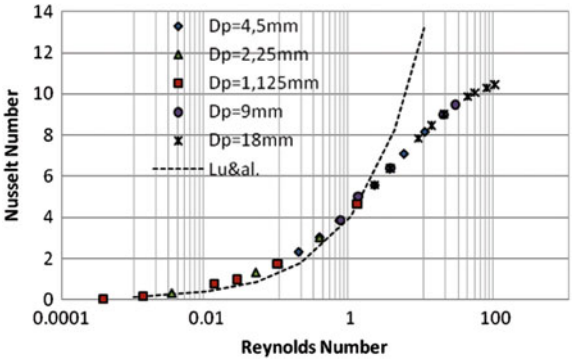

Fig. 5 Local Nusselt versus Reynolds. Direct numerical simulation and comparison with literature. Characteristic length: Strut diameter

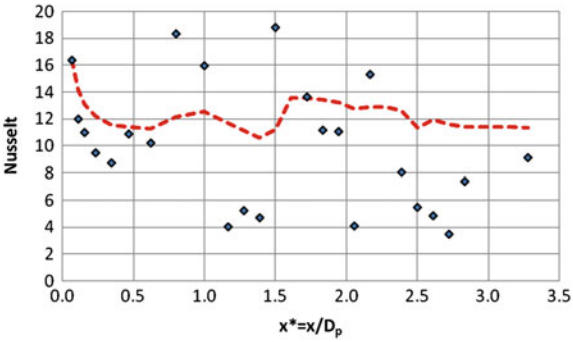

Fig. 6 Local (*dot*) and integrated (*line*) Nusselt number along the main flow axis. characteristic length: Strut diameter

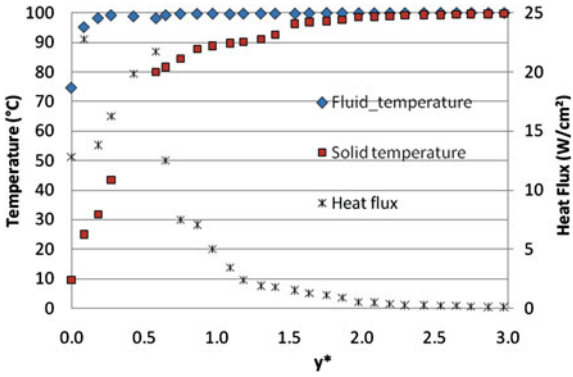

Fig. 7 Heat flux on the foam surface, temperature of both fluid and solid phase versus the distance from the heated wall. $x^* = 1.62$

Cells present a staggered arrangement and Nusselt increases in the vicinity of throats.The cell arrangement along the main flow axis limits global thermal and flow boundary layers formation. Madani et al. [36] have experimentally shown similar result. For application purpose, pore size should be chosen according to the (empty) channel boundary layer characteristic length.

Each of the previously defined box is cut again by planes parallel to the heated plate. In each box, average temperatures of both phases as well as exchanged heat

flux are calculated. Figure 7 shows these quantities plotted in function of the reduced distance from the heated wall.

Like a fin, foam efficiently contributes to heat transfer only on relatively short distance to the heated wall. This active length is defined as the distance where fluid and solid phases reach the same temperature (difference less than 5%).

On Fig. 7, we present the local heat flux exchanged between fluid and solid phases. Below $y^* = 0.5$, heat flux are very high. The heat flux decreases exponentially roughly above one pore diameter. One could see that the active length is close to $1.5D_p$. Above this distance from the heated wall, heat flux is close to zero.

2.3 Diffusion in Porous Media

2.3.1 Effective Thermal Conductivity

For a porous media filled (saturated) by a stagnant fluid, non reactive, and for an imposed temperature gradient, when thermal regime reaches a steady state, there is uniform thermal flux. Thus, it's possible to define an effective, or equivalent thermal conductivity k_{eff} [37]. Heat transfer is defined as a Fourier law:

$$\boldsymbol{\varphi} = -K_{eff} \nabla T \tag{10}$$

Several authors have developed models to predict the effective thermal conductivity of foams in a purely conductive regime. These models are based on the association of the thermophysical properties of both solid matrix and fluid on the one hand, and certain structural parameters of the foam on the other hand (for example the ratio between the average strut length and the size of the strut-junction nodes) [32, 38, 39]. Bhattacharya et al. [32] present a comprehensive analytical and experimental investigation for the determination of the effective thermal conductivity of high porosity metal foam. It is a based on a geometrical model of foam consisting on a two dimensional array of hexagonal cells where the fibers form the edge of the hexagon. Commercially available metal foams form a complex array of interconnected fibers (see [2] for more detailed description). Depending on manufacturer, an irregular lump of metal may be found at strut intersection.

Decker et al. [40] provided a detailed experimental characterization and a numerical modeling of the heat and mass transport properties of highly porous media for solar receivers and porous burners. Pan et al. [41] determined experimentally the effective thermal conductivities of aluminum and silicon alloy foams. Writz et al. [42] presented a semi-empirical model for the combined conduction and convection heat transfers in a thin porous wall. Bastawros [43] provided experimental measurements and modeling of the thermal and hydraulic aspects of cellular metals subjected to transverse airflow. Kim et al. [44], also investigated numerically the anisotropy of permeability and effective thermal conductivity and its effect on the performance of an aluminum heat sink. Without exception these works do not take the real morphology of the foam into account but assume an

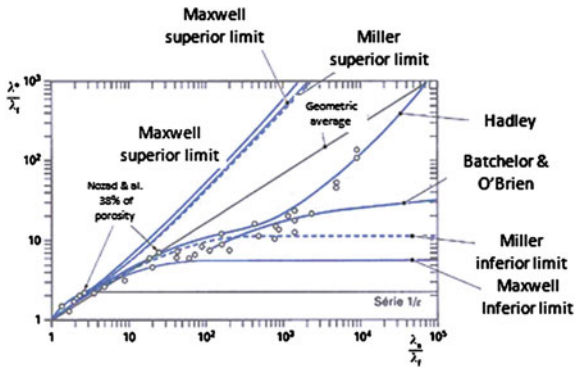

Fig. 8 Effective thermal conductivity versus solid over fluid phases conductivity ratio [37]

idealized periodic pattern. Besides, measurements are made with both stationary [38] and transient methods [45, 46]. Rigollet et al. [47] proposed experimental approach to determine effective conductivity of the solid phase using a photothermal method. These approaches allow one using one temperature model. In order to work with two temperatures models, effective thermal conductivities for each phase should be determined (Fig. 8).

2.3.2 Solid Effective Thermal Conductivity

In a similar manner, it's possible to consider only the solid phase and define an effective conductivity for the solid phase alone $k_{s\text{-}eff}$. This law is mathematically obtained by volume averaging method from microscopic conduction law to a macroscopic law [48]. Moreover this law could be generalized for anisotropic media. Thus k_{eff} is considered as a tensor $\overline{\overline{K_{eff}}}$. This effective thermal conductivity of the solid phase is a function of solid matrix geometric parameters (porosity, continuity, struts connection, etc.).

For metal foam, we showed that solid equivalent conductivity is roughly $k_s.(1-\varepsilon)/3$. Statistically, only the third of foam struts are oriented in any direction and thus, contribute to conduction along the main heat flux direction.

Numerically, solid effective conductivity is determined by a steady method. A temperature gradient is imposed between two opposite faces of foam cube [49]. Heat flux is thus deduced. By measuring all temperatures in each faces and perform simulation in all space direction, a tensor of effective conductivity is obtained (Fig. 9, Table 2).

2.3.3 Fluid Effective Thermal Conductivity

It is possible to define an effective thermal conductivity of the fluid phase such as the solid phase [37]. Nevertheless, for the fluid phase, this tensor is not only depending on the fluid thermal conductivity and pore space morphology. It also depends on fluid

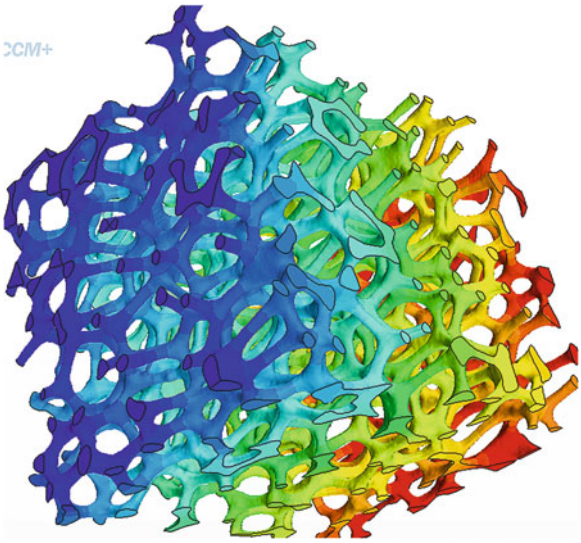

Fig. 9 Metal foam temperature field. Effective thermal conductivity of the solid phase is deduced from simulation

Table 2 Solid effective conductivity for ERG 10, 20 and 40 PPI along three orthogonal directions *X*, *Y* and *Z*

Conductivity (W/mK)	10PPI	20PPI	40PPI
Porosity (%)	87.96	90.41	89.78
X	10.44	6.49	9.06
Y	10.19	8.3	8.04
Z	13.36	10.96	10.06

K_{eff} depends on porosity and slight anisotropy is observed

velocity due to dispersion produced by microscopic velocity field heterogeneity. The effective thermal conductivity tensor of the fluid phase is defined as the sum of conductivity tensor for stagnant fluid and of thermal dispersion tensor:

$$\overline{\overline{K_{f\,eff}}} = \overline{\overline{K_{f\,eff}}}^{*} + \overline{\overline{K_{disp}}} \tag{11}$$

Some works deal with thermal dispersion in the case of classic porous media [22, 50, 51]. Nevertheless, no specific data pertaining to solid foam are available in open literature. Dispersion tensor is defined symmetric and positive for random structure such as metal foam. For isotropic media, non diagonal terms are equal to zero. Usually, the thermal diffusivity tensor is used:

$$\overline{\overline{D_{disp}}} = \frac{\overline{k_{disp}}}{(\rho \cdot C_p)_f} \tag{12}$$

For example, the following figure presents a transverse and longitudinal dispersion versus Péclet number for a granular bed. Taking into account dispersion effect is mandatory for heat exchanger application because of high fluid velocity.

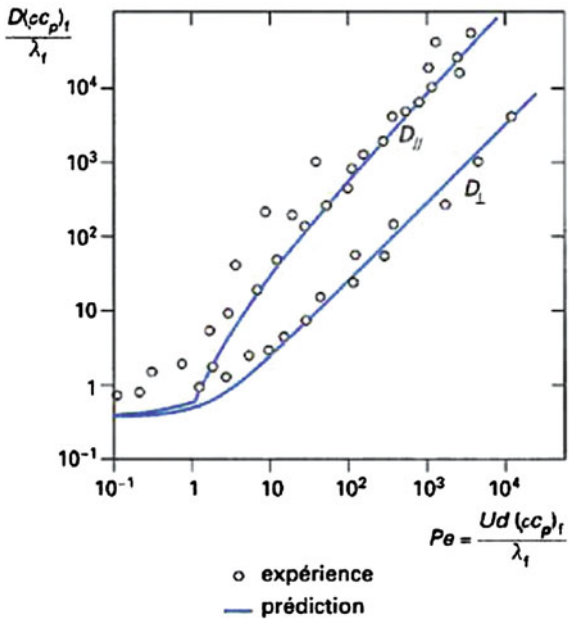

Fig. 10 Theoretical and experimental prediction of dispersion in granular bed from [37]

For example, air flow at 20 m/s in 1 cm characteristic length channel, Péclet number reaches roughly 20,000. Transverse conductivity is multiplied by 1,000.

Clearly ad hoc correlations are needed in order to allow accurate heat transfer calculation in metal foam (Fig. 10).

3 Representative Elementary Volume

Using effective properties of metal foams in a global model (heat exchanger for example), it's necessary to define minimal volume to measure effective properties. This volume must be large enough to be representative of the sample and apply the volume averaging method, and enough smaller to keep on a local characterization of the sample. This volume is called Representative Elementary Volume (REV). The REV is defined by the characteristic length r0 satisfying the relation: $d << r0 << L$ with d: microscopic length and L: characteristic porous sample length [2].

Brun et al. [26, 52] propose numerical tools to fully characterize metal foams morphology from foam pictures obtained by tomography. This tool allows determining geometrical REV based on foam morphology (porosity, pore diameter, specific surface, etc.) and generate mesh for numerical simulation. This simulation realized on in house or commercial software allows determining physical REV.

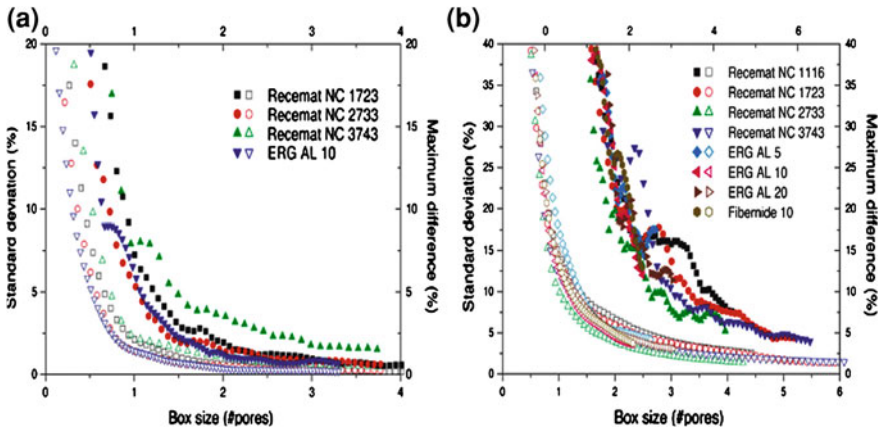

Fig. 11 Geometrical REV determination. **a** Porosity. **b** Specific surface

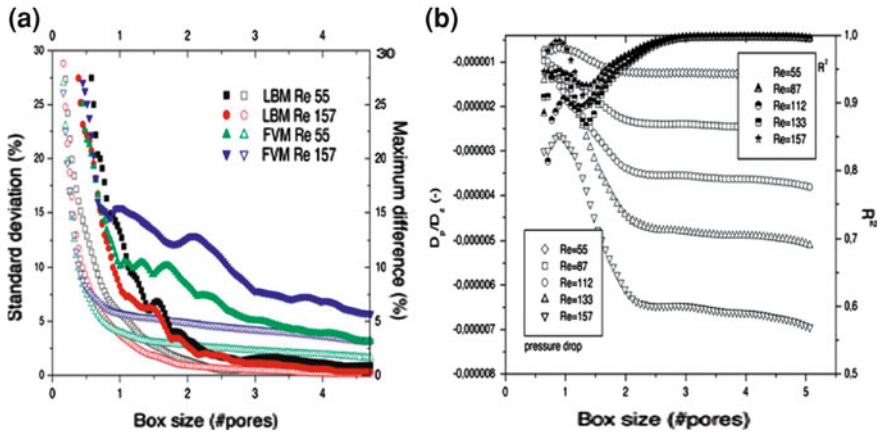

Fig. 12 Physical RVE determination. **a** Velocity. **b** Pressure gradient. *Hollow symbols*: standard deviation; *filled one*: maximum error

3.1 RVE Estimation and Discussion

To compare the different foams, the size of the box was normalized by the pore diameter. Moreover, the standard deviation and the maximum difference are normalized with the mean value of the property studied for the considered foam. Figures 11 and 12 show the evolution of the standard deviation and the maximum difference in function of the box size.

3.2 Geometrical RVE

Porosity and specific surface are estimated from the 3D density images obtained with X-ray tomography. Porosity is trivially obtained by counting the voxels of the different phase. The ''Marching Cubes'' algorithm uses the 3D density images to obtain the mesh of solid surface. Wodie and Levy [17] The mesh data triangles are ordered so that each triangle is included into a unique cubic mesh composing the 3D sample. Once the mesh has been generated for the sample, it is then easy to calculate a specific surface area within a small volume taken in the sample: the cubes composing the volume are retrieved and the surface area of the triangles contained in these cubes is summed. Figure 11 shows the influence of the box size on standard deviation and on the maximum difference of both porosity (a) and specific surface, (b) area distribution. For porosity we can define a unique RVE for these samples. In effect, we observe similar standard deviation variations for the several manufacturers. According to our 5% criteria, the RVE of porosity is a cube of 0.7 pore diameter side. Similar behavior in standard deviation variation is observed for the RVE of specific surface. A single size of RVE can be defined for all these samples: similar standard deviation variations are observed for the foams from different manufacturers. According to our 5% criteria, the RVE for specific surface is a cube roughly three dp in side length. The absence of differences between foams from different manufacturer can be explained by the fact that the manufacturing processes are roughly similar (replication of polymer foam) and lead to the same solid volume fraction (porosity around 90% is a manufacturer goal). Plateau law gives globally struts shape but local variations in the cells organization induce different shapes of struts inter-connection and strut cross section (roughly curved triangle). These perturbations may be due to several effects (gravity, drainage, deposition, casting, etc.) during manufacturing process. This gives insight on the fact that specific surface RVE size is far greater than porosity one, but further investigation needed to clarify this point.

3.3 Physical RVE

Figure 12a shows the influence of the box size on standard deviation and on the maximum difference of mean velocity. To establish RVE for the mean velocity value we used the velocity field obtained from the computations. No clear influence of the Reynolds number on RVE size can be identified on the studied range.. Figure 12b presents the estimation of the pressure gradient by a linear regression and its coefficient of determination R^2, for different volumes and different Reynolds numbers. The estimate of the pressure gradient is quite constant for a box three pore diameters in size and the coefficient of determination R^2 is good (>0.99). As a result, three pore diameters are sufficient to establish pressure drop RVE.

4 Foam Morphology Dependence on Physics Properties

We focus on the impact of porosity, throat diameter and pore shape elongation impact on flow behavior. In order to reduce the geometrical parameters number we use here idealized foam geometry. The solid matrix is created from the dual of packed interpenetrating spheres. We carry out numerical simulation at pore scale on a periodic structure representative of metallic foams to gain access to pressure and velocity fields and thus to all effective flow laws properties. These later are correlated to geometrical parameters.

4.1 Shape Control Method

Pore shape is varied using a stretching method while keeping constant the other shape parameters (mean pore diameter (equivalent volume sphere diameter), mean throat diameter (equivalent surface disc diameter) and porosity). The stretching factor N is applied in one direction and its inverse in one other direction. OX is always taken as the main flow axis

Shape deformations can be imposed and controlled. Pitches in X (main flow direction) and Y directions are fixed. Z pitch is modified to change porosity and mean throat diameter. Pitches between spheres are kept smaller than spheres diameter in order to allow communication between pores (Fig. 13).

4.2 Flow Law

Pressure gradient across the foam is function of geometry system (porosity, pore and ligament size, etc.), and physical properties of the fluid phase (viscosity, density) while K and β are intrinsic parameters of the solid matrix that depend only on its structural properties. Figure 14 shows clearly that flow properties are not depending only on porosity and mean pore diameter.

We combine here approaches used for porous media description and developed for multi-row tubes heat exchanger design. Effective properties are determined and correlated to porosity and specific surface as well as geometric parameters such as pore, strut and throat diameters. Three functions χ, J and F characterize the shape of the structure.

χ defines the constriction of the pore, it is defined as the ratio of throat and pore diameter and compare the larger and the smallest area crossed by the fluid. J and F describe solid structure stretching. F quantifies the variation of fluid cross section and J quantifies the evolution of hydraulic diameter in function of foam deformation.

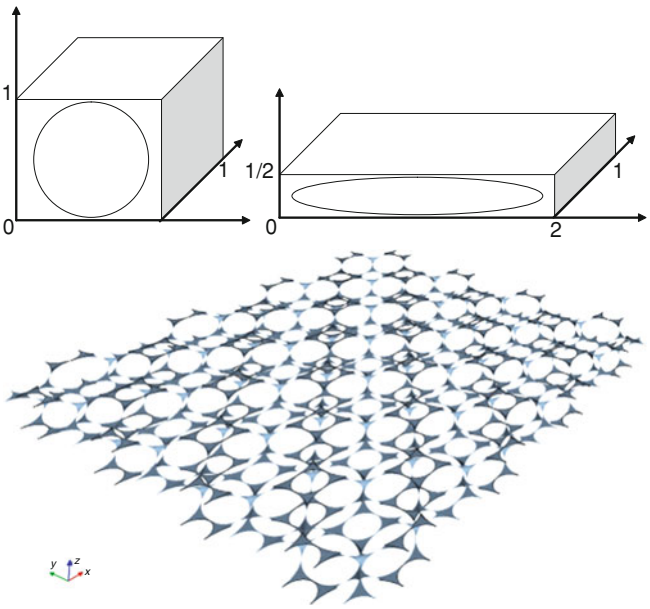

Fig. 13 Iso-porosity shape stretching and view of resulting structure

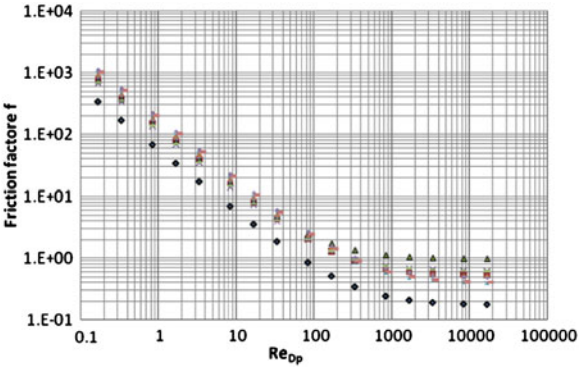

Fig. 14 Friction factor versus *Re* (characteristic length pore diameter). Results differs for foams with same pore diameter and same porosity

$$\chi = \frac{D_{throat}^2}{D_{pore}^2}; F = ScaleY.ScaleZ; J = 2\frac{ScaleY.ScaleZ}{ScaleY + ScaleZ} \tag{13}$$

We computed fluid flow laws on a large set of virtual samples. The Z pitch varies from $0.95D_p$ up to $0.99D_p$. Three stretch factors (1; 1.5; 2) have been applied on all axes. Samples are thus defined by the distance between two pores in "z" direction and their stretching in each direction and specific surface, porosity, throat diameter, J and F are thus calculated.

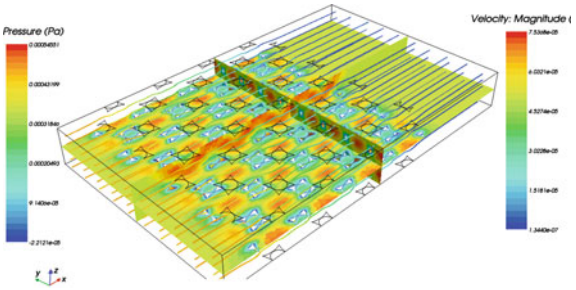

Fig. 15 Velocity field through idealized foam. Plane sections are colored by local velocity magnitude. Streamlines show fluid tortuosity

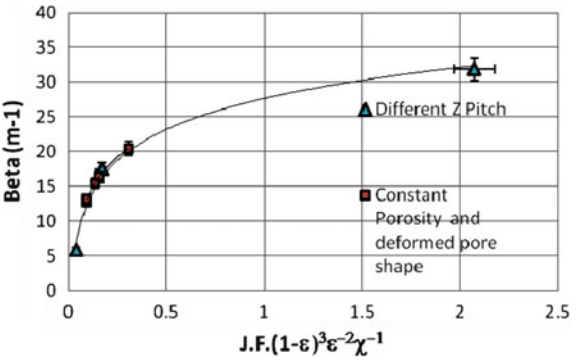

Fig. 16 Inertia coefficient versus B number. All samples

For each sample we simulate fluid flow over the Reynolds Number range $[10^{-2}–10^{4}]$. From average pressure gradient and velocity data (Fig. 15), inertia coefficient and permeability are identified. Results are summarized in Table 1.

Figure 16 shows Inertia coefficient plotted versus the non-dimensional group B detailed below. B increases with JF thus when confinement decreases. B increase also with compacity. B is a non-dimensional group that characterizes the foam shape using the different function described before:

$$B = J\,F\,\frac{(1-\varepsilon)^3}{\varepsilon^2\chi} \tag{14}$$

All results (obtained either at constant pitch or constant porosity) collapse on a single curve:

$$\beta = \frac{1}{D_p}\left(a\,Ln(B) + b\right) \tag{15}$$

This correlation describes inertia coefficient variation with accuracy better than 5% for all tested samples.

The number B can be divided in two terms $B_1 = J \cdot F$ and $B_2 = \frac{(1-\varepsilon)^3}{\varepsilon\chi}$. The first one, B_1 use the two functions J and F and is related to the elongation of pores

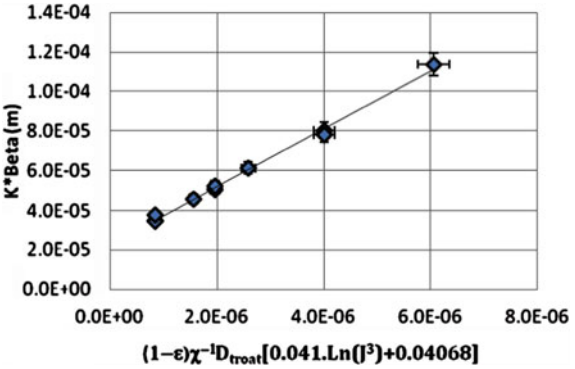

Fig. 17 $K\,\beta$ product versus non-dimensional group C. A linear correlation between flow law and geometric parameters is obtained. Tested samples

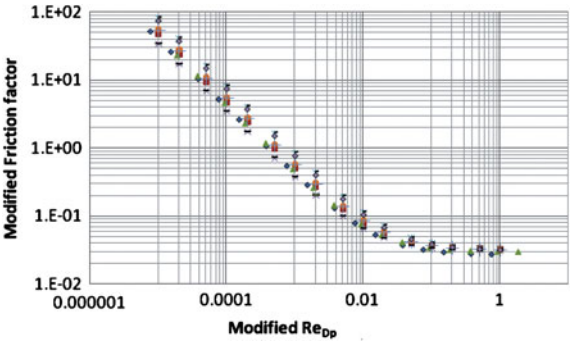

Fig. 18 Friction factor modified versus *Re* modified (characteristic length pore diameter). Results collapse on a unique curve

shape. It account for pore constriction and distance between constrictions. The second one, B_2 describes the influence of porosity following the classical porous media approach (Fig. 15).

We use a similar approach to evaluate the dependence of the term $K\,\beta$ on foam topology. We define a characteristic length C divided in two terms C_1 and C_2:

$$C = C_1\,C_2 = \frac{(1-\varepsilon)\cdot D_{throat}}{\chi}\left[d\,Ln\left(J^3\right) + e\right] \tag{16}$$

Figure 17 shows the linear evolution of $K\beta$ versus C for all samples. This dependence (Eq. 17) was then used to derive a correlation for K as a function of B and C.

$$K\,\beta = D_p(f\,C + g) \tag{17}$$

$$K = \frac{D_p^2(f\,C + g)}{(a\cdot Ln(B) + b)} \tag{18}$$

K is found to be proportional to D_{p}^2 as expected and exhibit more complex behavior in respect with the other parameters. As $K\beta$ define a characteristic length

Table 3 Geometrical parameters and flow laws results for idealized foams

REF	Pitch Z (mm)	Scale x	Scale y	Scale z	Beta (m^{-1})	K (m^2)	K·Beta (mm)	Sp (m^2/m^3)	Porosity (%)	R_{Throat} (mm)	J (–)	F (–)
1	14.20	1	1	1.	5.89	7.77E−06	0.05	110.00	99.40	3.52	1.00	1.00
2	14.50	1	1	1	17.49	3.50E−06	0.06	95.00	99.03	3.44	1.00	1.00
3	14.80	1	1	1	31.89	3.57E−06	0.11	117.00	97.80	3.32	1.00	1.00
4	14.50	1/3	1	1	20.47	3.92E−06	0.08	102.31	99.03	3.44	1.20	1.50
5	14.50	3/2	1	1/3	12.79	2.73E−06	0.03	116.50	99.03	3.44	0.80	0.67
6	14.50	1	1/3	3/2	16.54	3.05E−06	0.05	92.05	99.03	3.44	0.92	1.00
7	14.50	1	3/2	1/3	16.29	3.20E−06	0.05	116.50	99.03	3.44	0.92	1.00
8	14.50	3/2	1/3	1	13.20	2.61E−06	0.03	102.31	99.03	3.44	0.80	0.67
9	14.50	1/3	1	3/2	20.39	3.83E−06	0.08	92.05	99.03	3.44	1.20	1.50
10	14.50	1	1/2	2	15.43	2.44E−06	0.04	98.78	99.03	3.44	0.80	1.00

A slight dispersion of permeability and inertia coefficient is observed

scale for flow in porous media [23], we could use Eq. 16 to propose a pore diameter measured from geometrical parameters only and pertinent for flow law description. We propose a modified friction factor plotted versus a modified Reynolds number. f is divided by $(a \cdot Ln(B) + b)$ and Re_{Dp} is multiplied by $(f \cdot C + g)$. Results, for all tested samples, gather on a unique curve (Fig. 18).

A good agreement with theoretical values is obtained for inertial effects; f decrease toward $2.D_p$, whereas a small deviation is observed for permeability (Table 3).

5 Conclusions

We have discussed effective foam transport properties needed for heat exchanger design. Fluid flow and heat exchange laws were analyzed. Emphasis is given on diffusive (heat conduction) properties of foam. Size and determination method of representative elementary volume were given. Finally, impact of foam morphology on thermo-physical properties was presented. Both pore scale and macro-scale numerical simulations were used in conjunction with specific use of specific experimental set up to achieve this comprehensive study.

A pore scale, numerical investigation of flow law on both real and idealized foam geometries has been carried out. Local temperature, velocity and pressure fields have been determined and allow us to gain a better understanding of flow behaviour.

Effective macroscale flow law parameters have been deduced from microscopic results and summarized. Dispersion correlations adapted to metal foams are needed in order to accurately describe heat transfer.

Both porous and heat exchanger design approaches are used to correlate geometric parameters and flow effectives properties such as permeability and inertia coefficient. We show that inertia coefficient increases when confinement decreases and mean solid size increases. These trend being directly linked to the pore shape stretching and ratio between pore and throat diameter. Finally we propose a geometrical measure of flow law characteristic length proportional to $K\beta$.

Commercial available foam could be classified in three groups. The first one-replication foams with small pore size, i.e. <2 mm—is well suited for compact heat exchanger application using clean and/or high viscosity fluid. The second one—High porosity intermediate pore size, <5 mm—could be used for typical HVAC applications. The last one—casted high pore size foam—is more adapted for industrial application (catalytic heat exchanger for example).

References

1. Ashby, M.F., et al.: Metal Foams: A Design Guide. Butterworth - Heinemann, Boston (2000)
2. Brun, E., et al.: Microstructure and transport properties of cellular materials: representative volume element. Adv. Mater. Eng. **21** (2009)

3. Catillon, S., et al.: Influence of cellular structure in catalytic reactors for H2 production: application to improvement of methanol steam reformer by the addition of a copper foam. In: 2nd France–Deutchland Fuel Cells Conference, Belfort, France (2004)
4. Mahjoob, S., Vafai, K.: A synthesis of fluid and thermal transport models for metal foam heat exchangers. Int. J. Heat Mass Transf. **51**, 3701–3711 (2008)
5. Dukhan, N., et al.: One-dimensional heat transfer analysis in open-cell 10-ppi metal foam. Int. J. Heat Mass Transf. **48**, 5112–5120 (2005)
6. Tadrist, L., et al.: About the use of fibrous materials in compact heat exchangers. Exp. Therm. Fluid Sci. **28**, 193–199 (2004)
7. Holman, J.P.: Heat Transfer, Mechanical Engineering, 9th edn. Mcgraw-Hill, New York (2002)
8. Banhart, J.: Manufacture, characterization and application of cellular metals and metal foams. Prog. Mater. Sci. **46**, 559–632 (2001)
9. Topin, F., et al.: Experimental analysis of multiphase flow in metallic foam: flow laws, heat transfer and convective boiling. Adv. Mater. Eng. **8**(9), 890–899 (2006)
10. Bonnet, J.-P., Topin, F., Tadrist, L.: Flow laws in metal foams: compressibility and pore size effects. Transp. Porous Media **73**(2), 233–254 (2008)
11. Madani, B., et al.: Flow laws in metallic foams: Experimental determination of inertial and viscous contribution. J. Porous Media **10**(1), 51–70 (2007)
12. Brun, E., et al.: Characterization of the full thermal conductivity tensor of anisotropic metal foams—influence of the fluid phase. In: Metfoam 2007, Montreal (2007)
13. Vicente, J., et al.: Structural properties measurement: a morphological tool for transport properties determination. In: 4th International Conference on Porous Metals and Metal Foaming Technology, Kyoto, Japan (2005)
14. Brun, E., et al.: From 3D imaging of structures to diffusive properties of anisotropic cellular materials. In: 11th CMDS, Fontainebleau (2007)
15. Dullien, F.A.L.: Porous Media. Fluid Transport and Pore Structure. Academic Press, New York (1992)
16. Quintard, M., Whitaker, S.: Transport in chemically and mechanically heterogeneous porous media. I: Theoretical development of region-averaged equations for slightly compressible single-phase flow. Adv. Water Resour. **19**(1), 29–47 (1996)
17. Wodie, J.C., Levy, T.: Correction non linéaire de la loi de Darcy. C. R. Acad. Sci. **312**(2), 157–161 (1991)
18. Mei, C., Auriault, J.L.: The effect of weak inertia on flow through a porous medium. J. Fluid Mech. **222**, 647–663 (1993)
19. Firdaous, M., Guermond, J.L., Le Quere, P.: Nonlinear corrections to Darcy's law at low Reynolds numbers. J. Fluid Mech. **343**, 331–350 (1997)
20. Fourar, M., et al.: On the non-linear behavior of a laminar single-phase flow through two and three-dimensional porous media. Adv. Water Resour. **27**, 669–677 (2004)
21. Whitaker, S.: Flow in porous media I: A théoritical dérivation of Darcy's law. Transp. Porous Media **1**(1), 3–25 (1986)
22. Kaviany, M.: Principles of Heat Transfer in Porous Media. Mecanical Engineering Series. Springer, New York (1992)
23. Chauveteau, G.: Essai sur la loi de Darcy. Thèse, Université de Toulouse (1965)
24. Vicente, J., Topin, F., Daurelle, J.-V.: Open celled material structural properties measurement: from morphology to transport properties. Mater. Trans. **47**(9), 2195–2202 (2006)
25. Renard, P., Genty, A., Stauffer, F.: Laboratory détermination of the full permeability tensor. J. Geophys. Res. **106**(B11), 26443–26452 (2001)
26. Brun, E.: De L'imagerie 3D Des Structures A L'etude Des Mecanismes De Transport En Milieux Cellulaires. Université de Provence (2009)
27. Kim, S.Y., Kang, B.H., Kim, J.-H.: Forced convection from aluminum foam materials in an asymmetrically heated channel. Int. J. Heat Mass Transf. **44**(7), 1451–1454 (2001)

28. Hugo, J.-M., et al.: From pore scale numerical simulation of conjugate heat transfer in cellular material to effectives transport properties of real structures. In: IHTC 14, Washington (2010)
29. Madani, B.: Etude expérimentale des écoulements et de l'ébullition dans les milieux poreux cellulaires, USTHB: Alger (2007)
30. Daurelle, J.V., Vicente, J., Echangeur, T.F.: Compact à mousse métallique: Modèle à 2 températures et dispersion thermique. in SFT'06, Ile de Ré (2006)
31. Serret, D., Stamboul, T., Topin, F.: Transferts dans les mousses métalliques: Mesure du coefficient d'échange de chaleur entre phases in Congrès de la SFT, SFT 07. Ille des Embiez (2007)
32. Bhattacharya, A., Calmidi, V., Mahajan, R.L.: Thermophysical properties of high porosity metal foams. Int. J. Heat Mass Transf. **45**(5), 1017–1031 (2002)
33. Fetoui, M., et al.: Highly porous metal foams: effective thermal conductivity measurement using a photothermal technique. J. Porous Media **12**(10), 939–954 (2009)
34. Viskanta, X.F.R., Gore, J.P.: Measurement and correlation of volumetric heat transfer coefficients of cellular ceramics. Exp. Thermal Fluid Sci. **17**(4), 285–293 (1998)
35. Lu, T.J., Stone, H.A., Ashby, M.F.: Heat transfer in open-cell metal foams. Acta Mater. **46**(10), 3619–3635 (1998)
36. Madani, B., et al.: Mesure du coefficient de transfert de chaleur local paroi-fluide dans un canal à mousse métallique en écoulement liquide et en ébullition. In 12ième JITH, Tanger, Maroc (2005)
37. Bories, S., Pratt, M.: Transferts de chaleur dans les milieux poreux. In: Traité de génie energetique, Technique de l'ingénieur: Paris, pp. 1–32 (1996)
38. Calmidi, V.V., Mahajan, R.L.: The effective thermal conductivity of high porosity fibrous metal foams. J. Heat Transf. **121**, 466–471 (1999)
39. Boomsma, K., Poulikakos, D., Ventikos, Y.: Simulations of flow through open cell metal foams using an idealized periodic cell structure. Int. J. Heat Fluid Flow **24**, 825–834 (2003)
40. Decker, S., et al.: Detailed experimental characterization and numerical modeling of heat and mass transport properties of highly porous media for solar receivers and porous burners. In: Sixth International Conference on Technologies and Combustion for a Clean Environment (Clean Air VI), Porto, Portugal (2001)
41. Pan, H.L., et al.: Experimental Determination of the Effective Heat Conductivities of Highly Porous Media (2002)
42. Writz, R.A.: A semi-empirical model for porous media heat exchanger design. In: The American Society of Mechanical Engineers National Heat Transfer Conference, Baltimore, MD (1997)
43. Bastawros, A.F.: Effectiveness of open-cell metallic foams for high power electronic cooling. In: Symposium on the Thermal Management of Electronics (IMECE), Anaheim, CA (1998)
44. Kim, S.Y., Koo, J.-M., Kuznetsov, A.V.: Effect of anisotropy in permeability and effective thermal conductivity on thermal performance of and aluminum foam heat sink. Numer. Heat Transf. Part A: Appl. **40**(1), 21–36 (2001)
45. Fetoui, M., et al.: Caractérisation thermophysique de matériaux cellulaires: excitation temporelle de type créneau et mesure en face arrière. In Congrès de la SFT 04, Giens, France (2004)
46. Vicente, J., et al.: Thermal conductivity of metallic foam: simulation on real X-ray tomographied porous medium and photothermal experiments. In: IHTC13, 13TH International Heat Transfer Conference, Sydney (2006)
47. Rigollet, F., Topin, F., Tadrist, L.: Mesures de propriétés thermophysiques effectives de mousses métalliques par une méthode photothermique avec mesures simultanées sur les deux faces in 7èmes Journées d'études sur les milieux poreux. Bordeaux (2005)
48. Quintard, M., Whitaker, S.: One-and two-equations models for transient diffusion processes in two-phase system. Adv. Heat Transf. **23**, 369–464 (1993)

49. Topin, F.: Phénomènes de transport en milieux poreux: Matériaux cellulaires à forte perméabilité—Morphologie, ébullition et couplages, in Mécanique-Energétique, p. 220. Université de Provence, Marseille (2006)
50. Moyne, C.: Two-equation model for a diffusive process in porous media using the volume averaging method with an unsteady-state closure. Adv. Water Resour. **29**(2–3), 63–76 (1997)
51. Quintard, M., Cherblanc, F., Whitaker, S.: Dispersion in heterogeneous porous media: One-equation non-equilibrium model. Transp. Porous Media **44**, 181–203 (2001)
52. Brun, E., et al.: IMorph: A 3D Morphological Tool to Fully Analyse All Kind of Cellular Materials in Cellmet'08. Allemagne, Dresden (2008)

Heat and Mass Transfer in Matrices of Hygroscopic Wheels

C. R. Ruivo, J. J. Costa and A. R. Figueiredo

Abstract In the present chapter the sorption and the mass diffusion phenomena in the porous desiccant layer are described aiming a detailed numerical modelling of hygroscopic wheels. A particular desiccant medium (silica gel Regular Density) is characterized as well as a representative cell of the corrugated matrix. The heat and mass transfers in the gas domain of the matrix channels are analysed addressing also the validity of the so-called *low mass transfer rate theory*. The mass transfer convective coefficient is evaluated through the use of the Chilton-Colburn analogy. The detailed numerical model proposed for the simulation of the behaviour of a representative channel of the matrix is briefly described. Results of the cyclic behaviour of an element of the channel wall are presented and a parametric study is performed concerning the influence of the rotation speed and of the thickness of the desiccant layer on the behaviour of hygroscopic wheels.

C. R. Ruivo (✉)
Instituto Superior de Engenharia, Universidade do Algarve,
Campus da Penha, 8005-139, Faro, Portugal
e-mail: cruivo@ualg.pt

C. R. Ruivo · J. J. Costa · A. R. Figueiredo
ADAI-LAETA, Universidade de Coimbra, Rua Luís Reis Santos,
3030-788, Coimbra, Portugal
e-mail: jose.costa@dem.uc.pt

A. R. Figueiredo
e-mail: rui.figueiredo@dem.uc.pt

J. M. P. Q. Delgado (ed.), *Heat and Mass Transfer in Porous Media*,
Advanced Structured Materials 13, DOI: 10.1007/978-3-642-21966-5_10,

1 Introduction

Hygroscopic wheels are commonly used in industrial applications to promote dehumidification of a process airflow (desiccant wheel) or to promote heat and mass recovery in building ventilation systems (enthalpy wheel). In dehumidification applications, the rotation speed of the desiccant wheel is relatively low and the regeneration process of the matrix (desorption) is imposed by a hot airflow. The psychrometric evolutions in the process and regeneration airflows (flow 1 and 2, respectively) crossing the matrix of an equally split desiccant wheel are sketched in Fig. 1.

The approaching airflows in each zone are generally turbulent and can present instabilities and heterogeneities. However, the airflow is laminar inside the channels due to their low hydraulic diameter (frequently less than 5 mm) together with the moderate values of the frontal velocity (usually between 1 and 3 ms^{-1}). The matrices are relatively compact, occurring heat and mass convection on the gas side, as well as heat and mass diffusion and sorption processes in the solid domain of the channel walls. During the adsorption/desorption cycle, the matrix exhibits non uniform distributions of adsorbed water content and of temperature, and the angular gradients depend on the constitution of the wall matrix and on the rotation speed. The moisture removal capacity of a desiccant wheel is influenced by the airflow rates, the inlet states of the airflows as well as by the rotation speed.

The experimental and numerical investigation of systems incorporating hygroscopic wheels has been the object of numerous research works. When advanced numerical methods are used to simulate the behaviour of the matrix of a hygroscopic wheel, several critical issues still remain, such as the lack of knowledge of some parameters and properties of the desiccant medium, the numerical difficulties of handling the coupling between the different phenomena and the time consumption in the computational calculations.

In common desiccant matrices, the order of magnitude of the heat convective resistance is much greater than the thermal resistance inside the desiccant layer. Therefore the assumption of null-thermal-resistance in the cross direction of the channel wall is acceptable for simplified analyses.

Concerning the assumption of null mass transfer resistance a deeper analysis must be conducted due to the magnitude of the mass diffusion coefficients in the desiccant porous media. Moreover, the mass diffusion coefficients can present important variations during the sorption process, an issue that can only be clarified by using detailed models [1–5].

2 Adsorption and Mass Diffusion in the Desiccant Layer

The desiccant layer in the channel walls of the hygroscopic rotor can adsorb large amounts of water vapour, usually being assumed that the sorption process is a physical reversible phenomenon. The domain of the porous desiccant medium is

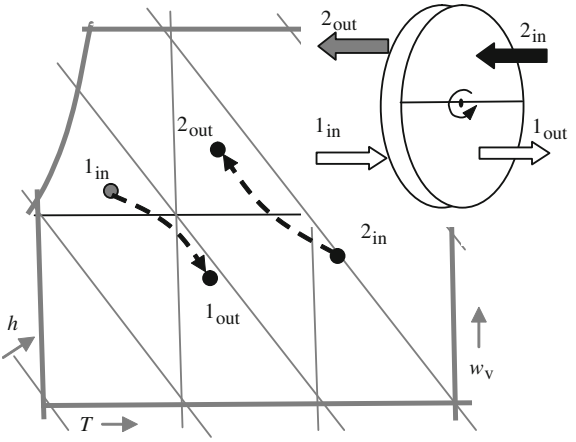

Fig. 1 Typical psychrometric evolutions in the process and regeneration airflows in a desiccant wheel

composed by dry desiccant, adsorbed water, water vapour and dry air, with the respective masses m_{sd}, m_ℓ, m_v and m_g. The adsorbed water content, in dry basis, is defined as:

$$X_\ell = \frac{m_\ell}{m_{sd}}. \tag{1}$$

The water vapour content of the moist air is defined through:

$$w_v = \frac{m_v}{m_g}, \tag{2}$$

and the corresponding mass fraction by:

$$\varphi_v = \frac{m_v}{m_v + m_g}. \tag{3}$$

The volume fraction $\varepsilon_{g\cdot v}$ associated to the volume occupied by the gaseous phase (water vapour and dry air) depends on X_ℓ as:

$$\varepsilon_{g\cdot v} = \varepsilon_{dpm} - X_\ell \frac{\rho^*_{sd}}{\rho_\ell}, \tag{4}$$

where ε_{dpm} and ρ^*_{sd} are, respectively, the porosity and the apparent density of the dry desiccant porous medium and ρ_ℓ is the density of the adsorbed water. The density of the moist air inside the porous medium is related with the densities of dry air and water vapour by:

$$\rho_{g\cdot v} = \rho_g + \rho_v. \tag{5}$$

Due to the range of temperature and partial pressures of the dry air (p_g) and of the water vapour (p_v) in the desiccant medium, the ideal gas behaviour is assumed, the densities being evaluated by:

$$\rho_{\mathrm{v}} = \frac{p_{\mathrm{v}}}{R_{\mathrm{v}}(T + 273.15)}, \tag{6a}$$

and

$$\rho_{\mathrm{g}} = \frac{p_{\mathrm{g}}}{R_{\mathrm{g}}(T + 273.15)}, \tag{6b}$$

where R_{g} and R_{v} are the particular values of the ideal gas constant for dry air and for water vapour, respectively. According to the Dalton's law, the total pressure of the mixture is given by $p = p_{\mathrm{v}} + p_{\mathrm{g}}$.

At saturation conditions, the maximum adsorbed water content of the desiccant porous medium is:

$$X_{\ell\,\mathrm{sat}} = \varepsilon_{\mathrm{dpm}} \frac{\rho_{\ell}}{\rho^{*}_{\mathrm{sd}}}. \tag{7}$$

The heat of adsorption h_{ads} corresponds to the energy involved in the phase change of water, and can be significantly higher than the heat of condensation or vaporization of free water, h_{fg}, mainly when the desiccant porous medium is very dry, a situation that is characterized by high bonding forces between the adsorbed water and the desiccant molecules. On the contrary, for high values of adsorbed water content, h_{ads} is close to h_{fg}.

The heat of adsorption can be interpreted as a modified heat of condensation and expressed by:

$$h_{\mathrm{ads}} = h_{\mathrm{fg}} + h^{\bullet}_{\mathrm{lig}}, \tag{8}$$

where $h^{\bullet}_{\mathrm{lig}}$ is generally known as the heat of wetting.

The adsorption isotherms represent the thermodynamic equilibrium between the adsorbed water, the water vapour in the moist air and the desiccant, being expressed as a relationship between the adsorbed water content and the water vapour pressure (p_{v}) or the water vapour content (w_{v}) for different temperature values. Another usual representation of the referred equilibrium condition is $X_{\ell} = f(\psi)$ or $\psi = g(X_{\ell})$, where the parameter ψ corresponds to the ratio between the partial pressure p_{v} and the saturation pressure p_{vs} at the particular value of the gas mixture temperature. It is important to stress that this ratio ($\psi = p_{\mathrm{v}}/p_{\mathrm{vs}}$) corresponds exactly to the relative humidity concept when temperature is equal or lower than the particular value of the water saturation temperature T_{sat} at the total pressure of the gas mixture (p). Consequently, the relative humidity concept is not applicable when the moist air temperature is greater than T_{sat}, a situation that is commonly found in regeneration airflow inlet conditions of the desiccant rotors.

Simultaneously to the adsorption/desorption phenomena, thermal conduction and mass diffusion of vapour and of adsorbed water also occur. The detailed numerical modelling of these coupled phenomena inside the desiccant porous medium and the interface convective phenomena requires an accurate evaluation of the fields of the different variables involved by solving a set of coupled non-linear differential equations. The temperature field in the desiccant porous

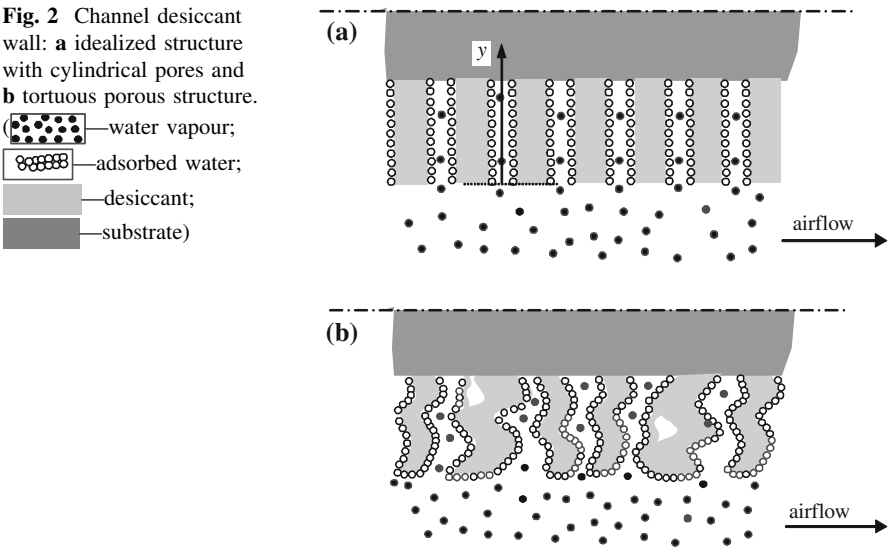

Fig. 2 Channel desiccant wall: **a** idealized structure with cylindrical pores and **b** tortuous porous structure.

domain depends on the internal sorption process as well as on the heat conduction and on the convective interaction with the airflow.

Figure 2a schematically illustrates the adsorption process due to the interaction of a moist airflow and a desiccant layer of a porous medium. It is an idealization of the problem where the pores of the desiccant medium are supposed to be equal, with straight and uniform cross section.

The transport of vapour inside the pore is of diffusive nature, co-existing ordinary Fick diffusion and Knudsen diffusion. When the section area of the pores is relatively small, namely in micropores, the contribution of the ordinary Fick diffusion is negligible. Due to the existence of gradients of adsorbed water content in the porous domain, the mass diffusion of adsorbed water, known as surface diffusion, must be also taken into account.

The mass flux diffusion of water vapour by Knudsen diffusion inside a cylindrical micropore, as illustrated in Fig. 2a, is evaluated by:

$$j_{\mathrm{v}} = -D_{\mathrm{K}} \frac{\partial C_{\mathrm{v}}}{\partial y}, \tag{9}$$

where the mass concentration of the water vapour corresponds to $C_{\mathrm{v}} = \rho_{\mathrm{g\cdot v}} \varphi_{\mathrm{v}}$.

The resistance to the mass Knudsen diffusion depends on the porous space occupied by the gaseous phase, increasing strongly with the decreasing of the average radius $r_{\mathrm{g\cdot v}}$, which depends on the amount of adsorbed water. The coefficient for Knudsen diffusion of water vapour is estimated by:

$$D_{\mathrm{K}} = 97 r_{\mathrm{g\cdot v}} \sqrt{\frac{T + 273.15}{M_{\mathrm{v}}}}, \tag{10}$$

where M_{v} is the molar mass of water.

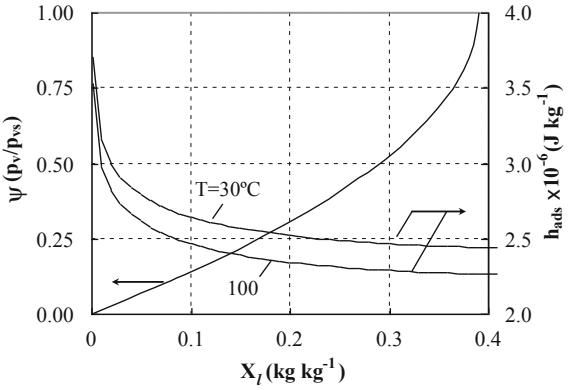

Fig. 3 Sorption equilibrium for the pair silica gel RD–water and heat of adsorption

When dealing with a real porous structure, as sketched in Fig. 2b, it is convenient to adopt the concept of an effective diffusion coefficient $D_{\mathrm{K,eff}}$ that takes into account the effects of both the tortuosity, $\tau_{\mathrm{g{\cdot}v}}$, and the volume fraction $\varepsilon_{\mathrm{g{\cdot}v}}$. The corrected diffusion coefficient is $D_{\mathrm{K,eff}} = D_{\mathrm{K}}\varepsilon_{\mathrm{g{\cdot}v}}/\tau_{\mathrm{g{\cdot}v}}$ and the diffusion mass flux is evaluated by:

$$j_{\mathrm{v}} = -D_{\mathrm{K,eff}} \frac{\partial(\rho_{\mathrm{g{\cdot}v}}\varphi_{\mathrm{v}})}{\partial y}. \tag{11}$$

For the purpose of numerical modelling, it is more convenient to use the following equivalent expression:

$$j_{\mathrm{v}} = -\frac{D_{\mathrm{K,eff}}}{\varepsilon_{\mathrm{g{\cdot}v}}} \frac{\partial\left(\rho^{*}_{\mathrm{g{\cdot}v}}\varphi_{\mathrm{v}}\right)}{\partial y}, \tag{12}$$

where the apparent density of the gaseous mixture is related by $\rho^{*}_{\mathrm{g{\cdot}v}} = \rho_{\mathrm{g{\cdot}v}}\varepsilon_{\mathrm{g{\cdot}v}}$.

The surface diffusion of adsorbed water is also formally quantified as a common diffusion law. In the case of the idealized structure represented in Fig. 2a, the surface mass diffusion flux in a cylindrical pore of radius r_{po} is evaluated by:

$$j_{\ell} = -\frac{2}{r_{\mathrm{po}}} D_{\mathrm{S}} \frac{\partial C'_{\ell}}{\partial y}, \tag{13}$$

where C'_{ℓ} represents the mass concentration of adsorbed water (kg of adsorbed water per unit of pore surface area). The coefficient of surface diffusion D_{S} can be correlated by the following equation [6]:

$$D_{\mathrm{S}} = D_{\mathrm{S0}} \exp\left(\frac{E}{R_{\mathrm{v}}(T + 273.15)}\right), \tag{14}$$

where the values of D_{S0} and of the activation energy E for diffusion depend on the nature of the porous desiccant medium.

Table 1 Data of dry silica gel RD particles [7]

Parameter	Value	Parameter	Value
Specific pore surface area ($m^2\ kg^{-1}$)	7.8×10^5	Specific pore volume ($m^3\ kg^{-1}$)	4.3×10^{-4}
Density ($kg\ m^{-3}$)	2,195.5	Apparent density ($kg\ m^{-3}$)	1,129
Porosity	0.485	Average pore radius (m)	1.1×10^{-9}
Thermal conductivity ($W\ m^{-1}\ °C^{-1}$)	0.144	Specific heat ($J\ kg^{-1}\ °C^{-1}$)	921
Tortuosity of adsorbed water path	2.24	Tortuosity of water vapour path	2.24

The mass surface diffusion flux of adsorbed water in the y direction of a real structure is evaluated by:

$$j_\ell = -\frac{D_S}{\tau_\ell} S_{po} \rho^*_{sd} \frac{\partial C'_\ell}{\partial y} \tag{15}$$

or by the following equivalent expression:

$$j_\ell = -D_{S,eff} \frac{\partial\left(\rho^*_{sd} X_\ell\right)}{\partial y}, \tag{16}$$

where the effective coefficient $D_{S,eff} = D_S/\tau_\ell$ takes into account the effect of the tortuosity τ_ℓ. The specific area of the pore S_{po} represents the ratio between the porous surface area and the mass of dry desiccant medium and corresponds also to $S_{po} = X_\ell/C'_\ell$.

3 Desiccant Characteristic Parameters and Properties

The knowledge of the accurate values of the properties of the desiccant media is crucial to perform a detailed numerical modelling of the mass and heat transfer phenomena inside the porous domain. Published studies presenting values or correlations for the evaluation of properties and parameters of dry desiccant porous media, as required for a detailed numerical modelling, are scarce. The research work of Pesaran [7] was focused on the moisture transport in silica gel particle beds (RD-Regular Density Silica Gel and ID-Intermediate Density Silica Gel). Table 1 summarizes the data of dry silica gel RD particles. The influence of the state of the desiccant on the sorption equilibrium and on the heat of adsorption is shown in Fig. 3 and the same influence on the effective mass diffusion coefficients are shown in Fig. 4. Although the referred work of Pesaran [7] was not focused on desiccant wheels, it has been taken as an important reference due to the exhaustive

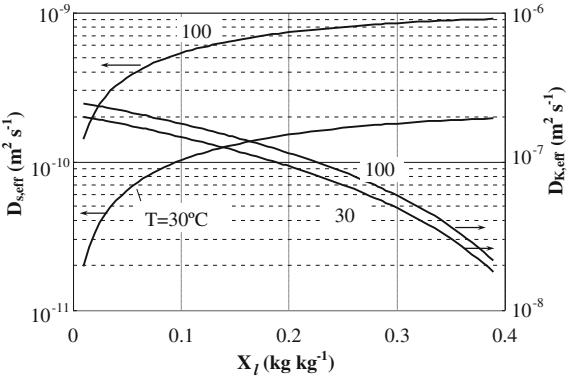

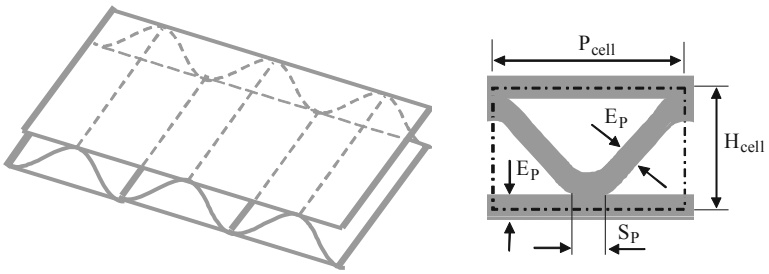

Fig. 4 Effective coefficients of surface and Knudsen diffusions

Fig. 5 Corrugated sheet and representative cell of a hygroscopic matrix

characterization of microporous media reported. In previous works [1–5, 8, 9] on the detailed modelling of the phenomena inside the wall desiccant layer of the channels of hygroscopic wheels, that information regarding properties and parameters of dry silica gel RD was considered, and the same holds in the present chapter.

The density of the adsorbed water as well as the specific heat and the thermal conductivity are assumed to be equal to those of liquid water. Based on the thermodynamics tables [10], the correlations of those properties were derived, taking into account the influence of the temperature in the range 0–200°C, by the following polynomial expression:

$$\gamma = c_0 + c_1 T + c_2 T^2 + c_3 T^3, \tag{17}$$

the values of the coefficients c_0, c_1, c_2 and c_3 being listed in Table 2.

The specific heat and the thermal conductivity of the dry air and of the water vapour were also estimated by the same correlation and the corresponding coefficients are indicated in Tables 3 and 4 for the same temperature range.

Table 2 Coefficients of the correlations for liquid water properties

Property	c_0	c_1	c_2	c_3
Density (kgm^{-3})	1,000.5	−0.0506	−0.0043	6×10^{-6}
Specific heat ($J\ kg^{-1}K^{-1}$)	4,205.4	−0.9215	−0.008	2×10^{-5}
Thermal conductivity ($Wm^{-1}K^{-1}$)	0.5646	0.0018	-7×10^{-6}	0

Table 3 Coefficients of the correlations for water vapour properties

Property	c_0	c_1	c_2	c_3
Specific heat at constant pressure ($J\ kg^{-1}K^{-1}$)	1,855.4	0.4724	0.0031	10^{-4}
Thermal conductivity ($Wm^{-1}K^{-1}$)	0.017206	4.4×10^{-5}	-3×10^{-7}	0

Table 4 Coefficients of the correlations for dry air properties

Property	c_0	c_1	c_2	c_3
Specific heat at constant pressure ($J\ kg^{-1}K^{-1}$)	1003.6	0.0287	0.0004	0
Thermal conductivity ($Wm^{-1}K^{-1}$)	0.0241	8×10^{-5}	-3×10^{-8}	0

The specific heat and the thermal conductivity of the moist air are estimated as weighted averages based on the dry air and water vapour mass fractions. Similarly, the specific heat and the thermal conductivity of the wet desiccant medium are estimated as weighted averages based on the mass fraction of each component (dry air, water vapour, adsorbed water and dry desiccant).

4 Heat and Mass Convection Transfer

The matrix of desiccant rotors has usually a compact honeycomb structure, manufactured with low density corrugated sheets. The specific transfer area of the most compact ones is about 5,000 $m^2\ m^{-3}$. The channel walls are relatively thin, with thickness of about 0.2 mm (v., e.g. [6]). The geometric parameters of the representative cell are the pitch P_{cell}, the height H_{cell}, the thickness of the plates E_p and the length S_p of the contact area between plane and wavy plates are represented in Fig. 5, for a sinusoidal configuration. In some hygroscopic rotors the corrugated sheet exhibits a curvature, as illustrated in Fig. 6. The effect of the curvature of a particular cell can be estimated by the evaluation of the following characteristic distance:

$$\delta_{sin} = r - \sqrt{r^2 - 0.25P_{sin}^2}. \tag{18}$$

This means that in real desiccant rotors the curvature effect is significant only in a very small fraction of the matrix around its axis.

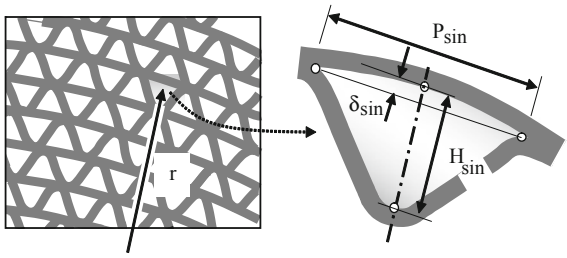

Fig. 6 Hygroscopic matrix composed by curved sheets and representative channel

According to the research of Zhang et al. [11], the wetted perimeter for a sinusoidal type corrugation sheet can be estimated as:

$$P_{w,cell} = 2H_{sin}\left[\alpha_{sin} + \sqrt{\alpha_{sin}^2 + \pi^2}\,\frac{3 + (2\alpha_{sin}/\pi)^2}{4 + (2\alpha_{sin}/\pi)^2}\right] - 4S_p, \tag{19}$$

where α_{sin} corresponds to the aspect ratio of the cell P_{sin}/H_{sin}. The specific transfer area and the porosity of the hygroscopic matrix can be related with the dimensions of the cell by:

$$a_s = P_{w,cell}/(P_{cell}H_{cell}) \tag{20}$$

and

$$\varepsilon_m = 1 - 0.5\left(P_{w,cell} - 4S_p\right)E_P/(P_{cell}H_{cell}), \tag{21}$$

respectively. Consequently the hydraulic diameter of the matrix channels is $d_{hyd} = 4\varepsilon_m/a_s$.

The numerical modelling of the heat and mass transfer processes in the airflow domain is usually performed by simple models assuming bulk flow pattern and the use of appropriate convective transfer coefficients depending on the cross section geometry of the channels.

Due to the fact that heat and mass transfers occur simultaneously it is important to evaluate the magnitude of the convective mass flux. To inspect the validity of the *low mass transfer rate theory* [12], a brief analysis of the mass transfer for Couette flow is presented. Considering that the water vapour mass fractions at the interface and in the bulk flow are respectively $\varphi_{v,i}$ and $\varphi_{v,f}$, the convective mass flux can be evaluated by [12]:

$$j_{v,gs} = g_{m,v}\beta, \tag{22}$$

where $\beta = \left(\varphi_{v,f} - \varphi_{v,i}\right)/\left(\varphi_{v,i} - 1\right)$ represents the potential for the mass transfer. The mass conductance $g_{m,v}$ is related with the mass conductance of the case of *low mass transfer rate theory* [12], $g^*_{m,v}$, by:

$$g_{m,v}\Big/g^*_{m,v} = \ln(1+\beta)/\beta. \tag{23}$$

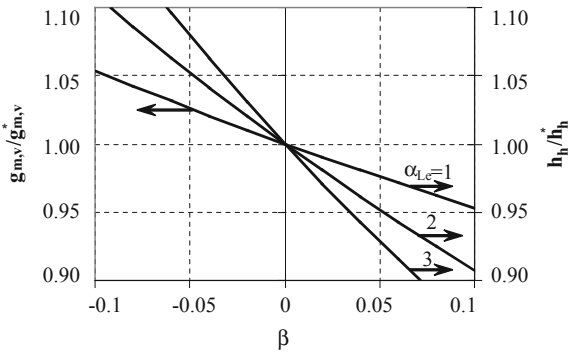

Fig. 7 Ratios of mass conductances and of heat convection coefficients

The convective heat flux coupled with mass transfer through the interface can be estimated by:

$$j_{h,gs} = h_h(T_f - T_i), \tag{24}$$

where T_f represents the bulk airflow temperature and T_i the interface temperature. The convective heat coefficient h_h is related with the convective heat coefficient for the case of *low mass transfer rate theory* [12], h^*_h, by:

$$h_h = j_{v,gs}c_{p_v}\left[\exp\left(\frac{j_{v,gs}c_{p_v}}{h^*_h}\right) - 1\right]^{-1}. \tag{25}$$

According to the *low mass transfer rate theory*, the convective coefficient h^*_h is estimated from the Nusselt number as in a classical analysis of pure heat convection. Therefore, considering the analogy between the heat and mass transfer processes, the conductance $g^*_{m,v}$ is evaluated by:

$$g^*_{m,v} = Le^{n-1}h^*_h/c_{p_f}, \tag{26}$$

where n usually assumes the value 1/3, (v., e.g. [10]) and Le represents the Lewis number:

$$Le = \lambda_f/(\rho_f c_{p_f} D_f). \tag{27}$$

The variables λ_f, ρ_f and c_{pf} represent, respectively, the thermal conductivity, the density and the specific heat at constant pressure of the moist air. The variable D_f is the mass diffusion coefficient of water vapour in the air. Eq. 25 can also be written in the form:

$$\frac{h_h}{h^*_h} = \frac{\alpha_{Le}\ln(1+\beta)}{\exp(\alpha_{Le}\ln(1+\beta)) - 1}, \tag{28}$$

where $\alpha_{Le} = Le^{n-1}c_{p_v}/c_{p_f}$ and c_{pv} is the specific heat of water vapour at constant pressure.

The dependences of the ratios of the mass conductances (Eq. 23) and of the heat convection coefficients (Eq. 28) are represented in Fig. 7.

The parameter α_{Le} depends on the temperature and on the water vapour content on the moist air properties, assuming values around 2. In common sorption dehumidification processes in desiccant wheels, the potential for the mass transfer β is relatively low ($| \beta | < 0.03$) and, according to Fig. 7, the ratios $g_{m,v}/g^*_{m,v}$ and h_h/h^*_h are close to 1. Consequently, the use of the *low mass transfer rate theory* becomes valid in the numerical modelling of the simultaneous heat and mass convective processes in hygroscopic matrices of desiccant wheels. The convective heat flux is evaluated by Eq. 24 considering $h_h = h^*_h$ and the mass flux is evaluated by:

$$j_{v,gs} = h_m \rho_f \frac{\varphi_{v,f} - \varphi_{v,i}}{1 - \varphi_{v,i}}. \tag{29}$$

The heat and mass convection coefficients h_h and h_m are estimated through the Nusselt and Sherwood numbers, respectively:

$$h_h = Nu \lambda_f / d_{hyd} \tag{30}$$

and

$$h_m = Sh D_f / d_{hyd}. \tag{31}$$

According to the Chilton-Colburn analogy, *Sh* is related with *Nu* by:

$$Sh = Nu \left[\lambda_f / (\rho_f c_{p_f} D_f) \right]^{1/3}. \tag{32}$$

In classic literature, the values of the Nusselt number for laminar flow are usually given for different channel configurations, for fully developed flow with constant properties (e.g. [10]), either for constant and uniform interface temperature Nu_T or for constant and uniform heat flux Nu_F.

Few research works have been dedicated to determine the required correlations for the Nusselt number taking into account: (1) the different geometries of the channels in common rotor matrices, (2) the simultaneous development of the velocity, temperature and concentration layers, and (3) the changes occurring in the airflow properties and in the interface state, as well as in the convective fluxes. For channels of sinusoidal corrugation type, Niu and Zhang [13] determined the Nu_T values for the laminar flow based on numerical modelling results. Moreover they investigated the influence of the ratio δ_{sin}/P_{sin} (cf. Fig. 6) in adjacent channels of the matrix with opposite curvature. After the results of Niu and Zhang [13], Ruivo et al. [8] derived the correlation for the Nusselt number represented in Fig. 8.

5 Numerical Results of the Behaviour of a Desiccant Matrix

The steady state behaviour of a desiccant wheel is usually determined by numerical modelling the cyclic behaviour of a representative channel of the matrix. The detailed modelling of momentum, heat and mass transfer in the airflow

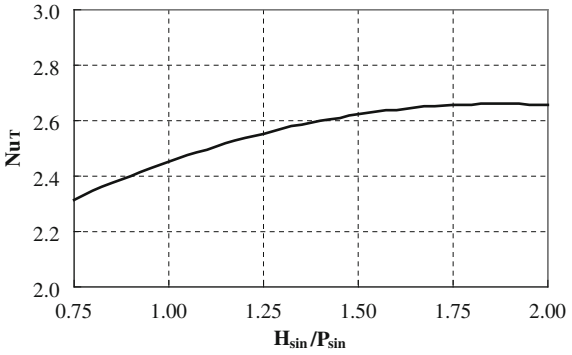

Fig. 8 Correlation for the Nusselt number Nu_T for laminar flow in sinusoidal channels

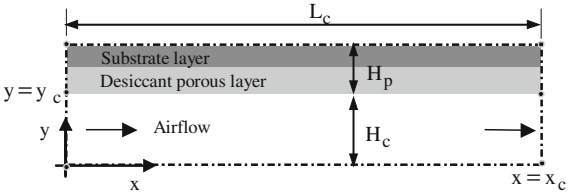

Fig. 9 Physical domain of the modelled channel

domain is relevant mainly for product optimization purposes and also for the assessment of simplifying assumptions that support simplified models.

For simplification reasons, the domain of the modelled channel is usually reduced to a half-channel of parallel plates [1, 3], as schematically represented in Fig. 9, that must be equivalent to the real channel configuration, by specifying $H_c = \varepsilon_m/a_s$ and $H_p = (1 - \varepsilon_m/a_s)$, and considering the same ratio of airflow rate to wetted perimeter. The value of H_p corresponds to the half-thickness of the real channel wall, in the cases where S_p tends to zero,

According to Fig. 9, the mass and energy conservation equations can be represented by the general form in the layers of the wall domain (substrate and desiccant):

$$\frac{\partial}{\partial t}\left(\rho_\phi \phi\right) = \frac{\partial}{\partial x_j}\left(\Gamma_\phi \frac{\partial \phi}{\partial x_j}\right) + S_\phi, \tag{33}$$

where ρ_ϕ, Γ_ϕ and S_ϕ assume different meanings according to the respective conservation equation [1, 3] ($\phi = X_\ell$—for the mass conservation of adsorbed water; $\phi = T$—energy conservation, $\phi = \varphi_v$—mass conservation of water vapour). The local equilibrium is usually assumed between the adsorbed water and the water vapour in the pores of the desiccant (Fig. 3), leading to the need of solving only one mass conservation equation, the one for the adsorbed water, where $\rho_\phi = \rho^*_{sd}$, $\Gamma_\phi = \rho^*_{sd} D_{s,eff}$ and the source term is expressed by:

$$S_\phi = \frac{\partial}{\partial x_j}\left[\frac{D_{K,eff}}{\varepsilon_{g.v}} \frac{\partial\left(\rho^*_{g.v}\varphi_v\right)}{\partial x_j}\right] - \frac{\partial\left(\rho^*_{g.v}\varphi_v\right)}{\partial t}. \tag{34}$$

In the substrate layer, it is assumed that only heat conduction occurs.

The airflow inside the channel is usually treated as a bulk flow, leading to the need of solving the one-dimensional conservation equations represented by the generic form:

$$\rho_f \phi + \frac{\partial}{\partial x}(\rho_f u_f \phi) = S_\phi. \tag{35}$$

where ρ_f and u_f represent, respectively, density and velocity of the bulk flow. The source-term S_ϕ assumes different forms according to the meaning of ϕ [1, 3] ($\phi = 1$—global mass conservation, $\phi = \varphi_v$—mass conservation of water vapour, $\phi = T$—energy conservation, $\phi = u_f$—momentum conservation). At the interface ($y = y_c$), the mass and heat convection fluxes are evaluated through Eqs. 24 and 29, considering the *low mass transfer rate theory* [12].

Uniform distributions of the temperature and of the adsorbed water content in the desiccant porous wall are imposed as initial condition of the cyclic adsorption/desorption process as well as the thermodynamic equilibrium between the desiccant porous wall and the airflow.

The inlet condition of the airflow in the channel is imposed by specifying the inlet temperature T_{in} and the water vapour mass fraction $\varphi_{v,in}$ (or the corresponding water vapour content, $w_{v,in}$), as well as the inlet velocity of the airflow $u = u_{in}$ (or the corresponding mass inlet velocity, $F_m = F_{m,in}$) in order to guarantee the same ratio of airflow rate to wetted perimeter as in the real channel geometry. The total pressure of the gas mixture is considered uniform and constant.

The numerical modelling is based on the solution of the differential conservation equations by the finite volume method. The diffusion coefficients at the control-volume interfaces are estimated by the harmonic mean, thus allowing the conjugate and simultaneous solution in both gas and solid domains [14]. Details and the complete description of the mathematical and numerical formulation of the model are presented in previous works [1, 3, 8].

Exhaustive parametric studies have been performed using the developed numerical model by Ruivo [1] to characterise the importance of a set of operating parameters on the behaviour of the hygroscopic matrix. The properties of the silica gel RD particles were assigned to the desiccant layer considered in those studies. The behaviour of one element of the channel of the matrix has also been investigated to analyse the validity of neglecting the resistances to the heat and mass transfer inside the desiccant layer [1, 2, 5].

5.1 Cyclic Behaviour of a Channel Wall Element

The cyclic behaviour of the channel element was also modelled [4] by a procedure that is equivalent to impose a very high value of the airflow rate when using the channel model, leading to null axial gradients of temperature and water vapour content, but considering the appropriate convective coefficients. The heat and mass transfer rates achieved in such conditions can be taken as ideal transfer rates or as

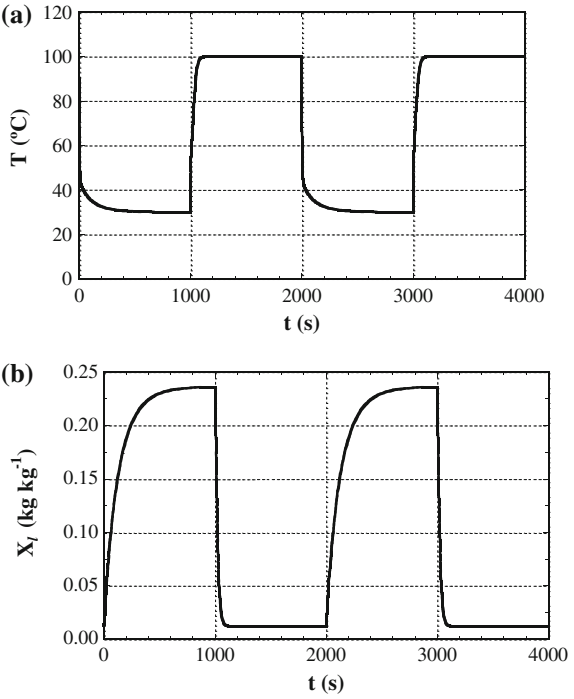

Fig. 10 Cyclic evolutions of: **a** average temperature and **b** average adsorbed water content in the desiccant wall of the channel

reference values for the evaluation of the sorption process effectiveness of a real desiccant wheel. As an example, Figs. 10 and 11 show the predicted modelling results for a channel wall element of a matrix composed only by a layer of silica gel with thickness of 0.1 mm. The specific transfer area and the porosity of the matrix were 1,932.9 m^2 m^{-3} and 0.806, respectively. The duration of the cycle was set to 2,000 s and the frontal areas of the adsorption and desorption zones are equal. The state of the airflow in the adsorption zone (process air) was characterized by the temperature and water vapour content values of 30°C and 0.01 kg kg^{-1}, respectively. In the desorption zone (regeneration airflow), the temperature and the water vapour values of 100°C and 0.01 kg kg^{-1} were assigned. The cyclic evolutions of the average values of he temperature and of the adsorbed water content of the desiccant wall represented in Fig. 10 were evaluated from the distribution of the respective variables predicted by the numerical modelling. The illustrated case corresponds to a sequence of two adsorption/desorption cycles, starting by the adsorption process. As expected, the temperature of the wall decreases and increases during the adsorption and desorption processes, respectively. It is observed that the desiccant wall achieves the equilibrium with the airflow in both the adsorption and desorption processes. In the adsorption period, the variations in the desiccant wall temperature occur during the first half. In the desorption process, those variations occur just in a short initial period.

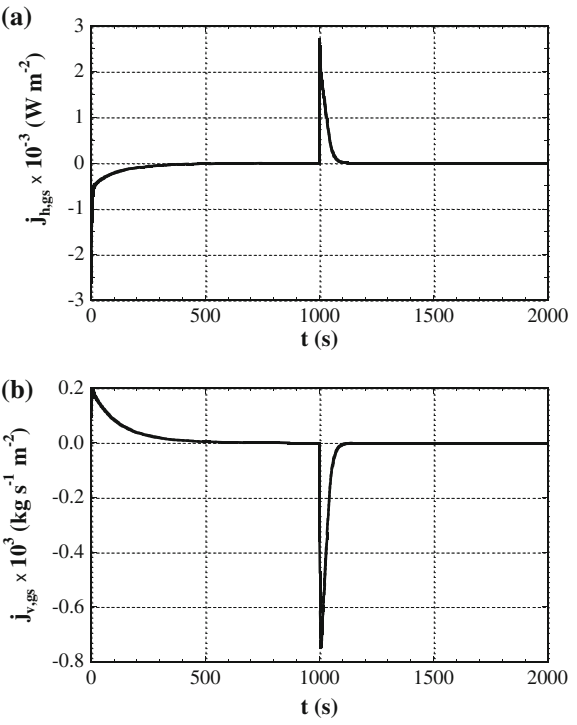

Fig. 11 Cyclic evolutions of the transfer rates per unit of transfer area of the matrix: **a** heat rate and **b** mass rate

The time required for stabilizing the adsorbed water content is greater in the adsorption than in the desorption period. The represented evolutions lead to the conclusion that, for dehumidification purposes, an improvement of the cycle can be performed by reducing the frontal area of the desorption zone, i.e., decreasing the desorption process duration and increasing the rotation speed of the matrix.

Figure 11a, b show the evolutions of the heat and mass transfer rates per unit of transfer area, respectively, during a typical adsorption/desorption cycle. These evolutions are related with those shown in Fig. 10. It is observed that after the sorption process transition (adsorption to desorption or vice versa), both transfer rates exhibit strong variations.

The results of a parametric study focused on the characterization of the influence of the duration of the cycle (τ_{cyc}) on the mass and heat transfer rates per unit of transfer area of the matrix in the channel element are presented in Fig 12. The states of the airflows and remaining data of the matrix are equal to those indicated above. It is observed from Fig. 12 the existence of an optimum value for the cycle duration that maximizes the mass transfer rate. Furthermore a monotonic dependence of the heat transfer rate on the cycle duration is observed, meaning that for energy recovery purposes the duration of the cycle must be relatively low.

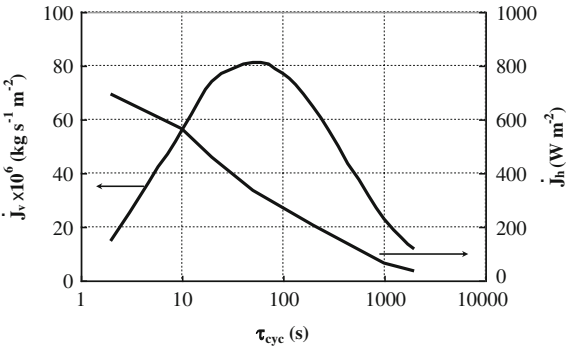

Fig. 12 Heat and mass transfer rates

5.2 Desiccant Wheel Performance

The cell dimensions, the desiccant wall thickness and the operating parameters influence the behaviour of the hygroscopic matrix of a desiccant wheel. The results here presented refer to desiccant wheels operating at steady state composed by cells B and C that are characterised in Table 5, assuming that $S_p = 0$ and $P_{cell} = P_{sin}$ (see Figs. 5 and 6).

The results presented in Fig. 13a, b refer to the hygroscopic rotor with equal adsorption and desorption zones, operating at atmospheric pressure (101325 Pa). The inlet temperature values of the process and regeneration airflows were 30 and 100°C, respectively. The inlet water vapour content and mass velocity in both airflows were considered equal to 0.01 kg kg^{-1} and 1.5 kg s^{-1} m^{-2}, respectively. The channel wall was assumed to be composed by a desiccant layer without substrate and the length channel was 0.3 m.

From Fig. 13 it is observed that the outlet temperature of the process air decreases with increasing cycle duration, meaning that the heat transfer rate is higher at high rotation speeds. It can also be observed that the heat transfer rate decreases when the desiccant layer thickness increases. The highest heat transfer rate corresponds to the case of the wheel having the lowest thickness of the desiccant layer, when operating at a low cycle duration, which is a characteristic of the operation of enthalpy wheels.

Due to the relatively low specific transfer area of the matrix with cells of family C, the temperature changes occurring in the process airflow are small, leading to low values of the heat transfer rate.

The dependence of the outlet water vapour content of the process airflow on the cycle duration is completely different from the one registered for the outlet temperature in both cell families. Optimum values of the cycle duration can be found that maximize the moisture removal capacity of the desiccant wheel. This is identified more clearly in Fig. 13a by the minimum values of the outlet water vapour content in the process airflow, which are practically independent of the

Table 5 Characteristic geometric parameters of cells of family B and C

Cell family	Cell	E_p (mm)	H_{sin} (mm)	ε_m	a_s (m^2 m^{-3})
B:	B1	0.05	1.38	0.918	3,280
H_{cell} = 1.5 mm	B2	0.075	1.33	0.879	3,239
P_{cell} = 3 mm	B3	0.1	1.27	0.84	3,198
	B4	0.25	0.95	0.627	2,980
C:	C1	0.05	4.88	0.975	1,004
H_{cell} = 5 mm	C2	0.075	4.82	0.963	1,000
P_{cell} = 10 mm	C3	0.1	4.76	0.950	995
	C4	0.25	4.42	0.878	972

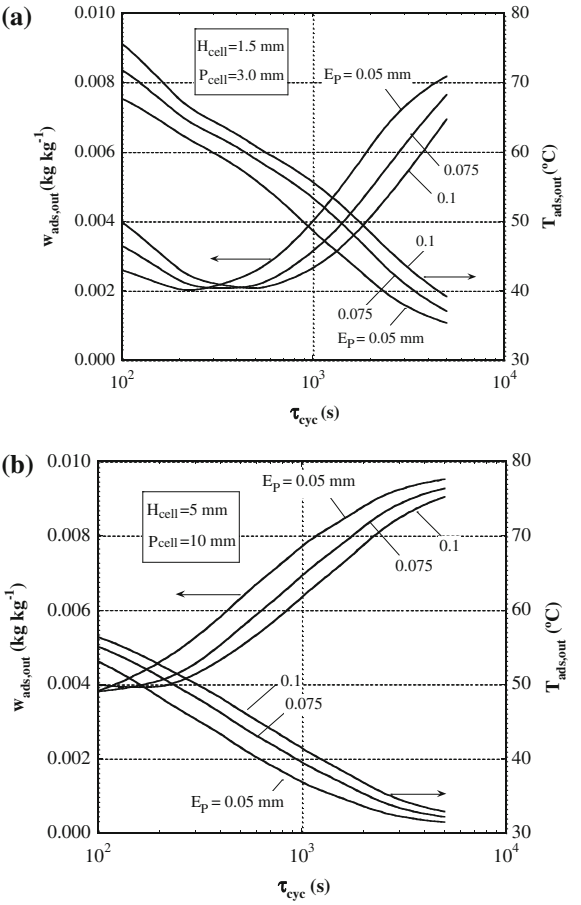

Fig. 13 Outlet state of the process airflow in a hygroscopic wheel composed by cells of: **a** family B and **b** family C

values of wall thickness considered. Furthermore, it is observed that the optimum value of the cycle duration for each cell family increases with the thickness of the desiccant layer. Moreover, the optimum values of the duration cycle in cells of family C are lower than those of the family B.

6 Conclusions

The numerical detailed modelling of the heat and mass transfer phenomena occurring in hygroscopic matrices of desiccant wheels requires the prior knowledge of a large number of parameters and properties of the desiccant porous medium. The adoption of simplifying assumptions is convenient to reduce the complexity of the analysis and the time consumption of the computational calculations. The validity of using the *low mass transfer rate theory* in evaluating the convective transfer rates in the coupled heat and mass transfer was demonstrated. The different parametric studies conducted with the detailed numerical model evidence important guidelines for the manufacturing optimization of desiccant wheels, namely regarding the rotation speed, the wheel partition, as well as the specific transfer area and porosity of the hygroscopic matrix.

References

1. Ruivo, C.: Modelação numérica dos fenómenos de transferência de calor e de massa em rodas higroscópicas, Ph.D thesis, University of Coimbra, Coimbra, Portugal (2005)
2. Ruivo, C., Costa, J., Figueiredo, A.: Analysis of simplifying assumptions for the numerical modeling of the heat and mass transfer in a porous desiccant medium. Numer. Heat Transfer, Part A: Appl. **49**, 851–872 (2006)
3. Ruivo, C., Costa, J., Figueiredo, A.: On the behaviour of hygroscopic wheels: part I—channel modelling. Int. J. Heat Mass Transfer **50**, 4812–4822 (2007)
4. Ruivo, C., Costa, J., Figueiredo, A.: Numerical study of the behavior of an elementary desiccant layer of a hygroscopic rotor. Numer. Heat Transfer, Part A: Appl. **53**, 1037–1053 (2008)
5. Ruivo, C., Costa, J., Figueiredo, A.: On the validity of lumped capacitance approaches for the numerical prediction of heat and mass transfer in desiccant airflow systems. Int. J. Therm. Sci. **47**, 282–292 (2008)
6. Kodama, A.: Experimental study on optimization of a honeycomb rotor continuous adsorber operated with thermal swing. Ph.D thesis, Faculty of Engineering, Kumamoto University, Japan (1996)
7. Pesaran, A.: Moisture transport in silica gel particle beds. Ph.D thesis, University of California, Los Angels (1983)
8. Ruivo, C., Costa, J., Figueiredo, A.: On the behaviour of hygroscopic wheels: part II—rotor performance. Int. J. Heat Mass Transfer **50**, 4823–4832 (2007)
9. Ruivo, C., Costa, J., Figueiredo, A.: Validity of pseudo-gas-side-controlled models to predict the behaviour of desiccant matrices. Int. J. Therm. Sci. **48**, 2171–2178 (2009)
10. Çengel, Y.: Heat Transfer—A Practical Approach. McGraw-Hill, New York (1998)
11. Zhang, X.J., Dai, Y.J., Wang, R.Z.: A simulation study of heat and mass transfer in a honeycomb rotary desiccant dehumidifier. Appl. Therm. Eng. **23**, 989–1003 (2003)
12. Mills, A.: Heat and Mass Transfer. CRC Press, Boca Raton (1994)
13. Niu, J.L., Zhang, L.Z.: Heat transfer and friction coefficients in corrugated ducts confined by sinusoidal and arc curves. Int. J. Heat Mass Transfer **45**, 571–578 (2003)
14. Patankar, S.: Numerical Heat Transfer and Fluid Flow. McGraw-Hill, Washington (1980)